DISSERTATION

INSIGHT INTO ALTERNATIVE BATTERY TECHNOLOGIES USING 3D CONFIGURATIONS, PROTECTIVE COATINGS, AND CHARACTERIZATION OF RESISTIVE PROPERTIES

Submitted by

Daniel S. Windsor

Department of Chemistry

In partial fulfillment of the requirements

For the Degree of Doctor of Philosophy

Colorado State University

Fort Collins, Colorado

Spring 2025

Doctoral Committee:

Advisor: Amy L. Prieto

James R. Neilson
Matthew P. Shores
Todd M. Bandhauer

ABSTRACT

INSIGHT INTO ALTERNATIVE BATTERY TECHNOLOGIES USING 3D CONFIGURATIONS, PROTECTIVE COATINGS, AND CHARACTERIZATION OF RESISTIVE PROPERTIES

The omni presence of lithium-ion batteries (LIBs) have revolutionized the modern world due to this technology's implementation as an energy storage device in smart phones, wearable electronics, and electric vehicles. Lithium-ion batteries are well suited for these applications owing to the light weight of these systems and their ability to store a large amount of charge. For these reasons, LIBs are classified as energy dense systems, which describes the amount of energy a technology can store per unit mass. A battery metric where LIBs struggle in terms of performance is power density, or the amount of power a technology can produce per unit mass. These systems, also, require expensive feedstock materials that are geographically isolated which has profound impacts on economics and supply chain considerations for LIBs. Thus, if rechargeable batteries are to continue to advance, alternative battery configurations and chemistries must be studied.

Chapter 1 describes the field of LIBs, in terms of the advantages and disadvantages of this technology. This discussion is followed by brief mentions of some of the champion materials found in the anodes, cathodes, and electrolytes currently implemented in LIBs. The discussion on the champion materials for LIBs also covers the drawbacks of each material, and ways in which future investigations can improve their performance. This is then followed by a section which highlights how alternative battery configurations and chemistries can address some of the inherent

disadvantages of the LIBs system. This chapter concludes with a discussion on some important soft skills the author learned during the completion of this degree.

Chapter 2 covers the development and advances made in the field of 3D batteries. This chapter begins with an introduction of the 3D battery field and includes a section which discusses the current advances made in the literature. This is then followed by a discussion on the computational advances made in the field of 3D batteries, where there is a critical need to develop digital twins of 3D batteries to better understand the chemo-mechanical dynamics of these complex systems. The following portion of this chapter covers the development of 3D batteries through the lens of critical performance metrics, being power density, energy density, and cyclability and scalability. For 3D batteries, this chapter identified that improvements in energy density is the area where further advances are most needed. Finally, this chapter discuss efforts being made in industry toward the commercialization of these 3D battery systems.

Chapter 3 covers an investigation into the fundamental effect of a polymer protective coating, cyclized-polyacrylonitrile (cPAN), on the Na-ion (de)insertion chemistry of antimony-based anodes in sodium-ion batteries (NIBs). This investigation was able to determine that the cPAN coating had the most pronounced effect on the early cycle (cycles 1-10) Na-ion (de)insertion chemistry of the antimony-based anodes. The interfacial resistance was, also, diminished by the presence of the cPAN protective layer which implies that the cPAN helps to facilitate Na-ion transport at the electrode-electrolyte interface.

Chapter 4 discusses a practical and beginners' approach to the learning electrochemical impedance spectroscopy (EIS) for rechargeable batteries. This chapter begins with a simple deconvolution of the EIS acronym, such that the reader has a deeper understanding of how each component of the acronym combines to create this technique. The chapter continues by discussing how to preform both qualitative and quantitative EIS analyses on rechargeable batteries, and finishes with a discussion on the EIS specifics of rechargeable battery systems.

Chapter 5 covers the future areas in which the work presented in Chapter 3 can be extended. In particular this chapter discusses the critical need to quantify the SEI products of a cPAN coated antimony electrode, as early cycle numbers, and ways in which cPAN can be applied to high surface area substrates to ideally formulate a 3D sodium-ion battery.

ACKNOWLEDGMENTS

This graduate school journey would not have been possible without the guidance, encouragement, and support from a plethora of people. First and foremost, I must thank Amy Prieto. Thank you, Amy, for letting me work for you and contribute to the Prieto Group. I appreciate your approach to science, your emotional quotient, and your patience. I know that I had some growing pains during my time in your group, so thank you for being patient and for helping me grow into the scientist and person I am today. I will forever strive to communicate science as you do, and I will forever attempt to be as personable, and kind as you have been these past five years.

I would also like to thank Kelly Nieto Ph.D. Thank you Kelly for your mentorship, patience, and comradery. I know, for a fact, that I would not be half the scientist I am today without your tutelage and guidance. You taught me how to ask scientific questions, and how to attack these questions in lab.

To my comrades in the struggle, I would like to thank Luke Salzar Ph.D., Monika Perez, and Nathan Neisius Ph.D. Luke, thank you for being an amazing friend and collaborator. The comradery you have shown me and the laughs we have shared have been instrumental in this crusade. Monika, thank you for holding it tf down and being a mega homie. Que tengas suerte con el resto de la aventura. Nate, thank you for being such a constant source of support and motivation. Your presence in the Prieto group and your essence as a human made this graduate school process possible. I simply would not have been able to complete this journey without you there. Thank you for being my 2BC brother and for being such a great guy.

To the Ducks, thank you for being a constant source of laughter and escape from the trials and tribulations of grad school. Eric and Jon, I relish the times we'd hop on a call on call and laugh ourselves sore over Wet Boy edits. Foster and Nathan, thank you both for all the hilarious and stimulating conversations. Spending time with you two has been an excellent escape from what at times seemed like a nightmare.

To Chris and Joseph, thank you guys for being an endless fountain of support. All of times watching cycling and riding bikes have filled me with so much joy. You two have been there for me when I have need it most. Chris, I have always left our hours long phone conversations feeling uplifted and. Joseph, our crazy adventures on the bicycle were amazing challenges to push myself, in every aspect of my life.

In addition, I would like to thank Kathy Lukas and Ron Costello as their roles as the foundation of the chemistry department at CSU. No Ph.D. would be possible without the ceaseless effort of these two amazing individuals. No one is more effective an administrator than Kathy, no one is as hard working and funny as Ron.

Tengo que decir gracias, también, al tío mío de España. José, gracias por todo el apoyo que me has dado durante de todo este tiempo. Nuestras conversaciones han estado tan importantes para mantener el foco and el ánimo necesario para completar esta aventura de locura. Gracias por todo, y te visitaré pronto.

The next person I must thank has been one of the most important factors in my ability to achieve this degree. Cort, thank you for being my day one comrade. Your poise and level headedness have had a profound impact on my ability to deal with the high highs and low lows of the grad school process. I truly feel lucky to have spent these last several years as your roommate!

One of the largest sources of support throughout this whole process has been my family. Thank you all such much for the unconditional love and support you have shown me throughout this whole process. I simply would not have made it this far without your encouragement! I love you all so dearly and am so lucky to have you as my family!

Finally, the biggest thank you goes to Alexandra Koegel Ph.D. You have been the most supportive and lovely partner I could ever have asked for. You taught me to tune out the noise, and how to validate myself as a student and a scientist. The troubles of the world melt away whenever I am with you, which holds particularly true when these troubles relate to graduate school. I know that the completion of this Ph.D. journey would not have been possible without you in my corner. I love you and will forever appreciate the shining example you have set! I will forever look up to you as a scientist and as a person.

DEDICATION

This work is dedicated to Katrin Schläppi, John Windsor, and Alexandra Koegel Ph.D.

TABLE OF CONTENTS

CHAPTER 1: Introduction

1.1 Rechargeable batteries, what are they and how do they work?

Since the development of the lithium-ion battery (LIB) by Whittingham, Yoshino, and Goodenough, LIBs have become an omnipresent part of the modern world. This technology is usually found in consumer electronic devices such as smartphones, wearables, and electric vehicles (EVs). Given the ubiquity of smartphones and the increase in the number of EVs on today's roads, it is no surprise that the market for LIBs is quite large. Specifically, the global LIBs market is about $54.6bn/year and should only grow in value as more EVs hit the road.[1]

A LIB is classified as a rechargeable (or reversible) electrochemical energy storage device, where charge (in the form of Li^+ ions) is stored within the lattices of solid-state electrode materials. A traditional LIB, as seen in **Figure 1.1**, consists of an anode (graphite), a cathode (lithium cobalt

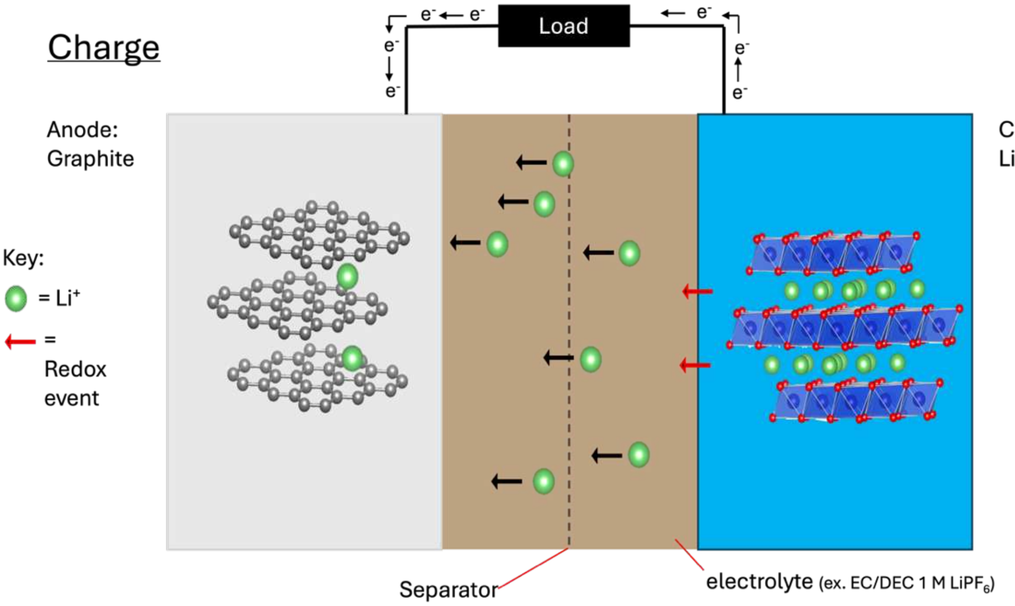

Figure 1.1: Schematic representation of a lithium-ion battery during the charge process. The anode material is graphite, the cathode material is lithium cobalt oxide (Li_xCoO_2), the electrolyte is a formulation of 1 M lithium hexafluorophosphate ($LiPF_6$) in ethylene carbonate (EC) and diethyl carbonate (DEC) in a 1:1 ratio by

oxide aka LCO), and a liquid organic electrolyte. Electrolytes in LIBs are usually formulated with carbonate-based solvents and lithium salts (e.g. $LiPF_6$ or $LiClO_4$).[2]

When a LIB is being charged the graphite anode is negatively polarized, and the positively charged Li-ions travel through the electrolyte toward the anode due to electrostatics. The Li-ions are inserted into the lattice of the graphite anode, where they can be stored. Due to the electrochemical requirement of charge balance, as Li-ions are inserted into the anode they must also be removed from the cathode at the same time. This process occurs until the anode has accepted as many Li-ions as is physically possible for the graphite anode. At this point the battery is classified as being fully charged. When the battery is discharged, **Figure 1.2**, the ions travel toward the LCO cathode.

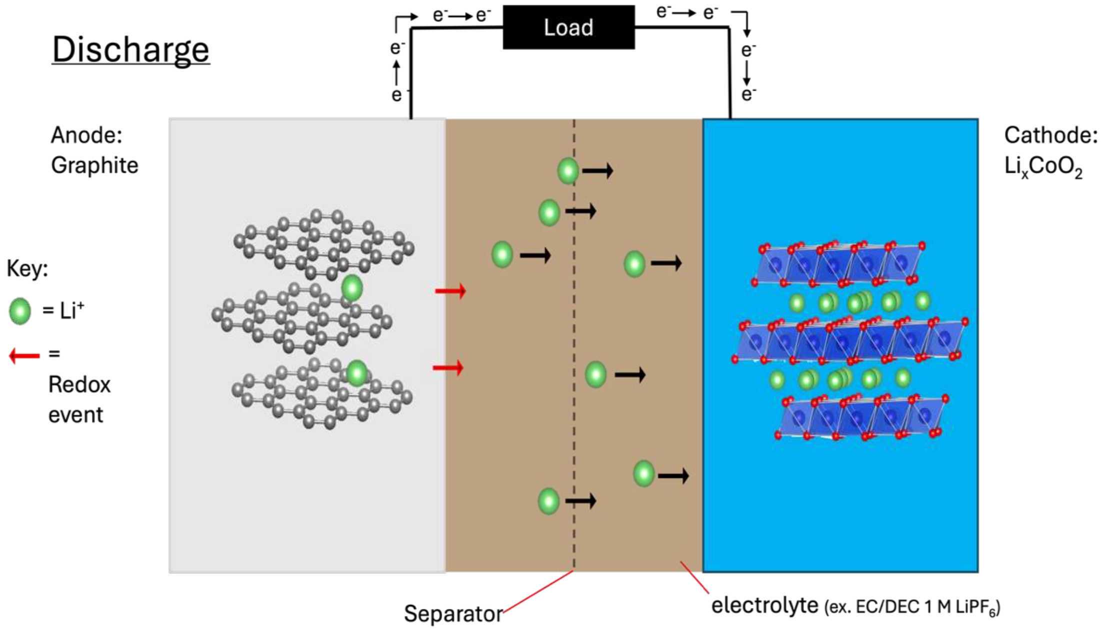

Figure 1.2: Schematic representation of a lithium-ion battery during the discharge process. The anode material is graphite, the cathode material is lithium cobalt oxide (Li_xCoO_2), the electrolyte is a formulation of 1 M lithium hexafluorophosphate ($LiPF_6$) in ethylene carbonate (EC) and diethyl carbonate (DEC) in a 1:1 ratio by volume.

This process can be thought of as the "downhill" reaction, where it is more energetically favorable for the Li-ions to reside in the lattice of the LCO cathode compared to the graphite anode. As ions are inserted into the LCO cathode, ions are removed from the graphite anode, once again to maintain charge balanced in the electrochemical system. As ions are removed from the graphite anode, electrons are generated and are shuttled into the external circuitry of the system. The electrons generated from the removal of Li-ions from the anode are used to do work (i.e., the electrons generated from the removal of ions from the anode are what powers a cell phone).

Since LIBs are classified as an energy storage device, the total amount of energy stored by these systems is incredibly important. To gauge a LIBs ability to store charge, investigators must assess both the operating voltage and specific capacities of the battery and electrode materials, respectively. The operating voltage defines the total amount of energy that can be stored by the battery. A battery with a high operating voltage allows the systems to release more stored energy than if the operating voltage was smaller. LIBs, for example, generally have a high operating voltage (roughly 3 V) which is one of the reasons this system is often applied as the energy storage device in portable electronics. The specific capacity of the electrodes provides insight into the amount of charge each electrode can store (with units of mAh/g or C/g). This metric is a crucial proxy for the energy a battery can provide, as the amount of charge each electrode can store is directly related to the amount of energy the battery can provide. Batteries that cannot store a lot of energy will require lots of recharging, making them ineffective for commercial application. Another important metric to gauge the performance of a battery is to understand how the battery behaves when cycled at a very high rate. This metric is classified as the rate performance and has profound implications on the amount of power a battery can provide. A battery that can provide high power is crucial for applications where a quick release of energy is needed (e.g. batteries in electric vehicles). Batteries with poor rate performance lead to systems with slow charge and discharge times, limiting the amount of power the system can provide. Finally, the interfacial stability of the interfaces within a battery is critical to understand if a battery is to perform well. The significance of the interfacial stability arises due to the various detrimental side reactions that occur between the electrodes and the electrolyte as the battery is cycling. For the anode, reactions with the electrolyte in LIBs form an interfacial layer termed the solid-electrolyte interphase (SEI) which has profound effects on the cycling performance of the battery. Poor interfacial stability in a battery has profound effects on the energy and rate performance of the battery and can lead to premature death of the system.

Another performance metric important for LIBs is associated with the safety of these systems. The safety concerns relate to the flammability of LIBs, which results from the volatility of the organic solvents traditionally used in the electrolyte.[3] These constituents can ignite from physical penetration of the battery or thermal runaway of the system and are compounded by the oxygen rich LCO cathode, functioning to fuel the fire. The result of these factors is that if a LIB catches fire, it will burn for a long time. An example of this can be found in the experience of TV presenter Richard Hammond. In 2017, Hammond was participating in a hill climb challenge and, unfortunately, crashed an electric supercar. The car shortly ignited and although Hammond was able to escape, the car burned for five whole days.[4]

Despite these safety concerns, the LIBs technology has become ubiquitous in the modern world due to the system's ability to reversibly store a high amount of charge with low weight. Current LIBs systems have decent rate performance and have been optimized to control the interfacial interactions between the electrodes and the electrolytes. The next section will discuss the materials currently included in LIBs, as well as ways in which these materials can be manipulated/changed to improve the energy, rate performance, interfacial stability, and safety of LIBs.

1.2 Current materials in lithium-ion batteries, and ways to improve them

Cathodes

Cathode materials in a LIB are classified as the positive electrode during the charge process (**Figure 1**). These materials must have high operating potentials to ensure a large voltage window for the battery and must also store Li-ions reversibly, participating in both oxidative and reductive reactions with Li-ions. As mentioned above, LCO is the traditional cathode material used in LIBs, and generally has the chemical formula of Li_xCoO_2.[5] The layered rock salt (isostructural to α-$NaFeO_2$) structure has edge sharing [CoO_6] octahedra which link to from sheets of CoO_2, which are separated by sheets of octahedrally coordinated lithium ions.[6] These lithium ions can travel via two-dimensional pathways, which allows for the insertion (intercalation) or removal (deintercalation) of Li-ions from the CoO_2 sheets.[5,6] **Equation 1.1** displays the reversible Li-ion (de)intercalation reaction from/to LCO.

$$LiCoO_2 \leftrightarrow Li_xCoO_2 + (1-x)Li^+ + (1-x)e^- \tag{1.1}$$

The presence of the Li_xCoO_2 in the right-hand side of **Equation 1** indicates that the Li-ions are not fully removed from the cathode structure during deintercalation.[7] This results from the increased electrostatic repulsion from the CoO_2 sheets that act to bind some percentage of the Li-ions within the cathode structure.[6] The stability of the layered Li_xCoO_2 structure during deintercalation provides for a wide voltage window (up to 4.25 V) for this material.[8] The high operating voltage and reversible (de)intercalation chemistry are reasons behind LCO vast application in LIBs.

There are, however, some disadvantageous aspects of the LCO system for LIBs cathodes. First and foremost, the feedstock materials for the LCO system are expensive and geographically isolated.[9] Cobalt is quite expensive with a price point of \$22,044/ton and is mostly mined in the Democratic Republic of the Congo.[10] These aspects of this material combine to greatly affect the environment and people who live in this region due to the economic factors driving the consumption of these materials.[11] In addition to the broader downsides to using LCO cathodes, this system also suffers from intrinsic properties of the material; such as the low electrical conductivity of LCO and its sluggish ion diffusion kinetics ($5x10^{-9}$ cm^2 s^{-1}), which lead to poor rate performance for this cathode.[5]

Given the disadvantages of the LCO cathode system, much work has been conducted in the field aimed at improving this system to be cheaper and have better rate performance. A common approach toward doing so is by substituting a certain percentage of Co from the LCO structure with different transition metals. There are a plethora of systems like this, however this discussion will focus on lithium nickel manganese oxide ($LiNi_ZMn_yCo_{1-z-y}O_2$ or NMC).[8] This system reduces the extent of Co incorporation by substituting for certain percentages of Ni and Mn. The Ni also participates in several redox reactions (Ni^{2+}/Ni^{3+} and Ni^{3+}/Ni^{4+}), which helps to improve the achievable capacity of the system.[12] High Ni content NMC, like $LiNi_{0.8}Mn_{0.1}Co_{0.1}O_2$ (NMC-811), has been shown to provide excellent rate performance and capacity (roughly 210 mAh g^{-1}), even at 3.8 V.[13] The high Ni content NMC, however, suffers from poor cycling stability when cycled to 4.2 V due to parasitic interactions with the electrolyte and dissolution of the transition metals from the NMC cathode.[14,15] Modifications of the surface of the NMC particles are a viable approach toward mitigating the poor performance of high Ni content NMC at high voltages.

A straightforward approach to the surface modification of high Ni content NMC is to use atomic layer deposition (ALD), which is a vapor-phase deposition technique with precise control of the deposited chemistry, traditionally a metal oxide. This control arises from the fact that ALD leverages self-mediated surface reactions between precursor gasses and the substrate, which are cycled to achieve the desired thickness of the deposited coating.[16] Concerning NMC cathodes, work in the field has been conducted which demonstrates improvements in the capacity and rate performance in high Ni content NMC via Al_2O_3 and Zr_xPO_y coatings.[14,17] These coatings serve to passivate the surface of the NMC cathode, which improves the interfacial stability at this electrode and helps reduce the amount of metal dissolution from the cathode into the electrolyte.

Anodes

Anode materials are classified as the negative electrode during the charge process. These materials must have a low operating voltage, to ensure a large voltage window for the battery. Traditionally, graphite is used as the anode materials in LIBs because it can stably and reversibly store Li-ions between the carbon layer sheets within the electrode for many cycles.[18] These aspects of graphite are the reasons behind this material's vast implementation in commercial LIBs. **Equation 1.2** displays the electrochemical (de)intercalation reaction of graphite with Li-ions.

$$C_6 + Li^+ + e^- \leftrightarrow LiC_6 \tag{1.2}$$

Graphite has a theoretical specific capacity of 372 mAh g^{-1}, which is rather low for anode materials.[19] This low theoretical capacity can be visualized in the right-hand side of **Equation 1.2**, where six units of graphite are required to store one Li-ion. Also, graphite has sluggish Li-ion diffusion kinetics, where the D_{Li} for graphite is on the order of 10^{-12}-10^{-14} cm^2 s^{-1}.[19] As such, graphite is that it is not able to store high quantities of charge (affecting the amount of energy that can be stored) and struggles with rate performance.[20]

Given the desire to increase the energy density of LIBs, the field is aimed at developing novel anode materials which can store more charge than graphite. One such class of materials is called conversion electrode materials. Conversion electrode materials are classified as materials that store charge (in the form of active ions) through the formation of a new phase between the active ion and the host material. The canonical example of these materials is Si, where **Equation 1.3** shows the (de)lithiation reaction of Si with Li-ions.

$$4Si + 15Li^{+} + 15e^{-} \leftrightarrow Li_{15}Si_{4} \tag{1.3}$$

Through this equation, 3.75 equivalents of Li-ions are stored per one unit of Si in the anode. This feature of Si conversion electrodes provides Si with a theoretical specific capacity of 3579 mAh g^{-1}, almost ten times greater than graphite.[21] The implication of this high theoretical capacity for LIBs means a significant increase in the energy density of the battery. Implementation of Si conversion anodes in LIBs is an incredibly popular and attractive approach toward improving the energy density of this battery technology.

Conversion anode like Si have serious drawback concerning the cycling stability of these systems. When Li-ions are reacted with Si a new crystallographic phase of lithium silicide ($Li_{15}Si_4$) is formed (**Equation 1.3**). The change in phase of the anode from Si to $Li_{15}Si_4$ causes a change in the unit cell volume of roughly 300%.[21] The result of this large amount of volume expansion is mechanical breakdown and fracturing of the Si electrode material. The mechanical pulverization of Si electrodes leads to unfavorable interactions with the electrolyte and loss of contact of the active material to the current collector; both of which contribute to a dramatic drop in the achievable capacity of the anode as it is cycled.[22] These factors lead to poor cycling stability of Si electrodes as anode for LIBs.

Given the potential to increase the energy density of LIBs through the inclusion of Si anodes, significant work in the field is aimed at improving the cycling stability of this system. Investigators have studied the effect of nanoparticle (NP) Si electrodes and the formulation of silicon-carbon (Si-C) composite materials on the cycling stability of Si. The benefit of using NP-Si is that the NPs can alleviate the mechanical stresses of the inherent volume expansion Si when it stores Li-ions.[23] Various studies have shown that the application of NP-Si in carbon composite electrodes greatly improves the cycling stability of Si anodes.[23–25] This is done by applying a conductive coating as a shell for a NP-Si core, or by including NP-Si in a high surface area carbon matrix during processing.[23] The improvement in the cycling stability if Si anodes through nano-structuring has led to industrial efforts toward the commercial implementation of Si anodes in LIBs. Companies such as Sila Nanotechnologies, Amprius Technologies, and Enovix are making progress in this respect.

An alternative system, the Li-metal anode, can store more charge than Si conversion electrodes by leveraging the Li/Li$^+$ plating/stripping reaction (**Equation 1.4)**.

$$Li^+ + e^- \leftrightarrow Li \tag{1.4}$$

The energy related to this redox reaction (-3.04 V vs. NHE) provides Li-metal anodes with a theoretical specific capacity of 3860 mAh g^{-1}.[26] While Li-metal anodes have the highest theoretical capacity, the system suffers from extremely unstable cycling under standard conditions several reasons. Firstly, the ductility of Li-metal results in a rough surface which leads to the localization of current density at specific points, which causes the formation of Li-dendrites.[26] Li-dendrites irreversibly consume the Li in the battery which can cause a short circuit and have produce profound safety implications.[27,28] Secondly, Li-metal anodes are extremely reactive with traditional liquid electrolytes which results in the excessive formation of the solid-electrolyte interphase (SEI). This excessive SEI formation depletes the Li-content in the cell and leads to an increase in the interfacial resistance at the anode-electrolyte interface.[27] The reactivity of Li-metal anodes with organic liquid electrolytes indicate that these two materials are incompatible in a LIB. To address this incompatibility, researchers have been studying the compatibility of solid-state electrolytes (SSEs) with Li-metal anodes.

Similar to the Si system, the LIBs research field is focused on ways Li-metal anodes can be stabilized to improve cycling performance of this anode system. A popular approach toward doing so is increasing the pressure applied to the battery, particularly for all solid-state battery (ASSB) systems.[27] Increasing the stack pressure applied to a Li-metal ASSB cell functions to improve the uniformity of the electric fields driving Li-transport in the battery, and the contact between the current collector and the Li-metal active material.[28]

Although the interactions between each battery component affects performance, the interactions between the anode and the electrolyte can affect the battery for better or for worst. The next section will cover electrolytes, and how their composition and reactivity can affect battery performance.

Electrolytes

Electrolytes in a LIB are the media in which Li-ions can travel between the two electrodes in the cell. An electrolyte must be an electric insulator to mitigate short circuiting between the anode and the cathode. High ionic conductivity is advantageous in an electrolyte, so that there is little resistance related to the movement of ions through this media. Traditionally, organic electrolytes are used in LIBs due to their high ionic conductivities and low electric conductivity.[2] These electrolyte formulations generally use carbonate-based solvents like ethylene carbonate

(EC), diethyl carbonate (DEC), or propylene carbonate (PC) with lithium containing salts like lithium hexafluorophosphate ($LiPF_6$) or lithium perchlorate ($LiClO_4$). Electrolytes formulated using lithium salts and carbonate-based solvents have ionic conductivities on the order of 10^{-3} S cm^{-1}.[2]

While the ionic conductivity of organic liquid electrolytes is quite high, these systems are unstable and decompose as a battery is cycling. This instability arises from the potential window used for LIBs cycling being outside of the electrochemical stability window of organic liquid electrolytes.[29] The result of the discrepancy between the potential window of battery cycling and the electrochemical stability of the electrolyte leads to reduction of the electrolyte components at the anode, which produces the SEI.

The formation of the SEI is inherent to any battery system where the electrolyte electrochemical stability window is inside the potential window of cycling. Formation of the SEI, compositionally speaking, comprises both organic and inorganic phases.[30] The characterization of this interphase is extremely challenging and requires the use of various, complementary, characterization techniques like XPS in conjunction with mass spectrometry.[31] The SEI passivation layer has a profound effect (for better or worse) on the performance of a LIB.[30] An SEI layer, if behaving optimally, will be a very thin layer that is electrically resistive, ionically conductive, and robust enough to remain intact during cycling. The result of an optimally functioning SEI is a battery that can cycle stably without deleterious side reactions associated with electrolyte degradation. If behaving detrimentally, the SEI can irreversibly consume Li-ions from the bulk electrolyte which can increase the resistance of this layer.[32] In addition, it can reform as the battery is cycled which results in more irreversible reactions consuming Li-ions and increasing the resistance of the SEI layer.[33]

Given the ubiquity of the SEI on anodes in LIBs with organic liquid electrolytes, serious efforts have been made in the field to understand ways to improve the stability of the as-formed SEI. These approaches generally use sacrificial electrolyte additives that reduce onto the anode surface prior to the reduction of the constituents of the bulk electrolyte. Two of the most popular sacrificial additives used in liquid organic electrolyte formulations are fluoroethylene carbonate (FEC) and vinylene carbonate (VC). These additives, in their own respects, clearly show an improvement the stability of the SEI and in the performance of a battery in which these additives are applied.[34,35]

Organic liquid electrolytes, with sacrificial additives, are commonly applied in commercial LIBs. These electrolyte systems still suffer from profound safety concerns related to the volatility of the organic solvents in these electrolyte systems. To mitigate these concerns, significant effort are being made in the battery field to develop solid-state materials that can function as the electrolyte in LIBs. These materials are classified as SSEs (solid-state electrolytes) and can be formulated via myriad different materials. Inorganic SSEs are multinary systems which contain ion channels in which Li-ions can travel.[36] The original example of an inorganic SSE is lithium phosphorous oxynitride (LiPON) with a general chemical formula of $Li_xPO_yN_z$.[3] LiPON SSE is not flammable and is electrically insulating enough to negate short-circuiting of the cell, making it a significantly safer electrolyte than traditional liquid organic formulations .[36] SSEs are well suited to serve as electrolytes for Li-metal systems, owing to the hypothesis that the mechanical properties of the SSE can alleviate the formation of Li-dendrites at the Li-metal electrode.[37]

Despite the advantages of LiPON, this system has an incredibly low ionic conductivity for Li-ions on the order of 10^{-6} to 10^{-8} S cm^{-1}.[3,38] Low ionic conductivity of LiPON leads to poor rate performance for the system in which the SSE is applied. However, sodium super ionic conductors

(NASICON) can provide significantly higher conductivities than LiPON on the order of x10^{-4} to x10^{-3} S cm^{-1}.[36] The high ionic conductivity of NASICON materials have the potential to make a massive impact on LIBs, as these ionic conductivity values are on the same order of magnitude as traditional liquid electrolyte formulations. These NASICON materials generally have the chemical formula of $AMM'P_3O_{12}$, where A is an alkali ion or alkaline earth metal ion (e.g. Li^+ or Na^+, Mg^{2+} or Ca^{2+}), M and M' are sites occupied by multi-valent transition metals (e.g. Zn^{2+}, Ti^{4+}, or V^{5+}) which can aid with charge balancing in the lattice.[38] The high ionic conduct ivies in these materials results the ability of the A cation to migrate in multiple dimensions.[38]

Although SSEs can provide for safer batteries and, in the case of NASICON materials, can also have high ionic conductivities, there is one aspect of these systems that still needs to be addressed. The contact resistance, or the interfacial resistance between solid-state electrode materials and SSEs, in batteries with SSEs can be quite high, serving to decreases the efficiency of Li-ion (de)insertion and can increase the overall ohmic resistance of the cell.[39] This issue can be mitigated by increasing the stack pressure used in fabrication of an ASSB, however the interfacial resistance between the SSE and the electrodes can still have a deleterious effect on battery performance.[39]

Even though the current materials used in LIBs can still be improved, the LIB technology is clearly very functional and applicable to modern electronic devices. In the energy storage field, LIBs are classified as being *energy dense*. This performance metric has units of Wh/kg (Wh=J) which is the measure of the amount of energy that can be stored per unit mass (horizontal axis in **Figure 1.3**). The reason LIBs are an energy dense system is because a lot of charge can be stored in the solid-state electrode materials; however, Lithium-ion batteries struggle in terms of the power they can provide. This metric is termed the *power density*, with units of W/kg, which is a measure

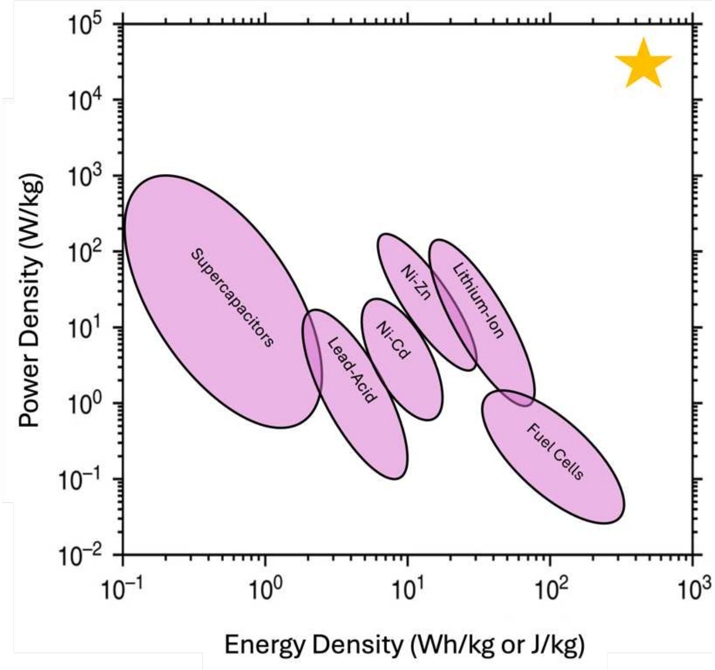

Figure 1.3: Ragone plot representing the energy and power densities of various energy storage systems. The star in the upper right-hand portion of the plot relates to the ideal position of an energy storage technology that is both energy and power dense. This figure was adapted from the work of Windsor and Nieto et al. 2024 (ref 43).

of the power a system can produce per unit mass (vertical axis in **Figure 1.3**). The reason LIBs struggle in terms of power density is that it is difficult to quickly insert/remove Li-ions from the lattice of solid-state electrode materials. In an ideal world, a technology would be developed that is both energy and power dense (yellow star in **Figure 1.3**). For this to occur with a battery system, advances in the performance of electrode materials and the way a battery is configured is needed. The following section will discuss materials commonly used in LIBs, as well as their limitations and ways in which investigators have tried to improve these materials.

1.3 Alternative configurations and chemistries

Lithium-ion batteries currently excel as an energy storage option for consumer electronic devices where high amounts of charge storage and light weight are important design criteria. There are application spaces, like micro-electronics and renewable energy storage, where LIBs are less suited compared to alternative technologies. Concerning micro-electronics, a battery that is very small while still storing high amounts of energy and producing high amounts of power is desired. This is done by interspersing the battery constituents and increasing the active surface area, forming what is classified as a 3D battery.[40] Regarding internment renewable energy systems, like a wind or solar energy, batteries are desired that can store high amounts of charge using cheap and abundant materials. The use of Na-ions as the charge carrier in a rechargeable battery to form a sodium-ion battery (NIB) is an excellent option for large scale charge storage owing to the cheap and a abundant feedstock materials, and the weight of the battery is not a design criterion for this system.

Alternative configurations

As mentioned above, current LIBs struggle to produce high power densities owing to the difficulty of the movement of ions through a solid media. Using traditional battery materials, this issue can be solved by reducing the thickness of the electrode materials which reduces the effect of solid-state diffusion in the system. The downside of this is that the battery will not be as energy dense because there is simply less material to store Li-ions. Thus, if a battery is to be both energy and power dense, alternative ways in which to configure the constituents of a battery are needed.

Theoretically, shorter diffusion paths between electrodes while maintaining the same general charge storage mechanism should provide for a battery system that is both energy and power dense. In practice, this can be done by interspersing the anode, electrolyte, and cathode in multiple dimensions to shorten the diffusion paths for the active ions while maintaining the advantageous energy density properties of LIBs. These battery systems are classified as 3D batteries. **Figure 1.4a** shows a schematic representation of an interdigitated 3D battery, where pillars of anode and cathode materials are interspersed amongst each other, separated by an SSE. **Figure 1.4b** displays a Ragone plot, where the ideal 3D battery is positioned to be both energy and power dense. Literature examples have demonstrated power density improvements, yet there is still a need to increase the energy density of these systems.[41–43]

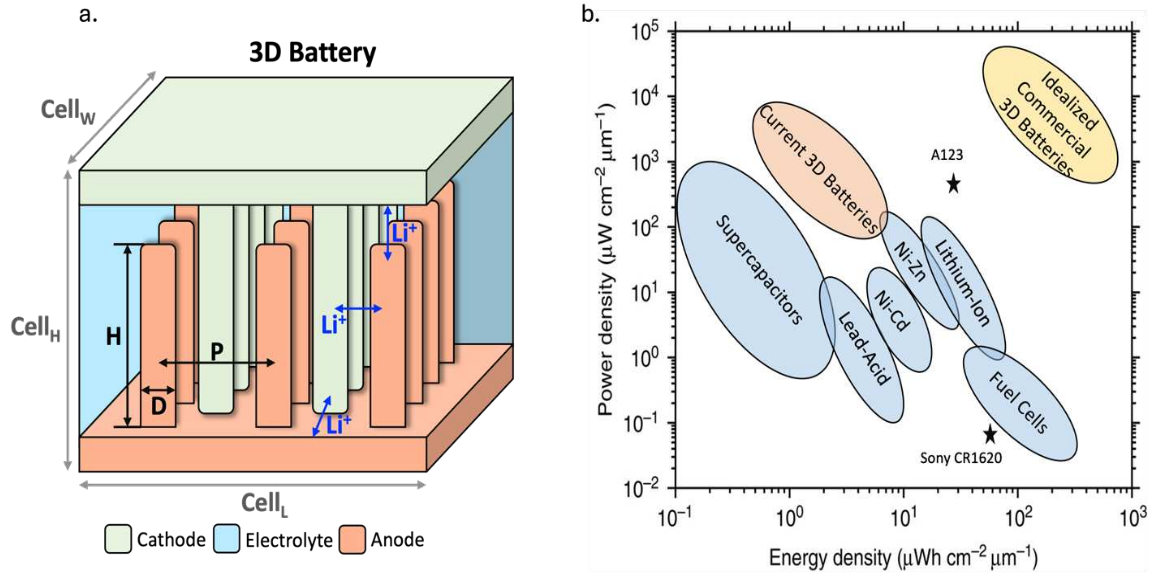

Figure 1.4: Configuration representation and performance metrics of 3D batteries. A) Schematic representation of an interdigitated 3D battery, where pillars of the cathode (green) and anode (orange) are interspersed amongst each other, separated by a solid-state electrolyte (blue). B) Ragone plot which displays the position of an ideal 3D battery (yellow) and current 3D batteries (orange), where a real 3D battery is positioned such that, it is more power dense than it is energy dense. This figure was adapted from the work of Windsor and Nieto et al. 2024 (ref 43).

Alternative chemistries

Lithium-ion batteries are not well suited for large scale energy storage applications due to the expensive nature of this technology's feedstock materials.[9,44] There are alternative battery chemistries that are better suited for larger scale energy storage requirements. Alternative battery chemistries utilize a different active ion as the charge carrier and different materials for the electrodes and electrolytes. Namely, these alternative chemistries are sodium-ion batteries and potassium-ion batteries (KIBs), which leverage Na-ions and K-ions as the charge carrier, respectively. **Table 1.1** compares various properties of lithium, sodium, and potassium.

Table 1.1: Tabulated comparison of the physical properties and price points for lithium, sodium, and potassium. This table was adapted from the work of Wu et al. (ref 44).

Properties	Lithium	Sodium	Potassium
Atomic number	3	11	19
Atomic mass (g mol^{-1})	6.94	22.99	39.09
Ionic radius (Å)	0.76	1.02	1.38
Crust abundance (wt%)	0.0017	2.3	1.5
Crust abundance (mol%)	0.005	2.1	0.78
Cost of carbonate (\$ ton^{-1})	6500	200	1000
Cost of APF_6 (\$ kg^{-1})	7113	2589	338
E^0 (V vs. NHE)	-3.04	-2.71	-2.94

It is clear to see in **Table 1.1** that sodium and potassium are significantly cheaper and more earth abundant compared to lithium.[44] The implication of these properties is that batteries for intermittent renewable energy storage could be cheaper and less harmful for the environment to harvest.[9,44] The redox potentials of sodium and potassium, also, are quite negative compared to the normal hydrogen electrode, which implies that these systems will be able to accommodate a large operating voltage, like in the lithium system.[45] With these factors in mind, alternative battery chemistries have the potential to make a positive impact on the way energy is stored.

These systems are still in development and an improvement in the performance of the electrode materials is still needed if these systems are to be implemented commercially.[22,46] Both the NIBs and KIBs systems require improvements in the performance of the cathode materials in these systems. Some of the issues with current cathode materials relate to the large ionic radii of Na and K-ions, which make it difficult for transition metal oxide cathodes to reversibly store these charge carriers.[46] Also, concerning NIBs, there is a push to study the degradation mechanism of conversion electrodes that function in the sodium system.[22,47] To improve the performance of any of these materials, a fundamental understanding of the electrochemical process that govern the charge storage of Na-ions and K-ions is imperative.

1.4 Dissertation Overview

The following chapters highlight investigations into alternative battery technologies through 3D configurations, protective coatings, and characterization of resistive properties. Chapter 2 discusses the development of 3D batteries, and critical performance metrics for the advancement of these energy storage. In this chapter, the development of 3D batteries is reviewed, in addition to discussions on the advancements 3D batteries have made, with respect to critical performance metrics (power density, energy density, and scalability and cyclability). This chapter details a review which was published in *Nature Reviews* titled “Performance Metrics and Mechanistic Considerations for the Development of 3D batteries”, authored by Windsor & Nieto et al. 2024. Appendix I contains the glossary information and tabulated literature examples of 3D batteries.

Chapter 3 covers an investigation into the fundamental effect of a cyclized-polyacrylonitrile (cPAN) protective coating on the Na-ion (de)insertion chemistry of antimony-based anodes in NIBs. The investigation determined that cPAN protective coatings facilitate Na-ion transport through the interfacial layer between the electrode and electrolyte in a Na-ion battery. These studies provide valuable insight into the functionality of cPAN protective coatings for Sb andoes in Na-ion batteries. This chapter details a project titled "Mutli-functional cyclized-polyacrylonitrile (cPAN) as a protective coating for Sb-based anodes in Sodium-ion batteries," and is currently under review for publication in *ACS Applied Materials and Interfaces*. Appendix II contains the supplementary information for Chapter 3.

Chapter 4 covers a beginners and practical guide to electrochemical impedance spectroscopy (EIS) for rechargeable batteries. The challenge with EIS is that it is quite easy to collect data, while the data interpretation is very difficult and involved. Thus, we have made strides to provide a concise and easy to read beginners guide to EIS, specifically focused on rechargeable batteries. This chapter details the work titled "Practical and Beginners Guide to EIS for Rechargeable Batteries," and is under preparation for submission to *ACS Journal of Chemical Education*. Appendix 3 contains the supplementary information for this work, ana list of activities developed to coincide with the work in Chapter IV and includes examples of Python 3 code which was developed for the activities.

The final chapter, Chapter 5, describes areas of future work related to the investigation in Chapter 3. Chapter 5 discusses the experimental approach required to assess the behavior of protective coatings on high surface area (3D) anode architectures for NIBs.

Appendix IV contains brief discussion on some soft skills that author learned while completing this Ph.D.

1.5 References

(1) *Lithium-Ion Batteries - Statistics & Facts*; Statisitica Reserach Deparrtment, 2024. https://www.statista.com/topics/2049/lithium-ion-battery-industry/#topicOverview.

(2) Goodenough, J. B.; Kim, Y. Challenges for Rechargeable Li Batteries. *Chem. Mater.* **2010**, *22* (3), 587–603. https://doi.org/10.1021/cm901452z.

(3) LaCoste, J. D.; Zakutayev, A.; Fei, L. A Review on Lithium Phosphorus Oxynitride. *J. Phys. Chem. C* **2021**, *125* (7), 3651–3667. https://doi.org/10.1021/acs.jpcc.0c10001.

(4) Lambert, F. *Richard Hammond Crashed a $1 Million Rimac Concept One All-Electric Supercar*; Web article; electrek, 2017. https://electrek.co/2017/06/10/richard-hammond-crash-rimac-concept_one-all-electric-supercar/.

(5) Mizushima, K.; Jones, P. C.; Wiseman, P. J.; Goodenough, J. B. *LixCoO 2 (0<x~l): A NEW CATHODE MATERIAL FOR BATTERIES OF HIGH ENERGY DENSITY*; 1980; Vol. 15, pp 783–789.

(6) Amatucci, G. G.; Tarascon, J. M.; Klein, L. C. CoO2, The End Member of the Li x CoO2 Solid Solution. *J. Electrochem. Soc.* **1996**, *143* (3), 1114–1123. https://doi.org/10.1149/1.1836594.

(7) Vetter, J.; Novák, P.; Wagner, M. R.; Veit, C.; Möller, K.-C.; Besenhard, J. O.; Winter, M.; Wohlfahrt-Mehrens, M.; Vogler, C.; Hammouche, A. Ageing Mechanisms in Lithium-Ion Batteries. *J. Power Sources* **2005**, *147* (1–2), 269–281. https://doi.org/10.1016/j.jpowsour.2005.01.006.

(8) Wang, K.; Wan, J.; Xiang, Y.; Zhu, J.; Leng, Q.; Wang, M.; Xu, L.; Yang, Y. Recent Advances and Historical Developments of High Voltage Lithium Cobalt Oxide Materials for Rechargeable Li-Ion Batteries. *J. Power Sources* **2020**, *460*, 228062. https://doi.org/10.1016/j.jpowsour.2020.228062.

(9) Hirsh, H. S.; Li, Y.; Tan, D. H. S.; Zhang, M.; Zhao, E.; Meng, Y. S. Sodium-Ion Batteries Paving the Way for Grid Energy Storage. *Adv. Energy Mater.* **2020**, *10* (32). https://doi.org/10.1002/aenm.202001274.

(10) Kim B. Shedd. *Materials Commodity Summary-Cobalt 2020*; Materials Commodities Summaries; 2020.

(11) Siddharth Kara. *Cobalt Red: How the Blood of the Congo Powers Our Lives*, 1st ed.; St Martin's Press, 2023.

(12) Li, T.; Yuan, X.-Z.; Zhang, L.; Song, D.; Shi, K.; Bock, C. Degradation Mechanisms and Mitigation Strategies of Nickel-Rich NMC-Based Lithium-Ion Batteries. *Electrochem. Energy Rev.* **2020**, *3* (1), 43–80. https://doi.org/10.1007/s41918-019-00053-3.

(13) Märker, K.; Reeves, P. J.; Xu, C.; Griffith, K. J.; Grey, C. P. Evolution of Structure and Lithium Dynamics in $LiNi_{0.8}Mn_{0.1}Co_{0.1}O_2$ (NMC811) Cathodes during Electrochemical Cycling. *Chem. Mater.* **2019**, *31* (7), 2545–2554. https://doi.org/10.1021/acs.chemmater.9b00140.

(14) Akella, S. H.; Taragin, S.; Wang, Y.; Aviv, H.; Kozen, A. C.; Zysler, M.; Wang, L.; Sharon, D.; Lee, S. B.; Noked, M. Improvement of the Electrochemical Performance of $LiNi_{0.8}Co_{0.1}Mn_{0.1}O_2$ via Atomic Layer Deposition of Lithium-Rich Zirconium Phosphate Coatings. *ACS Appl. Mater. Interfaces* **2021**, *13* (51), 61733–61741. https://doi.org/10.1021/acsami.1c16373.

(15) Li, J.; Downie, L. E.; Ma, L.; Qiu, W.; Dahn, J. R. Study of the Failure Mechanisms of $LiNi_{0.8}Mn_{0.1}Co_{0.1}O_2$ Cathode Material for Lithium Ion Batteries. *J. Electrochem. Soc.* **2015**, *162* (7), A1401–A1408. https://doi.org/10.1149/2.1011507jes.

(16) Létiche, M.; Eustache, E.; Freixas, J.; Demortière, A.; De Andrade, V.; Morgenroth, L.; Tilmant, P.; Vaurette, F.; Troadec, D.; Roussel, P.; Brousse, T.; Lethien, C. Atomic Layer Deposition of Functional Layers for on Chip 3D Li-Ion All Solid State Microbattery. *Adv. Energy Mater.* **2017**, *7* (2). https://doi.org/10.1002/aenm.201601402.

(17) Huang, H.; Qiao, L.; Zhou, H.; Tang, Y.; Wahila, M. J.; Liu, H.; Liu, P.; Zhou, G.; Smeu, M.; Liu, H. Efficacy of Atomic Layer Deposition of Al2O3 on Composite LiNi0.8Mn0.1Co0.1O2 Electrode for Li-Ion Batteries. *Sci. Rep.* **2024**, *14* (1), 18180. https://doi.org/10.1038/s41598-024-69330-6.

(18) Song, X. Y.; Kinoshita, K.; Tran, T. D. Microstructural Characterization of Lithiated Graphite. *J. Electrochem. Soc.* **1996**, *143* (6), L120–L123. https://doi.org/10.1149/1.1836896.

(19) Xu, J.; Dou, Y.; Wei, Z.; Ma, J.; Deng, Y.; Li, Y.; Liu, H.; Dou, S. Recent Progress in Graphite Intercalation Compounds for Rechargeable Metal (Li, Na, K, Al)-Ion Batteries. *Adv. Sci.* **2017**, *4* (10), 1700146. https://doi.org/10.1002/advs.201700146.

(20) Obrovac, M. N.; Chevrier, V. L. Alloy Negative Electrodes for Li-Ion Batteries. *Chem. Rev.* **2014**, *114* (23), 11444–11502. https://doi.org/10.1021/cr500207g.

(21) Jin, Y.; Zhu, B.; Lu, Z.; Liu, N.; Zhu, J. Challenges and Recent Progress in the Development of Si Anodes for Lithium-Ion Battery. *Adv. Energy Mater.* **2017**, *7* (23). https://doi.org/10.1002/aenm.201700715.

(22) He, J.; Wei, Y.; Zhai, T.; Li, H. Antimony-Based Materials as Promising Anodes for Rechargeable Lithium-Ion and Sodium-Ion Batteries. *Mater. Chem. Front.* **2018**, *2* (3), 437–455. https://doi.org/10.1039/c7qm00480j.

(23) Piper, D. M.; Yersak, T. A.; Son, S. B.; Kim, S. C.; Kang, C. S.; Oh, K. H.; Ban, C.; Dillon, A. C.; Lee, S. H. Conformal Coatings of Cyclized-PAN for Mechanically Resilient Si

Nano-Composite Anodes. *Adv. Energy Mater.* **2013**, *3* (6), 697–702. https://doi.org/10.1002/aenm.201200850.

(24) Chew, S. Y.; Guo, Z. P.; Wang, J. Z.; Chen, J.; Munroe, P.; Ng, S. H.; Zhao, L.; Liu, H. K. Novel Nano-Silicon/Polypyrrole Composites for Lithium Storage. *Electrochem. Commun.* **2007**, *9* (5), 941–946. https://doi.org/10.1016/j.elecom.2006.11.028.

(25) Erk, C.; Brezesinski, T.; Sommer, H.; Schneider, R.; Janek, J. Toward Silicon Anodes for Next-Generation Lithium Ion Batteries: A Comparative Performance Study of Various Polymer Binders and Silicon Nanopowders. *ACS Appl. Mater. Interfaces* **2013**, *5* (15), 7299–7307. https://doi.org/10.1021/am401642c.

(26) Hatzell, K. B.; Chen, X. C.; Cobb, C. L.; Dasgupta, N. P.; Dixit, M. B.; Marbella, L. E.; McDowell, M. T.; Mukherjee, P. P.; Verma, A.; Viswanathan, V.; Westover, A. S.; Zeier, W. G. Challenges in Lithium Metal Anodes for Solid-State Batteries. *ACS Energy Lett.* **2020**, *5* (3), 922–934. https://doi.org/10.1021/acsenergylett.9b02668.

(27) Raj, R. Stack Pressure and Critical Current Density in Li-Metal Cells: The Role of Mechanical Deformation. *Acta Mater.* **2021**, *215*, 117076. https://doi.org/10.1016/j.actamat.2021.117076.

(28) Doux, J.; Nguyen, H.; Tan, D. H. S.; Banerjee, A.; Wang, X.; Wu, E. A.; Jo, C.; Yang, H.; Meng, Y. S. Stack Pressure Considerations for Room-Temperature All-Solid-State Lithium Metal Batteries. *Adv. Energy Mater.* **2020**, *10* (1), 1903253. https://doi.org/10.1002/aenm.201903253.

(29) Zhang, X.; Kostecki, R.; Richardson, T. J.; Pugh, J. K.; Ross, P. N. Electrochemical and Infrared Studies of the Reduction of Organic Carbonates. *J. Electrochem. Soc.* **2001**, *148* (12), A1341. https://doi.org/10.1149/1.1415547.

(30) Peled, E.; Menkin, S. Review—SEI: Past, Present and Future. *J. Electrochem. Soc.* **2017**, *164* (7), A1703–A1719. https://doi.org/10.1149/2.1441707jes.

(31) Otto, S.-K.; Moryson, Y.; Krauskopf, T.; Peppler, K.; Sann, J.; Janek, J.; Henss, A. In-Depth Characterization of Lithium-Metal Surfaces with XPS and ToF-SIMS: Toward Better Understanding of the Passivation Layer. *Chem. Mater.* **2021**, acs.chemmater.0c03518. https://doi.org/10.1021/acs.chemmater.0c03518.

(32) Jung, R.; Metzger, M.; Haering, D.; Solchenbach, S.; Marino, C.; Tsiouvaras, N.; Stinner, C.; Gasteiger, H. A. Consumption of Fluoroethylene Carbonate (FEC) on Si-C Composite Electrodes for Li-Ion Batteries. *J. Electrochem. Soc.* **2016**, *163* (8), A1705–A1716. https://doi.org/10.1149/2.0951608jes.

(33) He, M.; Guo, R.; Hobold, G. M.; Gao, H.; Gallant, B. M. The Intrinsic Behavior of Lithium Fluoride in Solid Electrolyte Interphases on Lithium. https://doi.org/10.1073/pnas.1911017116/-/DCSupplemental.

(34) Gimble, N. J.; Kraynak, L. A.; Schneider, J. D.; Schulze, M. C.; Prieto, A. L. X-Ray Photoelectron Spectroscopy as a Probe for Understanding the Potential-Dependent Impact of Fluoroethylene Carbonate on the Solid Electrolyte Interface Formation in Na/Cu2Sb Batteries. *J. Power Sources* **2021**, *489*. https://doi.org/10.1016/j.jpowsour.2020.229171.

(35) Michan, A. L.; Parimalam, B. S.; Leskes, M.; Kerber, R. N.; Yoon, T.; Grey, C. P.; Lucht, B. L. Fluoroethylene Carbonate and Vinylene Carbonate Reduction: Understanding Lithium-Ion Battery Electrolyte Additives and Solid Electrolyte Interphase Formation. *Chem. Mater.* **2016**, *28* (22), 8149–8159. https://doi.org/10.1021/acs.chemmater.6b02282.

(36) Zhao, W.; Yi, J.; He, P.; Zhou, H. Solid-State Electrolytes for Lithium-Ion Batteries: Fundamentals, Challenges and Perspectives. *Electrochem. Energy Rev.* **2019**, *2* (4), 574–605. https://doi.org/10.1007/s41918-019-00048-0.

(37) Herbert, E. G.; Tenhaeff, W. E.; Dudney, N. J.; Pharr, G. M. Mechanical Characterization of LiPON Films Using Nanoindentation. *Thin Solid Films* **2011**, *520* (1), 413–418. https://doi.org/10.1016/j.tsf.2011.07.068.

(38) Anantharamulu, N.; Koteswara Rao, K.; Rambabu, G.; Vijaya Kumar, B.; Radha, V.; Vithal, M. A Wide-Ranging Review on Nasicon Type Materials. *J. Mater. Sci.* **2011**, *46* (9), 2821–2837. https://doi.org/10.1007/s10853-011-5302-5.

(39) Vadhva, P.; Hu, J.; Johnson, M. J.; Stocker, R.; Braglia, M.; Brett, D. J. L.; Rettie, A. J. E. Electrochemical Impedance Spectroscopy for All-Solid-State Batteries: Theory, Methods and Future Outlook. *ChemElectroChem* **2021**, *8* (11), 1930–1947. https://doi.org/10.1002/celc.202100108.

(40) Cohen, E.; Menkin, S.; Lifshits, M.; Kamir, Y.; Gladkich, A.; Kosa, G.; Golodnitsky, D. Novel Rechargeable 3D-Microbatteries on 3D-Printed-Polymer Substrates: Feasibility Study. *Electrochimica Acta* **2018**, *265*, 690–701. https://doi.org/10.1016/j.electacta.2018.01.197.

(41) Pearse, A.; Schmitt, T.; Sahadeo, E.; Stewart, D. M.; Kozen, A.; Gerasopoulos, K.; Talin, A. A.; Lee, S. B.; Rubloff, G. W.; Gregorczyk, K. E. Three-Dimensional Solid-State Lithium-Ion Batteries Fabricated by Conformal Vapor-Phase Chemistry. *ACS Nano* **2018**, *12* (5), 4286–4294. https://doi.org/10.1021/acsnano.7b08751.

(42) Ashby, D. S.; Choi, C. S.; Edwards, M. A.; Talin, A. A.; White, H. S.; Dunn, B. S. High-Performance Solid-State Lithium-Ion Battery with Mixed 2D and 3D Electrodes. *ACS Appl. Energy Mater.* **2020**, *3* (9), 8402–8409. https://doi.org/10.1021/acsaem.0c01029.

(43) Windsor, D.; Nieto, K.; Vishnugopi, B.; Mukherjee, P.; Prieto, A. Performance Metrics and Mechanistic Considerations for the Development of 3D Batteries. *Nat. Rev. Chem.* **2024**, *Accepted*.

(44) Wu, Z.; Zou, J.; Chen, S.; Niu, X.; Liu, J.; Wang, L. Potassium-Ion Battery Cathodes: Past, Present, and Prospects. *J. Power Sources* **2021**, *484*, 229307. https://doi.org/10.1016/j.jpowsour.2020.229307.

(45) Bard, J. A.; Faulkner, R. L. *Electrochemical Methods, Fundamentals and Applications*; John Wiley & Sons, Inc: New York City, 2001.

(46) Rajagopalan, R.; Tang, Y.; Ji, X.; Jia, C.; Wang, H. Advancements and Challenges in Potassium Ion Batteries: A Comprehensive Review. *Adv. Funct. Mater.* **2020**, *30* (12), 1909486. https://doi.org/10.1002/adfm.201909486.

(47) Nieto, K.; Windsor, D. S.; Kale, A. R.; Gallawa, J. R.; Medina, D. A.; Prieto, A. L. Structural Control of Electrodeposited Sb Anodes through Solution Additives and Their Influence on Electrochemical Performance in Na-Ion Batteries. *J. Phys. Chem. C* **2023**, *127* (26), 12415–12427. https://doi.org/10.1021/acs.jpcc.3c01086.

CHAPTER 2: Performance Metrics and Mechanistic Considerations for the Development of 3D Batteries[1]

2.1 Overview

There is an urgent need for improved energy storage devices to enable advances in markets ranging from small scale applications (such as portable electronic devices) to large scale energy storage for transportation and electric-grid energy. Next-generation batteries must encompass high energy density, high power density, fast charging capabilities, operation over a wide temperature range, and safety. To achieve such ambitious performance metrics, creative solutions that synergistically combine state-of-the-art material systems with advanced architectures must be developed. The development of 3D batteries is a promising solution for achieving these feats. However, considerable challenges remain related to integrating the various components of a battery into an architecture that is truly 3D. In this review, we describe the status of 3D batteries, highlight key advances in terms of mechanistic insights and relevant performance descriptors, and suggest future steps for translating current concepts to commercially relevant solutions.

2.2 Introduction[2]

The need for technological improvements for renewable energy applications is enabled by the rapid advancement of current energy storage devices. The rapid advancement of energy

---

[1] A version of this text of this is published in *Nature Reviews* (10.1038/s41570-024-00659-2) with Daniel S. Windsor, Kelly Nieto, Bairav S. Vishnugopi, Partha Mukherjee, and Amy L. Priteo, which is currently in production. Daniel S. Windsor and Kelly Nieto co-authored the work, contributing to the literature research and writing of the text. Bairav S. Vishnugopi and Partha Mukherjee, from Purdue University, researched and wrote the section on computational advances in 3D batteries. Amy L. Prieto project administration, writing, and manuscript editing.

[2] Portions of this introduction are published in the dissertation of Kelly Nieto Ph.D, 2023.

storage devices is enabled by the is enabled by the need for technological improvements related to renewable energy applications. Present-day battery systems such as Li-ion batteries (LIBs) have been able to keep up with the energy demands for portable electronic devices, but many other applications have demands that might not be met by LIBs. The miniaturization of batteries to power implantable devices, autonomous sensors, and additional Internet of things-based (IoT) applications would enable new technology.[1–3] The need for batteries with both high energy and power densities in a smaller footprint area, but on large scale, are also of interest for applications such as emerging transportation systems (both ground-based transportation and electric aviation) and grid-level storage.[4,5] However, improving energy and power density while reducing the footprint of the battery is a nontrivial problem that requires novel architectures.

There is an inherent tradeoff in conventional planar two-dimensional (2D) batteries, wherein high active-material loadings lead to increased capacity but poor power performance, and low loadings lead to high power but low capacities. Traditionally, 2D batteries consist of layered planar electrodes, which may possess complex geometries individually, but only overlap in one geometric plane. To improve energy density in these systems, the active-material loading must be increased, however this requires thicker electrodes that offer limited performance due to greater mechanical degradation and restrict the achievable power density due to rate-limiting resistivities and lithium concentration gradients.[6–8] When trying to improve the power density, higher surface areas could lead to improved kinetics, but this generally leads to batteries with a larger footprint area or a decrease in active-material loading, which results in lower energy densities.[9,10] These challenges highlight the limitations in improving performance metrics for current 2D architectures and necessitate advances in multiple geometric planes, such as 3D batteries.[11–13] The ultimate outcome of an advanced 3D battery would be a single device that possesses the highest energy density possible for the implemented system with the power density of a supercapacitor, eliminating the tradeoffs inherent to 2D batteries.

While numerous definitions of 3D batteries have been proposed in the literature,[13–17] in this review, we define a 3D battery as a battery where all the components (that is, electrodes and electrolyte) overlap in multiple planes. There are three main classes of 3D batteries; interdigitated, concentric, and aperiodic. Interdigitated configurations consist of periodically dispersed arrays of cathode and anode plates or rods. The electrodes have a fixed distance from one another and are separated by void space filled with liquid electrolytes, or a solid electrolyte membrane. Concentric-based configurations have a similar periodic nature and typically consist of an electrode with a conformally coated electrolyte followed by a conformal coating or void filling with the remaining electrode. Based on this definition, aperiodic structures may be considered 'semi-concentric' as they also consist of conformal coverage of the electrolyte onto a 3D network of either the anode or cathode. This is followed by coverage or filling of the remaining electrode. The base structure of an aperiodic configuration originates from a randomly ordered current collector or self-standing electrode, such as a foam, and does not possess the ordered nature of the concentric configuration. Implementation of any of the described configurations is highly dependent on the application as each application has its own cost-effective fabrication technique, such as atomic layer deposition (ALD) for microbatteries (interdigitated) or electroplating for foams (aperiodic).[13,18–21] The manufacturing methods chosen can lead to challenges in creating uniform coatings with control over interfacial resistances. The promise of 3D architectures for batteries is that they take advantage of the third dimension, height, to enable greater areal loadings while minimizing the diffusion paths between electrodes and, which means that the energy and power densities can be decoupled.

The field of 3D battery research has progressed considerably since first described by Long et al. in 2004. Substantial efforts have been made for individual components (advances in 3D electrodes,[16,17,22–26] solid electrolytes,[18,27] current collectors,[28] and computational approaches[29–32]), as reported in published reviews. Much of the previous work on 3D batteries has focused on specific components (e.g. electrode configurations, electrolyte materials, etc) that can be arranged into a 3D battery. An aspect of these systems that makes them so difficult to study — and is often overlooked — is that the interplay between all the components can greatly affect the measured performance, making it a challenge to decouple deficiencies introduced by one component of the battery versus the advantages of the architecture. The field is currently at the point, however, where fully integrated 3D batteries have been demonstrated. Thus, this review will only focus on full 3D batteries, where all components (cathode, anode, electrolyte) are incorporated into the 3D configuration. It is not the objective of this review to be a comparative study, determining the ideal 3D battery. Our hypothesis is that there is no single perfect battery, but rather that there are application-specific metrics that make one architecture better suited, potentially, than others. Herein we discuss key factors in the development of full 3D batteries, and what bottlenecks still need to be overcome to improve performance. We then discuss critical performance metrics in gauging the viability of full 3D batteries such as power density, energy density, as well as cyclability and scalability. Although the performance metrics are considerable as standalone parameters, they are also highly dependent on each other, owing to the magnitude and complexity of the interacting components in 3D batteries. As such, it is important that each component of a 3D battery is developed in concert with the other components. This entails discussions on application-dependent performance criteria, latent issues within the literature, as well as experimental and computational approaches for assessing performance increases and degradation pathways of these complex systems.

2.3 Key Parameters to Consider in the Initial Development of 3D Batteries

In the broader field of battery research, a commonly held sentiment is, "there is no one perfect battery for every application". While this is the case for traditional rechargeable battery technologies, it is more pronounced for 3D batteries and their development. This is clear when assessing how a 3D battery should perform, in terms of energy and power requirements, with respect to its final application. A 3D battery, for example, developed for on-chip (microbattery) applications should aim to maximize the energy and power achievable per footprint area (Wh µm^{-2} and W cm^{-2}), owing to the size limitations for these devices and the value of real estate for on-chip applications.[33,34] Alternatively, 3D batteries developed for electric vehicle (EV) applications should maximize the energy and power achievable per mass (Wh kg^{-1} and W kg^{-1}), as the weight of the battery has a large effect on the vehicles range.[11,35,36]

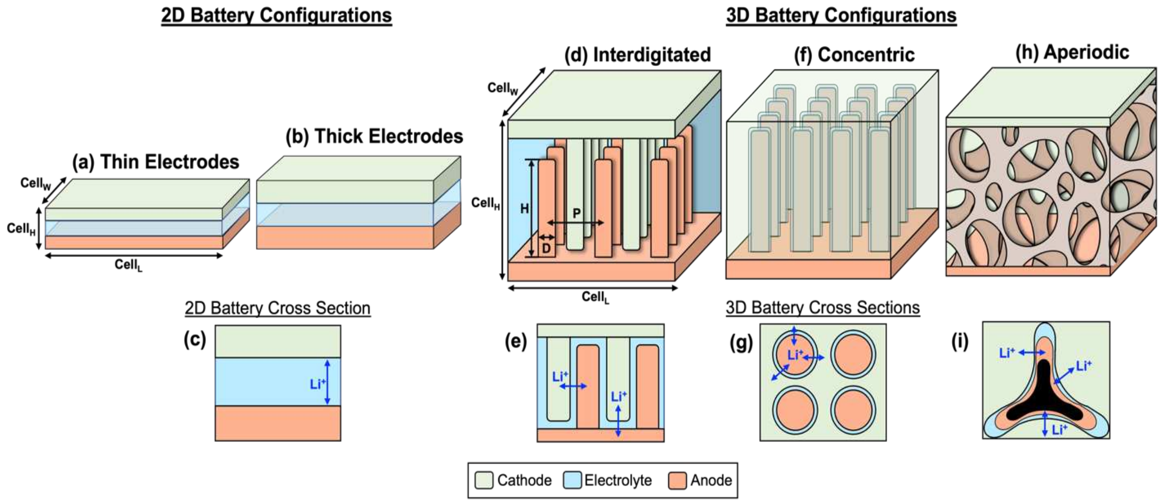

Figure 2.1: Geometric configurations for 2D and 3D Batteries**.** Schematic of thin (a) and thick (b) 2D batteries, where energy density is generally improved by increasing the electrode thickness. 2D configurations may have complex geometrics but only allow for Li-ion diffusion in one plane (c). 3D batteries can be produced in a range of geometric configurations, but generally fall into the categories of interdigitated (d, e), concentric (f, g), and aperiodic (h, i). The cross sections of these geometries demonstrate the multiple pathways Li ions may travel when the cell is cycled (e, g, i).

Examples of 3D battery architectures, and their differences from 2D batteries (**Figure 2.1a-c**), are shown in **Figure 2.1**, which are interdigitated (**Figure 2.1d**), concentric (**Figure 2.1f**), and aperiodic (**Figure 2.1h**). **Figure 2.1e**, **Figure 2.1g**, and **Figure 2.1i** demonstrate the various planes where ionic transport can occur in these systems, respectively.[14,15,20,22] These different configurations lend themselves to different final applications (e.g. interdigitated for microbatteries and aperiodic for larger systems) and require different design and performance criteria. Also, different manufacturing methods lend themselves better to certain architectures versus others. Very precise, but more costly, methods such as ALD lend themselves better to microbatteries for on-chip applications, whereas electroplating of materials for large scale, low cost, manufacture of larger batteries would be ideal for aperiodic structures.

To relate 3D battery application to design and construction, **Table A.I.I** and **A.I.II** were formed which highlights several publications of full 3D batteries for a variety of applications. The columns of this table represent important factors which are critical for understanding the current performance of 3D batteries, and to point out existing bottlenecks in their development. The power density of 3D batteries has been improved, while the advances related to increased energy density are less pronounced. Other important performance metrics such as scalability and cyclability are also associated with the data (fabrication technique and capacity retention, respectively) in **Table A.I.I** and **A.I.II**. Scalability and cyclability, however, are difficult to immediately assess when looking at 3D battery literature, as these factors are either not discussed or must be extrapolated from figures or any supplemental information. These performance metrics are critical to assess if 3D batteries can achieve their potential and are discussed below.

The data highlighted in **Table A.I.I** and **A.I.II** provides an opportunity to discuss various latent issues within the field of 3D batteries, which revolve around the fact that the performances between two 3D batteries of different design and configuration are difficult to compare because of a discontinuity between how the performances batteries are reported. Some investigations prioritize the reporting of fundamental performance metrics (that is specific capacity and rate capability) while other studies prioritize reporting performance metrics with respect to the holistic performance of the cell (Wh kg^{-1} or W L^{-1}).[26,37] The differences in what types of data are reported makes it difficult to assess how a 3D battery, and its performance metrics relate to the desired application. For the development of 3D batteries, it is imperative to report both the fundamental and late-stage performance metrics, in order to reduce the need for excessive, or unreasonable, data extrapolation. This arises from the fact that the fundamental performance relates to how certain materials behave, while late-stage performance metrics provide insight into how the battery performs, accounting for broader considerations, such as packaging (non-active materials needed for a commercial battery) and material use. In this review, we propose that future studies on full 3D batteries should report information and data in line with the columns of **Table A.I.I** and **A.I.II**. Reporting information related to application, materials selection, and performance (in several ways) will make the field of 3D batteries easier to navigate for the next generation of battery scientists.

Although comparisons between different 3D batteries of various configurations is difficult, direct comparisons between a 3D battery and its 2D analog are important for enabling an understanding of the physical attributes due to the architecture of the cell, decoupled from the materials. This is because such comparisons can provide insight into discrepancies between expected 3D battery performance, and actual 3D battery performance, using 2D systems as controls. To experimentally compare a 3D battery to its 2D counterpart, one must assess the performance via the area enhancement factor (AEF). The AEF is a geometrically calculated value that measures the increase in the internal surface area of a 3D battery ($A_{internal}$) compared to the area of its footprint ($A_{footprint}$). This metric is often mentioned in the literature with different terminologies, such as geometric area gain, area gain factor, and area enlargement factor.[13,38–40] A simplified equation for the AEF is described in **Equation 2.1**.[38,41,42] Studying a 3D battery in comparison to its 2D analog (where AEF = 1) will allow investigators to assess the impact of geometry and interactions between different components while controlling the electrochemical behavior. An important factor to consider is that the AEF is a tool to compare performance between a 3D battery and its 2D analog and should not be used for comparisons between different 3D batteries or configurations. This is because the performance of a 3D battery is dependent on a variety of factors, such as the materials selection, configuration and design, and application.

$$AEF = \frac{A_{internal}}{A_{footprint}} \tag{2.1}$$

The AEF is more straightforward to calculate for certain 3D architectures compared to others. For example, the AEF of an interdigitated Si-well or Si-pillar configuration (**Figure 2.2a**) can be calculated directly from geometric measurements of the battery scaffold owing to the homogeneous spacing of each well or pillar.[39,41,43] On the other hand, AEF values on foam substrates cannot be determined through mathematical approximations alone due to the aperiodicity of the architecture.[19,38] However, the AEF is still crucial to calculate for aperiodic scaffolds and can be performed through either electric double-layer capacitance measurements, underpotential deposition, or via the Brunauer-Emmett-Teller (BET) method.[42,44,45]

It must be noted that the AEF is a measure of the increase in surface area and does not account for active versus inactive lithiation sites on the electrode surface (more directly measured by measuring the electrochemically active surface areas). Inactive regions of an electrode contribute to the volume or weight of the cell and negatively affect the accessible energy density. Therefore, marginal improvements with power and energy density with a 3D configuration that has a high AEF can be due to excess inactive surface area. Despite this caveat, the AEF is still a relevant descriptor for guiding improvements and still provides important insights on how advancing to 3D geometries can influence performance metrics.

The validity of AEF measurements for the development of 3D batteries is seen when assessing energy and power density improvements compared to 2D analogs. An excellent example can be found in the work of Pearse et al.[41] This study fabricated a 3D Si-well based interdigitated (**Figure 2.2a**) microbattery and calculated the AEF via **Equation 2.2**, [32] where this equation takes into account the geometry of the tested 3D electrode.

$$AEF(Cylindrical\ Si\ Wells) = 1 + \frac{2\pi\sqrt{3}}{3}\frac{Dh}{s^2} \tag{2.2}$$

In this equation *D* represents the diameter of the cylindrical pore, *s* represents the center to center spacing between the pores, and *h* is the depth or height of the pore. This investigation created battery systems, via ALD (**Figure 2.2b**) with AEFs of 1 (for a 2D battery), and 4 and 10 for the 3D configuration. As clearly seen in **Figure 2.2c** and **2.2d**, the energy density and power density (assessed by evaluating the battery's capacity retention as a function of current density) both increase with increasing AEF.[41] For the power density improvements, the AEF 10 system only had a small drop in the discharge capacity upon increasing the cycling current from 100 μA/cm^2 to 10mA/cm^2, **Figure 2.2d**. For the energy density improvements, the AEF 10 battery had a discharge capacity of roughly 28 μAh cm^{-2}, while the planar battery had a discharge capacity of approximately 4 μAh cm^{-2}, **Figure 2.2d**. These data clearly show that a 3D battery system with a larger AEF can perform better than its 2D counterpart, yet the increase in performance is not directly proportional to the AEF value. This highlights an important detail concerning the AEF, being that it is a tool to estimate increases in 3D battery performance and is not an absolute maker of such. Differences in expected 3D battery performance and actual performance can provide insight into possible degradation mechanisms and design flaws in these systems.

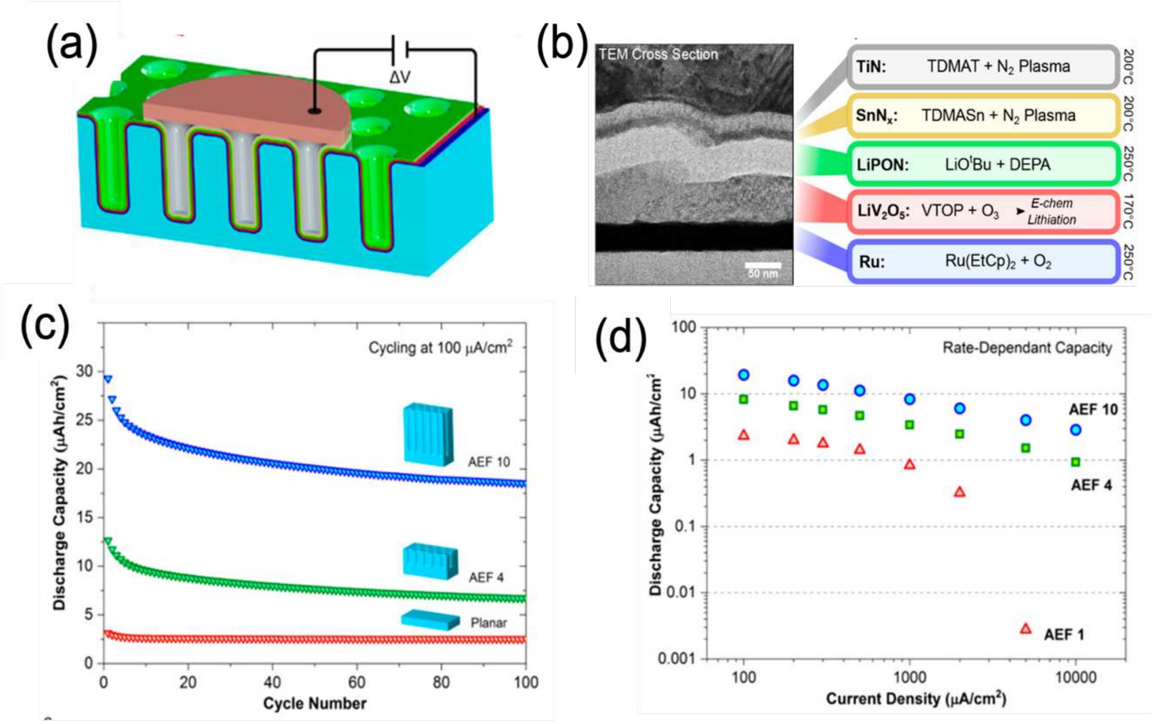

Figure 2.2: Effect of area enlargement factor (AEF) on energy and power densities. (a) schematic of 3D interdigitated microbattery, where all of the relevant battery materials are interdigitated within the wells of the silicon (Si) base. Reproduced with permission from Ref [41]. (b) cross-sectional transmission electron microscope (TEM) image of 3D interdigitated microbattery with materials classification with a tin nitride (SnN_x) anode, lithium phosphorous oxynitride (LiPON) solid-state electrolyte, and a lithium vanadium oxide (LiV_2O_5) cathode. The titanium nitride (TiN) and ruthenium (Ru) layers are included as current collectors, with the temperatures relating to process temperature for each layer. Reproduced with permission from Ref [41]. (c) cycle life plot of batteries with AEF 1 (planar), 4, and 10 where the discharge capacity increases as a function of AEF, demonstrating the relationship between AEF and charge storage. Reproduced with permission from Ref [41]. (d) capacity over current density plot of batteries with AEF 1 (planar), 4, and 10 demonstrating the effect of AEF on rate capability, demonstrating that an increase of the AEF relates to better discharge capacity as a function of increasing current density. Reproduced with permission from Ref [41].

Given that the parameter space for discovery of new materials and the optimization of performance — particularly at interfaces — is so large, a simple trial and error approach using physical experiments is not always feasible. Computational modeling and simulations play a pivotal part in offering mechanistic insights and guidelines toward achieving the desired performance metrics. These methods have matured and offer a way to rapidly iterate a given structure via descriptions of the effects of chemomechanics on performance.[30,46,47]

2.4 Critical Need for Theoretical and Computational Advances In 3D Batteries

Although 3D batteries should eliminate the tradeoff between accessible energy density and power density present in a conventional 2D battery, challenges concerning electrode architecture, material properties (such as, transport and mechanics), and the resulting evolution of physicochemical fields still need to be understood. The development of mechanistic models will play a pivotal role in the fundamental interrogation and design of such 3D architectures. In this regard, prior computational work on the electrochemical response of 3D batteries have offered insights into the spatial distribution of reaction currents and the utilization of electrode active-material (**Figure 2.3a-b**).[9,23,29,32,48] A major focus has been on the geometric optimization of these architectures, and investigating the underlying transport limitations for different design concepts (**Figure 2.3a**) such as interdigitated, concentric and aperiodic porous electrodes.[9,31] To this end, continuum scale simulations have been combined with data-driven approaches to identify optimal electrode architectures from a wide range of candidate geometries (**Figure 2.3c-d**).[46] Along similar lines, other strategies based on Monte Carlo Tree Search and machine-learning-based performance simulators have enabled geometric configurations with reduced internal resistances, and consequently higher power and energy densities.[30,47]

While geometric optimization is critical in the design of 3D batteries, fundamental understanding of performance-limiting scenarios and synergistic advancements in material- and electrode-design rely on the mechanistic, physics-based modeling of 3D battery architectures. Modeling frameworks provide the bridge between pore-scale characteristics, architectural design and cell-level performance metrics. The key advantage of 3D batteries in enabling higher power and energy densities stems from their ability to preserve short transport lengths with increasing electrode thicknesses.[15,29] However, this behavior is predicated on a combination of material

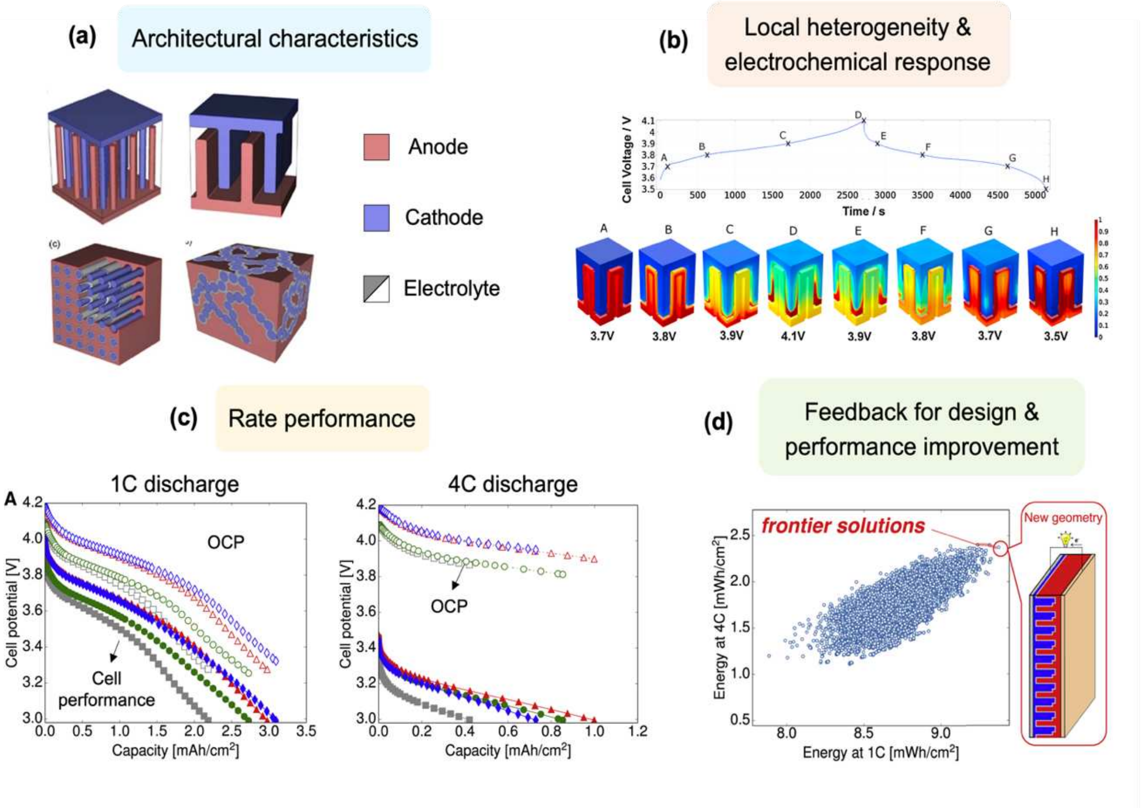

Figure 2.3: Mechanistic and computational considerations in the development of 3D batteries. (a) Incorporation of architectural details including accurate computational modelling of ionic tortuosity and active area. Reproduced with permission from Ref [12]. (b) Capturing local heterogeneity in electrochemical response such as electrode state-of-charge, where position d relates to the stopping point of the positive potential sweep. This figure demonstrates the degree of lithiation as a function of charge. Reproduced with permission from Ref [23]. (c) Rate performance predictions used to understand tradeoffs in accessible energy and power density. Here, the square, circle, triangle, and diamond represent different 3D battery geometries; the open and closed symbols denote the open circuit potential (OCP) and discharge curves (cell performance), respectively. These plots relate the capacity to the reference geometries used in these simulations. Reproduced with permission from Ref [46]. (d) Model-informed systematic design feedback toward improved performance, displaying the validity of the predictions made by these simulations. Reproduced with permission from Ref [46].

properties such as the ionic conductivity of the electrolyte and solid-state diffusivity of the electrode. For instance, with a reduction in the ionic conductivity, a larger gradient in electrolyte potential will manifest with changes in the electrode thickness, eventually resulting in a non-homogenous utilization of active-material. Thus, computational modeling of such 3D systems should guide design strategies in identifying optimal material-architecture interactions. As prior efforts using density functional theory have quantified the dependence of electrode properties (for example Young's modulus) on lithium concentration,[49,50] such insights should be hierarchically incorporated into mesoscale descriptions that can capture the dynamic electrochemical, transport and mechanical response of 3D electrodes during cell operation.

With rapid improvement in computational power and simulations over a broad range of length scales, we expect the development of digital twins for 3D batteries to play a considerable role in deriving systematic guidelines for enhanced rate performance. These virtual frameworks can provide mechanistic platforms for rapid screening of electrode architecture designs, performance-limiting factors, and associated degradation modes for 3D batteries. An accurate description of effective electrode properties, such as tortuosity for ionic transport and electrochemically active area, should be incorporated into the digital twin frameworks. Gaining an architecture-dependent understanding of the underlying transport and kinetic properties and heterogeneities can reveal the fundamental structure-property-performance relationships in 3D battery electrodes. In addition, the modeling efforts should involve inputs pertaining to the architectural arrangement from experimental characterization techniques and mechanistic validation strategies, cognizant of local state-of-charge distribution (**Figure 2.3b**) and rate performance (**Figure 2.3c**). A bottom-up modeling approach incorporating the multidimensional and heterogenous nature of the electrode architecture, transport across a range of length scales, and mechanical properties of the electrode and electrolyte, and cell design is essential. Such theoretical and computational advances should occur in tandem with the experimental efforts in characterization and design of 3D batteries. Through synergistic multiscale modeling and experiments, a comprehensive re-thinking and identification of mechanistic bottlenecks in 3D batteries — knowing the different application-specific requirements — is required. By decoupling the effect of material properties, architectural considerations, and operating conditions, computational modeling and data-driven approaches are crucial in providing targeted design principles (**Figure 2.3d**) toward achieving enhanced power and energy densities in 3D batteries.

2.5 Progress in the Field and Performance Metric Considerations to Improve 3D Batteries

This section will focus on the progress made by the field on the four critical performance metrics for 3D batteries. These performance metrics are power density, energy density, cyclability, and scalability.

2.5.1 Power Density

The power density of a 3D battery is an incredibly important performance metric to consider, given the low power density performance of most high capacity 2D batteries. Power density is calculated by normalizing the power output (nominal voltage multiplied by output current) gravimetrically, volumetrically, or areally (that is W kg^{-1}, W L^{-1}, W cm^{-2}). Unfortunately, studies in the literature rarely report power density improvements in terms of these units. Instead, most studies evaluate power density by assessing the batteries' capacity retention as a function of increasing current density or based on the area of the electrodes without considering packaging. In the literature there are two practical aspects of 3D batteries that affect their power density: fabrication method and the choice of electrolyte. Specifically, the fabrication method often determines the types of structural geometry and electrolytes, a 3D battery can use. For example, an interdigitated microbattery design generally requires the use of ALD, which enables the control of a material's thickness and provides a conformal coating of the entire 3D battery architecture.[41,51,52] This method is currently the most commonly used in the 3D battery literature. The precision of ALD, and the structural regularity Si-etching processes provide, means that very short diffusion paths can be created in Si-based interdigitated 3D batteries, leading to improved power densities.[16,39,41] An excellent example is seen in Pearse et al.[41], where deep reactive ion etching (DRIE) was used to create a Si-well architecture, and subsequently applied all other materials with ALD. The interdigitated system with a SnN_x anode, LiPON solid electrolyte, and LiV_2O_5 cathode (**Figure 2.2b**) was able to achieve an excellent power density given the small drop in capacity upon increasing the current density by two orders of magnitude (**Figure 2.2d)**.[41] The excellent capacity retention for this 3D battery is a result of a high active surface area, as described by the AEF for this system. Moreover, this type of interdigitated 3D battery is scalable given that Si-etching and ALD are already well developed from the semiconductor industry.[18] One caveat is that ALD may have some disadvantages given current limitations in the volume and time of deposition and types of materials amenable to ALD.

ALD can deposit a range of solid inorganic electrolytes, such as LiPON or a NASICON derivative, onto a substrate.[18] However, inorganic solid electrolytes do have drawbacks. In the case of LiPON, the most common class of solid electrolyte for interdigitated microbatteries, the ionic conductivity is rather low (3×10^{-7} S cm^{-1} for $Li_{0.99}PO_{2.55}N_{0.30}$), which can severely hinder ion transport between electrodes despite the short diffusion paths found in 3D batteries.[18,39,41,53] Alternative inorganic electrolytes, like sodium-ion superconducting (NASICON) materials, can have ionic conductivities (1.5×10^{-4} S cm^{-1} for $Li_{1.4}Al_{0.4}Ti_{1.6}(PO_4)_3$), considerably closer to an organic liquid electrolyte (10^{-3} S cm^{-1}).[18,53] These types of inorganic solid electrolytes can alleviate concentration gradients due to their high cationic transference numbers.[54,55] Thus, the architectural advantage of 3D batteries for addressing transport challenges coupled with the use of improved inorganic solid electrolytes offers an opportunity to enable high charge/discharge rates for solid state batteries. Currently, the role of mechanical stress at such solid-solid interfaces, and the rigid

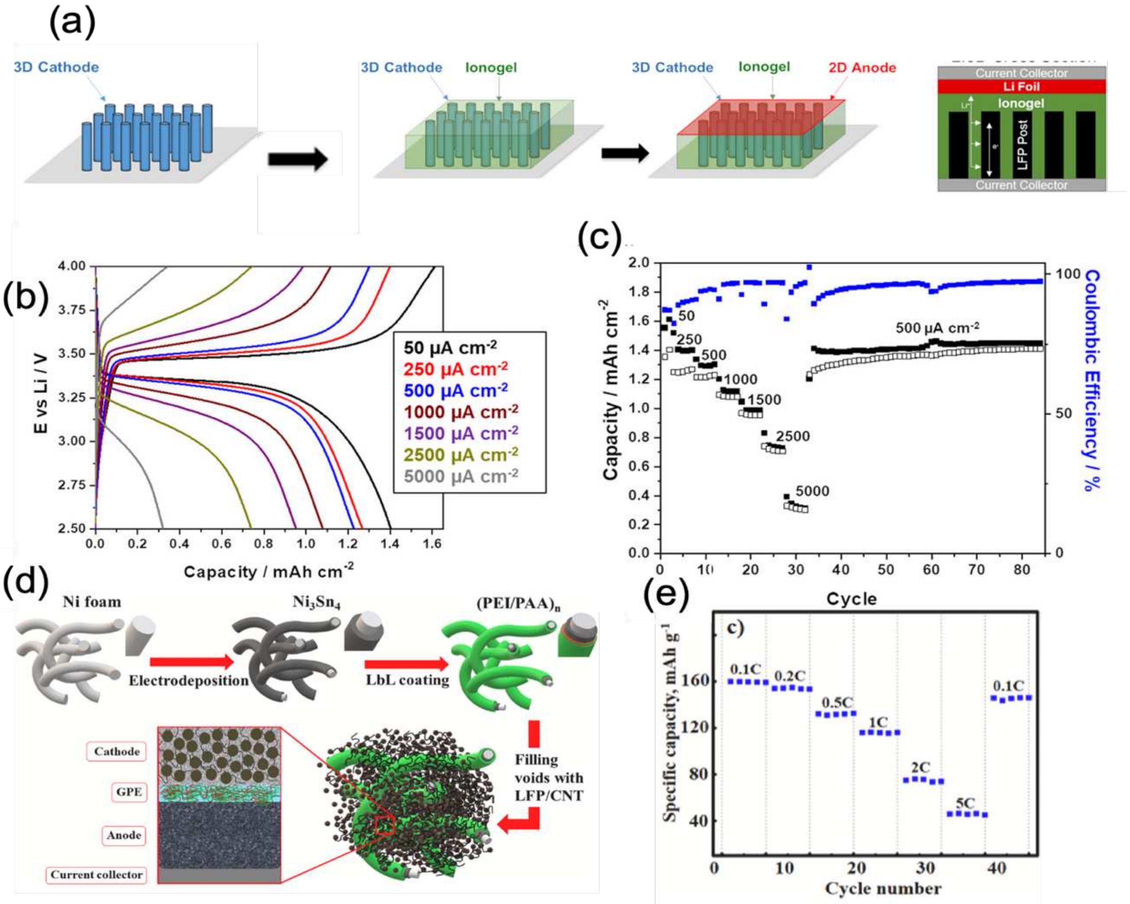

Figure 2.4: Improvements in power density with gel electrolytes. (a) schematic of semi-3D battery fabrication with lithium iron phosphate (LFP) cathodes, ionogel electrolyte, and Li-metal anodes. Reproduced with permission from Ashby et al. Ref [61]. (b) voltage versus capacity plots as a function of current density for a semi-3D battery, demonstrating good power density for this system given that the capcity slightly fades as the current density is increased. Reproduced with permission from Ashby et al. Ref [61] (c) rate capability plot as a function of current density for a semi-3D battery with the blue squares showing the coulombic efficiency, while the filled and open boxes relate to the charge and discharge capacities, respectively. These data show good rate capability and good efficiency for the semi-3D battery shown in panel a. Reproduced with permission from Ashby et al. Ref [61] (d) schematic of the fabrication of a 3D battery on an aperiodic foam which used an electroplated Ni_3Sn_4 anode, a gel-polymer electrolyte, and a composite lithium iron phosphate/carbon nanotubes (LFP/ CNT) cathode. Reproduced with permission from Tolganbek et al. Ref [19]. (e) Rate capability plot an aperiodic foam-based 3D battery, demonstrating good power density as the capacity does not significantly drop as the current density is increased. Reproduced with permission from Tolganbek et al. Ref [19].

nature of these materials, substantially hinders their cyclability.[56,57] The degree of interfacial contact and resulting effects on reaction and stress hotspots within such architectures need further investigation. These heterogeneities at solid-solid interfaces critically influence the electrochemical usage at high charge/discharge rates, and can influence the mechanical degradation of electrodes.[58,59] Although inorganic solid electrolytes have their drawbacks, the applicability and safety advantages of these materials support their inclusion in 3D batteries.

To address some of the challenges presented by inorganic solid electrolytes, several investigations have employed more flexible alternatives, namely ionogels and gel-polymer electrolytes (GPE).[60,61] Iono-gels are comprised of ionic liquids which interpenetrate, or are confined by, a solid framework.[62] Gel-polymer electrolytes are formed by impregnating (gelling) a liquid organic electrolyte into a polymeric network.[63] Although configured differently, both systems have advantages over inorganic solid electrolytes in that the iono-gel and GPE systems have incredibly high ionic conductivities and can be mechanically flexible.[62,63] A study demonstrated how an ionogel polymer electrolyte beneficially affected the power density of a semi-3D battery system, where the capacity of the LFP-post/iono-gel/Li-metal system (**Figure 2.4a**) only faded 21.4% when changing the galvanostatic cycling current from 50 μA cm^{-2} to 1,000 μA cm^{-2} (**Figure 2.4a** and **2.4c)**.[61] This class of solid electrolyte is also applicable to a variety of 3D architectures, ranging from pillar structures to aperiodic foams.[5119,38] A different study started with Ni-foam, and electrodeposited a Ni_3Sn_4 alloy anode material directly onto the Ni scaffold (**Figure 2.4d**).[19] From there, a layer-by-layer approach was used to apply a PEI/PAA polymer electrolyte gelled with 1M $LiPF_6$ in EC/DEC/DMC achieving excellent ionic conductivity for the electrolyte — roughly $8.0x10^{-3}$ S cm^{-1}.[19,64] The Ni_3Sn_4/GPE/LFP 3D system was shown to have good power density, losing 25% capacity upon an order of magnitude increase in the current density (**Figure 2.4e**). Polymer-based solid electrolytes, however, can be difficult to conformally coat onto aperiodic substrates. An advanced 3D battery system with poor electrolyte coverage can lead to short-circuiting of the battery, as seen in the work of Sun et al. for their aperiodic foam substrate coated with a GPE.[38]

3D batteries have advanced greatly since initial schematics were published in the early 2000's: firstly, in terms of successfully integrating all components of a battery in three dimensions, and secondly, with regards to the measured power density. Although power density can be improved by reducing the diffusion pathway for ions, improving the energy density while maintaining high power density and cyclability is challenging.

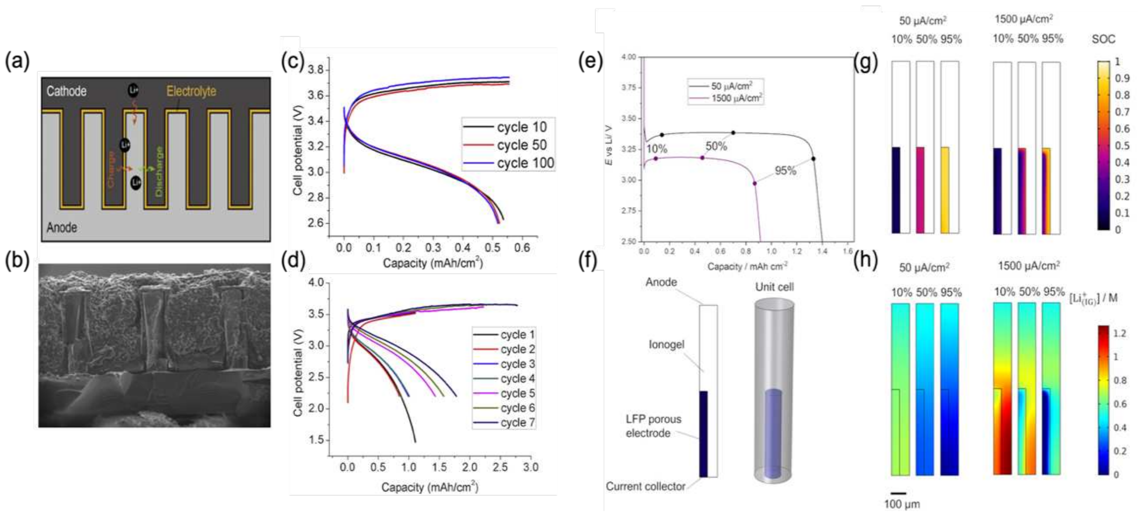

Figure 2.5: Using scaffolds, ionogels, and geometric considerations to improve energy density. Two proof-of-concept full batteries have been tested (a) and (b) and were galvanostatically cycled at 0.66 mA cm^{-2}/0.22 mA cm^{-2} (a) and 0.22 mA cm^{-2}/0.11 mA cm^{-2} (b), where the battery in panel a shows stable charge and discharge traces, while the battery in panel b shows stable discharging and less than stable charging. (c) charging schematic of the interdigitated 3D battery studied by Hur et al. consisting of Si pillars coated with an SU-8 solid electrolyte, and lithium nickel cobalt aluminum oxide (NCA) as the cathode. The corresponding scanning electron microscopy image of the assembled full 3D battery (d). Reproduced with permission from Hur et al. Ref [37] Modeling and simulations of the 2.5D battery with lithium iron phosphate (LFP) pillars coated by an ionogel tested by Ashby et al. (e-h). Simulations of discharge cycles at 50 µA cm^{-2} and 1500 µA cm^{-2} (e), schematic representation of the geometry of the pillars used for these simulations (f), and the corresponding state-of-charge (SOC) (g), and lithium concentration maps of the electrolyte (h) at 10, 50, and 95% states of charge. These panels demonstrate that the lithiation of the pillars does not occur uniformly, leading to underutilization of the electrode material. Panels a-d were reproduced with permission from Hur et al. Ref [37] and panels (e-h) were reproduced with permission from Ashby et al. Ref [61].

2.5.2 Energy Density

Numerous advances in the development of 3D batteries have demonstrated how this configuration can enhance energy density by increasing the surface area and degree of active-material per footprint area of the battery.[37,65–67] Several key challenges such as low active-material use, material stability, and large amounts of inactive-material weight, must be addressed for the energy densities of 3D batteries to become competitive with 2D batteries for industrial applications. Energy density is calculated by the product of the nominal battery voltage and capacity, divided by the weight or volume of the cell. This formula is a guide to help explain steps needed to increase energy density.

One way to improve the energy density is by increasing the battery voltage (through the choice of anode and cathode material) and the capacity (by improving the active-material composition and packing density of both electrodes). Considerable efforts have gone into the development of materials for 3D batteries by using what has already been discovered in the 2D LIB field. Examples include the use of ‘champion’ materials such as lithium iron phosphate (LFP), lithium cobalt oxide (LCO), lithium manganese oxide (LMO), and vanadium oxide (V_2O_5) as cathode materials and graphite, silicon, lithium titanium oxide (LTO), and other intercalation oxides as anode materials.[25,42,68–71] Solid electrolytes such as LiPON, LiPONB and LiSiPON are also of interest as they can act as both the electrolyte and the separator between the cathode and anode.[18,19,52,61] Conversion electrodes can also be adapted for use in 3D batteries due to the empty space present in certain configurations that can accommodate for any volume expansion.[72–74] Simultaneously, the high energy density provided by Li metal anodes can be used effectively because of the reduced propensity for dendrite formation from improved current distributions induced by certain 3D architectures and the mechanical integrity provided by solid electrolytes.[17,75,76] However, the use of these materials is highly dependent on the size of the battery (microbatteries versus larger applications) and the fabrication technique for conformal coverage (ALD, physical vapor deposition, electrophoretic deposition (EPD), electrodeposition, spin coating, and others).[13,18,20,77] Additionally, some of the previously listed materials need binders and additives to achieve good conductivity and adhesion to the current collector, but this reduces the loading of active-material and increases the overall weight of the cell. The scaffold used in 3D battery configurations can also heavily influence the calculated energy density depending on whether the material can be lithiated/delithiated. Therefore 'self-standing' electrode materials could improve the overall energy density.[69] One example is the use of 3D carbon scaffolds that can also be used in active lithiation/delithiation, but problems then arise in the cyclability and lifetime of the cell after continuous use of the scaffold.[78]

There have been several studies that have addressed these challenges and demonstrated improved energy densities (**Table A.I.I**). Hur et al., demonstrated the importance of using the scaffold material to increase energy density by cycling their 3D Si scaffold at 10% of the theoretical capacity.[37] Using this approach, they report discharge capacities of up to 1.8 mAh cm^{-2} (5.2 mWh cm^{-2}) and cycling stability of 100 cycles at 0.5 mAh cm^{-2} (1.6 mWh cm^{-2}, **Figure 2.5a-b)**. Their 3D microbattery was composed of the partially lithiated Si scaffold as the negative electrode, SU-8 as the solid electrolyte, and a $LiNi_{0.8}Co_{0.15}Al_{0.05}O_2$ (NCA) slurry as the cathode (**Figure 2.5c-d)**. However, capacity retention was highly dependent on the depth of discharge, and the reported discharge capacity corresponded to approximately 40% of the total theoretical capacity of the cell. This underutilization was due to lithium concentration gradients in the silicon scaffold, uniformity of the cathode, and packing of the electrolyte. Previous studies on sintered 3D LCO cathodes used the same approach of restricting capacity to eliminate the degradation of cathode material, demonstrating energy densities of >350 Wh L^{-1}, at power densities exceeding

150 W L^{-1} (C/3 or higher) with microbatteries that were ~6mm^3 in volume.[65] The capacity limitations in this study were due to the mechanical strain transition metal oxides experience upon lithium insertion, and was not due to hot spots of current density degrading the material.

A key study by Ashby et al. on a 2.5D battery composed of LFP pillars, an ionogel electrolyte, and a lithium metal laminate, demonstrated the importance of ionic conductivity of the electrolyte in order to use more active-material and improve the accessible energy density.[61] The ionogel used in their study was composed of a molten salt confined in an inorganic matrix, which possessed a high ionic conductivity of 10^{-3} S cm^{-1}. This study demonstrated that with a high ionic conductivity in the electrolyte, short distances between electrodes are not as crucial to improve ion diffusion. They achieved high capacities (3.7 mWh cm^{-2} at 2.8 mW cm^{-2}), but simulations demonstrated that underutilization was still present at the center of the LFP pillars at higher rates

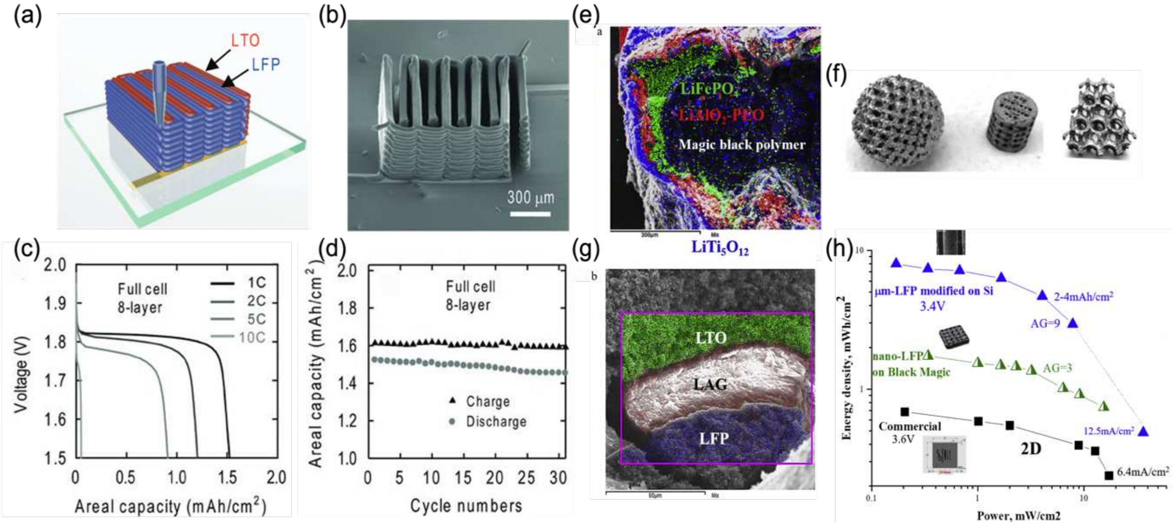

Figure 2.6: Using 3D printing to adapt geometries and materials more controllably**.** Schematic (a) and corresponding scanning electron microscopy image (b) of a 3D printed 3D interdigitated microbattery. The discharge areal capacity at different rates (c) and the areal capacity as a function of cycle number (d) for the 8 layered full 3D cell. Scanning electron microscope (SEM) cross-sections and energy dispersive spectroscopy mapping of the concentric like 3D battery composed of lithium iron phosphate-lithium aluminum oxide: poly ethylene oxide-lithium titanium oxide (LFP-LAO:PEO-LTO) (e) and lithium iron phosphate-lithium aluminum germanium phosphate: polyethyleneimine-lithium titanium oxide (LFP-LAGP:PEI-LTO) (g) that were studied by Cohen et al. Examples of 3D printed polymer scaffolds achieved by Cohen et al. (f). A ragone plot comparing the performance of the 3D printed cell composed of nano-LFP on BLACKMAGIC3D graphene-based polymer substrate to a commercial thin-film battery and a cell composed of LFP on a perforated silicon scaffold (h). Panels (a-d) were reproduced with permission from Sun et al. Ref [84] and panels (e-h) were reproduced from Cohen et al. Ref [85].

due to Li-ion transport in the electrolyte (**Figure 2.5e-h**), which would presumably be reduced by shorter transport distances (enabled by a fully interdigitated 3D architecture). Previous computational studies also demonstrate how non-uniform lithiation is intensified in 2.5D configurations due to non-uniform electrolyte thicknesses.[79] The extent of this non-uniformity in electrolyte thickness is heavily dependent on the geometric parameters, such as cathode thickness, height, width, and pitch of the microcolumns. The study by Ashby et al. attempted to circumvent these issues by including their high ionic conductivity ionogel, yet still had issues with electrode utilization.[61] All of the studies above underline the need to improve ionic conductivity and uniformity of the electrolyte in tandem with the geometry of the electrode to improve the overall energy density at higher current densities.

To tune geometric parameters additive manufacturing techniques, like 3D printing, have gained momentum for use in developing full 3D batteries.[21] The 3D printing process is a facile fabrication technique that is scalable, yet requires developing colloidal suspensions for inks and tuning parameters, such as the viscosity of the extrusion[21,80], particularly for the complex cathode and anode materials.[20,75,81–83] Experiments with 3D printing self-standing interdigitated cathodes and anodes composed of LFP and LTO, respectively, (**Figure 2.6a-b)** onto gold coated glass substrates have been performed[84]. The electrodes were then annealed at 600 ˚C to remove organic additives that were necessary for the colloidal suspension during printing. This annealing step leads to porous electrodes similar to the sintered electrodes described previously.[65] By removing the inactive organic material leads to a greater active surface area exposed to the electrolyte (improving the power density), and also decreases the overall weight of the cell to improve the energy density. When testing an 8-layer cell versus a 16-layer cell it was found that electronic conductivity was limited by the height of the interdigitated electrodes as both configurations exhibited the same capacities at lower charge/discharge rates. This lack of electrical conductivity underscores the need for further improvements in 3D printed electrode materials by including conductive additives or further tuning 3D configurations. Regardless of these limitations, the unpackaged 3D interdigitated microbattery by Sun et al., provided energy densities of 9.7 J cm^{-2} (2.69 mWh cm^{-2}) at 2.7 mW cm^{-2} (**Figure 2.6c-d),** demonstrating the applicability of 3D printing such batteries.[84] On the other hand, when the cell was packaged, the capacity dropped to 1.2 mAh cm^{-2} and had a poor cycle life due to the lack of air-free conditions provided by the 3D printed packaging.

In addition to inefficient packaging, 3D printing also introduces challenges in producing separation membranes or solid electrolytes with high ionic conductivities, limiting both power and energy densities. Challenges in producing solid state electrolytes may arise from the viscous nature of typical polymer-based electrolytes that are not compatible with conventional 3D printing techniques.[84–86] To circumvent these issues, ionogel-based solid electrolytes, first implemented by Delannoy et al. through ink-jet printing, were successfully deposited onto porous LFP and LTO electrodes.[81] The ionogel was composed of a mesoporous silica structure synthesized from the polycondensation of tetramethyl orthosilicate and combined with N-methyl-N-propylpyrrolidinium bis(trifluoromethan)suflonylimide (PYR13-TFSI), with lithium bis(trifluoromethan)sulfonylimide (Li-TFSI). The ink-jet printed ionogel demonstrated ionic conductivities of ~1×10^{-3} S cm^{-1} at room temperature, about 100 times higher than LiPON. By using this ionogel, they were able to achieve a surface capacity of 300 µAh cm^{-2} with up to 100 cycles for a 2D battery. A subsequent study also developed a thick conformally coated membrane made of $Li_{1+x}Al_yFE_{2-y}(PO_4)_3$-PEI (LAGP) nanoparticles with LiTFSI–PYR_{14}TFSI liquid electrolyte onto a 3D printed polymer scaffold with a reported ionic conductivity of 0.2×10^{-3} S cm^{-}

^{1}.[85] The LAGP nanoparticles were deposited onto the substrate via square-wave AC-electrophoretic deposition (EPD), and was one of the first studies to use EPD to conformally coat a quasi-solid electrolyte onto a 3D printed polymer-based 3D substrate (**Figure 2.6e-g)**.[85] This study also demonstrated the versatility of 3D printing by using polymers such as poly(lactic acid) (PLA), conductive graphene (a specific type called BLACKMAGIC3D), and ABS polymer mixed with carbon fibers. Through this technique they finely-tuned the size and shape of the scaffold to a resolution of 20 µm (**Figure 2.6f)**. Although scaffolds with complex geometries can be 3D printed, considerable challenges remain in implementing all other components of the battery, thus necessitating additional fabrication techniques like EPD. After forming the high aspect ratio polymer scaffold, they were able to use EPD again to conformally deposit LFP — the polymer-in-ceramic membrane — and LTO. While inactive components, such as the polymer scaffold, binders, and conductive additives in the EPD coatings were present, they still achieved appreciable areal capacities of 400–500 µAh cm^{-2} and better energy and power densities when compared to a commercial 2D Li-ion cell (**Figure 2.6h)**.[85] This study demonstrated the compatibility of 3D printing with EPD to achieve 3D structured microbatteries on perforated high-aspect-ratio polymer substrates, despite their low performance metrics. However, a study by Ji et al., has shown the possibility of simultaneously printing all components in an all-in-one fibrous Li-ion wire.[87] This system is not considered a full 3D battery by our definition, but adaptations to this technique could potentially lead towards 3D batteries with components that are entirely 3D printed.

As previously mentioned, 3D batteries can exacerbate inhomogeneous current densities, lithium concentration gradients, and underutilization of electrode materials due to the composition of the material and geometric factors. These issues have also been highlighted through computational studies, which indicate hot spots with highly concentrated current densities, dependent on the battery's particular architecture.[29,77,88] Inhomogeneous current densities may also arise from increasing the height of certain configurations, such as nanorods or pillars, and can lead to the underutilization of electrode materials, leading to lower energy densities.[32,77] Overutilization of electrode materials can also occur due to current density hotspots, and can lead to mechanical degradation related to volume expansion and/or other physical effects (e.g. delamination of active material from the current collector, excessive SEI formation, trapping of active ions) on the electrodes. Therefore, these physical parameters must be considered in computational modeling to demonstrate the full effect of inhomogeneous current densities to systematically improve the energy density and overall performance of 3D batteries.

2.5.3 Cyclability and Scalability

The substantial advances and current limitations to the power and energy densities achieved by today's 3D batteries were discussed in the previous section and are important for understanding how to advance these systems in terms of performance metrics. To proceed towards the commercialization and implementation of 3D batteries, cyclability and scalability must also be considered, and they should be emphasized in published research. Cyclability — or cycle life — is the ability of a battery to retain capacity over many cycles, and is a topic that has been well-explored for a variety of planar battery chemistries.[35,89,90] Unsurprisingly, given the nascency of the fields, few studies have focused on optimizing or understanding the cyclability of 3D batteries. This fact arises from both academic and industrial considerations. On the academic side, most investigations are focused on the fundamental electrochemistry in the 3D battery and are not focused on studying the system's ability to cycle stably. From an industrial perspective, information related to how a commercial 3D battery cycles is likely a trade secret for said company. Table 1 highlights this clearly, where few studies reported cycling data past 100 cycles.

This likely arose because extended cycle life studies were beyond the scope of the publications or are simply often not practical in an academic setting. While this is certainly understandable for preliminary investigations, extended cycle life studies are imperative as they provide insight into degradation mechanisms and inform researcher whether the system in question is predisposed for a specific application.

Extending the cycle life of unstable battery systems, like Li-metal batteries (unstable due to excessive side reactions), requires detailed studies on the interfacial interactions between the electrolyte and Li-metal anode.[91] This same principle is often applied to 3D batteries of all configurations, as the potential for deleterious reactions between components of the battery is assumed to be greater due to the enlarged interfacial surface area of these systems. While investigations have looked at interfacial interactions in 3D electrodes, and in some cases 3D batteries, these interactions and processes were not the primary focus of the investigations.[77] Focused characterization of the anode-electrolyte and electrolyte-cathode interfaces, for all 3D battery configurations, are excellent areas to begin investigating how these interactions affect the cyclability of 3D batteries. With this in mind, however, investigations on interfacial interactions in 3D batteries must consider the configuration of the battery. The importance of assessing cyclability with respect to 3D battery configurations results from the differences in the materials used and the different fabrication methods used for different types of 3D batteries (interdigitated versus aperiodic). Failure mechanisms in champion 2D materials, for example, will be exacerbated in 3D interdigitated systems owing to uneven current distributions and underutilization of active-material.[61] As such, there is a great need for focused studies on the cyclability of 3D batteries (experimentally and computationally) to provide insight into how these system degrade as a function of cycle number. Given the maturity of 3D batteries, the field is poised to achieve considerable improvements in terms of extending cycle life of these high surface area architectures.

Scalability, the ease with which a technology can progress from laboratory to commercial viability, is another factor to consider when developing 3D batteries. This metric is related to commercialization and is difficult to assess when reading fundamental studies. This challenge in data extrapolation is heightened by the — often large — gap in knowledge between academic and industrial circles. An example of this can be seen in reference to **Table A.I.I** and **A.I.II**, where the only indication of scalability is related to the 3D battery configuration and desired application, even though none of these studies considered if the methods used in the lab to create 3D batteries were potentially scalable on industrial levels. This arises from the fact that the scope of fundamental scientific studies does not often include considerations on scalability. However, there have been improvements in developing the communication between academic (fundamental, or use-inspired research) and industrial research communities, which will accelerate 3D battery research and their commercialization.

While fundamental insights are crucial in the development of 3D batteries, they do not always provide an understanding into how these systems can advance toward industrial implementation. A perspective by Firth et al. provides an industrial appraisal of the field of LIBs. Concerning scalability, the authors detail a road map for commercialization of new technologies and discuss practical considerations and speedbumps, with respect to capital expenditure and risk.[36] For 2D LIBs, some factors which affect scalability are supply chain considerations, cost forecasting, and manufacturing processes. All these factors also apply to the scalability of 3D batteries, yet there is added importance to the manufacturing processes. This arises from the fact that electrode and scaffold fabrication, conformal coating techniques, and packaging procedures are highly specific to each 3D battery configuration and application. With this in mind, a few 3D battery configurations are already well set-up to be scaled with pre-existing industrial processes (interdigitated microbatteries through the semi-conductor industry, aperiodic batteries via electroplating, concentric batteries via 3D printing).[18,41,92] The ease of scalability should not be overstated, as the packaging of these cells can be challenging. A perfect example of this is the case of inorganic solid electrolytes, requiring substantial stack pressures for operation, which may require auxiliary components and has implications on the overall energy density.[93] This results from the fact that, although some electrode and electrolyte fabrication methods are amenable to current industrial processes, the packaging of the complex (and often fragile) systems do not yet exist in industry. For example, 3D batteries using solid inorganic electrolytes will need accommodating auxiliary components resulting from the stack pressure requirements.[94,95] The importance of developing functional packaging methods and procedures is imperative, given the well-known relationship between external packaging and performance metrics (e.g. decrease in gravimetric energy and power densities from additional mass of packaging materials).[11]

2.6 Outlook and the Path Towards Commercialization of 3D Batteries

The need for advances in energy storage will only increase over the next several decades, with projections of the LIB market reaching 2,000 GWh in the United States by 2030 (based on a BloombergNEF Insight report). Current 2D LIBs are reaching their limit of performance and the range of applications that need better batteries continues to grow. The promise of 3D batteries is to enable improved performance by increasing the power densities along with high energy densities. As we've described above, these physical parameters enable peripheral improvements, such as the ability of fast-charging energy dense cells. The field must move from proof-of-concept to demonstrating the ability to scale to volumes relevant for different applications, which necessitates creative jumps in our approaches to solving these problems.

In this review, we have highlighted current advances in 3D batteries, as well as areas in which improvements can be made toward industrial realization. We have intentionally not defined a ‘best’ architecture of 3D batteries, given that individual applications are enabled by different combinations of the attributes provided by different 3D architectures. The challenge with developing commercially relevant 3D batteries has been that the research required has not fully transitioned from the fundamental or use-inspired levels to the more advanced process engineering stage related to industry. Fundament development is rarely pursued in industry due to the uncertainty of the time required for discovery (and the potential lost cost of failed research and industrial projects), and rarely funded in academia because of the need for optimization and refinement, which is not a focus for academic funding.

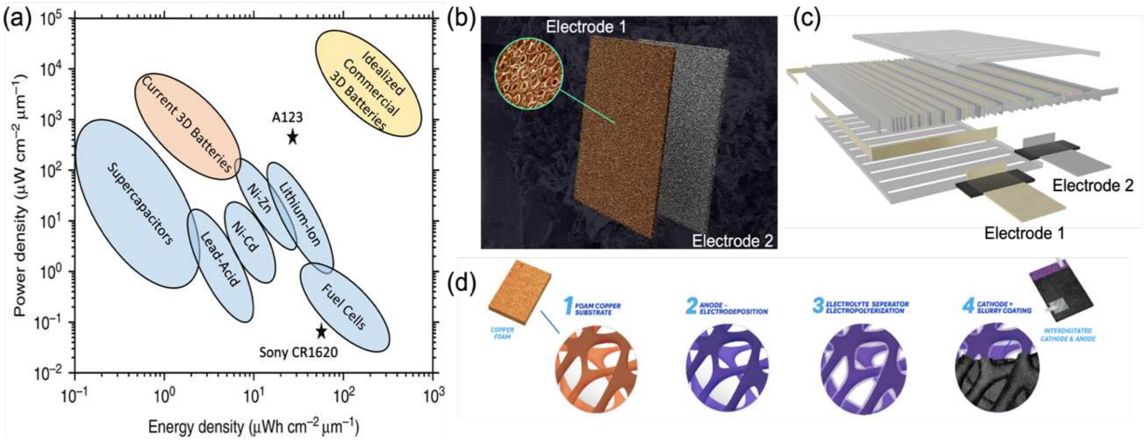

Figure 2.7: Progress towards the commercialization of 3D Batteries. (a) Ragone plot with general markings of the energy and power densities for current and idealized commercial 3D batteries, along with other types of energy storage systems already available on the market or of scientific interest. Modified from Ref [26]. (b) A schematic of a commercial high surface area metal foam-based (aperiodic) electrode from Addionics^{TM}. (c) 3D view of overlapping (concentric) parallel electrodes from Enovix. (d) schematic of metal foam-based full (aperiodic) 3D battery preparation from Prieto.

The performance of a specific material in concert with all other components of a battery can be difficult to decouple and understand if there are multiple bottlenecks (i.e. kinetic limitations or mechanical degradation) in the battery. This is particularly challenging for 3D batteries, which have high interfacial surface areas, and complex chemo-mechanical interactions, such that any degradation occurring at the electrode and electrolyte interface is exaggerated. While an individual 3D electrode may have impressive performance under idealized conditions, once integrated into a full 3D battery the overall performance of the cell may be limited. For this reason, although substantial advances in the architectures of individual components have been made, progress in the full integration of all components of a 3D battery has been challenging and their performance are still lacking in comparison to commercial 2D Li-ion batteries (**Figure 2.7a)**. Improvements, however, are being made to bridge this gap.

To advance technology, it is often important to take a step back — after all, the first automobiles were slower and less convenient than horse drawn carts, but quickly became more advanced and faster. The field is nearing the point where full integration of 3D batteries is very close, and improvements in energy density, cycle life, and scalability are critical. This means that the amount of optimization necessary for reasonable performance are increased, compared to traditional batteries, because all components must be iteratively improved in contact with each other. A high quality of materials, manufacturing processes, and interfaces are required before any expected benefits of the 3D architecture are obtained. Advancements in computational methods are also key to understand complex phenomena and predict what aspect of the 3D battery could be the bottleneck for a particular materials set.

The large size of the total accessible markets enabled by battery innovations are the motivation to push advances in 3D and is being demonstrated industrially. This is especially true because 2D rechargeable batteries will be unable to fill the same application spaces as 3D systems. Companies such as Addionics, Enovix, and Prieto (**Figure 2.7b-d**) have demonstrated considerable progress toward commercializing lithium-metal and lithium-ion batteries with advanced architectures. Companies such as these use a diverse set of advanced manufacturing methods that link key advances in other industries, such as semiconductor manufacturing, 3D printing, and electroplating. New 3D battery technology is not limited to drop-in replacements for current battery systems. By leveraging the third dimension, 3D battery technologies will allow for innovation across a large swath of applications and market sectors.

2.7 References

1. Atzori, L., Iera, A. & Morabito, G. The Internet of Things: A survey. *Comput. Netw.* **54**, 2787–2805 (2010).

2. Swan, M. Sensor Mania! The Internet of Things, Wearable Computing, Objective Metrics, and the Quantified Self 2.0. *J. Sens. Actuator Netw.* **1**, 217–253 (2012).

3. Nathan, M. *et al.* Three-dimensional thin-film Li-ion microbatteries for autonomous MEMS. *J. Microelectromechanical Syst.* **14**, 879–885 (2005).

4. Masias, A., Marcicki, J. & Paxton, W. A. Opportunities and Challenges of Lithium Ion Batteries in Automotive Applications. *ACS Energy Lett.* **6**, 621–630 (2021).

5. Viswanathan, V. *et al.* The challenges and opportunities of battery-powered flight. *Nature* **601**, 519–525 (2022).

6. Weiss, M. *et al.* Fast Charging of Lithium-Ion Batteries: A Review of Materials Aspects. *Adv. Energy Mater.* **11**, 2101126 (2021).

7. Vishnugopi, B. S., Verma, A. & Mukherjee, P. P. Fast Charging of Lithium-ion Batteries via Electrode Engineering. *J. Electrochem. Soc.* **167**, 090508 (2020).

8. Mistry, A., Usseglio-Viretta, F. L. E., Colclasure, A., Smith, K. & Mukherjee, P. P. Fingerprinting Redox Heterogeneity in Electrodes during Extreme Fast Charging. *J. Electrochem. Soc.* **167**, 090542 (2020).

9. Miranda, D., Costa, C. M., Almeida, A. M. & Lanceros-Méndez, S. Computer simulations of the influence of geometry in the performance of conventional and unconventional lithium-ion batteries. *Appl. Energy* **165**, 318–328 (2016).

10. Hung, C., Allu, S. & Cobb, C. L. Modeling Current Density Non-Uniformities to Understand High-Rate Limitations in 3D Interdigitated Lithium-ion Batteries. *J. Electrochem. Soc.* (2021) doi:10.1149/1945-7111/ac2ac5.

11. Hung, C.-H., Huynh, P., Teo, K. & Cobb, C. L. Are Three-dimensional Batteries Beneficial? Analyzing Historical Data to Elucidate Performance Advantages. *ACS Energy Lett.* **8**, 305 (2023).

12. Horowitz, Y., Strauss, E., Peled, E. & Golodnitsky, D. How to Pack a Punch – Why 3D Batteries are Essential. *Isr. J. Chem.* **61**, 38–50 (2021).

13. Roberts, M. *et al.* 3D lithium ion batteries - From fundamentals to fabrication. *J. Mater. Chem.* **21**, 9876–9890 (2011).

14. Arthur, T. S. *et al.* Three-dimensional electrodes and battery architectures. *MRS Bull.* **36**, 523–531 (2011).

15. Long, J. W., Dunn, B., Rolison, D. R. & White, H. S. Three-dimensional battery architectures. *Chem. Rev.* **104**, 4463–4492 (2004).

16. Liu, L., Zhao, H. & Lei, Y. Advances on three-dimensional electrodes for micro-supercapacitors : A mini-review. 74–84 (2019) doi:10.1002/inf2.12007.

17. Long, J. W., Dunn, B., Rolison, D. R. & White, H. S. 3D Architectures for Batteries and Electrodes. *Adv. Energy Mater.* **10**, 2002457–2002457 (2020).

18. Han, L., Hsieh, C.-T., Chandra Mallick, B., Li, J. & Ashraf Gandomi, Y. Recent progress and future prospects of atomic layer deposition to prepare/modify solid-state electrolytes and interfaces between electrodes for next-generation lithium batteries. *Nanoscale Adv.* **3**, 2728–2740 (2021).

19. Tolganbek, N. *et al.* Design and preparation of thin film gel polymer electrolyte for 3D Li-ion battery. *J. Power Sources* **493**, (2021).

20. Ferrari, S. *et al.* Latest advances in the manufacturing of 3D rechargeable lithium microbatteries. *J. Power Sources* **286**, 25–46 (2015).

21. Lyu, Z. *et al.* Design and Manufacture of 3D-Printed Batteries. 89–114 (2021) doi:10.1016/j.joule.2020.11.010.

22. Rolison, D. R. *et al.* Multifunctional 3D nanoarchitectures for energy storage and conversion. *Chem. Soc. Rev.* **38**, 226–252 (2009).

23. Priimägi, P. *et al.* Optimizing the design of 3D-pillar microbatteries using finite element modelling. *Electrochimica Acta* **209**, 138–148 (2016).

24. Long, J. W. & Rolison, D. R. Architectural design, interior decoration, and three-dimensional plumbing en route to multifunctional nanoarchitectures. *Acc. Chem. Res.* **40**, 854–862 (2007).

25. Valvo, M. *et al.* Electrochemical elaboration of electrodes and electrolytes for 3D structured batteries. *J. Mater. Chem. A* **1**, 9281–9293 (2013).

26. Pikul, J. H., Gang Zhang, H., Cho, J., Braun, P. V. & King, W. P. High-power lithium ion microbatteries from interdigitated three-dimensional bicontinuous nanoporous electrodes. *Nat. Commun.* **4**, 1732 (2013).

27. Zadin, V. & Brandell, D. Modelling polymer electrolytes for 3D-microbatteries using finite element analysis. *Electrochimica Acta* **57**, 237–243 (2011).

28. Jin, S., Jiang, Y., Ji, H. & Yu, Y. Advanced 3D Current Collectors for Lithium-Based Batteries. *Adv. Mater.* **30**, 1802014 (2018).

29. McKelvey, K., Brunet Cabré, M. & Esmeraldo Paiva, A. Continuum simulations for microscale 3D batteries. *Curr. Opin. Electrochem.* **21**, 76–83 (2020).

30. Miyamoto, K., Broderick, S. R. & Rajan, K. Data-driven optimization of 3D battery design. *J. Power Sources* **536**, 231473 (2022).

31. Clancy, T. M. & Rohan, J. F. Simulations of 3D nanoscale architectures and electrolyte characteristics for Li-ion microbatteries. *J. Energy Storage* **23**, 1–8 (2019).

32. Zadin, V., Kasemägi, H., Aabloo, A. & Brandell, D. Modelling electrode material utilization in the trench model 3D-microbattery by finite element analysis. *J. Power Sources* **195**, 6218–6224 (2010).

33. Salot, R., Martin, S., Oukassi, S., Bedjaoui, M. & Ubrig, J. Microbattery technology overview and associated multilayer encapsulation process. *Appl. Surf. Sci.* **256**, S54–S57 (2009).

34. Zhu, Z. *et al.* Recent Advances in High-Performance Microbatteries: Construction, Application, and Perspective. *Small* **16**, 2003251 (2020).

35. Lin, Z., Liu, T., Ai, X. & Liang, C. Aligning academia and industry for unified battery performance metrics. *Nat. Commun.* **9**, 8–12 (2018).

36. Frith, J. T., Lacey, M. J. & Ulissi, U. A non-academic perspective on the future of lithium-based batteries. *Nat. Commun.* **14**, 420 (2023).

37. Hur, J., I., Smith, L. C. & Dunn, B. High Areal Energy Density 3D Lithium-Ion Microbatteries. *Joule* **2**, 1187–1201 (2018).

38. Sun, B. *et al.* Toward Solid-State 3D-Microbatteries Using Functionalized Polycarbonate-Based Polymer Electrolytes. *ACS Appl. Mater. Interfaces* **10**, 2407–2413 (2018).

39. Létiche, M. *et al.* Atomic Layer Deposition of Functional Layers for on Chip 3D Li-Ion All Solid State Microbattery. *Adv. Energy Mater.* **7**, 1601402 (2017).

40. Moitzheim, S., Put, B. & Vereecken, P. M. Advances in 3D Thin-Film Li-Ion Batteries. **1900805**, 1–17 (2019).

41. Pearse, A. *et al.* Three-Dimensional Solid-State Lithium-Ion Batteries Fabricated by Conformal Vapor- Phase Chemistry. (2018) doi:10.1021/acsnano.7b08751.

42. Asfaw, H. D. *et al.* Nanosized $LiFePO_4$ -decorated emulsion-templated carbon foam for 3D micro batteries: a study of structure and electrochemical performance. *Nanoscale* **6**, 8804–8813 (2014).

43. Liu, J. *et al.* Atomic Layer Deposition of Hierarchical CNTs@FePO4 Architecture as a 3D Electrode for Lithium-Ion and Sodium-Ion Batteries. *Adv. Mater. Interfaces* **3**, (2016).

44. Voiry, D. *et al.* Best Practices for Reporting Electrocatalytic Performance of Nanomaterials. *ACS Nano* **12**, 9635–9638 (2018).

45. Duran, S. *et al.* Electrochemical Active Surface Area Determination of Iridium-Based Mixed Oxides by Mercury Underpotential Deposition. *ChemElectroChem* **8**, 3519–3524 (2021).

46. Miyamoto, K., Broderick, S. & Rajan, K. Three-dimensional microbattery design via an automatic geometry generator and machine-learning-based performance simulator. *Cell Rep. Phys. Sci.* **2**, 100504 (2021).

47. Miyamoto, K., Sasaki, T., Nishi, T., Itou, Y. & Takechi, K. 3D-Microbattery Architectural Design Optimization Using Automatic Geometry Generator and Transmission-Line Model. *iScience* **23**, 101317 (2020).

48. Wang, Z., Ni, J., Li, L. & Lu, J. Theoretical Simulation and Modeling of Three-Dimensional Batteries. *Cell Rep. Phys. Sci.* **1**, 100078 (2020).

49. Shenoy, V. B., Johari, P. & Qi, Y. Elastic softening of amorphous and crystalline Li–Si Phases with increasing Li concentration: A first-principles study. *J. Power Sources* **195**, 6825–6830 (2010).

50. Qi, Y., Hector, L. G., James, C. & Kim, K. J. Lithium Concentration Dependent Elastic Properties of Battery Electrode Materials from First Principles Calculations. *J. Electrochem. Soc.* **161**, F3010–F3018 (2014).

51. Kozen, A. C., Pearse, A. J., Lin, C.-F., Noked, M. & Rubloff, G. W. Atomic Layer Deposition of the Solid Electrolyte LiPON. *Chem. Mater.* **27**, 5324–5331 (2015).

52. Pearse, A. J. *et al.* Nanoscale Solid State Batteries Enabled by Thermal Atomic Layer Deposition of a Lithium Polyphosphazene Solid State Electrolyte. *Chem. Mater.* **29**, 3740–3753 (2017).

53. Liu, Y. *et al.* Stabilizing the Interface of NASICON Solid Electrolyte against Li Metal with Atomic Layer Deposition. *ACS Appl. Mater. Interfaces* **10**, 31240–31248 (2018).

54. Vishnugopi, B. S. *et al.* Challenges and Opportunities for Fast Charging of Solid-State Lithium Metal Batteries. *ACS Energy Lett.* **6**, 3734–3749 (2021).

55. Hatzell, K. B. *et al.* Challenges in Lithium Metal Anodes for Solid-State Batteries. *ACS Energy Lett.* **5**, 922–934 (2020).

56. Zhao, W., Yi, J., He, P. & Zhou, H. Solid-State Electrolytes for Lithium-Ion Batteries: Fundamentals, Challenges and Perspectives. *Electrochem. Energy Rev.* **2**, 574–605 (2019).

57. Nestler, T. *et al.* Separators and electrolytes for rechargeable batteries: Fundamentals and perspectives. *Phys. Sci. Rev.* **4**, (2019).

58. Koerver, R. *et al.* Chemo-mechanical expansion of lithium electrode materials – on the route to mechanically optimized all-solid-state batteries. *Energy Environ. Sci.* **11**, 2142–2158 (2018).

59. Naik, K. G., Vishnugopi, B. S. & Mukherjee, P. P. Heterogeneities affect solid-state battery cathode dynamics. *Energy Storage Mater.* **55**, 312–321 (2023).

60. Ashby, D. S., DeBlock, R. H., Lai, C. H., Choi, C. S. & Dunn, B. S. Patternable, Solution-Processed Ionogels for Thin-Film Lithium-Ion Electrolytes. *Joule* **1**, 344–358 (2017).

61. Ashby, D. S. *et al.* High-Performance Solid-State Lithium-Ion Battery with Mixed 2D and 3D Electrodes. *ACS Appl. Energy Mater.* **3**, 8402–8409 (2020).

62. Le Bideau, J., Viau, L. & Vioux, A. Ionogels, ionic liquid based hybrid materials. *Chem Soc Rev* **40**, 907–925 (2011).

63. Cheng, X., Pan, J., Zhao, Y., Liao, M. & Peng, H. Gel Polymer Electrolytes for Electrochemical Energy Storage. *Adv. Energy Mater.* **8**, 1702184 (2018).

64. Lundgren, H., Behm, M. & Lindbergh, G. Electrochemical Characterization and Temperature Dependency of Mass-Transport Properties of $LiPF_6$ in EC:DEC. *J. Electrochem. Soc.* **162**, A413–A420 (2015).

65. Lai, W. *et al.* Ultrahigh-Energy-Density Microbatteries Enabled by New Electrode Architecture and Micropackaging Design. *Adv. Mater.* **22**, E139–E144 (2010).

66. Cirigliano, N. *et al.* 3D Architectured Anodes for Lithium-Ion Microbatteries with Large Areal Capacity. *Energy Technol.* **2**, 362–369 (2014).

67. Yoshima, K., Munakata, H. & Kanamura, K. Fabrication of micro lithium-ion battery with 3D anode and 3D cathode by using polymer wall. *J. Power Sources* **208**, 404–408 (2012).

68. Lai, J., Nsabimana, A., Luque, R. & Xu, G. 3D Porous Carbonaceous Electrodes for Electrocatalytic Applications. *Joule* **2**, 76–93 (2018).

69. Ellis, B. L., Knauth, P. & Djenizian, T. Three-Dimensional Self-Supported Metal Oxides for Advanced Energy Storage. *Adv. Mater.* **26**, 3368–3397 (2014).

70. Moitzheim, S. *et al.* Toward 3D Thin-Film Batteries: Optimal Current-Collector Design and Scalable Fabrication of TiO2 Thin-Film Electrodes. *ACS Appl. Energy Mater.* **2**, 1774–1783 (2019).

71. Tan, S., Perre, E., Gustafsson, T. & Brandell, D. A solid state 3-D microbattery based on Cu 2Sb nanopillar anodes. in *Solid State Ionics* vol. 225 510–512 (2012).

72. Wang, Z. *et al.* Microspheres of Si@Carbon-CNTs composites with a stable 3D interpenetrating structure applied in high-performance lithium-ion battery. *J. Colloid Interface Sci.* **629**, 511–521 (2023).

73. Nurpeissova, A., Murat, E., Adi, A. & Bakenov, Z. 3D intermetallic anodes for Lithium-ion batteries. *Mater. Today Proc.* **5**, 22877–22881 (2018).

74. Baggetto, L., Niessen, R. A. H., Roozehoom, F. & Notten, P. H. L. High energy density all-solid-state batteries: A challenging concept towards 3D integration. *Adv. Funct. Mater.* **18**, 1057–1066 (2008).

75. Jetybayeva, A., Uzakbaiuly, B., Mukanova, A., Myung, S. T. & Bakenov, Z. Recent advancements in solid electrolytes integrated into all-solid-state 2D and 3D lithium-ion microbatteries. *J. Mater. Chem. A* **9**, 15140–15178 (2021).

76. Parker, J. F. *et al.* Rechargeable nickel–3D zinc batteries: An energy-dense, safer alternative to lithium-ion. *Science* **356**, 415–418 (2017).

77. Talin, A. A. *et al.* Fabrication, Testing, and Simulation of All-Solid-State Three-Dimensional Li-Ion Batteries. *ACS Appl. Mater. Interfaces* **8**, 32385–32391 (2016).

78. Zhang, T. & Ran, F. Design Strategies of 3D Carbon-Based Electrodes for Charge/Ion Transport in Lithium Ion Battery and Sodium Ion Battery. *Adv. Funct. Mater.* **31**, 2010041 (2021).

79. McKelvey, K., Talin, A. A., Dunn, B. & White, H. S. Microscale 2.5D Batteries. *J. Electrochem. Soc.* **164**, A2500 (2017).

80. Ponnada, S., Gorle, B., Bose, S. C. & Kiai, S. Current Insight into 3D Printing in Solid-State Lithium-Ion Batteries : A Perspective. **202200223**, (2022).

81. Delannoy, P.-E. *et al.* Toward fast and cost-effective ink-jet printing of solid electrolyte for lithium microbatteries. *J. Power Sources* **274**, 1085–1090 (2015).

82. Zhang, M. & Mei, H. 3D printing of structured electrodes for rechargeable batteries. 10670–10694 (2020) doi:10.1039/d0ta02099k.

83. Wei, T., Ahn, B. Y., Grotto, J. & Lewis, J. A. 3D Printing of Customized Li-Ion Batteries with Thick Electrodes. **1703027**, 1–7 (2018).

84. Sun, K. *et al.* 3D Printing of Interdigitated Li-Ion Microbattery Architectures. *Adv. Mater.* 4539–4543 (2013) doi:10.1002/adma.201301036.

85. Cohen, E. *et al.* Novel rechargeable 3D-Microbatteries on 3D-printed-polymer substrates: Feasibility study. *Electrochimica Acta* **265**, 690–701 (2018).

86. McOwen, D. W. *et al.* 3D-Printing Electrolytes for Solid-State Batteries. *Adv. Mater.* **30**, 1707132 (2018).

87. Ji, D., Zheng, H., Zhang, H., Liu, W. & Ding, J. Coaxial 3D-printing constructing all-in-one fibrous lithium-, sodium-, and zinc-ion batteries. *Chem. Eng. J.* **433**, 133815–133815 (2022).

88. Cobb, C. L. & Blanco, M. Modeling mass and density distribution effects on the performance of co-extruded electrodes for high energy density lithium-ion batteries. *J. Power Sources* **249**, 357–366 (2014).

89. Guo, J., Sun, A., Chen, X., Wang, C. & Manivannan, A. Cyclability study of silicon–carbon composite anodes for lithium-ion batteries using electrochemical impedance spectroscopy. *Electrochimica Acta* **56**, 3981–3987 (2011).

90. Han, Z. *et al.* Challenges and key parameters in exploring the cyclability limitation of practical lithium–sulfur batteries. *J. Mater. Chem. A* **9**, 24215–24240 (2021).

91. Liu, J. *et al.* Pathways for practical high-energy long-cycling lithium metal batteries. *Nat. Energy* **4**, 180–186 (2019).

92. Gimble, N., Nieto, K. & Prieto, A. Electrodeposition as a Powerful Tool for the Fabrication and Characterization of Next-Generation Anodes for Sodium Ion Rechargeable Batteries. *Electrochem. Soc. Interface* **30**, 59–63 (2021).

93. Lee, C. *et al.* Stack Pressure Measurements to Probe the Evolution of the Lithium–Solid-State Electrolyte Interface. *ACS Energy Lett.* **6**, 3261–3269 (2021).

94. Vishnugopi, B. S. *et al.* Asymmetric Contact Loss Dynamics during Plating and Stripping in Solid-State Batteries. *Adv. Energy Mater.* **13**, 2203671 (2023).

95. Xu, L. *et al.* Toward the Scale-Up of Solid-State Lithium Metal Batteries: The Gaps between Lab-Level Cells and Practical Large-Format Batteries. *Adv. Energy Mater.* **11**, 2002360 (2021).

96. Bard, J. A. & Faulkner, R. L. *Electrochemical Methods, Fundamentals and Applications*. (John Wiley & Sons, Inc, New York City, 2001).

97. Winter, M. & Brodd, R. J. What are batteries, fuel cells, and supercapacitors? *Chem. Rev.* **104**, 4245–4269 (2004).

98. Lawrence E. Malvern. *Introduction to the Mechanics of a Continous Medium*. (Prentice-Hall, Inc., 1969).

99. Browne, C. B. *et al.* A Survey of Monte Carlo Tree Search Methods. *IEEE Trans. Comput. Intell. AI Games* **4**, 1–43 (2012).

100. Anantharamulu, N. *et al.* A wide-ranging review on Nasicon type materials. *J. Mater. Sci.* **46**, 2821–2837 (2011).

101. Choi, C. S. *et al.* Synthesis and Properties of a Photopatternable Lithium-Ion Conducting Solid Electrolyte. *Adv. Mater.* **30**, 1703772 (2018).

102. Xiao, J., Shi, F., Glossmann, T., Burnett, C. & Liu, Z. From laboratory innovations to materials manufacturing for lithium-based batteries. *Nat. Energy* **8**, 329–339 (2023).

CHAPTER 3: Multi-functional cyclized-polyacrylonitrile (cPAN) as a coating for Sb-based anodes in Sodium-ion Batteries[3]

3.1 Overview

Conversion electrodes, like antimony (Sb), are high energy density electrode materials for sodium-ion batteries (NIBs). These materials are limited in their performance due to the mechanical instability of these systems resulting from volume expansion of the material during cycling. Stabilizing conversion materials using a conductive polymer binder (CPB) protective layer is an effective way to enhance the performance of these materials. There is, however, a lack of clear understanding of how CPBs affect the (de)insertion and surface chemistry of these systems. Herein, we report the systematic investigation of the effects on Na-ion (de)insertion chemistry of a cyclized-polyacrylonitrile (cPAN) layer on Sb-based conversion electrodes in NIBS. Through electrochemical characterization, it was determined that the inclusion of a cPAN layer increases the achievable capacity of the electrode system, due to the storage of Na-ions by the cPAN layer and facilitates Na-ion transport to the Sb active material at early cycles by reducing the charge transfer resistance of the ensemble electrode.

---

[3] A version of this chapter is published in *ACS Applied Materials and Interfaces* (10.1021/acsami.4c13887) with Daniel S. Windsor, Monika J. Perez, Erin R. Snyder, Nathan A. Neisius, Rhys A. Otten, Sarah C. Hall, Clara A. Tibbetts, Amber T. Krummel, and Amy L. Prieto. Daniel S. Windsor developed the initial hypotheses, designed experiments, analyzed data, and led the writing of the manuscript. Monika J. Perez collected, fit, and visualized the XPS data and assisted in writing the manuscript. Erin S. Snyder fit XPS data and assisted in writing the manuscript. Nathan A. Neisius collected PXRD data and conducted Rietveld Refinements, in addition to assisting in the writing of the manuscript. Rhys A. Otten collected and visualized the Vickers Hardness data, in addition to assisting in the writing of the manuscript. Sarah C. Hall, Clara A. Tibbetts, and Amber T. Krummel collected the FTIR data and assisted in writing the manuscript. Amy L. Prieto assisted in the conceptualization of the project, project administration, data interpretation, and manuscript editing.

3.2 Introduction

The development of renewable energy storage technologies have garnered much attention and capital because of their potential to reduce humanity's dependence on hydrocarbon-based energy sources to mitigate the effects of climate change.[1,2] Of the many renewable energy technologies under development, secondary battery (rechargeable) technologies have become ubiquitous.[3,4] Developed in the late 20th-century, Lithium-ion batteries (LIBs) have become an integral part modern life, owing to their inclusion in technologies ranging from mobile electronics to electric vehicles.[2,4,5] Despite the popularity and omnipresence of LIBs, there is no single battery technology that is perfect for every application, and as a result LIBs are not suitable for every energy storage application due to low natural abundance of lithium, cost, and geographical availability of the materials needed for this technology.[6,7] Sodium-ion batteries (NIBs) are an exciting alternative to LIBs for large scale energy storage applications, owing to the relative abundance of NIBs feedstock materials and a lower price point (\$6500/ton for Li_2CO_3, \$200/ton for Na_2CO_3).[8,9] Although NIBs are an exciting alternative to LIBs for grid-level energy storage, the materials that function in the NIBs system are not as well developed as are the materials for LIBs.

The NIBs system is amenable to a variety of different electrode materials. One class of high energy density materials for NIBs anodes are conversion electrodes. Conversion electrodes differ from intercalation electrodes, such as hard carbon, in that the active ions are not stored in interstitial positions within the lattice but are incorporated into new crystallographic phases.[10–15] Of the conversion electrodes studied for application in NIBs, antimony (Sb) is one of the most popular with a theoretical capacity of 660 mAh/g as well as good thermal stability and electrical conductivity.[16,17]

Although conversion electrode materials (like Sb) generally have higher theoretical capacities than intercalation electrodes, these materials are all inhibited by large volumetric expansions of the material when converted to the fully sodiated phase. The (de)sodiation of Sb begins with pristine Sb, either amorphous or trigonal Sb ($R\bar{3}m$), and fully sodiates to the hexagonal Na_3Sb ($P6_3/mmc$) before returning the original Sb (amorphous or phase trigonal) during desodiation.[18] These changes in the composition of the material lead to changes of up to 293% in the unit cell volume, which detrimentally affects the ability of this material to cycle stably in a battery.[17]

These volumetric changes between phases, during insertion/deinsertion of ions, are manifested in mechanical stresses and strains in the electrode material. As a result, the electrode material is pulverized, leading to a loss of reversible capacity through excessive solid-electrolyte interphase (SEI) growth, and can even lead to delamination of the electrode active material from the current collector.[14,16] Thus, to include conversion electrode materials in NIBs for high energy density systems, the stabilization of these materials is imperative.

To stabilize conversion electrodes, investigators have evaluated creative approaches toward stabilizing these systems. Some of these approaches include nanostructuring the active material[12,17,19], utilization of carbon to form composite electrodes[20], or incorporating inactive yet mechanically robust constituents in the electrode[14,15], as well as electrolyte optimization.[21,22] Of the many different approaches applied toward the stabilization of conversion electrodes, an increasingly popular approach is through the inclusion of conductive polymer binders (CPBs) in the electrode framework. The popularity of CPBs arises from the mechanical compliance of the polymeric layers, which alleviates the detrimental effects of the volume expansion.[12,23,24] The conductive nature of these polymers allows for pulverized pieces of active material to remain in electrical contact with the remainder of the bulk electrode.[12,25] A highly studied CPB in the LIBs literature is cyclized-polyacrylonitrile (cPAN), which is formed by pyrolyzing the polyacrylonitrile (PAN) precursor.[26,27] The cPAN polymer as a protective coating has been shown to enhance the performance of conversion electrodes (Si, Sn, Sb) in a variety of electrode configurations which is attributed to the mechanical robustness and electrical conductivity of the polymer.[11,12,28] The cPAN polymer has, also, been shown to actively store alkali metal ions as a standalone organic cathode.[28,29] In a recent study Zhang et al. reported that a slurry cast cPAN electrode had an achievable cycling capacity of 280 mAh/g, which is comparable to the achievable capacity of hard carbon anodes in NIBs.[28]

Despite the depth of work on cPAN in the battery literature, there is a distinct lack of understanding as to how the inclusion of cPAN, as a protective coating affects the Na-ion insertion/deinsertion, and surface chemistry of the anode it is applied to. Given the complexity of battery systems, a clear understanding of the functionality of the constituents in a battery are imperative if we are to understand how different materials impact cell degradation, leading to informed design principles. Therefore, the objective of this investigation is to study the effects of cPAN on the fundamental electrochemistry of the anode system it is applied to. To achieve this, a layered coating-active material configuration, with the cPAN precursor (PAN) spin-coated onto thin-film electrodeposited Sb, was used. The advantage of this configuration is that it negates the convoluting effects of constituents of in slurry cast electrodes on the electrochemical data and the effects of nano scales active materials or nano-fabricated structures.[16,30] For these reasons, the layered coating-active material configuration aides in the study of the fundamental interactions occurring at the electrode in question.

Herein, we reported a detailed investigation aimed at characterizing the effect of a cPAN protective layer on the fundamental (de)sodiation chemistry and surface chemistry (SEI formation) of Sb-based anodes in NIBs. We tested the effect of cPAN on the achievable capacity, initial capacity loss (ICL), coulombic efficiency (CE), and rate capability of Sb-based electrodes through galvanostatic cycling experiments. Differential capacity (dQ/dV) analysis was used to assess the effect of cPAN on the (de)sodiation chemistry of Sb, while constant-current constant-voltage (CCCV) with electrochemical impedance spectroscopy (EIS) was used to assess the effect of cPAN on the resistive properties of Sb during cycling. A cPAN protective coating not only increases the achievable capacity of the anode, but it also facilitates Na-ion conduction at the electrode-electrolyte interface.

3.3 Results and Discussion

3.3.1 Anode Characterization

The cyclization of PAN to form cPAN, while be easily conducted through the partial pyrolysis of the polymer, is highly dependent on the temperature and time of the heating process.[26,27,33] To determine the extent of PAN cyclization from an annealing process a 1M PAN solution in DMF was spin-coated onto a stainless-steel disk, followed by annealing in a tube furnace under flowing argon for 4 hours at 300 ℃. The ATR-FTIR spectra of a PAN@stainless-steel disk (blue) and an annealed PAN@stainless-steel disk (black) are displayed in **Figure 3.1a**. The pre annealed system shows a sharp peak at 2244 cm^{-1} which is indicative of C-N triple bond stretching from the nitrile group in the PAN structure.[26,33] This feature disappears upon annealing of the sample. In addition, the annealed sample displays a strong peak at roughly 1600 cm^{-1} which relates to C-N double bond stretching in a conjugated system.[26,34] The absence of a peak at 2244 cm^{-1} and the presence of a peak at roughly 1600 cm^{-1} indicate that the annealing process results in the cyclized PAN structure, which are in good agreement with the literature.[12,26,33,34] The broad resonances at roughly 2900 cm^{-1} in the blue spectrum relate to the extent of hydrogenation on the PAN polymer backbone.[26]

The diminished intensity of this peak in the annealed PAN spectrum demonstrates that the annealing process leads to some extent of conjugation of the carbon backbone itself, which further indicates the cyclization of this material.

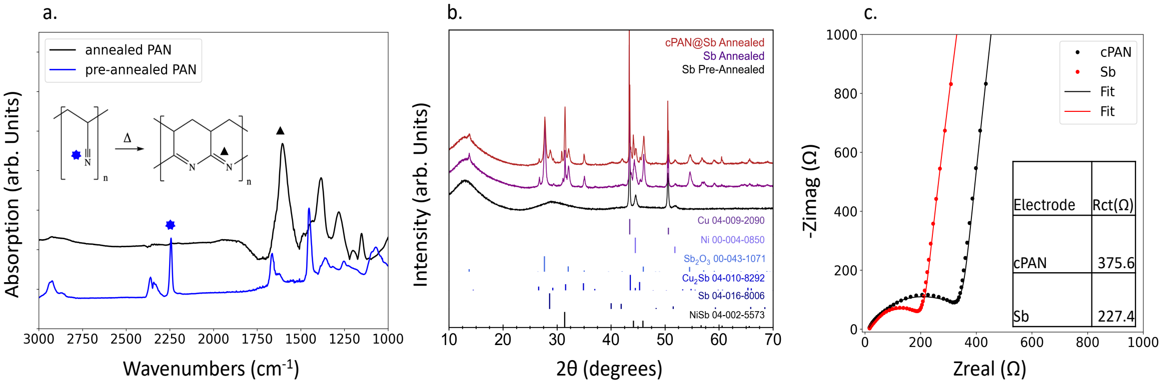

Electrode	Rct(Ω)
cPAN	375.6
Sb	227.4

Figure 3.1: Materials characterization of cPAN@Sb-based and Sb-based electrodes. A) Fourier-Transfrom Infrared spectroscopy (FTIR) of spin-coated polyacrylonitrile (PAN), blue, and annealed cyclized-polyacrylontrile (cPAN), black. B) Powder X-ray diffraction (PXRD) patterns of a Sb electrode, pre- and post-annealing, with a cPAN@Sb annealed pattern. C) is an electrochemical impedance spectroscopy (EIS) Nyquist plot with cPAN@Sb-based (black) and Sb-based (red) in Swagelok half-cells prior to battery cycling.

A thin film, layered, active material-coating configuration (**Schematic 3.1a**) allows for fundamental insight into the effect of the cPAN coating on the electrochemistry of the Sb active material, without convoluting effects from binders and additives common in battery electrodes for NIBS (**Schematic 3.1b**). Given the temperature requirements for the cyclization of PAN, and the thin-film layered configuration for the coating/active material, it was imperative to assess how the annealing process affected the composition of the Sb thin film deposition. After the annealing process a conversion of the electrodeposited Sb results in the formation of crystalline Sb, Sb_2O_3, NiSb, and Cu_2Sb, **Figure 3.1b**.

The composition of the cPAN and Sb systems were assessed via powder X-ray diffraction (PXRD) and scanning electron microscopy (SEM)/energy-dispersive X-ray spectroscopy (EDS). Pre-annealed films resemble previously reported diffraction data from our group, where a low crystalline, strained, Sb phase is represented by the broad (10-2) peak at 29° 2θ.[35] This artifact has been widely investigated and is attributed to the formation of a densely packed Sb phase (strain), while the decrease in the crystallinity is due to CTAB acting as a capping ligand for small Sb particles.[35] A Ni layer was also deposited to the tCu substrate to reduce the extent of Cu-diffusion during the annealing step, which is also present in the pre-annealed diffraction pattern.[36] **Figure A.II.I** displays an image of an Sb@tCu electrode after the annealing step, where it is clear to see that the solid-state diffusion of the Cu into the Sb layer resulted in a mechanically unstable electrode system.[36] The presence of surface oxides (hypothesized to be Sb_2O_3) is confirmed with SEM/EDS, **Figure A.II.II**, and is further highlighted to be on the surface or amorphous due to the absence of crystalline Sb_2O_3 in the pre-annealed diffraction pattern. The presence of Sb_2O_3 likely arises from a surface oxide layer that becomes incorporated into the Sb electrodeposited material via the annealing process as a crystalline Sb_2O_3 phase, given that the annealing process occurs under an Ar atmosphere. The Sb-O phase diagram supports the formation of this Sb-oxide phase, which has been reported to a multicomponent Sb + Sb_2O_3 phase at temperatures close to 375 °C.[37]

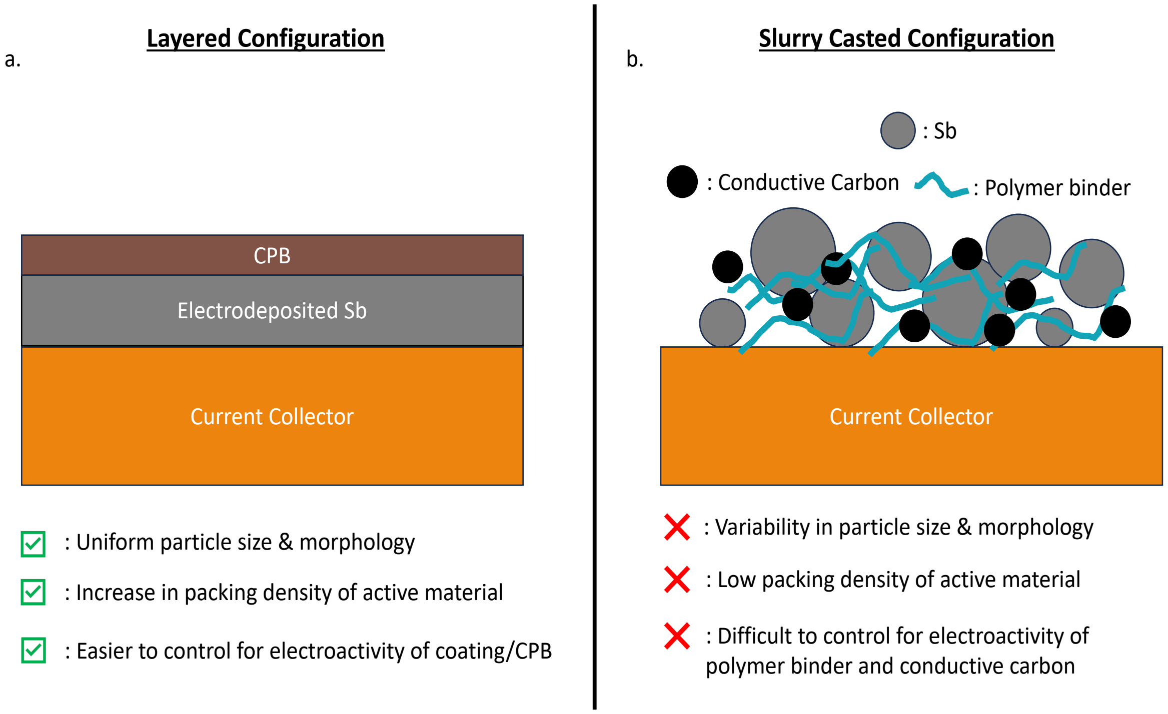

Schematic 3.1: Electrode configurations for fundamental studies. A) Layered configuration of thin film, electrodeposited, Sb on a current collector, coated by a conductive polymer binder. B) Representation of a traditional slurry cast electrode with binders and conductive additives within the electrode system.

This temperature for Sb + Sb_2O_3 formation is high than the annealing temperature used in this investigation, however the presence of Sb_2O_3 under these conditions can be explained owing to the reduced pressure (between -0.05 and -0.1 MPa) utilized for the annealing of the PAN polymer.

The NiSb and Cu_2Sb phases arise from the solid-state diffusion of Ni and Cu from the substrate into the Sb material during the annealing step, which occurs due to the thin film (layered) electrode configuration used in this study. The formation of the Cu_2Sb phase has been shown to occur to Sb thin-films deposited onto Cu-current collectors when annealed 300 °C, which is also supported by the Cu-Sb phase diagram which shows that this phase can form at roughly 260 °C.[38,39] Assessment of the Ni-Sb phase diagram, also, helps to explain the presence of the Ni-Sb phase, which can form at the temperatures used in the annealing process for this investigation.[40] Quantitative analysis of the PXRD patterns in **Figure 3.1b** was conducted via Rietveld Refinements, as represented in **Figure A.II.III**. The refinements show that most of the crystalline phases are comprised of Sb_2O_3 in both the cPAN@Sb and Sb systems, with small amounts of crystalline NiSb and Cu_2Sb. Concerning Sb, the refinements shown in Figure S3 are consistent with the results of the work of Nieto et al., which has been shown to be low crystalline, mostly amorphous, bulk Sb.[35] The refinements, in both systems, display peaks at roughly 30 and 60 degrees 2θ which were unable to be assigned with the reference PDFs used for these analyses. These phases likely relate to minor byproducts from the annealing process and could consist of a ternary Cu-Ni-Sb phase or an NiSb phase of a different crystal structure to the NiSb assigned in the refinements, **Figure A.II.III**. Raw Rietveld Refinement data, with weight percentages and weight percent errors, are reported in the supplementary information.

$$m_{dep} = \frac{MW}{nF} Q \tag{3.1}$$

Given the mixed composition of the resulting film, the mass of the active material was determined during from the charge passed during the Sb electrodeposition, as described by **Equation 3.1**. In other words, the active material mass used to normalize the electrochemical data in this investigation accounts for the ensemble Sb present in the film, regardless of the extent of Ni, Cu, or O incorporation. The presence of cPAN at the annealed Sb film does not appreciably change the composition of the film, compared to the annealed Sb film without the cPAN, which serves for the purposes of studying the fundamental impact of cPAN on the (de)sodiation and surface chemistry of Sb.

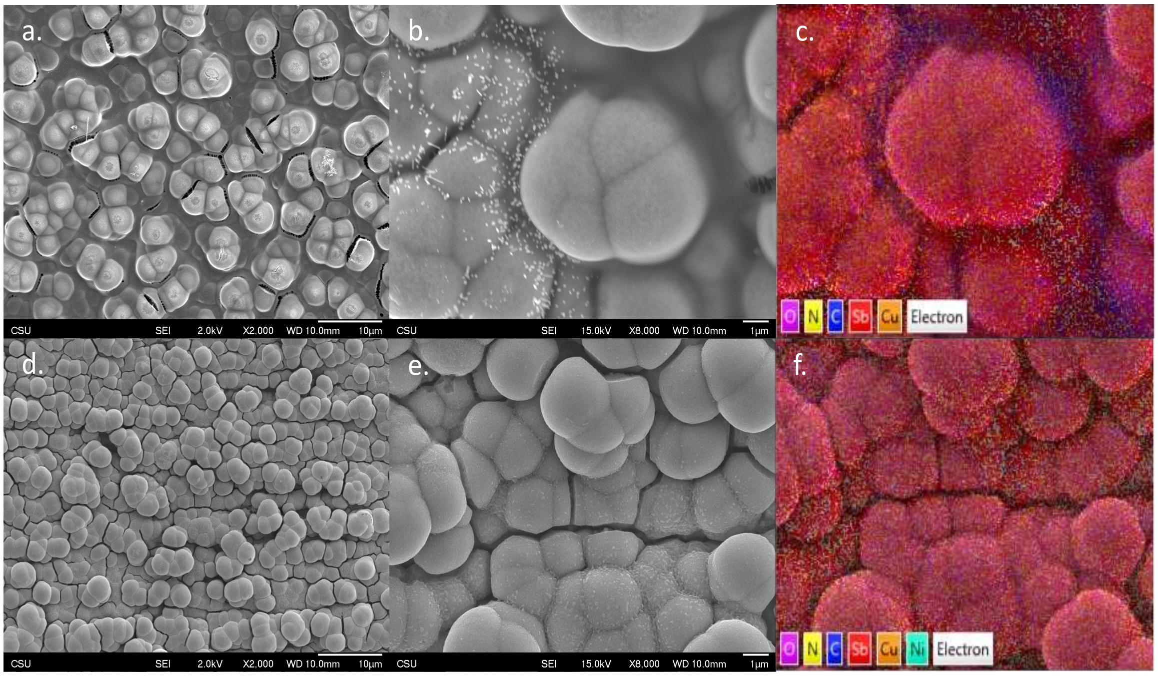

Figure 3.2: Scanning electron microsope (SEM) with X-ray energy dispersive spectroscopy (EDS) characterization of annealed cPAN@Sb and Sb systems. A) SEM image of a pre-cycled cPAN@Sb electrode at x2000 magnification with an accelerating voltage of 2kV. B) SEM image of a pre-cycled cPAN@Sb electrode at x8000 magnification with an accelerating of 15kV where C) is the accompanying EDS elemental map. D) SEM image of a pre-cycled Sb electrode at x2000 magnification with an accelerating voltage of 2kV. E) SEM image of a pre-cycled Sb electrode at x8000 magnification with an accelerating of 15kV where F) is the accompanying EDS elemental map.

The morphology and composition of the cPAN@Sb and Sb systems after the annealing process were determined via SEM/EDS, as seen in **Figure 3.2**. The electrodeposited Sb-based system retains the cauliflower shaped structure in accordance with previous work from our group.[14,35] The inclusion of the cPAN layer does not change the structure of the Sb particles, instead the cPAN polymer acts to fill in the gaps between the Sb domains, **Figure 3.2a** and 3.**2b**. Elemental mapping with EDS for the cPAN@Sb (**Figure 3.2c**) and Sb (**Figure 3.2f**) systems demonstrate the composition of the post-annealed films are similar, in accordance with the PXRD results from **Figure 3.1b**. Elemental EDS maps of each identified element are displayed in **Figure A.II.IV** and **A.II.V** for the cPAN@Sb and Sb systems, respectively. In the elemental map of the cPAN@Sb and Sb systems show uniform distribution of Sb, Cu, and O over the bulbous Sb features. In Figure S3, the carbon distribution is concentrated at the spaces between the Sb features in the thin-film, which implies that the cPAN is centered at the void spaces between Sb bulbs.

The thickness of the spin-coated and annealed cPAN was determined via cross-sectional SEM of a spin-coated cPAN@Si-wafer, **Figure A.II.VI**, which resulted in a cPAN thickness of roughly 250 nm. Even though cPAN inclusion to an Sb electrode resulted in an Sb film with filled in gaps between the Sb particles, the electrochemical active surface area (ECSA) of the cPAN@Sb-based (4.79±0.59 cm^2) system was larger than that of the Sb-based (3.84±0.40 cm^2) system alone, **Figure A.II.VII**. This difference in the ECSA may result from the porosity of the cPAN layer.[29]

Indentation testing of the cPAN and Sb systems, prior to cycling, demonstrated that the inclusion of cPAN to the Sb electrode increased the hardness of the electrode system, **Figure A.II.VIII**. As seen in **Figure A.II.VIIIe**, the Vickers Hardness for the cPAN@Sb system was 42.5 Hv, while the Sb system had a Vickers hardness of 32.5 Hv. A study by Moon et al. demonstrated the correlation between particle hardness and cycling performance in lithium-ion battery cathodes, however this notion has yet to be validated for anodes in NIBs.[41] It must be noted that these measurements relate to the entire electrode, and not solely the cPAN. Despite the lack of information on the mechanical properties of cPAN, these measurements do provide insight into the effect of cPAN on the hardness of the ensemble Sb-based electrode, and thus the structure's resistance to local plastic deformation, which is the purpose of the investigation herein. As seen in the hardness plot, the inclusion of cPAN to the Sb-based electrode does improve the hardness of the entire electrode system, which we would expect to increase the cycle life of the Sb electrode the cPAN is applied to.

The charge transfer resistance (R_{CT}), characterized by EIS, of the pristine cPAN@Sb-based electrode was greater than that of the pristine Sb-based system alone, **Figure 3.1c**. The EIS spectra were fit to a modified Rondels equivalent circuit model which has been previously used for the analysis of Sb anodes in NIBs, as seen in **Figure A.II.IX**.[20,35,42] Although cPAN has mixed conducting properties, most of this conductivity likely arises from the conjugated polymer backbone provided by the cyclization of this material.[33] As such, we initially hypothesized that the cPAN system would have a higher charge transfer resistance (Rct) compared to the Sb-based system, given that the polymer layer should impede the passage of Na-ions, which is supported by the pristine EIS analysis. This implies that the cPAN system should have lower ICL than the Sb control, and points to the notion that the cPAN may not be behaving solely as a conductive film.

3.3.2 Electrochemical characterization

Inclusion of the cPAN to the Sb anode increases the achievable capacity and reduces the initial capacity loss (ICL) compared to the bare Sb system. The most straightforward approach toward assessing the effect of cPAN on the charge storage capabilities of Sb is through galvanostatic (constant current) cycling of the two batteries systems to conduct cycle life analysis. Cycle life analysis assesses how the cPAN affected the capacity, ICL, and Coulombic efficiency (CE) of the cPAN and Sb systems, **Figure 3.3a**. The voltage (voltage-capacity) profiles for the cPAN@Sb and

Sb cycling experiments, plotted from cycle 1 to 51 in increments of 10 cycles, can be found in **Figure A.II.X**. In the literature cPAN has been shown to actively store Na-ions in the work of Zhang et al.[28] which reported a realized Na-ion storage capacity of 280 mAh/g. Second, cPAN is well known in the literature to stabilize conversion electrodes due to the mechanical properties of the polymer.[12,24] As such, we hypothesized that the cPAN layer should provide a higher capacity than the Sb-based system, which should result in distinct (de)sodiation features from the cPAN, in addition to the (de)sodiation features of Sb in a NIBs system. We would also expect to the cPAN@Sb-based system to have lower initial coulombic efficiency (CE) and a large initial capacity loss (ICL) given the increased resistance provided by the cPAN, as seen in **Figure 3.1c**. Contrary to our initial hypothesis, the ICL for the cPAN was 215 mAh/g, while for the Sb system the ICL was 247 mAh/g. These differences in the ICL may result from the added charge storage capabilities of the cPAN polymer on the ensemble electrode. These systems, also, displayed Coulombic efficiency values of 98-99%, which is consistent with the Coulombic efficiencies reported by the work of Nieto et al.[35]

To confirm that the cPAN layer was itself contributing the capacity of the anode, cPAN slurry cast electrodes were fabricated with conductive carbon and a PVDF binder, like the work of Zhang et al. These electrodes were prepared as detailed by the work of Nieto et al.[16] and were cycled in 2032-coin cells at a rate of 14 mA/g, which can nominally be described as a rate of C/20. The potential window for these cells was 0.15 to 1.5 V vs. Na/Na^+ to omit any contributions to the recorded capacity from Na plating/stripping at the electrode. As seen in **Figure A.II.XI**, cPAN slurry cast electrodes did store Na-ions stably for 50 cycles, however at a significantly lower capacity (roughly 25 mAh/g) compared to what has been reported in the literature.[28] Despite the differences in the realized capacity between this study and the work of Zhang et al., the data in

Figure A.II.XI clearly demonstrate that cPAN is capable of reversibly storing Na-ions. The mechanism by which cPAN stores Na-ions is certainly non-faradic in nature, as seen in the differential capacity plots in **Figure A.II.XI**, indicated by the offset from zero for both the sodiation and desodiation half-cycles with no sharp/distinct features in the plot. Due to the lack of distinct features in the dQ/dV plot in **Figure A.II.XId**, and the small magnitude of the (de)sodiation features, it was expected to be difficult to assess exactly how the cPAN affected the (de)sodiation chemistry of the Sb anode.

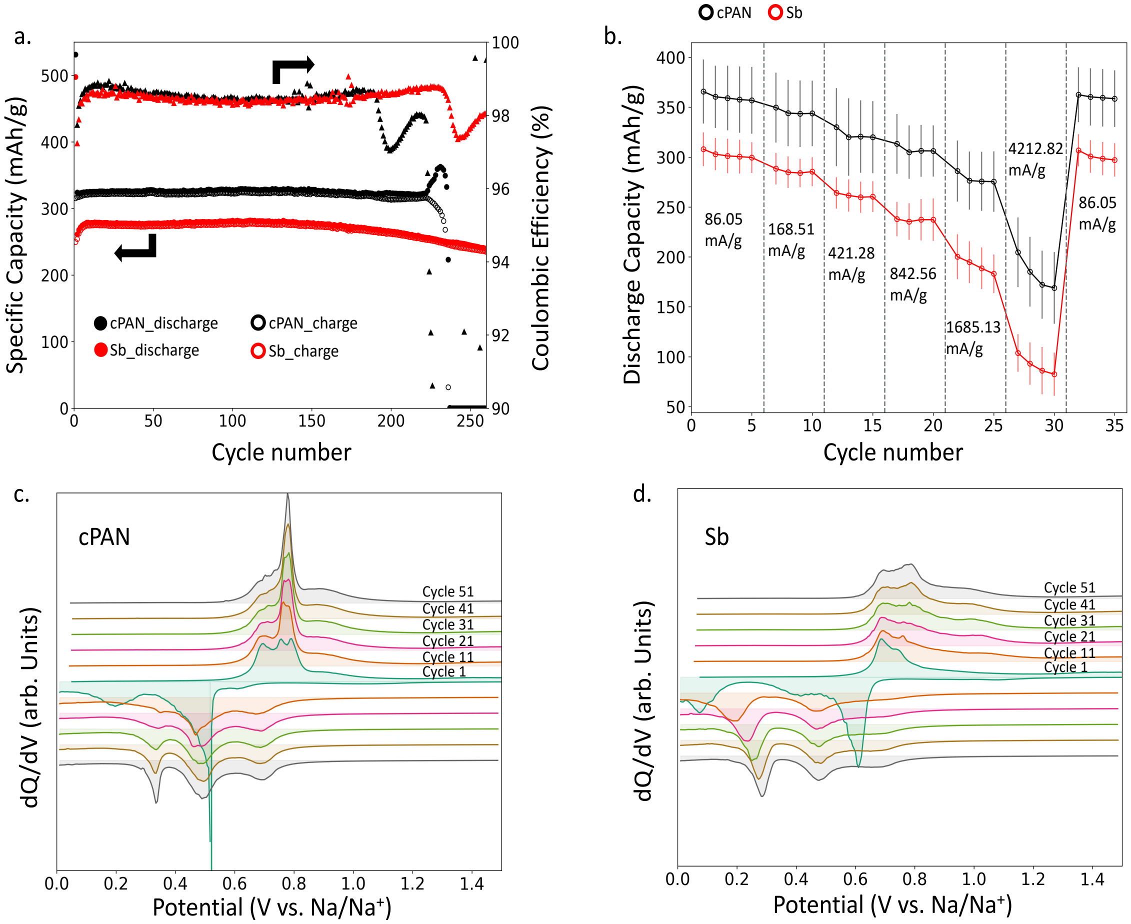

Figure 3.3: Electrochemical Characterization of cPAN@Sb-based and Sb-based electrodes. A) Galvanostatic cycling data and coulombic efficiency of cPAN@Sb-based (black) and Sb-based (red) electrodes in Na-ion half-cells at a rate of 117.16 mA/g. The cPAN@Sb-based system has higher capacity and lower initial capacity loss compared to the Sb-based system. B) Rate capability testing of cPAN@Sb-based (black) and Sb-based (red) electrodes plotted with 90% confidence intervals. The cPAN@Sb-based system has better rate capability compared to the Sb-based control. C) and D) related to offset differential capacity (dQ/dV) plots of cPAN@Sb and Sb electrodes, respectively.

An interesting feature of the cycle life analysis can be found at the point where both systems begin to display signs of failure. At roughly 225 cycles in **Figure 3.3a**, the CE of the cPAN system dramatically decreases, which is shortly followed by a sharp decrease in the charge capacity with a sharp increase in the discharge capacity. These features imply that, as the cycle number increases, the cPAN system can accept charge more easily than it is able to release it. This decay feature in the cycle life plot may result from delamination of the cPAN and Sb from the current, exposing the electrode to fresh electrolyte resulting in the irreversible consumption of charge due to SEI formation.[14] The worse cycle life performance for the cPAN system in this study, contrary to the consensus in the field, likely arises from the electrode-polymer layer configuration. Traditionally, in the field, cPAN is used to stabilize conversion materials on the nanoparticle scale in a core-shell configuration which results in the alleviation of the effects of volume expansion of the core by the shell (cPAN) in three dimensions.[12] This, then, suggests that a nano-structured or composite electrode configuration is necessary to achieve cycle life improvements with the cPAN protective coating. While the layered coating-active material did not provide for the expected cycle life improvement usually seen with cPAN coated electrode, it did provide this investigation with a system capable of highlighting and deconvoluting degradation effects for these systems.

Rate capability tests demonstrated that the cPAN has a higher capacity and better capacity retention, as a function of rate, compared to the Sb system (**Figure 3.3b**). The use of rate capability tests provide information into how the electrode system in question functions are increasing current loads, which is preliminary information on the achievable power density of the system. These rate tests were conducted at the increasing current densities (86.05 mA/g, 168.51 mA/g, 421.28 mA/g, 842.56 mA/g, 1685.13 mA/g, 4212.82 mA/g, and 86.05 mA/g) over 36 cycles following a 10-cycle formation period, plotted with 90% confidence intervals. Concerning the capacity retention as a function of rate, the cPAN system retained 90.5% of the capacity upon transitioning from 842.56 mA/g to 1685.13 mA/g, and 65.6% upon the transition from 1685.13 mA/g to 4212.82 mA/g. The Sb system retained 80.9% of the capacity upon transitioning from 842.56 mA/g to 1685.13 mA/g, and 47.7% upon the transition from 1685.13 mA/g to 4212.82 mA/g. These results demonstrate that the inclusion of cPAN to an Sb-based electrode increase the overall capacity and capacity retention as a function of rate. This may arise from the mechanical stabilization from the increased hardness, which could confer an overall resistance to self-pulverization of the cPAN@Sb-based system, or a difference in the composition of the SEI at the anode-electrolyte interface provided cPAN. While these rate capability test provide information on electrode capacity as a function of rate, they do not provide any insight into the effect of cPAN on the (de)sodiation chemistry of Sb.

The cPAN layer most affected the early cycle (de)sodiation chemistry of the Sb anode it was applied to. Initially we hypothesized that the cPAN layer, given its activity toward Na-ions, would affect the observed (de)sodiation chemistry of the ensemble electrode. To test this hypothesis, differential capacity (dQ/dV) plots were generated to assess where on the potential landscape the major (de)sodiation events occurred for the cPAN@Sb-based and Sb-based systems. The data used to generate the dQ/dV plots can be found in **Figure A.II.X**, where the differential of the raw data displayed in the voltage profiles is taken such that the platues in the voltage profiles turn into peaks in the dQ/dV plots. **Figures 3.3c** and **3.3d** display the dQ/dV plots in increments of 10 cycles from the 1st cycle to the 51st for the cPAN@Sb-based and Sb-based systems, respectively. The first cycle in both 2.c and 2.d display a distinct electrolyte reduction peak at roughly 500 mV vs. Na/Na^+ for the cPAN system, and 600 mV vs. Na/Na^+ for the Sb system, which is indicative of SEI formation.[43] The increase in the overpotential for the electrolyte reduction in the cPAN system is attributed larger Rct of the cPAN system, which is displayed in **Figure 3.1c**. Concerning cycles

11, 21, and 31 in **Figure 3.3d**, the main sodiation peak for the Sb-based system occurs at significantly more negative potentials (roughly 100mV vs. Na/Na$^+$), which transitions to more positive potentials as a function of cycle number. This behavior likely arises from the excess energy required to break the M-Sb or O-Sb bonds present in the starting material, **Figure 3.1b**. For the cPAN system at early cycles, the main sodiation peak arrives at significantly more positive potentials (roughly 450mV vs. Na/Na$^+$), which implies that the cPAN facilitates the sodiation of Sb, despite the increased interfacial resistance of the pristine electrode. These differences in the dQ/dV plots for the initial cycles of the cPAN@Sb-based and Sb-based electrodes is of great interest, and points to the importance of both the interfacial chemistry and resistance phenomena over the applied potential window. By 51st cycle, both systems display 3 distinct sodiation events, which are representative of the sodiation of electrodeposited Sb electrodes seen in previous work by this group.[16,35] Concerning the desodiation events, the cPAN system has much more distinct features at the main desodiation event compared to the Sb system. At roughly 1.0 V vs. Na/Na$^+$, both systems display a broad shoulder after the main desodiation event, which is indicative of Sb_2O_3 desodiation, as seen in previous work.[16] The results of the electrochemical experiments demonstrate that the inclusion of cPAN increases the capacity and improves the better rate capabilities of the Sb anode.

The increase in the capacity results from the charge storage capabilities of the cPAN polymer, while the improved rate capability is attributed to the improved hardness of the electrode system (**Figure A.II.VIII**) or differences in the as formed SEI. Interestingly, despite the improved hardness provided by the polymer, the cPAN system had a shorter cycle life compared to the Sb control, which likely occurs from delamination of the cPAN@Sb from the current collector. This is likely an artifact of the coating-active material configuration used in this investigation (layered configuration, **Scheme 3.1b**) and suggests that nano-structuring of the coating and active material is crucial to achieve the cycle life improvements from cPAN seen in the literature. Concerning the effect of cPAN on the Sb (de)sodiation chemistry, we see that the cPAN helps to facilitate Na-ion insertion at more positive potentials than in the Sb system over the first 40 cycles or so. While

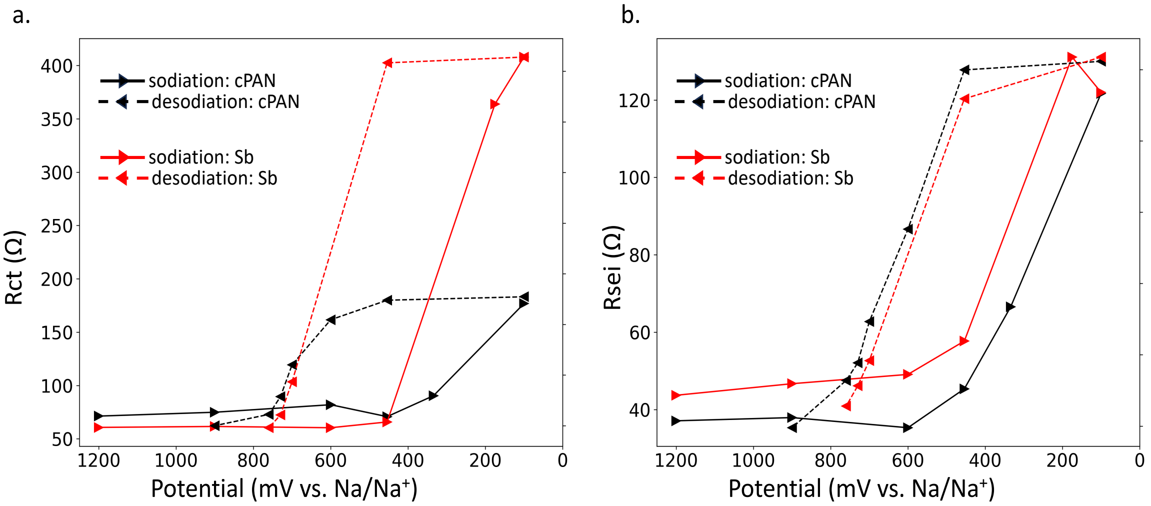

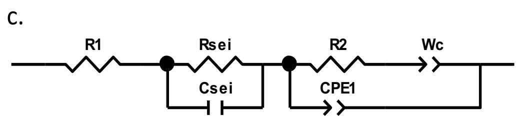

d.

Electrode system	**Rct @ 0.1V vs. Na/Na⁺ (Ω)**	**Rsei @ 0.1V vs. Na/Na⁺ (Ω)**
cPAN@Sb	176.8	121.7
Sb	407.9	122

Figure 3.4: Electrochemical impedance spectroscopy analysis of cPAN@Sb and Sb electrodes as a function of potential. A) Charge transfer resistance (Rct) plotted as a function of potential with the sodiation sweep being represented by the solid line, while the dashed line relates to the desodiation sweep. B) Solid electrolyte interphase resistance (Rsei) plotted as a function of potential with the sodiation sweep being represented by the solid line, while the dashed line relates to the desodiation sweep. C) Schematic representation of the modified Randles circuit used to fit the EIS data. D) Table representing the Rct and Rsei values for the cPAN@Sb and Sb systems at 0.1V vs. Na/Na+ at the 10th cycle.

these results demonstrate the effect of cPAN on the early cycle (de)sodiation chemistry of Sb, they do not provide insight into how cPAN affects the resistive nature of the Sb active material as a function of potential. Although these results clearly show that cPAN influences the cycling performance and early cycle chemistry of Sb, they do not examine how the cPAN is affecting these changes. To address how cPAN is affecting the Sb electrode, it is imperative to consider how cPAN affects the resistive properties of the ensemble electrode during cycling.

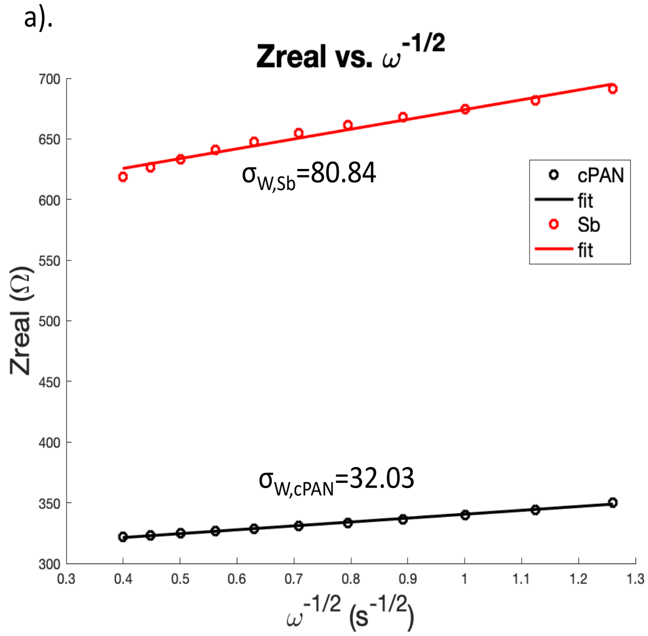

b).

$$Z_{re}=R_{sol}+R_{ct}+\sigma_w\omega^{-1/2}$$

c).

$$D_{Na}=\frac{R^2T^2}{2A^2n^4F^4C^2\sigma_w^2}$$

d).

Electrode system	**D_{Na} (cm^2 s^{-1})**
cPAN@Sb	2.29×10^{-16}
Sb	7.72×10^{-17}

Figure 3.5: Na-ion diffusion coefficient calculations. A) Real impedance plotted as a function of the inverse of the square root of angular frequency for the low frequency region (0.1 to 1.0 Hz), where the slope is the Warburg coefficient (σ_W). B) Equation relating the real impedance (Z_{re}) to the Warburg coefficient. C) Equation used for calculating the D_{Na} of the cPAN@Sb and Sb electrodes. D) Table displays the D_{Na} for the cPAN@Sb and Sb electrodes at the 10th cycle and at 0.1V vs. Na/Na$^+$.

Analysis of the resistive properties, as a function of potential, demonstrate that while cPAN reduces the R_{ct} of the electrode system, the R_{SEI} of the cPAN and Sb systems were very similar. These parameters were determined through the application of Constant-Current Constant-Voltage (CCCV), **Figures A.II.XIIa** and **A.II.XIIa**b polarization for EIS analysis at the potentials where the major (de)sodiation appeared over the potential window. **Figure A.II.XIIc** and **A.II.XIId** display the dQ/dV plots of a 10-cycle formation period for the cPAN@Sb and Sb systems, respectively. The arrows indicate the potentials at which EIS spectra where taken. **Figure**

A.II.XIII displays the EIS spectra of the sodiation sweep for the cPAN system at the indicated potentials of interest. The EIS spectra collected at the desired potentials were fit to a modified Randles equivalent circuit model with the inclusion of an SEI component, as seen in **Figure 3.4c**. In this model, the Rsei||Csei components model the impedance behavior related to the movement of ions through the SEI. Specifically, the Rsei models the resistance related to the movement of ions in the SEI, and the Csei models reactance related to the capacitive (charge accumulation) effects of the SEI. This model has been used in the literature to evaluate the impedance response of Sb electrodes in a NIB half-cell.[20,35] **Figures 3.4a** and **3.4b** display the Rct and Rsei plotted as a function of potential for the cPAN@Sb and Sb systems, respectively. The Rct and Rsei values for the EIS spectra taken at 0.1 V vs. Na/Na^+ for the 10th cycle sodiation sweep are displayed in **Figure 3.4d**. In **Figure 3.4a**, it is clear to see that the cPAN has a smaller Rct over the potential window compared to the Sb system. Interestingly, the Rsei for both systems are very similar. These results imply that while the cPAN aids in lowering the resistance of the charge transfer process during Na-ion insertion into the Sb electrode, it does not measurably affect the impedance properties of the as formed SEI layer. The lack of differences in the Rsei for these two systems leads to the notion that the cPAN layer does affect the composition of the SEI formed while the battery is cycling, despite the potential differences of the main sodiation events at early cycles. Another important factor to consider is how the cPAN protective layer affects the Na-ion diffusion coefficient for the ensemble electrode.

The calculated Na-ion diffusion coefficients (D_{Na}) for the cPAN@Sb and Sb systems were $2.29x10^{-16}$ cm^2/s and $7.73x10^{-17}$ cm^2/s, respectively (**Figure 3.5d**). This work calculated the D_{Na} at 100mV vs. Na/Na^+ after the 10th cycle to assess how the cPAN layer affected the Na-ion diffusion in the ensemble electrode. These parameters were used for the D_{Na} calculations given the clear dependence on the calculated diffusion coefficients based on the cycle number and state of charge of the electrode under examination.[44,45] **Figure 3.5a** displays the real impedance plotted as a function of the inverse of the square root of the angular frequency over the low frequency region of the EIS spectra (0.1 to 1.0 Hz). **Figures 3.5b** and **3.5c** display the relationship between the real impedance and the angular frequency of the measurements, and the equation used to calculate D_{Na}, respectively. These results demonstrate that the cPAN layer improves the Na-ion diffusion for the ensemble electrode it is applied to.

Thus far the cPAN protective layer has been shown to increase the achievable capacity of the ensemble electrode, resulting from the charge storage properties of the cPAN, and has acted to reduce the R_{ct} of the electrode (due to the conductive properties of the polymer layer) while enhancing the ensemble electrode's D_{Na}. The cPAN layer has, also, been shown to affect the early cycle (de)sodiation chemistry of Sb and improve the rate capability of the electrode, both of which could result from differences in the surface chemistry imparted by the cPAN. Interestingly, the R_{SEI} values (Figure 4b) for the cPAN@Sb system was strikingly similar to the R_{SEI} of the Sb control, which implies that the surface chemistries of these systems are similar. To disprove the hypotheses that the differences in the early cycle (de)sodiation chemistry and enhanced rate capability of the cPAN system result from cPAN's effect on the surface chemistry of the Sb electrode, and to assess the R_{SEI} values seen in **Figure 3.4b**, characterization of the surface chemistry was conducted via X-ray photoelectron spectroscopy (XPS).

3.3.3 Characterization of Surface Chemistry

The surface chemistry of the cPAN@Sb and Sb systems after the 1st discharge and 10th cycle are not significantly different (particularly in the carbon environments) to account for the differences in the electrochemical and resistive phenomena between the cPAN@Sb and Sb systems. X-ray photoelectron spectroscopy (XPS) was conducted on the cPAN@Sb and Sb systems for pristine electrodes, electrodes after the 1st discharge cycle, and electrode after the 10th cycle to evaluate the effect of cPAN on the surface chemistry of the Sb active material. **Figure 3.6** displays the high-resolution XPS spectra of the C1s environments for the cPAN@Sb and Sb systems for pristine, after 1st discharge, and after the 10th cycle electrode conditions.

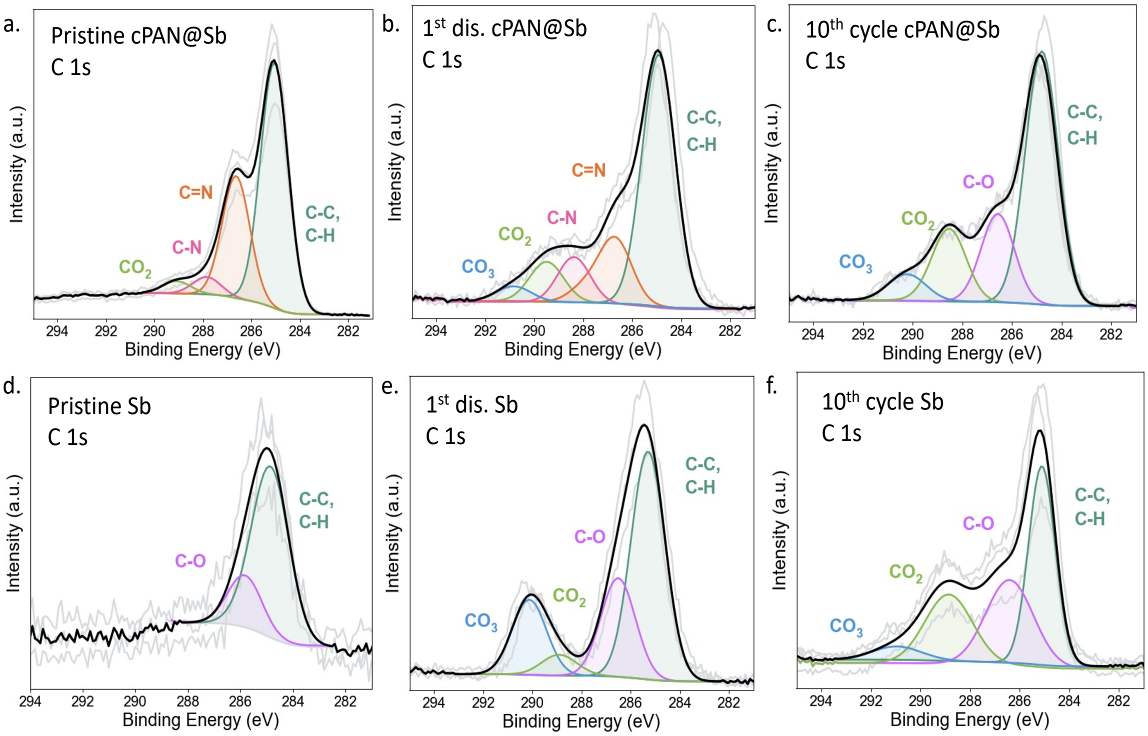

Figure 3.6: Electrode surface chemistry characterization with X-ray photoelectron spectroscopy (XPS). A) The C1s spectrum for the pristine cPAN@Sb electrode demonstrates CO_2, C-N, C=N, C-C, and C-H environments. B) The C1s spectrum for a cPAN@Sb electrode after the 1st discharge half-cycle which displays CO_3, CO_2, C-N, C=N, C-C, and C-H environments. C) The C1s spectrum for a cPAN@Sb electrode after the 10th cycle which displays CO_3, CO_2, C-O, C-C, and C-H environments. D) The C1s spectrum for the pristine Sb electrode demonstrates C-O, and C environments. E) The C1s spectrum for an Sb electrode after the 1st discharge half-cycle which displays CO_3, C-C, and C-H environments. F) The C1s spectrum for an Sb electrode after the 10th cycle which displays CO_3, CO_2, C-O, C-C, and C-H environments.

The C1s spectrum for the pristine cPAN (**Figure 3.6a**) system shows peaks at 285 eV, 286.58 eV, 287.77 eV, and 289.01 eV which relate to C-C, C-N, C=N, and CO_2 environments, respectively. The C-C environments for the pristine system relate to the C-C bonds in the polymer backbone of the cPAN coating, with the C=N species resulting from the C=N bonds of the pyridine structure in cPAN.[12,28] The presence of C-N environments in the pristine cPAN sample could be indicative of a graphitic species in addition pyridine structures, although these moieties are present at low levels.[46] The presence of both the C=N and C-N environments in the C1s spectra are corroborated by the presence of corresponding C=N and C-N environments in the N1s spectra, **Figure A.II.XIV**. Exposure of the pristine cPAN@Sb sample to the air during sample transfer to the XPS instrument likely accounts for presence of environments related to CO_2 structures, which has been seen for pristine cPAN samples annealed under an argon atmosphere in the past.[33] Concerning the C1s spectrum for the pristine Sb (**Figure 3.6d**) system, the main environments present relate to C-C and C-O structures, at roughly 285 eV and 286 eV, respectively. These environments result from adventitious carbon, which is common for all XPS experiments (even on systems that do not contain carbon) and are in good agreement with previous XPS characterization of pristine Sb films.[35,47] Concerning the overlapping O1s and Sb3d environments for the pristine cPAN system the presence of Sb_2O_3, indicated by the peak at 540 eV in **Figure A.II.XVa**, is in good with the post-annealing PXRD analysis from **Figure 3.1b**. These overlapping O1s and Sb3d environments for the pristine cPAN system also contains a peak at roughly 532 eV, which relates to presence of C-O constituents on the surface which is consistent with what is seen in **Figure 3.6a**. Regarding the pristine Sb system, the overlapping O1s and Sb3d environments clearly indicate the presence of Sb_2O_3 via peaks at 540 eV (Sb_2O_3 3/2) and 531 eV (Sb_2O_3 5/2), **Figure A.II.XVd**, which is in good agreement with the results summarized in **Figure 3.1b**.

The C1s spectrum for the cPAN system after the 1st discharge step (**Figure 3.6b**) shows an increase in the presence of C-O bonding environments (CO_3 at 291 eV and CO_2 at 289.5 eV), which is expected due to the electrolyte reduction to form the initial SEI during the 1st discharge half-cycle.[48] These environments are corroborated by a peak at 531 eV in the overlapping O1s and Sb3d environments, as seen in **Figure A.II.XVb**, related to C-O environments. The presence of binding environments at 534 eV in **Figure A.II.XVb** relate to either a CO_2 or ClO_4 species, both of which are expected in the SEI after the first discharge half cycle.[48] Regarding the C-N environments, the C1s spectrum demonstrates a decrease in the presence of the C-N and C=N environments. In the N1s spectrum the C-N and C=N environments are still present which indicates that although the organic component of the SEI increases after the 1st discharge cycle the SEI is not so thick that the nitrogen environments from the cPAN layer are undetectable. Future work will test this hypothesis via XPS sputtering experiments aimed at characterizing the thickness of the SEI layer in relation to the cPAN coating. Concerning the Sb system after the 1st discharge cycle (**Figure 3.6e**) the C1s spectrum displays a sharp increase CO_3 compounds in the SEI, in addition to an increase in the presence of C-O signatures, which are corroborated via the XPS spectrum for the overlapping O1s and Sb3d environments (**Figure A.II.XVe**) in the form of C=O and C-O signatures. The overlapping O1s and Sb3d environments also show the opresence of either CO_2 and/or ClO_4. These increases in the CO_3 and C-O environments, and the presence of CO_2 and/or ClO_4, are common for the initial SEI formation, which occurs during the 1st discharge cycle in these systems.[22,48] Upon comparison of the 1st discharge C1s spectra for the cPAN and Sb, it is clear to see that the Sb system has a surface layer with a higher extent of C-O bond containing compounds. The compositional differences in the 1st discharge SEI (**Figure 3.6b** and **3.6e**) help to explain the 1st cycle discharge traces in **Figure 3.3c** & **3.3d**, which supports the hypothesis that the cPAN layer is affecting the composition of the initial SEI. These compositional differences could arise for several reasons, including increased surface area of the cPAN compared to the Sb (**Figure A.II.VII**), chemical interactions between the cPAN and the electrolyte, or the higher Rct of the pristine cPAN system compared to Sb. These hypotheses will be the focus of future investigations into the role of cPAN on the early cycle surface chemistry of Sb electrodes.

The C1s spectra for the cPAN and Sb after the 10th cycle are dominated by the same species, namely, CO_3, CO_2, C-O, and C-C environments, **Figure 3.6c** and **3.6f**. Concerning the cPAN system specifically, the C-N and C=N environments disappear with a commensurate increase in the peaks relating to the carbon-oxygen environments, which is easily rationalized by a growth in the SEI layer from the 1st cycle to the 10th cycle.[49] The presence of carbon-oxygen species in the C1s spectra are supported by the spectra for the overlapping O1s and Sb3d environments, **Figure A.II.XVc** and **A.II.XVf**. Regarding **Figure A.II.XVf** peaks at 537 eV and 528 eV relate to Sb3/2 and Sb5/2 environments, respectively. These environments likely arise in the spectrum from the breakdown of the SEI layer, which could occur from the washing procedure or localized fracturing of the SEI (particularly since there are no peaks related to Sb in **Figure A.II.XVe**). The similarities in the C1s spectra between the cPAN and Sb systems (after the 10th cycle) help to support the Rsei values from **Figure 3.4b**, where the SEI resistance values were similar for both the cPAN and Sb systems. These similarities, also, disprove the notion that the improved rate capability for the cPAN system (**Figure 3.3b**) results from differences in the surface chemistry. Thus, the cPAN layer does not significantly change or affect the composition of the as formed organic components of the SEI at later cycle numbers.

Concerning the inorganic components of the SEI, NaF is apparent in both the cPAN and Sb systems after both the 1st discharge and the 10th cycle, as seen by the peaks at roughly 684.9 eV and 1072 eV in the fluorine and sodium spectra, respectively (**Figure A.II.XVI** and **Figure A.II.XVII**). The NaF is well understood to improve the as formed SEI due to the mechanical and conductive properties of this material, and forms from the decomposition of the FEC electrolyte additive.[21,48] Given that NaF is present in the SEI of both systems, after the 1st discharge and after 10 cycles, we can confirm that the enhanced Rct (**Figure 3.4a**) for the cPAN system relates to the conductive properties of the coating, and not from differences in the inorganic component of the as-formed SEIs.

3.4 Conclusions

In this work, we have characterized the multi-functionality of a cPAN coating on Sb-based anode materials in NIBs. The inclusion of a cPAN layer increases the achievable capacity of the electrode system it is applied to and increases the capacity retention as a function of rate. These results arise from the ability of cPAN to actively store Na-ions and its ability to increases the hardness of the material it is applied to, respectively. The cPAN coating, also, helps to facilitate the transfer of Na-ions from the electrolyte to the Sb active material because of the conductive nature of the polymer, which become more conductive as the battery is cycled. This, also, leads to an increase in the D_{Na} of the cPAN coated electrode compared to a bare Sb-based system.

The cPAN coating, interestingly, provided for worse cycle life compared to the Sb control system despite the deep literature understanding of cPAN as a protective coating. This result likely stems from the layered coating-active material configuration used in this investigation for the purposes of studying the fundamental effect of cPAN on Sb electrodes in NIBs. The worse cycle life for the layered cPAN@Sb electrode, in conjunction with the literature on cPAN in batteries, implies that cPAN needs to be applied to nanoscale active materials or used to form a composite electrode to impart cycle life improvements to the active materials.

The cPAN layer most affects the early cycle (de)sodiation chemistry of the Sb electrode it is applied to. This result is somewhat in line with the initial hypothesis that the cPAN layer would affect the (de)sodation chemistry of the Sb electrode. Yet, the (de)sodiation chemistry of the cPAN@Sb and Sb systems are strikingly similar at higher cycle numbers. This trend is mirrored in the XPS analysis of the SEI of the cPAN and Sb systems, where the largest differences in the as formed SEI are present after the 1st discharge half-cycle. By the time the electrodes reach the 10th cycle, the organic and inorganic components of the SEIs for both the cPAN and Sb systems are similar, implying that the properties of cPAN which are imparting the early cycle differences in the (de)sodiation and surface chemistry of Sb are no longer present at higher cycle numbers. Future investigations should focus on quantifying the constituents present in the early cycle SEI of cPAN coated electrodes to assess exactly how the resistive properties of cPAN effect the as formed SEI, providing insight into the relationship between SEI formation and the conductive properties of the electrode in NIBs. This information will provide fundamental insight which will aide in design principles for CPBs as protective coatings for conversion electrodes in NIBs.

3.5 Materials and Methods

3.5.1 Electrodeposition solution preparation.

A nickel-deposition solution was formed by adding 1.066 M $NiSO_4$ $6H_2O$ (140 g, Millipore Sigma, ≥ 98%), 45 g/L $NiCl_2$ $6H_2O$ (22.5 g, Alfa Aesar, 99.%), 0.189 M citric acid (8.5 g, Millipore Sigma, ≥99.5%), 0.0109 M sodium saccharin (1.0 g, Fischer), and 0.0023 M 2-butyne-1,4-diol (0.1 g, Millipore Sigma, 99%) to 500mL millipore water (18Ω) . This solution was then stirred for 30min before being titrated to pH 4.5. An antimony deposition was formed by mixing 30 mM (1-hexadecyl)trimethylammonium bromide (CTAB, 2.18 g, Alfa Aesar, 98%), and sodium gluconate (8.64 g, Milipore Sigma, ≥99%) to 200 mL milipore water before being left to stir. After stirring for 5-10 minutes, 30 mM antimony chloride (1.37 g, Milipore Sigma, ≥99%) was added to the solution. The solution was left to stir on a stir plate overnight.

3.5.2 Electrodeposition of Sb@Ni@tCu.

A textured copper (tCu) foil substrate was utilized in this investigation and was prepared for deposition via a washing treatment of concentrated phosphoric acid, then water, and finally absolute ethanol for 30s each. The nickel deposition solution was heated to 60℃ using a VWR water heater/cooler. The nickel solution was then placed in a custom deposition cell (described in the work of Nieto et al.[16]) using the cleaned tCu as the working electrode (Oak-Mitsui, TBL-DS Cu foil), a stainless-steel mesh counter electrode (316 stainless steel, Elmhurst, P.O.# AC-75973470), and a saturated calomel (SCE) reference electrode. The deposition of nickel onto the textured copper working electrode occurred at -1.0 V vs. SCE for 60s, forming Ni@tCu. The remaining nickel solution was removed from the deposition cell and the substrate was immediately rinsed thoroughly with milipore water before the addition of the antimony deposition solution, which was then let to rest for 10min in order to allow to maximum wetting of all surfaces. The antimony deposition onto the Ni@tCu was conducted at -1.05 V vs. SCE under chronocoulmbic conditions until a charge limit of 3 C/cm2 was reached, forming Sb@Ni@tCu. The electrodeposited Sb@Ni@tCu was then washed with water and ethanol prior to storage in a vacuum desiccator. The mass of the deposited Sb was calculated from the electrochemical data using **Equation 3.1**.

3.5.3 PAN solution synthesis.

1 M polyacrylonitrile (PAN) in N,N-dimethyl-formamide (DMF) solution, based on moles on monomer units, was prepared by adding PAN powder (10.6 g, Sigma, 181315, average M/W 150,000) to DMF (200 mL, Fischer Scientific). The solution was stirred at approximately 80 °C until dissolution was established, about 3 hours. The solution was allowed to cool before being

used in the spin-coater set-up. For the sodium bromide PAN solution, 0.5 M sodium bromide (0.5145 g, Millipore Sigma, ≥99%) was added to a 1 M PAN in DMF solution, as described above.

3.5.4 PAN coating parameters.

1/2” diameter substrates were coated with the 1 M PAN solution with an MTI VTC-100 vacuum spin coater (MTI, CR2025 spacer, SS304, Φ 15.5 mm by T 0.2 mm). Spin coating parameters were 2000 rpm for 30 s followed by 8000 rpm for 10 s. The PAN solutions were applied to the spinning substrates with a syringe pump (Kent Scientific Corp, Genie Touch Syringe Pump). The PAN solutions were applied to the substrate at a rate of 0.5 mL/min for the entirety of the 2000-rpm step. For the 8000-rpm step, the syringe pump was stopped so that excess PAN did not build up on the substrate.

3.5.5 Substrate annealing parameters.

All electrodes were annealed in a Lindberg tube furnace (model 55322-3, 2” OD alumina tube) under flowing argon. The electrodes were placed in an alumina boat, which was positioned in the center of the tube. The tube was sealed and subsequently purged three times before argon was flown over the sample at 60-80 mL/min. Samples were allowed to sit under ambient temperature for 30 min after the purge cycles. The temperature of the furnace was ramped to the desired annealing temperature at a rate of 50 °C/min, after which the annealing time was started. After the specified annealing time had elapsed, the samples were allowed to cool to 100 °C before the tube furnace was opened.

3.5.6 Battery assembly and cycling conditions.

Coated and uncoated substrates were assembled into Na-ion half-cells in an argon filled glovebox (O_2 ppm <1ppm, H_2O ppm < 0.5 ppm). For the Na-ion half-cells, 1M sodium perchlorate ($NaClO_4$) in propylene carbonate (PC) with 5% by volume fluoroethylene carbonate (FEC). 2032 coin-cells (MTI) were utilized for cycle life and rate capability testing and were fabricated with a Na-foil counter/reference, a glass filter-paper separator (21 mm ⌀, GE Whatman), and the substrate in question with 80 μL of electrolyte before being sealed with a coin-cell press at 0.9 tons (MTI, MSK-160E). For the XPS and EIS experiments, Swagelok half-cells were used where a Na-metal counter/reference, 200 μL of electrolytes, glass filter-paper separator (21 mm ⌀, GE Whatman), and polypropylene separators (MTI, Li-ion battery separator film, 25 μm thick, Batch #120313) were used.

3.5.7 Electrochemical testing.

All electrochemical cells were allowed to rest for at least 12 hrs before any testing. The galvanostatic cycle life, rate capability, and formation experiments were conducted on an Arbin battery cycler (Model LBT20084 or Model BT-2143). Potentiostatic electrochemical impedance spectroscopy (EIS) experiments were conducted using a Gamry Reference 3000 potentiostat. EIS experiments were run between 100 kHz-100 mHz with an excitation of 10 mV (RMS) vs. OCV. For the constant-current constant-voltage experiments (CCCV), the chronopotentiometry step was conducted at ±0.00001 A, while the chronoamperomery step was held for 6 hours at the desired potential selected from differential capacity (dQ/dV) analysis. Cyclic voltammetry for surface area characterization was conducted over a potential window from 2.0 to 2.6 V vs. Na/Na^+. The scan rates for this experiment were 50 mV/s, 100 mV/s, 150 mV/s, 200 mV/s, and 250 mV/s. The peak current as a function of scan rate was selected at 2.3 V vs. Na/Na^+.

3.5.8 Materials characterization

PAN-coated samples were analyzed via FT-IR spectroscopy (Bruker HYPERION 3000, Ge-ATR objective, 64 scans, freq. resolution: 2cm^{-1}, $N_{2(l)}$ cooled MCT detector). All electrodeposited substrates were characterized via powder X-ray diffraction (Bruker D8 Discover DaVinci, Cu Kα radiation) in the ARC-MMA laboratory, in addition to the X-ray photoelectron spectrometer (PHI 5800 series Mutli-Technique ECSA system, monochromatic Al Kα). The PXRD patterns were indexed with DRIFFRAC.EVA (Bruker, V5.2) using reference patterns for Cu (PDF 04-009-2090), Ni (PDF 00-004-0850), Sb_2O_3 (PDF 00-043-1071), Cu_2Sb (PDF 04-010-8292), Sb (PDF 04-016-8006), and NiSb (PDF 04-002-5573). Refinements were performed using TOPAS v6 (Bruker AXS). A double-Voight approach to model both size and strain was used to fit the peak profiles. The cif files were added on top of a predetermined instrument parameter with corrections to the surface roughness[31] and specimen displacement. Refinement parameters such as, crystallite lattice parameters, size, strain, atomic occupancy and isotopic displacement factor (beq) were refined individually for each structure in the following sequential order: Sb_2O_3, Cu, NiSb, Sb, Cu_2Sb, and Ni. The background terms (Chebychev polynomial) were also refined which is displayed with a gray line in the refinements. Diffraction data was visualized using Python in the Jupyter Notebook v6.4.12. For the XPS experiments on electrodes after the 1st discharge and 10th cycle, batteries were disassembled in an argon filled glovebox. The disassembled electrodes were then washed with 1mL of dimethylcarbonate (DMC) and were then loaded into an air-free XPS holder described in the work of Schneider et al.[32] Scanning electron microscope (JOEL JSM-6500F) images of pre-cycling electrodes were taken in the ARC-ISS.

3.6 References

(1) Winter, M.; Brodd, R. J. What Are Batteries, Fuel Cells, and Supercapacitors? *Chem. Rev.* **2004**, *104* (10), 4245–4269. https://doi.org/10.1021/cr020730k.

(2) Goodenough, J. B.; Kim, Y. Challenges for Rechargeable Li Batteries. *Chem. Mater.* **2010**, *22* (3), 587–603. https://doi.org/10.1021/cm901452z.

(3) Rapier, R. *Funding For Battery Technology Companies Exploded in 2020*. Forbes.

(4) Rathi, A.; Murray, P.; Dottle, R. *The Hidden Science Making Batteries Better, Cheaper and Everywhere*. Bloomberg Green.

(5) Harper, G.; Sommerville, R.; Kendrick, E.; Driscoll, L.; Slater, P.; Stolkin, R.; Walton, A.; Christensen, P.; Heidrich, O.; Lambert, S.; Abbott, A.; Ryder, K.; Gaines, L.; Anderson, P. Recycling Lithium-Ion Batteries from Electric Vehicles. *Nature* **2019**, *575* (7781), 75–86. https://doi.org/10.1038/s41586-019-1682-5.

(6) Peng, L.; Zhu, Y.; Chen, D.; Ruoff, R. S.; Yu, G. Two-Dimensional Materials for Beyond-Lithium-Ion Batteries. *Adv. Energy Mater.* **2016**, *6* (11). https://doi.org/10.1002/aenm.201600025.

(7) Chirambatte Peter, S.; sarkar, shreya. An Overview on Sb-Based Intermetallics and Alloys for Sodium-Ion Batteries: Trends, Challenges and Future Prospects from Material Synthesis to Battery Performance. *J. Mater. Chem. A* **2021**. https://doi.org/10.1039/D0TA12063D.

(8) Hirsh, H. S.; Li, Y.; Tan, D. H. S.; Zhang, M.; Zhao, E.; Meng, Y. S. Sodium-Ion Batteries Paving the Way for Grid Energy Storage. *Adv. Energy Mater.* **2020**, *10* (32). https://doi.org/10.1002/aenm.202001274.

(9) US Department of the Interior. Mineral Commodity Summaries 2023. *USGS Minieral Commod. Summ.* **2023**.

(10) Dunlap, N. A.; Kim, J.; Guthery, H.; Jiang, C.-S.; Morrissey, I.; Stoldt, C. R.; Oh, K. H.; Al-Jassim, M.; Lee, S.-H. Towards the Commercialization of the All-Solid-State Li-Ion Battery: Local Bonding Structure and the Reversibility of Sheet-Style Si-PAN Anodes. *J. Electrochem. Soc.* **2020**, *167* (6), 060522. https://doi.org/10.1149/1945-7111/ab84fc.

(11) Piper, D. M.; Evans, T.; Leung, K.; Watkins, T.; Olson, J.; Kim, S. C.; Han, S. S.; Bhat, V.; Oh, K. H.; Buttry, D. A.; Lee, S. H. Stable Silicon-Ionic Liquid Interface for next-Generation Lithium-Ion Batteries. *Nat. Commun.* **2015**, *6*. https://doi.org/10.1038/ncomms7230.

(12) Piper, D. M.; Yersak, T. A.; Son, S. B.; Kim, S. C.; Kang, C. S.; Oh, K. H.; Ban, C.; Dillon, A. C.; Lee, S. H. Conformal Coatings of Cyclized-PAN for Mechanically Resilient Si

Nano-Composite Anodes. *Adv. Energy Mater.* **2013**, *3* (6), 697–702. https://doi.org/10.1002/aenm.201200850.

(13) Mosby, J. M.; Prieto, A. L. Direct Electrodeposition of Cu2Sb for Lithium-Ion Battery Anodes. *J. Am. Chem. Soc.* **2008**, *130* (32), 10656–10661. https://doi.org/10.1021/ja801745n.

(14) Schulze, M. C.; Belson, R. M.; Kraynak, L. A.; Prieto, A. L. Electrodeposition of Sb/CNT Composite Films as Anodes for Li- and Na-Ion Batteries. *Energy Storage Mater.* **2020**, *25*, 572–584. https://doi.org/10.1016/j.ensm.2019.09.025.

(15) Zheng, X. M.; You, J. H.; Fan, J. J.; Tu, G. P.; Rong, W. Q.; Li, W. J.; Wang, Y. X.; Tao, S.; Zhang, P. Y.; Zhang, S. Y.; Shen, S. Y.; Li, J. T.; Huang, L.; Sun, S. G. Electrodeposited Binder-Free Sb/NiSb Anode of Sodium-Ion Batteries with Excellent Cycle Stability and Rate Capability and New Insights into Its Reaction Mechanism by Operando XRD Analysis. *Nano Energy* **2020**, *77*. https://doi.org/10.1016/j.nanoen.2020.105123.

(16) Nieto, K.; Gimble, N.; Rudolph, L.; Prieto, A. Electrodeposition vs Slurry Casting: How Binders & Additives Affect the Electrochemical Performance of Sb-Based Electrodes. *J. Electrochem. Soc.* **2022**.

(17) He, J.; Wei, Y.; Zhai, T.; Li, H. Antimony-Based Materials as Promising Anodes for Rechargeable Lithium-Ion and Sodium-Ion Batteries. *Mater. Chem. Front.* **2018**, *2* (3), 437–455. https://doi.org/10.1039/c7qm00480j.

(18) Caputo, R. An Insight into Sodiation of Antimony from First-Principles Crystal Structure Prediction. *J. Electron. Mater.* **2016**, *45* (2), 999–1010. https://doi.org/10.1007/s11664-015-4260-0.

(19) Ma, W.; Wang, J.; Gao, H.; Niu, J.; Luo, F.; Peng, Z.; Zhang, Z. A Mesoporous Antimony-Based Nanocomposite for Advanced Sodium Ion Batteries. *Energy Storage Mater.* **2018**, *13*, 247–256. https://doi.org/10.1016/j.ensm.2018.01.016.

(20) Dashairya, L.; Das, D.; Saha, P. Binder-Free Electrophoretic Deposition of Sb/rGO on Cu Foil for Superior Electrochemical Performance in Li-Ion and Na-Ion Batteries. *Electrochimica Acta* **2020**, *358*, 136948. https://doi.org/10.1016/j.electacta.2020.136948.

(21) Jung, R.; Metzger, M.; Haering, D.; Solchenbach, S.; Marino, C.; Tsiouvaras, N.; Stinner, C.; Gasteiger, H. A. Consumption of Fluoroethylene Carbonate (FEC) on Si-C Composite Electrodes for Li-Ion Batteries. *J. Electrochem. Soc.* **2016**, *163* (8), A1705–A1716. https://doi.org/10.1149/2.0951608jes.

(22) Bodenes, L.; Darwiche, A.; Monconduit, L.; Martinez, H. The Solid Electrolyte Interphase a Key Parameter of the High Performance of Sb in Sodium-Ion Batteries: Comparative X-Ray Photoelectron Spectroscopy Study of Sb/Na-Ion and Sb/Li-Ion Batteries. *J. Power Sources* **2015**, *273*, 14–24. https://doi.org/10.1016/j.jpowsour.2014.09.037.

(23) Li, J.; Cai, Y.; Wu, H.; Yu, Z.; Yan, X.; Zhang, Q.; Gao, T. Z.; Liu, K.; Jia, X.; Bao, Z. Polymers in Lithium-Ion and Lithium Metal Batteries. *Adv. Energy Mater.* **2021**. https://doi.org/10.1002/aenm.202003239.

(24) Dunlap, N. A.; Kim, J.; Oh, K. H.; Lee, S.-H. Slurry-Coated Sheet-Style Sn-PAN Anodes for All-Solid-State Li-Ion Batteries. *J. Electrochem. Soc.* **2019**, *166* (6), A915–A922. https://doi.org/10.1149/2.0151906jes.

(25) Datta, M. K.; Kumta, P. N. Silicon and Carbon Based Composite Anodes for Lithium Ion Batteries. *J. Power Sources* **2006**, *158* (1), 557–563. https://doi.org/10.1016/j.jpowsour.2005.09.016.

(26) Leroy', S.; Boiziau, C.; Perreau-, J.; Reyxaud, C.; Zalczer, G.; Lkayow', G.; Gressus, C. I. Molecular Structure of Electropolymerized Polyacrylonitrile Film and Its Pyrolyzed Derivatives. *J. Mol. Struct.* **1985**, *128*, 269–281.

(27) Xue, T. J.; Mckinney, M. A.; Wilkie, C. A. The Thermal Degradation of Polyacrylonitrile. *Polym. Degredation Stab.* **1997**, *58*, 193–202.

(28) Zhang, W.; Sun, M.; Yin, J.; Abou-Hamad, E.; Schwingenschlögl, U.; Costa, P. M. F. J.; Alshareef, H. N. A Cyclized Polyacrylonitrile Anode for Alkali Metal Ion Batteries. *Angew. Chem. - Int. Ed.* **2021**, *60* (3), 1355–1363. https://doi.org/10.1002/anie.202011484.

(29) Liu, Q.; Xiao, Z.; Cui, X.; Deng, S.; He, Q.; Zhang, Q.; Lin, Z.; Yang, Y. Conjugated Cyclized-Polyacrylonitrile Encapsulated Carbon Nanotubes as Core-Sheath Heterostructured Anodes with Favorable Lithium Storage. *J. Mater. Chem. A* **2021**, *9* (11), 6962–6970. https://doi.org/10.1039/d0ta12243b.

(30) Gimble, N.; Nieto, K.; Prieto, A. Electrodeposition as a Powerful Tool for the Fabrication and Characterization of Next-Generation Anodes for Sodium Ion Rechargeable Batteries. *Electrochem. Soc. Interface* **2021**, *30* (50), 59–63.

(31) Pitschke, W.; Hermann, H.; Mattern, N. The Influence of Surface Roughness on Diffracted X-Ray Intensities in Bragg–Brentano Geometry and Its Effect on the Structure Determination by Means of Rietveld Analysis. *Powder Diffr.* **1993**, *8* (2), 74–83. https://doi.org/10.1017/S0885715600017875.

(32) Schneider, J. D.; Agocs, D. B.; Prieto, A. L. Design of a Sample Transfer Holder to Enable Air-Free X-Ray Photoelectron Spectroscopy. *Chem. Mater.* **2020**, *32* (19), 8091–8096. https://doi.org/10.1021/acs.chemmater.0c01895.

(33) Schulze, M. C.; Prieto, A. L. Mixed-Conducting Properties of Annealed Polyacrylonitrile Activated by n-Doping of Conjugated Domains. *Chem. Sci.* **2022**, *13* (1), 225–235. https://doi.org/10.1039/d1sc02350k.

(34) Arbab, S.; Mirbaha, H.; Zeinolebadi, A.; Nourpanah, P. Indicators for Evaluation of Progress in Thermal Stabilization Reactions of Polyacrylonitrile Fibers. *J. Appl. Polym. Sci.* **2014**, *131* (11). https://doi.org/10.1002/app.40343.

(35) Nieto, K.; Windsor, D. S.; Kale, A. R.; Gallawa, J. R.; Medina, D. A.; Prieto, A. L. Structural Control of Electrodeposited Sb Anodes through Solution Additives and Their Influence on Electrochemical Performance in Na-Ion Batteries. *J. Phys. Chem. C* **2023**, *127* (26), 12415–12427. https://doi.org/10.1021/acs.jpcc.3c01086.

(36) Schulze, M. C.; Schulze, R. K.; Prieto, A. L. Electrodeposited Thin-Film Cu:XSb Anodes for Li-Ion Batteries: Enhancement of Cycle Life via Tuning of Film Composition and Engineering of the Film-Substrate Interface. *J. Mater. Chem. A* **2018**, *6* (26), 12708–12717. https://doi.org/10.1039/c8ta01798k.

(37) Asryan, N. A.; Alikhanyan, A. S.; Nipan, G. D. P–T–x Phase Diagram of the Sb–O System. *Inorg. Mater.* **2004**, *40* (6), 626–631. https://doi.org/10.1023/B:INMA.0000031997.59271.0f.

(38) Gierlotka, W.; Jendrzejczyk-Handzlik, D. Thermodynamic Description of the Cu–Sb Binary System. *J. Alloys Compd.* **2009**, *484* (1–2), 172–176. https://doi.org/10.1016/j.jallcom.2009.05.056.

(39) Bryngelsson, H.; Eskhult, J.; Nyholm, L.; Edström, K. Thin Films of Cu2Sb and Cu9Sb2 as Anode Materials in Li-Ion Batteries. *Electrochimica Acta* **2008**, *53* (24), 7226–7234. https://doi.org/10.1016/j.electacta.2008.05.005.

(40) Firdu, F. T.; Taskinen, P. Thermodynamics and Phase Equilibria in the (Ni, Cu, Zn)-(As, Sb, Bi)-S Systems at Elevated Temperatures (300 – 900oC).

(41) Moon, J.; Jung, J. Y.; Hoang, T. D.; Rhee, D. Y.; Lee, H. B.; Park, M.-S.; Yu, J.-S. The Correlation between Particle Hardness and Cycle Performance of Layered Cathode Materials for Lithium-Ion Batteries. *J. Power Sources* **2021**, *486*, 229359. https://doi.org/10.1016/j.jpowsour.2020.229359.

(42) Lalau, C. C.; Low, C. T. J. Electrophoretic Deposition for Lithium-Ion Battery Electrode Manufacture. *Batter. Supercaps* **2019**, *2* (6), 551–559. https://doi.org/10.1002/batt.201900017.

(43) Gimble, N. J.; Prieto, A. L. Spontaneous Solid Electrolyte Interface Formation in Uncycled Sodium Half-Cell Batteries: Using X-Ray Photoelectron Spectroscopy to Explore the Pre-Passivation of Sodium Metal by Fluoroethylene Carbonate before Potentials Are Applied. *Sustain. Energy Fuels* **2022**, *6* (20), 4736–4740. https://doi.org/10.1039/D2SE00888B.

(44) Wang, L.; Zhao, J.; He, X.; Gao, J.; Li, J.; Wan, C.; Jiang, C. Electrochemical Impedance Spectroscopy (EIS) Study of LiNi1/3Co1/3Mn1/3O2 for Li-Ion Batteries. *Int. J. Electrochem. Sci.* **2012**, *7* (1), 345–353. https://doi.org/10.1016/S1452-3981(23)13343-8.

(45) Meddings, N.; Heinrich, M.; Overney, F.; Lee, J.-S.; Ruiz, V.; Napolitano, E.; Seitz, S.; Hinds, G.; Raccichini, R.; Gaberšček, M.; Park, J. Application of Electrochemical Impedance Spectroscopy to Commercial Li-Ion Cells: A Review. *J. Power Sources* **2020**, *480*, 228742. https://doi.org/10.1016/j.jpowsour.2020.228742.

(46) Son, S.-B.; Gao, T.; Harvey, S. P.; Steirer, K. X.; Stokes, A.; Norman, A.; Wang, C.; Cresce, A.; Xu, K.; Ban, C. An Artificial Interphase Enables Reversible Magnesium Chemistry in Carbonate Electrolytes. *Nat. Chem.* **2018**, *10* (5), 532–539. https://doi.org/10.1038/s41557-018-0019-6.

(47) Gengenbach, T. R.; Major, G. H.; Linford, M. R.; Easton, C. D. Practical Guides for X-Ray Photoelectron Spectroscopy (XPS): Interpreting the Carbon 1s Spectrum. *J. Vac. Sci. Technol. Vac. Surf. Films* **2021**, *39* (1), 013204. https://doi.org/10.1116/6.0000682.

(48) Gimble, N. J.; Kraynak, L. A.; Schneider, J. D.; Schulze, M. C.; Prieto, A. L. X-Ray Photoelectron Spectroscopy as a Probe for Understanding the Potential-Dependent Impact of Fluoroethylene Carbonate on the Solid Electrolyte Interface Formation in Na/Cu2Sb Batteries. *J. Power Sources* **2021**, *489*. https://doi.org/10.1016/j.jpowsour.2020.229171.

(49) Darwiche, A.; Bodenes, L.; Madec, L.; Monconduit, L.; Martinez, H. Impact of the Salts and Solvents on the SEI Formation in Sb/Na Batteries: An XPS Analysis. *Electrochimica Acta* **2016**, *207*, 284–292. https://doi.org/10.1016/j.electacta.2016.03.089.

CHAPTER 4: Practical and Beginners Guide to Electrochemical Impedance Spectroscopy (EIS) for Rechargeable Batteries[4]

4.1 Overview

Rechargeable or secondary batteries have become a crucial part of our daily lives from consumer electronics to electric vehicles.[1] The most common rechargeable battery is the lithium-ion battery (LIB), which was awarded the Nobel prize in chemistry in 2019.[2] While LIBs are commonly employed for a number of energy storage applications, the chemical processes occurring within a battery are complex and convoluted. These processes happen at varying timescales while occurring simultaneously leading to challenges in evaluating individual processes. Electrochemical Impedance Spectroscopy (EIS) is an effective tool for probing multiple chemical processes happening simultaneously with a single experiment. EIS allows for this by describing the behavior of a chemical process in a battery by its resistive features (e.g. resistance associated with mass transport through and electrolyte solution).[3,4] A challenge associated with applications of EIS arise from the simplicity of data collection and the complexity of analyzing the collected data, quantitatively. This knowledge gap is not readily filled by the available resources for newcomers to learn about EIS.[5] Some resources are designed as introductory and are too surface level, using ideal systems while not providing insight to complex, practical systems. Other works are designed for EIS specialists and can be difficult to approach for a novice. The present work aims to build a bridge between the simplicity of data collection and challenges in proper data analysis for the EIS of rechargeable batteries. Here, we will discuss the relationship

---

[4] A version of this text is in preparation for publication in *ACS Journal of Chemical Education* with Daniel S. Windsor, Monika J. Perez, Yisrael L. Lamb, and Amy L. Prieto. Daniel S. Windsor and Monika J. Perez developed the initial scope of the project, conducted literature research, and led the writing of the manuscript. Yisrael L. Lamb, assistant professor of Chemistry at Fort Lewis College, was responsible for manuscript editing. Amy L. Prieto assisted with conceptualization of the project, project administration, and editing of the manuscript.

between the electrochemistry and impedance of a battery, as well as provide tools to for data analysis.

4.2 Breaking down the acronym of EIS

4.2.1 the E in EIS

Rechargeable batteries, like LIBs, are classified as electrochemical energy storage devices, storing electrical energy (electro-) through the insertion and removal of charge carriers (Li^+) within solid-state electrode materials (-chemistry). These charge carriers or “active ions” are driven toward an electrode when it is polarized with the opposite charge. For an active ion to reach the electrode material it must travel through an electrolyte solution, represented in the blue region of **Figure 4.1a**. Typically, electrolytes for batteries are solutions of active ion inorganic salts (e.g. $LiPF_6$) in an organic liquid solvent (e.g. ethylene carbonate). These electrolyte solutions are highly ionically conductive and as a result the movement of an active ion through this media occurs quickly. Once an active ion travels through the electrolyte, the active ions travel through the electrolyte-electrode interface, represented as the green region in **Figure 4.1a**. The chemical behavior of interfacial regions are defined by the redox reaction (charge transfer, Faradaic) between the active ion and the electrode material, and passivation layers that allow for the accumulation of charge at the interface (no charge transfer, non-Faradaic). After traveling through the interfacial region, the active ion can be stored within the solid-state electrode material, represented as the orange region in **Figure 4.1a**. The storage of ions in solid-state electrode necessitates the insertion of ions at all available sites, which results in the mass transport of ions throughout the entire electrode.

Since batteries like LIBs are rechargeable, all these chemical processes must occur under both oxidative and reductive conditions for a battery to operate over many cycles. Furthermore, each of the chemical processes occurs *concurrently* during both charge and discharge steps. The fact that all chemical processes in a battery occur simultaneously as a battery is operating makes analyses of these systems quite challenging. For example, it is difficult to deconvolute the data related to ions moving through an electrolyte vs. an electrode material using standard electrochemical analyses since both processes occur at the same time during battery operation (even though they occur over different timescales). Investigators can leverage the "electro" aspect of electrochemistry to aid in deconvoluting the data.

Since a battery is an electro-chemical system, electrical values, like resistance and capacitance, can be ascribed to a chemical process occurring in a battery. The electrical values provide a quantitative descriptor for chemical processes within a system and can easily be measured and tracked during battery operation. For example, examining the electrolyte via its resistance to the active ion movement can provide insight into electrolyte degradation as a battery ages.[4] What follows is a discussion of how several chemical processes in a battery are described by their electrical values.

Figure 4.1 highlights the relationships between chemical processes in a battery (**Figure 4.1a**) and their resistive descriptions (**Figure 4.1b**). The Nyquist plot (**Figure 4.1b**) displays the graphical representation of the electrochemical behavior related to three processes occurring in a battery during charging. Further discussion of Nyquist plots can be found in **Section 4.2.3**. In **Figure 4.1c**, a mathematical model is displayed which is comprised of solid-state circuit elements that can be used to simulate and model the resistive behavior of a battery (vide infra). The resistive behavior trace, represented as a Nyquist plot, and mathematical model in **Figure 4.1c** represent an *ideal* system, where the resistance data behaves exactly as described by the mathematical model. Naturally, few practical battery systems behave ideally, which will be discussed in detail in **Section 4.3.**

As mentioned previously, the storage of an active ion in a rechargeable battery must include the mass transport of the active ion through the electrolyte. The electrolyte will resist the transport of ions due to the physical properties of the solution and due to the presence of a concentration gradient in the electrolyte.[6] This *solution resistance* (R_{sol}) manifests itself as an offset from zero along the horizontal axis in a Nyquist plot (blue region in **Figure 4.1b**), and is represented by a resistor in the mathematical model (blue region in **Figure 4.1c**). The timescale at which this process occurs is considered short for a battery system, which indicates that this process occurs at higher frequencies.

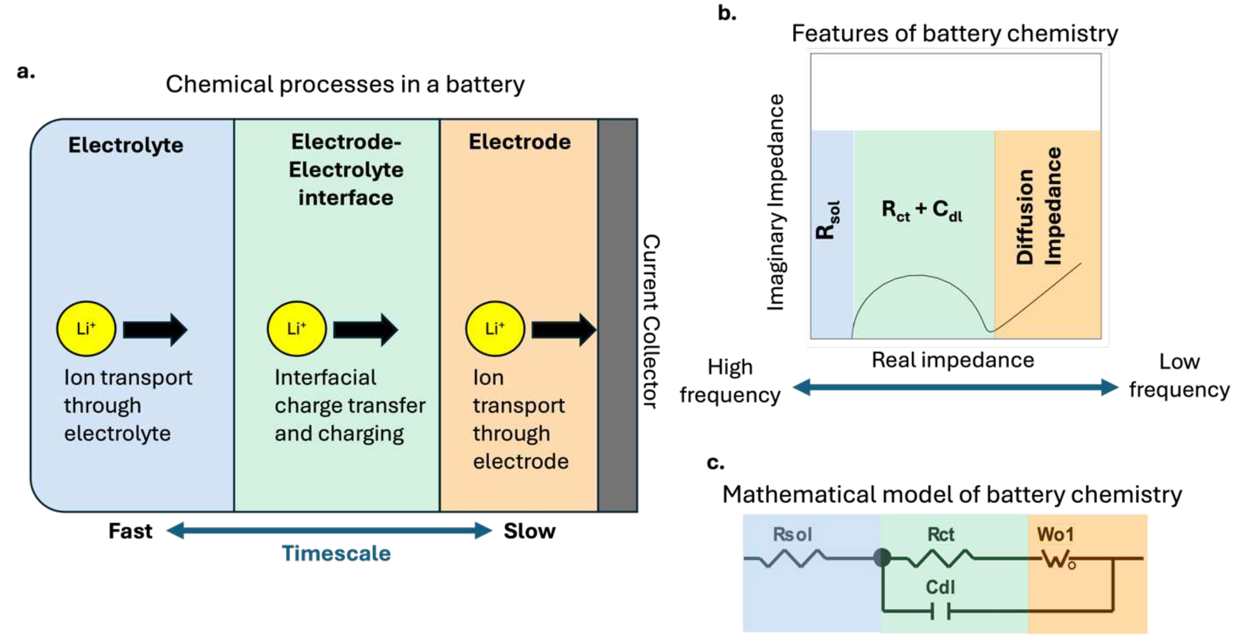

Figure 4.1: Relationship between common active ion insertion processes and their resulting representation in an EIS Nyquist plot. A) Schematic representation of active ion insertion in a rechargeable battery, illustrating mass transport of the active ion through the liquid electrolyte (blue), charge transfer from the active ion to the electrode material at the electrode-electrolyte interface (green), and mass transport of the active ion in the electrode material (orange). B) Resulting Nyquist plot relating the general shapes of an EIS spectrum to a physical process in a battery representing the solution resistance (blue), charge transfer resistance (green), and diffusion impedance (orange). C) Randels Circuit used for mathematical modeling where the blue, green, and orange blocks correspond to the regions of the same color in panels A and B.

Upon arrival at the electrolyte-electrode interface, active ions are then transferred into the electrode material for storage. There are several ways ions can be inserted (see the SI), yet they are all governed by the fundamental chemical reaction governing the insertion mechanism. Ion insertion mechanism are related to the rate constant (k) of the chemical reaction, between the active ion and the electrode material, and has an effect on the chemical behavior of the interfacial region, green region in **Figure 4.1a**.[6] In the Nyquist plot, **Figure 4.1b**, the kinetic information is represented as a semicircle and is classified as the *charge transfer resistance*, or R_{ct}.[3,4] The interfacial region, also, can experience non-Faradaic charge separation (no charge transfer) which is results from charging of the electric-double layer (E_{dl}).[6] In a battery, this is classified as the double-layer capacitance (C_{dl}) and has implications on the resistance of the interfacial region (in conjunction with R_{ct}). To model the interfacial region, a resistor and capacitor are connected in parallel, which produces the semi-circular shape in the ideal Nyquist plot, **Figure 4.1c**.[6] The chemical processes that occur at the electrode-electrolyte interface happen over an intermittent timescale for battery systems, which means that these events occur at intermittent frequencies.

After the active ion has been initially inserted into the material, it must travel deeper into the electrode material to allow for more active ions to be inserted behind it. This process is heavily dependent on physical properties ion diffusion coefficient and ionic conductivity of the solid-state electrode, **Figure 4.1a**.[3] The ion transport through a solid media is characterized by *diffusion impedance* and is represented in a Nyquist plot (**Figure 4.1b**) by a tail feature at low frequencies.[4] Concerning the mathematical representation of the diffusion impedance, a circuit element called a *Warburg element* is used to model this chemical process in an ideal system (**Figure 4.1c**). The diffusion impedance occurs over a slow timescale for a battery, which indicates that this process is present on a Nyquist plot at low frequencies. The shape of the diffusion impedance tail often changes depending on the electrode material and the conditions of the cell, which will be discussed in more detail in **Section 4.3**.

4.2.2 the I in EIS

Since the chemical processes described in a battery occur simultaneously, it can be challenging to isolate the electrochemical chemical behavior of a single process with typical direct current (DC) experiments. To deconvolute chemical processes occurring simultaneously but at various timescales, alternating current (AC) experiments are needed. By using AC experiments, a frequency parameter is introduced allowing for resulting data to be frequency specific. For example, AC measurements at higher frequencies, such as 100,000 Hz or 0.0001 s, provides insight into chemical processes occurring over fast timescales. While AC experiments are useful for assessing time-dependent chemical processes within batteries, implementing sinusoidal components leads to changes in the relationship between potential and current.

The relationship of potential to current in a direct current (DC) system is E=IR shown by Ohm's law. When alternating current (AC) is applied the expression becomes E=IZ, where Z is the impedance of the system and the "I" in EIS. Impedance can be considered the AC analog to DC resistance resulting from the combination of resistance (R) and reactance (X).[7] Both components oppose the flow of current, but reactance is frequency dependent while resistance in frequency independent.[4]

Since EIS is an AC measurement, the potential and current are represented as sine waves. For a practical experiment, an investigator can use either the potential or the current as the perturbation or input signal. For the purposes of this discussion, the perturbation signal will be a sine wave of potential (E in E=IZ) and the response signal will be a current sine wave (I in E=IZ), which is represented in **Figure 4.2**. The potential perturbation and current response in **Figure 4.2** have several distinct features.

(1) Amplitude. In this example, input (voltage) and output (current) signals have an amplitude |E| or |I|, respectively. The output amplitude can vary with impedance at a given frequency.

(2) Period determined by the angular frequency, ω ($\omega = 2\pi f$) where f is the frequency.

(3) Phase Shift, ϕ. Current response to a perturbation experiences a shift along the time axis resulting from the reactive contributions of the system.

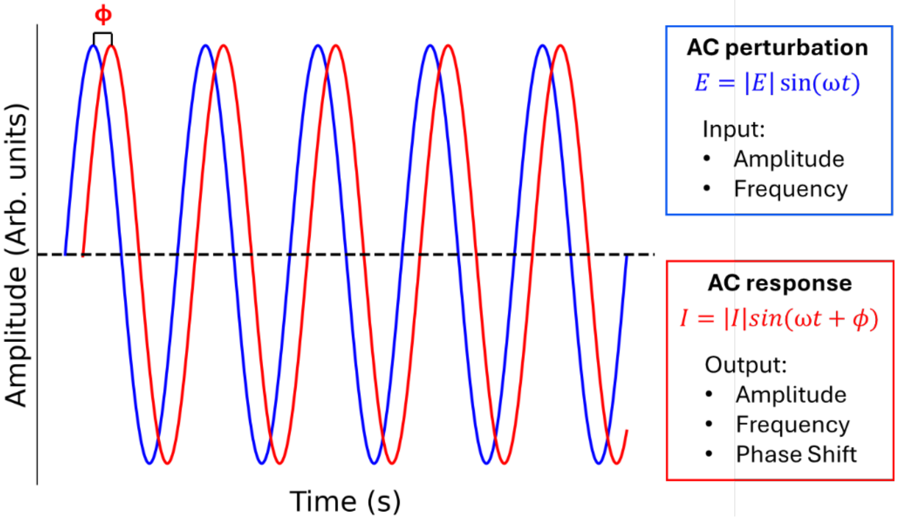

Figure 4.2: Sinusoidal potential perturbation and input parameters (blue) with sinusoidal current response and output parameters (red) at a single frequency. The phase shift, ϕ, is the difference in the peak position between the perturbation and response.

Using Ohm's law, an expression for impedance can be derived from the sinusoidal waveform expressions (**Equation 4.1**). The impedance as described in **Equation 4.1** can, also, be converted to display the impedance in terms of its resistance and reactance using Euler's formula (full derivation available in the Appendix V). Shown in **Equation 4.2**, the relationship between trigonometric functions (sinusoidal waves) and complex numbers introducing the term j, representative of imaginary unit ($-1^{1/2}$). From **Equations 4.1** and **4.2**, Z, is described as the ratio of potential perturbation to the current response which has a magnitude of impedance, |Z|, and phase shift, ϕ (**Equation 4.3**). The magnitude of the impedance, |Z|, provides insight into how the system resists the flow of AC current while the phase shift, ϕ, provides insight into the extent of the reactive contributions to Z_{total}. For example, a system that displays purely resistive behavior (no reactive contributions to the impedance) the phase shift will have a value of 0°. While a system that displays purely reactive behavior (no resistive contributions to the total impedance) will have a phase shift of 90°. Further explanations of the ϕ parameter as they relate to graphical representations of the impedance will be conducted in **Section 4.3.1**.

The |Z| and ϕ parameters are used to express the impedance in polar coordinates which do not express the impedance in terms of the resistive and reactive components. To assess the impedance in terms of resistance and reactance, a Cartesian coordinate system must be in place. **Figure 4.3a** displays the relationship between the Polar (|Z| and ϕ) and Cartesian (Z_{re} and Z_{imag}) expressions of the impedance for a measurement at a single frequency. In this figure, the Polar expression of the impedance result as a vector with a magnitude of |Z| which is offset from the horizontal axis by the ϕ parameter in degrees. To convert the impedance to Cartesian coordinates, **Equations 4.4** and 4.**5** can be used such that the |Z| and ϕ parameters are converted to the real impedance (Z_{re} or Z') and the imaginary impedance (Z_{im} or Z"). The expression in **Equation 4.6** displays how impedance is expressed in terms of its resistive and reactive components, where Z_{re} represents the resistance and Z_{im} represents the reactance. The benefits of assessing the impedance in Polar vs. Cartesian coordinate systems will be explained in **Section 4.2.3**.

Here, the transformation of sinusoidal waveforms into complex impedance values at a single frequency has been discussed. The next section will discuss the importance of measuring the impedance over a range of frequencies.

$$Z = \frac{E}{I} = |Z| \frac{sin(\omega t)}{sin(\omega t + \phi)} \tag{4.1}$$

$$Z = |Z| e^{-j\phi} = |Z| \frac{e^{j\omega t}}{e^{j(\omega t + \phi)}} \tag{4.2}$$

$$E = IZ = I|Z|e^{-j\phi} \tag{4.3}$$

$$|Z| = \sqrt{(Z_{re})^2 + (jZ_{im})^2} \tag{4.4}$$

$$\phi = \tan^{-1} \frac{Z_{re}}{jZ_{im}} \tag{4.5}$$

$$Z = Z' + jZ" \tag{4.6}$$

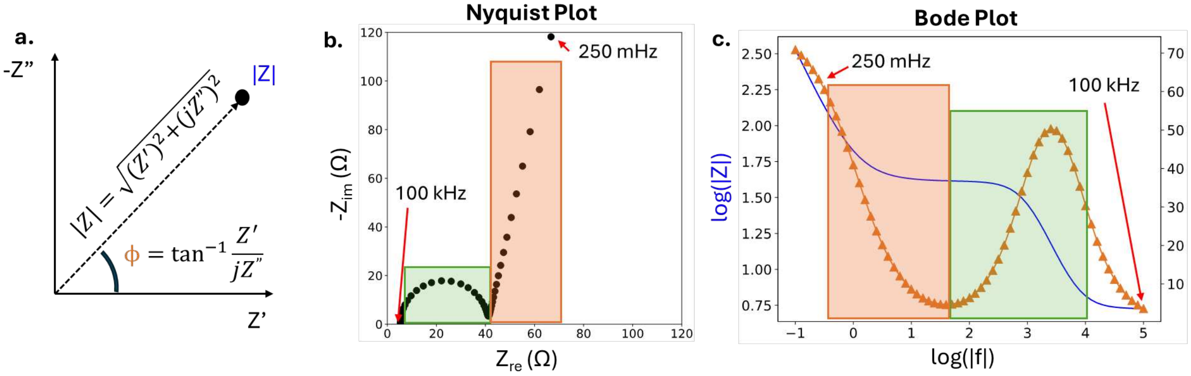

Single frequency

Spectrum of frequencies (Cartesian)

Spectrum of frequencies (Polar)

Figure 4.3: Impedance representations in Cartesian and Polar coordinates. A) An Argand diagram or a geometric plot of complex impedance values at a single frequency as a function of real and imaginary impedances. B) Nyquist plot displaying the real and imaginary impedances over a spectrum of frequencies (100 kHz to 250 mHz). C) The same frequency spectrum represented in a Bode plot. Green and orange regions in the Nyquist and Bode plots are used to highlight the same data displayed through different representations.

4.2.3 the S in EIS

As mentioned above, **Figure 4.3a** displays the relationship between Polar and Cartesian expressions of impedance for a measurement at a single frequency. Recall that chemical processes in a battery, like mass transport in the electrolyte and through the electrode occur at fast and slow timescales respectively. Thus, an EIS measurement at a single frequency will only provide insight into the chemical process occurring at that frequency and not the ensemble behavior of the battery.

To probe multiple chemical processes and the resulting impedance behavior of a battery occurring at various timescales, EIS experiments conducted over a *spectrum* of frequencies is required. A spectrum of EIS measurements plotted in Cartesian coordinates are represented in a Nyquist plot, while for the Polar coordinate system a spectrum of EIS measurements is displayed in a Bode plot.

The complex Cartesian plot, known as a Nyquist plot, represents an impedance spectrum where the impedance is plotted in terms of its Z' and Z" components (**Figure 4.3b**). Since Nyquist plots contain complex numbers, there are plotting conventions that should be followed, further described in **Box 1**. The same spectrum of impedances can be displayed as Bode plots where |Z| and ϕ are plotted as functions of frequency (**Figure 4.3c**). While Nyquist and Bode plots are constructed from the same data, they display different information. Nyquist plots are helpful for visualizing resistance (Z_{Re}) and reactance (Z_{Im}) information but do not plot the data as a function of frequency, while Bode plots help visualize frequency dependent changes of |Z| and ϕ. To highlight the relationship between Nyquist and Bode plots, two regions have been highlighted in **Figure 4.3b** and **4.c**: green is an electrochemical process occurring at intermittent frequencies while orange is a process occurring at low frequencies.

Box 1. Axes must be proportional!

A Nyquist plot is a complex plot where points have a real and imaginary components with a magnitude of impedance. Square the axes so any point can be read as a magnitude, a phase angle and to prevent distortion of features.

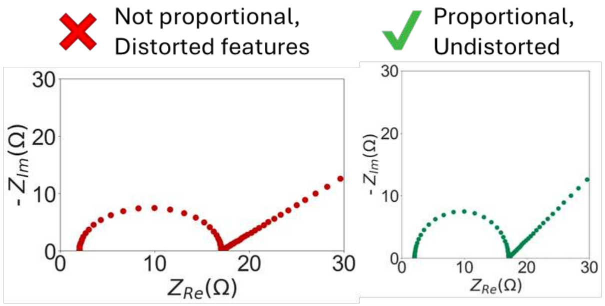

Through Nyquist and Bode plots, battery processes described in **Section 4.2.1** can be visualized and analyzed qualitatively. With respect to the Nyquist plot, the shape of the plot reveals whether the system is kinetically limited, or diffusion limited. If the system is kinetically limited, the depressed semicircle (green region in **Figure 4.3b**) will contain most of the impedance values.

In other words, the process of ion insertion and removal described in **Section 4.2.1** will control the electrochemical performance of the battery. If the system is diffusion controlled, the tail (orange region in **Figure 4.3b**) in the Nyquist plot will contain most of the impedance values indicating the system is dominated by movement of ions through the electrode (mass transport limited).

Activity 1:

At this point, the reader should be armed with the necessary knowledge to complete **Activity 1**, which can be found in Appendix III.

4.3 Steps toward quantitative analysis of EIS spectra

4.3.1 How solid-state circuit components can be used to represent impedance phenomena.

The previous section covered various chemical processes occurring in batteries, the relationship between chemical processes in batteries and their resistive descriptions, and how qualitative information can be obtained based solely on the shapes of Nyquist plots. Quantitative analysis of batteries with EIS is significantly more involved than simple visualizing of graphical shapes. For quantitative analysis of batteries with EIS, a reference model must be formed such that it behaves analogously to the battery being studied. These models are classified as equivalent circuit models (ECMs). These ECMs consist of solid-state circuit elements which approximate the impedance behavior to the electrochemical system in question.[5] The most common solid-state circuit elements used in ECMs are resistors, capacitors, constant phase elements (CPEs), and Warburg elements. To truly model the impedance behavior of a battery using an ECM, the same experimental parameters used for the EIS experiment must be applied to the ECM. From there, ECM circuit elements are used to assign physical values to the electrochemistry occurring in the battery. This section highlights common circuit elements used to form ECMs and what aspect of the total impedance in a battery each component models.

A resistor is a solid-state circuit element that hinders the flow of current[6] and has a frequency independent impedance response described by the equation in **Figure 4.4a**, where the impedance of a resistor is equal to resistance. The frequency independence of a resistor results in a point along the horizontal (Z_{re}) axis of a Nyquist plot. For a Bode plot, the frequency independence of a resistor manifests as a horizontal line for the log(|Z|) axis with a ϕ value of 0°. Remember, the ϕ parameter provides insight into the extent of reactive contributions to the total impedance and since a resistor does not have any reactive contributions to the total impedance, the resulting ϕ parameter for resistors is 0°. In a battery, resistors can model processes related to either the movement or transfer of charge.[8] This includes processes like mass transport of the active ion through the electrolyte, and charge transfer (Faradaic events) from the electrode to the active ion, blue and green regions in **Figure 4.1**.

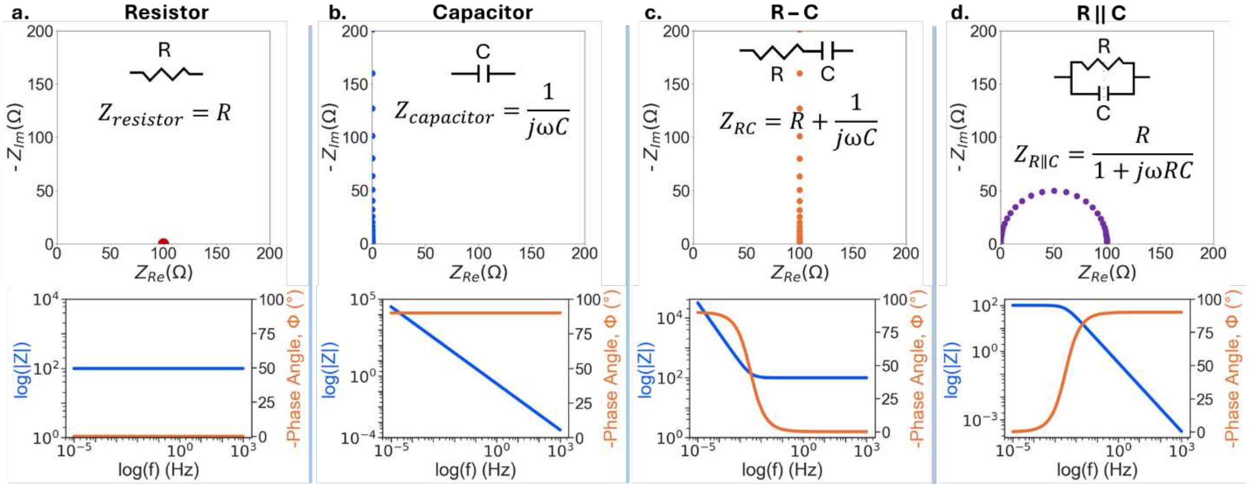

Figure 4.4: Simulated Nyquist and Bode plots showing the relationship between circuit elements and the shapes of Nyquist and Bode plots where R = 100 Ω and C = 0.5 F for all simulations between 0.01 mHz to 1kHz of a A) resistor, B) capacitor, C) resistor and capacitor connected in series, D) resistor and capacitor in parallel. Note that the axes on a Nyquist plot are equal, magnitude of impedance and frequency are on a log scale and phase angle is negative. This figure was adapted from the work of ref 2.

A capacitor stores charge between two plates, opposing electron flow once fully charged until the energy in the capacitor can be released (discharged).[6] Under AC conditions, the impedance of a capacitor is frequency *dependent* as shown by $Z_{cap} = \frac{1}{j\omega C}$, where C is capacitance

(**Figure 4.4b**). Since a capacitor has no resistive (Z_{re}) contribution to its impedance, its impedance is purely reactive shown by a vertical line centered at Z_{re}=0 on the Nyquist plot. The Bode plot |Z| axis demonstrates the frequency dependence where at high frequencies, the current opposition is lower and the phase shift of 90°, which indicates that the contribution of a capacitor to the total impedance is purely reactive. In a battery, capacitors can model the electric-double layer charging (C_{dl}) at the interface between an electrode and the electrolyte (green regions in **Figure 4.1**). The electrolyte-electrode interface can be thought of as behaving like a solid-state capacitor, where the electrode and electrolyte function as the plates of a capacitor with the electric-double layer acting as the dielectric material in-between the plates.

The panels in **Figure 4.4c** and **4.4d** display the representations of the impedance for an R-C circuit connected in series and parallel, respectively. It is important to note, here, that the configuration of ECM elements influences how impedance manifests. For an RC circuit connected in series, the impedance is a combination of resistor and capacitor impedance manifesting as a vertical line (reactive impedance) shifted along the Z_{re} (resistive impedance) (**Figure 4.4c**). When connected in parallel, at high frequencies the impedance goes to zero and at low frequencies the impedance becomes R, resulting in a semi-circular shape in the Nyquist plot (**Figure 4.4d**). These differences are related to how impedances are added when circuit elements are connected in series vs. in parallel (see Appendix V for more detail).

Solid-state circuit elements can effectively model the impedance behavior of a system when arranged into an ECM. Electrochemical systems, however, often do not behave ideally and are not easily described by a simple ECM made of resistors and capacitors. The "non-ideal" behavior of electrochemical systems arises from a variety of factors which cannot be described by a traditional solid-state circuit element. A perfect example of this is the electric double-layer (Edl) and its double-layer capacitance (C_{dl}). The charging of the Edl is dependent on the potential of the electrochemical system, which implies that the C_{dl} is also potential dependent.[6] Thus, application of a solid-state capacitor to model the C_{dl} is not identical to the function of a solid-state capacitor, as the charging of a solid-state capacitor is independent of the potential of the system.[6] Additionally, non-ideal behavior includes potential dependent charging of the C_{dl}, surface roughness of the electrode, and a distribution of reaction rates.[4,9] Owing to the non-ideal behavior of electrochemical systems, with respect to the application of ECMs for quantitative EIS analysis, investigators often use the following circuit element to account for non-ideal charging and diffusion impedance behavior.

$$Z(\omega) = \frac{1}{(j\omega)^{\alpha} Q} \tag{4.7}$$

A very common circuit element applied to ECMs to account for non-ideal behavior is the constant phase element (CPE). The role of a CPE is to model processes that have several different time constants, or a *dispersion* of time constants.[5] For a battery, non-ideal behavior manifests due to the charge/discharge process, charging of the SEI, and non-idealized solid-state diffusion.[3–5] A CPE element does not have a physical basis and is instead a mathematical tool as described by **Equation 4.7**. In this equation, the term $1/(j\omega\tau_0)^{\alpha}$ represents the imaginary impedance, where j is the imaginary unit, ω is the angular frequency, τ_0 is the distribution of time constants, Q is the unit contains capacitive information, and α is a frequency independent value that has a massive impact on the behavior of this circuit element. If the alpha parameter is zero, then the CPE behaves like a resistor (indicating the impedance is purely resistive). If the alpha parameter is one, then the CPE behaves like a capacitor (indicating that the impedance is purely reactive). Referencing **Equation 4.7** helps to cement this point, where the alpha parameter defines what the value of the imaginary component of the CPE will be. In practice, CPEs often replace capacitors in ECMs to model non-ideal E_{dl} charging. This substitution is made when the charge transfer semi-circle is oblong or depressed. Also, CPEs are applied to ECMs to model the diffusion impedance, which we will discuss in the following section. There are several critical caveats to consider when using a CPE in an ECM, which will be discussed in the following section.

The Warburg element is used to model diffusion within the electrode material, where the diffusion length is much smaller than the diffusion region, or semi-infinite. Classic Warburg diffusion modeling strictly follows many assumptions that are not easily translated to practical systems.[10,11] Commonly used thin film electrodes have a finite thickness where the diffusion length is equal to the diffusion region. With this deviation from the semi-infinite diffusion regime, transmissive or reflective boundary conditions must be applied.[12,13] A transmissive boundary describes the (de)intercalation of active ions at the electrolyte/electrode interface where a Faradaic, or charge transfer process occurs (**Figure 4.5a**). The transmissive boundary resembles charge transfer processes in the high frequency region and manifests as a depressed arc at low frequencies (**Figure 4.5c**). A reflective boundary is used to describe diffusion of electroactive species to an impermeable or blocking boundary where charge transfer does not occur (**Figure 4.5b**). This blocking electrode feature leads to accumulation of charge which displays capacitive behavior manifesting as a vertical line at low frequencies (**Figure 4.5d**).[14–16]

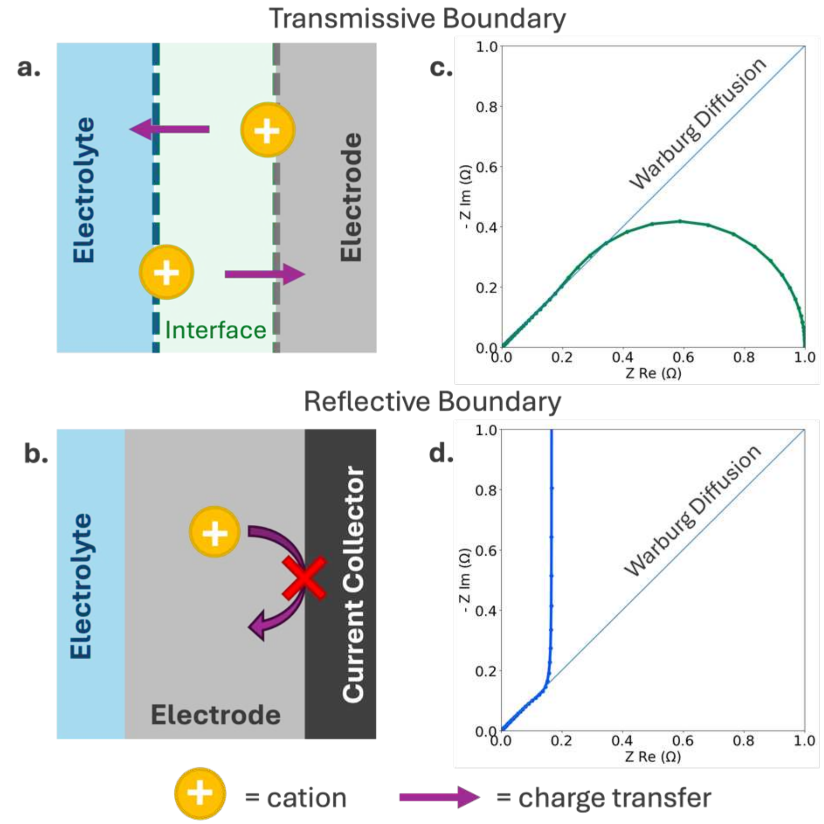

Figure 4.5: Schematic representations of (a) charger transfer process at a transmissive boundary, and (b) blocking behavior of a reflective boundary, where charge transfer processes are represented by purple arrows. Simulated Nyquist plots for (c) transmissive and (d) reflective boundary conditions with classical Warburg diffusion represented by the blue 45° line.

Individual solid state circuit elements, how they manifest on a Nyquist plot and their physical representations have been presented. No single element can be used to describe a complex system such as a battery, so construction of an ECM is needed to model the processes occurring while a battery operates. With the knowledge of individual circuit elements, qualitative visual analysis of impedance data can be used as a starting point for circuit modeling. A resistor element manifests as an offset from zero along the Z_{re} axis (**Figure 4.4a**), therefore, we can use a visual analysis of a Nyquist diagram to begin constructing an ECM (**Box 2**).

4.3.2 How circuits of solid-state components can be used to model EIS spectra for quantitative analysis.

Box 2. Nyquist Features at a glance:

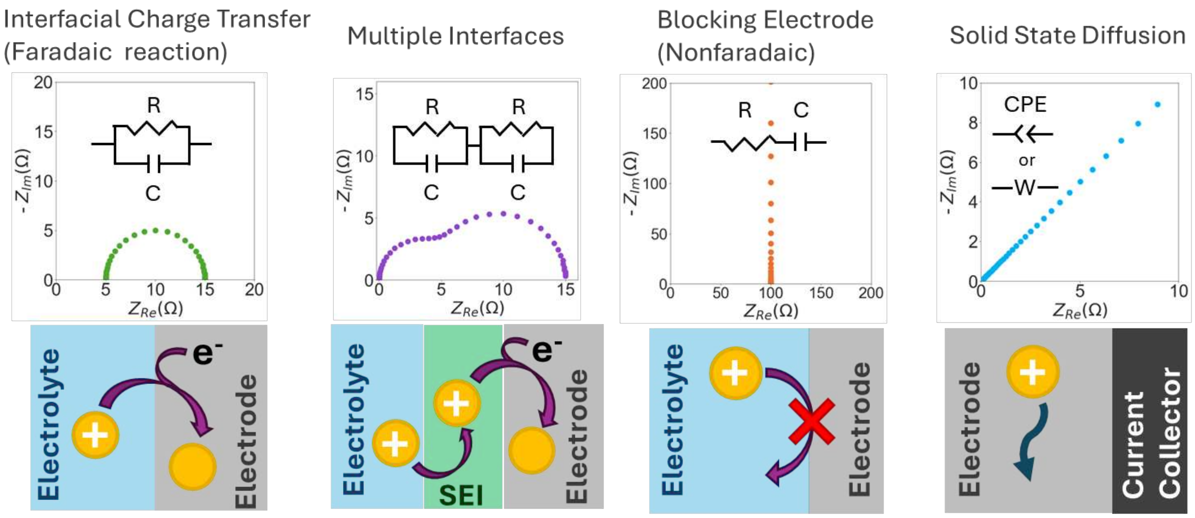

Interfacial Charge Transfer (Faradaic reaction)

Multiple Interfaces

Blocking Electrode (Nonfaradaic)

Solid State Diffusion

After selecting the circuit elements for an ECM, the next step is to fit your EIS data to models to assign impedance values to battery processes. The modeling is done by applying the same experimental parameters from the EIS measurement to the ECM with EIS specific software. Once the fitting is complete, the researcher can assign the impedance values from the ECM to a specific chemical process in a battery. The quantitative analysis of EIS data, however, is challenging and system dependent. This section will focus on the quantitative analysis of rechargeable batteries as it relates to model selection, model validation, and internal factors and analyses that help with this process. For the reader interested in more general descriptions of quantitative EIS, this work recommends the work of Lazanas and Prodromidis, and the seminal work of Orazem and Tribollet.[4,5]

The most common ECM for batteries is the Randels Circuit (**Figure 4.6**), often with several modifications. In this circuit, the first resistor (R_{sol}) models the mass transport impedance related to the movement of an active ion through the liquid electrolyte. The resistor and capacitor in parallel in the next part of the circuit models processes that occur when an active ion arrives at the electrode-electrolyte interface. The resistor models Faradaic charge transfer from the electrode to the active ion, represented as R_{ct}, while the capacitor models the charging of the electric-double layer. This portion of the circuit manifests as a semi-circle in the Nyquist plot, offset along the x-axis by R_{sol}. The final circuit element is the Warburg element, modeling diffusion of the active ion through the solid-state electrode material.

Given the large amount of non-ideal processes in a battery, modifications to the conical Randels circuit are often made in the literature.[14,17] **Figure 4.6** displays several Randels circuits where **Figure** 4.**6a** shows a traditional Randels circuit, **Figure 4.6b** displays a modified Randels circuit where the Warburg element is substituted for a CPE, and **Figure 4.6c** displays a modified Randels circuit that substitutes both the Warburg element and capacitors with CPEs. Modifications to the canonical Randels with CPEs, while being common, should be made carefully. The need for caution arises from the simplicity of the math described by **Equation 4.7** compared to the

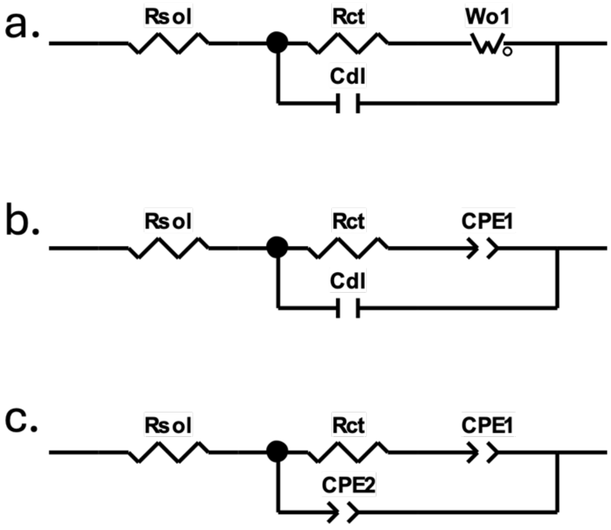

Figure 4.6. Schematic representations of various Randels circuits. A) A traditional Randels Circuit. B) A modified Randels Circuit where the Warburg element has been replaced with a CPE. C) A modified Randels Circuit where CPEs replace both the Warburg element and the capacitor in the circuit.

distributions of time constants it is accounting for.[5] A CPE does not have a physical or empirical backing in an electrochemical system, indicating that the CPE may not be adequately modeling the electrochemical process that it is representing in the ECM.[4,5] These inherent pitfalls can result in overfitting, where the model may provide an excellent fit on paper while not actually accounting for the chemical process that is occurring. This is not to say that CPEs should not be used in ECMs for the analysis of battery systems. Instead, caution is recommended when using CPEs and, above all, model validation is imperative.

Box 3. Lines imply fitted data

Remember each point represents impedance at a single frequency. Adding a solid line to a Nyquist plot implies the data has been fit with an equivalent circuit model. Using a solid line to represent raw data can lead to misrepresentation of impedance.

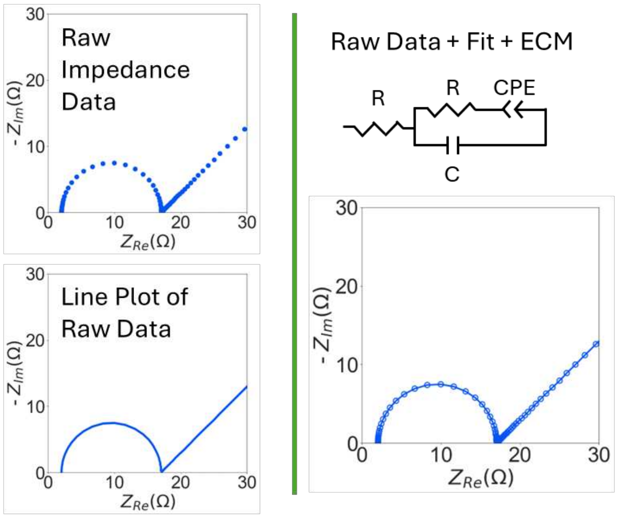

Validation of an ECM requires subsequent experimentation to provide a physical measurement to corroborate the results of the ECM fitting. The type of experiment needed, however, is highly dependent on what aspect of the battery system is being studied. For example, if a set of EIS experiments points toward increased resistance at the electrode-electrolyte interface due to excessive SEI formation, then the characterization of the composition of the SEI is imperative. This can be done, for example, by conducting X-ray photoelectron (XPS) experiments targeted at determining if or how the SEI is adding to the resistance of the interface. An excellent example of a combinatorial EIS-XPS analysis can be found in the work of Marino et al.[15] In this study, the investigators paired EIS with XPS on TiSnSb anodes to link the impedance phenomena of this system to the surface chemistry at the anode, during cycling. These researchers were able to determine that SEI resistance increased as the potential of the electrode became more negative. This work will not dive into the plethora of experimental techniques (both in situ and ex situ) that can help with ECM validation. Instead, this work highly recommends that the interested reader go to the work of Meddings et al. which has a comprehensive discussion of the types of experimental techniques which are useful for ECM validation for LIBs systems.[3]

If an ECM is deemed valid, then a statistical analysis of the ECM fit can be extremely helpful in refining the ECM parameters. The most common metric for the goodness of fit for an ECM is the chi-squared (χ^2). This metric provides a gauge of the difference between the experimentally collected data and the simulated (fit) data.[16] The lower the χ^2 value, the smaller the difference between the experimental EIS data and the simulated ECM fit. Typically, a χ^2 value on the order of $x10^{-4}$ is considered a "good" fit.[4] It is important to remember that ECMs are mathematical representations of the electrochemical processes in a battery. This means that although an ECM might fit the data extremely well, it may not provide any physical meaning if the circuit elements in the ECM are not representative of the battery system. The χ^2 can still provide useful information for tweaking the ECM parameters to help optimize the resulting fit. While the χ^2 value is a good metric for determining the goodness of an ECM fit, there are also a variety of external factors which can affect the measured impedance spectra and, also, the resulting ECM fit. For conventions in plotting impedance data that has been fit, see **Box 3**.

Now it is important to discuss some key conditions that the battery must meet if the EIS experiment is to be considered valid. These conditions are *Linearity, Causality*, and *Stationarity*. For *Linearity*, the electrochemical system in question must behave linearly. Simply put, the input and output signals must be proportional to each other. For *Causality*, an EIS measurement is valid if the measured output signal results from the applied input perturbation. Intuitively this condition makes sense, since it would be impossible to draw strong conclusions from an EIS measurement if the output signal was affected by unrelated parameters not related to the input signal. For *Stationarity*, an EIS is valid if the system under investigation does not change as a function of time. This is to say that steady state conditions are required. These three requirements for EIS measurements can be assessed both mathematically and experimentally and will be discussed in detail below.

Fortunately, the conditions highlighted above can be validated mathematically using the Kramers-Kronig relations. These relations allow for the calculation of the real impedance from the imaginary impedance, and the calculation of the imaginary impedance from the real impedance. Applying these relations to validate EIS spectra is called the Kramers-Kronig (K-K) transform. For the purposes of this work, we will not dive into the math behind this transformation, and instead direct the interested reader to the following resources.[4,5] The K-K relations can only be satisfied if the big three criteria (Linearity, Causality, Stationarity) are met. Simply put, the K-K transform is the quickest way to mathematically assess if the big 3 criteria for an impedance measurement are met. A practical way to assess if the battery system meets the big 3 criteria is to simply re-run the EIS measurement where the starting and final frequencies are swapped. Applying the K-K transform to an EIS spectrum will provide a χ^2 value, related to the difference between the experimental data and the K-K transform. In practice, K-K transforms with χ^2 values greater than x10^{-4} are considered invalid values between x10^{-5} and x10^{-6} are considered good, and values less than x10^{-6} are considered excellent.[4]

4.3.3 Impact of external factors on EIS measurements in batteries.

In addition to all the internal conditions that need to be met for valid quantitative EIS analysis, there are also a variety of external factors that can greatly affect the resulting EIS spectra.

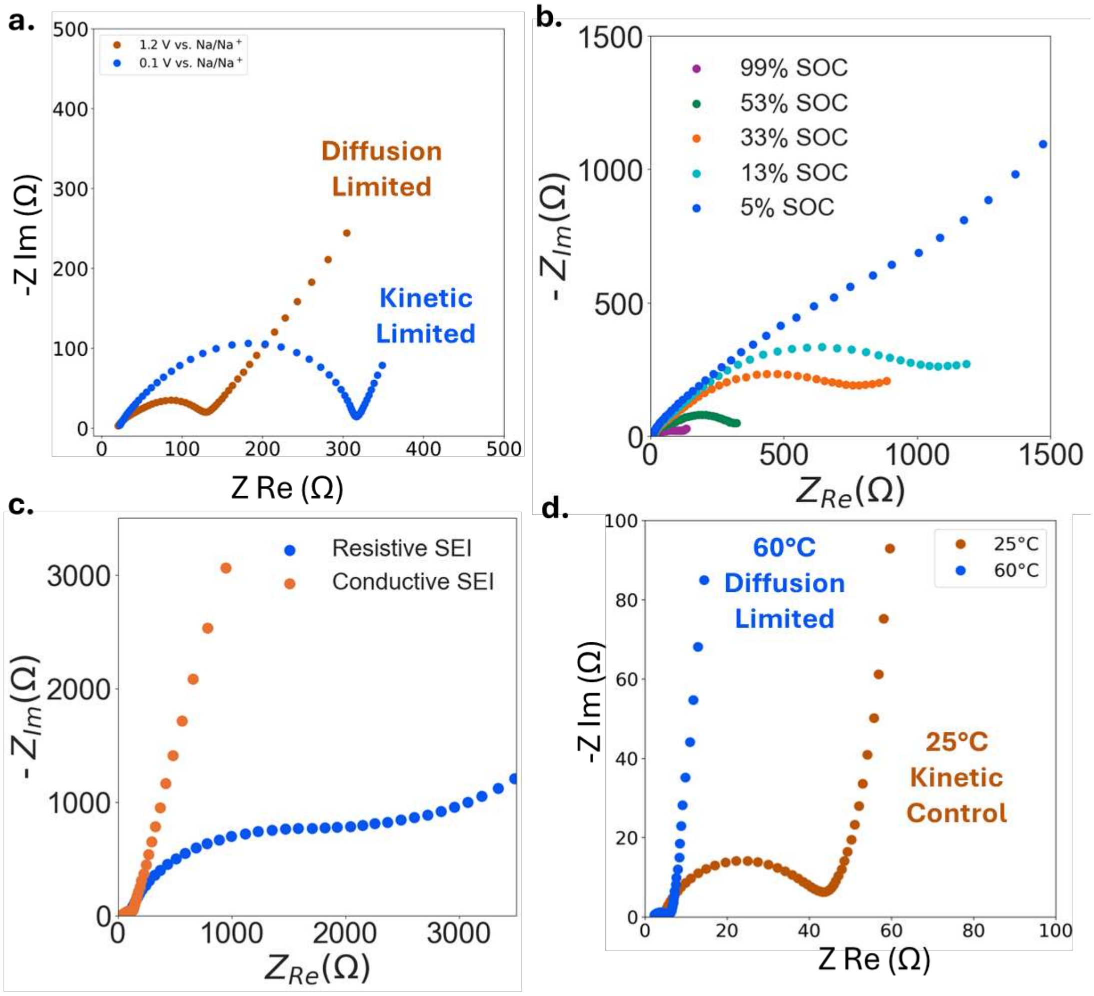

Figure 4.7: Various Nyquist plots representing the effect of external parameters on the resulting EIS spectra. A) Nyquist plot displaying EIS spectra from an Sb electrode in a Na-ion half-cell at 1.2 V vs. Na/Na$^+$(orange) and at 0.1 V vs. Na/Na$^+$ (blue). B) Nyquist plot representing EIS spectra of $Li_xMo_3Nb_{14}O_{44}$ as a function of potential from 1.0 to 2.0 V vs. Li/Li$^+$during the Li-ion deinsertion process. C) Nyquist plot displaying EIS spectra from an Sb electrode in a Na-ion half-cell under pristine (no cycling) conditions (orange) and after 10 cycles (blue) in an electrolyte of 1 M $NaClO_4$ PC with 5% VC. D) EIS spectra of a graphite electrode in a Li-ion half-cell at 25 ℃ (orange) and at 60 ℃ (blue).

Some of the main external factors which affect the EIS spectra of batteries are the potential of the electrode, state of charge (SOC) of the electrode, temperature of the cell, and the number of cycles undertaken by the battery. The following section will describe how these different external factors affect EIS spectra in batteries.

The potential of the battery has a large effect on the resulting EIS spectra. **Figure 4.7a** is a Nyquist showing the EIS spectra from an Sb electrode in a sodium-ion half-cell at 1.2 V vs. Na/Na^+ (orange) and at 0.1 V vs. Na/Na^+ (blue). Qualitatively, the shapes of the two Nyquist plots are clearly different, where the blue has a much larger charge transfer resistance circle than the orange trace. These qualitative distinctions provide insight into which process is contributing most to the impedance of the system which, for an electrode like Sb, also sheds light on how the impedance is related to the reaction between the active ion and the electrode material.

The SOC of a battery influences the resulting EIS spectrum. When Li-ions are inserted into the $Li_xMo_3Nb_{14}O_{44}$ material (**Figure 4.7b**), the EIS traces in a Nyquist plot will shift to the left as the percent SOC increases. This trend indicates that, for the ECM fitting, the values of the circuit elements in the ECM will be smaller as the SOC increases. Intuitively this notion makes sense since the addition of active ions to the electrode material will inherently increase the conductivity of the system, resulting in smaller resistance values. In some cases, increasing the SOC of a battery can greatly change the shape of the resulting EIS traces.

Resistances associated with electrochemical processes should change as batteries are cycled. Solution resistance, R_{sol}, should increase due to consumption of active ions and electrolyte decomposition as the SEI is formed manifesting as a larger shift along the Z_{re} axis. This trend has been shown in the work of Lyu et al. where they found that a commercial LIBs lithium cobalt oxide (Li_xCoO_2) system, cycled over 300 times, demonstrated a shift to the right of the EIS spectra in Nyquist plots, due to depletion of the Li-content in the

Box 4. How many charge transfer events?

In a pristine, uncycled cell a single charge transfer event is expected at the electrolyte | electrode interface. Upon cycling an additional charge transfer process is expected with the formation of the SEI. This is also system dependent.
Approach this question by being familiar with the system under investigation, evaluate the Bode plots, try different ECMs and supplement by using complementary techniques like distribution of relaxation times (DRT).

bulk electrolyte.[18] Changes in charge transfer resistances resulting from formation of the SEI should also be taken into consideration when analyzing impedance data for a cycled cell. **Figure 4.7c** shows the EIS spectra for antimony (Sb) electrodes after 10 cycles with different electrolyte compositions resulting in the formation of different passivation layers. Electrolyte A decomposes to form a highly resistive SEI where the impedance is dominated by the charge transfer kinetics at the interface shown (**Figure 4.7c** in blue). Additionally, this electrolyte displays a shift along the Z_{Re} axis indicating the large consumption of electrolyte components leading to a decreased ionic conductivity. Electrolyte B is solid state diffusion controlled indicating the formation of a low resistance passivation layer (**Figure 4.7c** in orange). These results highlight the importance of understanding how the electrochemical processes and associated resistances may change over the lifetime of the battery. Identifying the number of charge transfer events can be challenging if the timescales they occur are similar, see **Box 4** for more information.

Applying EIS to a battery, also, has a large dependence on the temperature of the system. **Figure 4.7d** displays a Nyquist plot with two EIS spectra from a graphite anode in a LIBs half-cell at 25°C (orange) and at 60 °C (blue). Increasing the temperature of the battery system will reduce both the R_{sol} and R_{ct} values, as is clearly shown in these spectra. This reduction in R_{sol} and R_{ct} arises from the fact that less energy will be required to move an ion through the electrolyte, or to transfer charge from the electrode to the ion, because extra energy has already been added to the system resulting from the temperature.[3]

Activity 2:

At this point, the reader should be armed with the necessary knowledge to complete **Activity 2**, which can be found in Appendix III.

4.4 Conclusions

Characterization of the impedances related to chemical processes in a battery is useful as it allows insight into concurrent processes occurring over different timescales. The application of EIS for battery analysis is incredibly common in the field, despite the difficulties related to EIS data analysis. The objective of this work is to bridge the gap between the ease of data collection and data analysis with respect to the EIS analyses of rechargeable batteries. The reader should understand the relationship between the chemical processes in a battery and their respective impedances, and how the impedance spectrum is represented graphically. The reader should also feel comfortable representing impedance traces in a Nyquist plot with an equivalent circuit model, with an additional understanding of difficulty associated with representing impedance spectra mathematically. Finally, the reader should understand some conditions in a rechargeable battery affect the resulting impedance spectra.

Activity 3:

At this point, the reader should be armed with the necessary knowledge to complete **Activity 3**, which can be found in Appendix III.

4.5 References

(1) Atzori, L.; Iera, A.; Morabito, G. The Internet of Things: A Survey. *Comput. Netw.* **2010**, *54* (15), 2787–2805. https://doi.org/10.1016/j.comnet.2010.05.010.

(2) Brédas, J.-L.; Buriak, J. M.; Caruso, F.; Choi, K.-S.; Korgel, B. A.; Palacín, M. R.; Persson, K.; Reichmanis, E.; Schüth, F.; Seshadri, R.; Ward, M. D. An Electrifying Choice for the 2019 Chemistry Nobel Prize: Goodenough, Whittingham, and Yoshino. *Chem. Mater.* **2019**, *31* (21), 8577–8581. https://doi.org/10.1021/acs.chemmater.9b04345.

(3) Meddings, N.; Heinrich, M.; Overney, F.; Lee, J.-S.; Ruiz, V.; Napolitano, E.; Seitz, S.; Hinds, G.; Raccichini, R.; Gaberšček, M.; Park, J. Application of Electrochemical Impedance Spectroscopy to Commercial Li-Ion Cells: A Review. *J. Power Sources* **2020**, *480*, 228742. https://doi.org/10.1016/j.jpowsour.2020.228742.

(4) Lazanas, A. Ch.; Prodromidis, M. I. Electrochemical Impedance Spectroscopy─A Tutorial. *ACS Meas. Sci. Au* **2023**, *3* (3), 162–193. https://doi.org/10.1021/acsmeasuresciau.2c00070.

(5) Mark E. Orazem; Bernard Tribollet. *Electrochemical Impedance Spectroscopy*; John Wiley & Sons, 2008.

(6) Bard, J. A.; Faulkner, R. L. *Electrochemical Methods, Fundamentals and Applications*; John Wiley & Sons, Inc: New York City, 2001.

(7) Cohen, H. *Complex Analysis with Applications in Science and Engineering*; Springer US: Boston, MA, 2007. https://doi.org/10.1007/978-0-387-73058-5.

(8) Choi, W.; Shin, H.-C.; Kim, J. M.; Choi, J.-Y.; Yoon, W.-S. Modeling and Applications of Electrochemical Impedance Spectroscopy (EIS) for Lithium-Ion Batteries. *J. Electrochem. Sci. Technol.* **2020**, *11* (1), 1–13. https://doi.org/10.33961/jecst.2019.00528.

(9) Lasia, A. The Origin of the Constant Phase Element. *J. Phys. Chem. Lett.* **2022**, *13* (2), 580–589. https://doi.org/10.1021/acs.jpclett.1c03782.

(10) Warburg, E. Ueber Das Verhalten Sogenannter Unpolarisirbarer Elektroden Gegen Wechselstrom. *Ann. Phys.* **1899**, *303* (3), 493–499. https://doi.org/10.1002/andp.18993030302.

(11) Huang, J. Diffusion Impedance of Electroactive Materials, Electrolytic Solutions and Porous Electrodes: Warburg Impedance and Beyond. *Electrochimica Acta* **2018**, *281*, 170–188. https://doi.org/10.1016/j.electacta.2018.05.136.

(12) Bisquert, J.; Garcia-Belmonte, G.; Fabregat-Santiago, F.; Bueno, P. R. Theoretical Models for Ac Impedance of Finite Diffusion Layers Exhibiting Low Frequency Dispersion. *J. Electroanal. Chem.* **1999**, *475* (2), 152–163. https://doi.org/10.1016/S0022-0728(99)00346-0.

(13) Bisquert, J. Theory of the Impedance of Electron Diffusion and Recombination in a Thin Layer. *J. Phys. Chem. B* **2002**, *106* (2), 325–333. https://doi.org/10.1021/jp011941g.

(14) Dashairya, L.; Das, D.; Saha, P. Binder-Free Electrophoretic Deposition of Sb/rGO on Cu Foil for Superior Electrochemical Performance in Li-Ion and Na-Ion Batteries. *Electrochimica Acta* **2020**, *358*, 136948. https://doi.org/10.1016/j.electacta.2020.136948.

(15) Marino, C.; Darwiche, A.; Dupré, N.; Wilhelm, H. A.; Lestriez, B.; Martinez, H.; Dedryvère, R.; Zhang, W.; Ghamouss, F.; Lemordant, D.; Monconduit, L. Study of the Electrode/Electrolyte Interface on Cycling of a Conversion Type Electrode Material in Li Batteries. *J. Phys. Chem. C* **2013**, *117* (38), 19302–19313. https://doi.org/10.1021/jp402973h.

(16) William Navidi. *Statistics for Engineers and Scientists*, 2nd ed.; MaGraw-Hill, 2008.

(17) Nieto, K.; Windsor, D. S.; Kale, A. R.; Gallawa, J. R.; Medina, D. A.; Prieto, A. L. Structural Control of Electrodeposited Sb Anodes through Solution Additives and Their Influence on Electrochemical Performance in Na-Ion Batteries. *J. Phys. Chem. C* **2023**, *127* (26), 12415–12427. https://doi.org/10.1021/acs.jpcc.3c01086.

(18) Lyu, C.; Zhang, T.; Luo, W.; Wei, G.; Ma, B.; Wang, L. SOH Estimation of Lithium-Ion Batteries Based on Fast Time Domain Impedance Spectroscopy. In *2019 14th IEEE Conference on Industrial Electronics and Applications (ICIEA)*; IEEE: Xi'an, China, 2019; pp 2142–2147. https://doi.org/10.1109/ICIEA.2019.8834119.

CHAPTER 5: FUTURE DIRECTIONS

The work presented herein aimed to uncover insights into alternative battery technologies by the critical analysis of 3D batteries and their development (Chapter 2), determination of the fundamental interfacial interactions of cPAN coated Sb electrodes in NIBs (Chapter 3), and a beginner friendly approach for learning EIS (Chapter 4). Concerning future directions of investigation, the work highlighted in Chapter 3 has some exciting areas where future investigations should be pushed. These areas of future research are quantification of the early cycle SEI imparted when cPAN is used as protective coating for Sb electrodes in NIBS, and the application of cPAN protective coatings to conversion electrode materials on aperiodic 3D structure in NIBs. This chapter can act as a starting point for younger graduate students who might be interested in continuing and expanding the work detailed in this text.

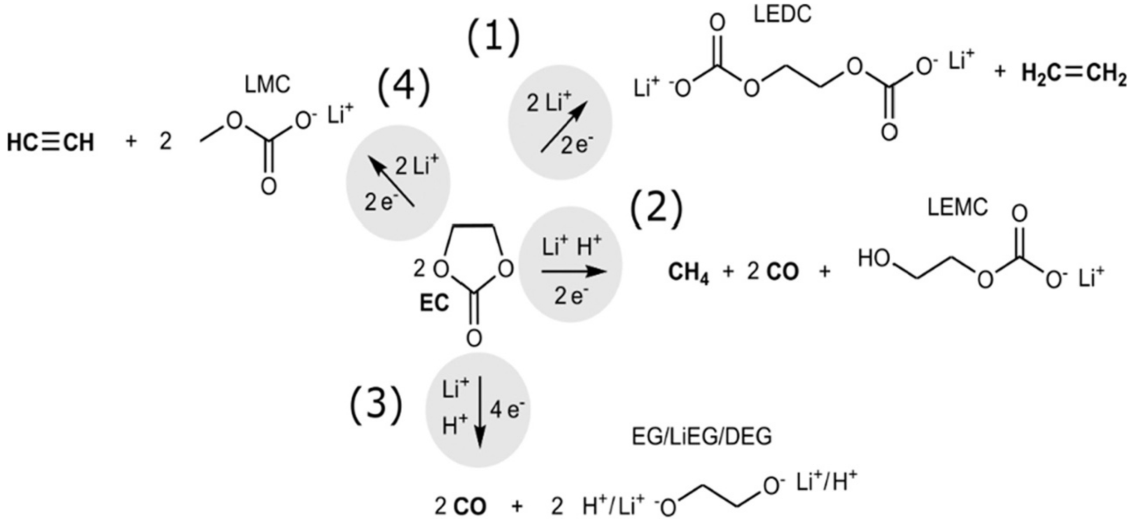

Figure 5.1: Decomposition of ethylene carbonate (EC) as determined by Operando GC-MS. The numbers denoted in the figure relate to the proposed decomposition pathways of EC as it forms the SEI at a lithium-metal anode. This figure was adapted from the work of Hobold et al. (ref 3).

5.1 Quantification of early cycle SEI products

As discussed in Chapter 3, cPAN as a protective coating had the most significant effect of the (de)sodiation chemistry of Sb anodes at early cycle numbers (**Figure 3.3c**). These differences in the early cycle (de)sodiation chemistry of Sb, however, were not maintained as the cPAN@Sb and Sb systems were cycled. The XPS data supports this notion, where the biggest differences between the C 1s and O 1s/Sb 3d environments occur at early stages of cycling (after 1st discharge). This XPS data, however, is only useful in the qualitative assignments of the chemical composition of the SEI and does not provide any insight into the concentration of the different components in the SEI. Thus, to understand *how* the cPAN is affecting both the composition of the SEI and the concentration of its constituents, quantitative XPS analysis of the SEI is required.

Quantitative analysis of SEI layers in rechargeable batteries is challenging. This arises from the fact that SEI layers can be very thin, are air-sensitive, and are difficult to assess the form and function of this layer as a battery is cycling.[1,2] The reduction, and thus decomposition, of the bulk electrolyte can also occur via multiple reaction pathways. **Figure 5.1** displays a schematic of a proposed degradation mechanism of ethylene carbonate (EC) from the work of Hobold et al.[3] In this scheme, it is clear to see that there are several different paths EC can be decomposed, which results in the possibility of a variety of different SEI products being present in the as formed SEI.

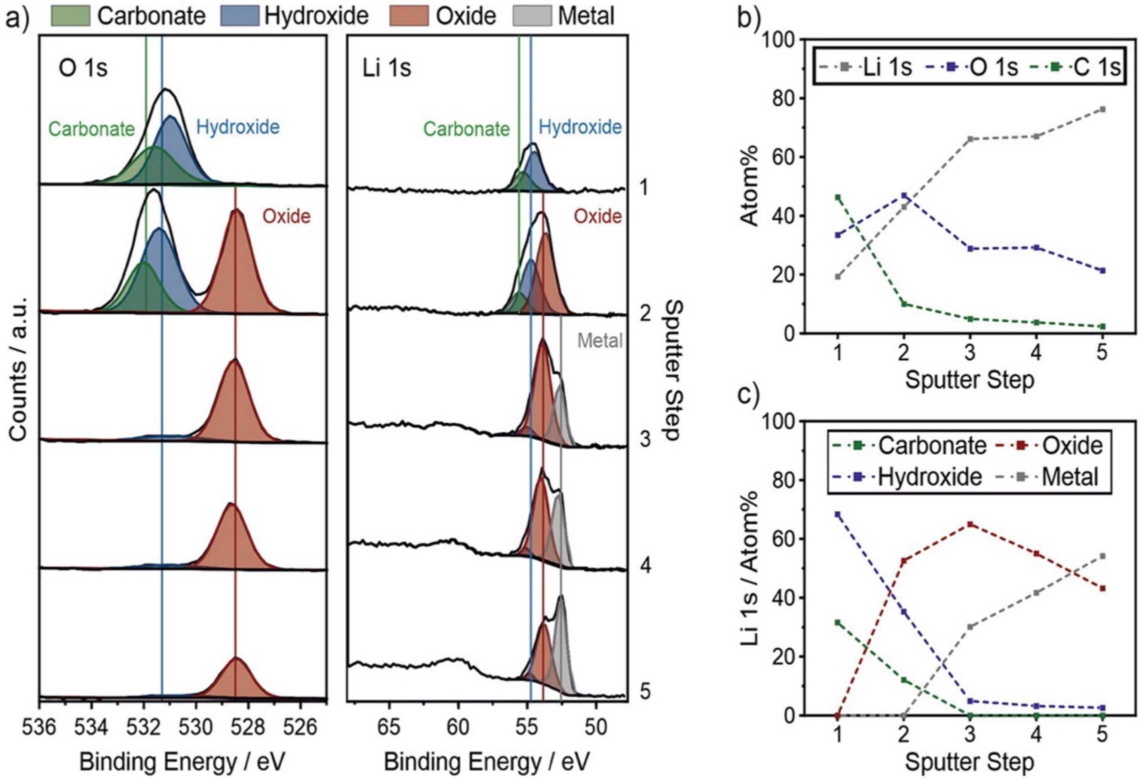

Figure 5.2: X-ray photoelectron spectroscopy (XPS) depth profiling and quantitative analysis of SEI layers in Li-metal batteries. A) The O1s and Li1s XPS spectra of an SEI on a Li-metal anode as a function of Ar-ion beam sputtering step, where the presence of carbonate and hydroxide containing SEI species are primarily found at shallower depths in the SEI layer. B) Atomic percentages of Li, C, and O containing SEI species as a function of sputter step, where the C and O environments are higher in concentration at the surface of the SEI, while the Li content increases deeper into the layer. C) Atomic percents as a function of sputtering step where the percentages relate to the Li1s corresponding to Li-carbonates, Li-oxides, Li-hydroxides, and Li-metal environments. This figure has been adapted from the work of Otto et al. (ref 5).

The decomposition of EC, also, is only one constituent of the bulk electrolyte that is decomposed when the SEI is formed.[4] Thus, it is extremely challenging to concretely report the mechanism in which the SEI is formed due to the plethora of different potential SEI products that might be present in this interphase.

Despite the difficulties in quantitative SEI analysis, there are example in the literature of this analysis being conducted.[5–7] These studies, universally, use X-ray photoelectron spectroscopy (XPS) as a major characterization component in these investigations. The application of XPS for SEI analysis is crucial, as it is a surface sensitive technique that provides compositional insights into the chemical environments. This makes XPS a perfect characterization technique for the compositional analysis of the SEI, which is inherently located at the surface of the anode in a battery.[4] The implementation of XPS, however, is quite challenging if a quantitative understanding of the SEI is desired. This difficulty arises from the heterogeneous connectivity of the SEI, which is composed of intermixed organic and inorganic phases.[4] Due to this heterogeneity, the XPS spectra collected on the surface of an anode material can have significant differences depending on the location of where the spectra were collected.[1] Thus, volumes of data must be collected and analyzed to provide a quantitative understanding of the components of the SEI. This can take quite some time, as many chemical environments would need to be assessed over a wide range of locations on the sample surface. The surface sensitivity of XPS, also, limits insight into the SEI composition across the depth of the interfacial layer as the penetration depth of a standard XPS experiment is 5-10 nm in depth.[8] To gain insight into how the SEI changes as a function of depth (thickness), an Ar-ion beam is applied to etch away the surface of the sample such that XPS can be applied to the constituents of the SEI deeper into the SEI layer. **Figure 5.2a** displays Li 1s and O 1s XPS spectra as a function of sputter time, where **Figure 5.2b** and **5.2c** display the atom percentages of Li, O, and C as a function of etching time. These data, collected on a Li-metal anode from the work of Otto et al., clearly demonstrate the compositional changes to the surface of the anode material as the XPS spectra were collected deeper within the SEI layer.[5] Depth-profiling, however, tends to increase the timeline for XPS experiments as the etch process must occur prior to any survey or high resolution XPS scans. Although there are some limitations to the application of XPS for quantitative analysis of SEI layers, it is still the most used technique for this type of insight into surface interactions in batteries.

Although XPS is the most common characterization technique for the composition of the SEI, it is too often implemented as a stand-alone analysis. Applying XPS as the stand-alone technique analysis does not provide for a full understanding of the connectivity of the SEI, as XPS struggles to produce insight into the SEI in terms of the lateral and depth connectivity and composition of this surface layer.[5] To gain this sort of insight into an SEI layer, complementary characterization techniques should be applied to either support or refute the results of an XPS analysis. A characterization technique that compliments the information provided by XPS is called Time of Flight Secondary ion mass spectrometry (TOF-SIMs). This technique uses a high energy ion beam to irradiate the sample, ejecting a certain percentage of charged species (secondary ions) which are then separated as a function of charging based on their travel time through an electric field.[8] Since the incident ion beam can be swept over the surface of the sample, TOF-SIMs allows for insight into the lateral and depth identification of surface layer elements.[9] **Figure 5.3** displays the TOF-SIMs mass spectra of the SEI on Li-metal anodes where **Figure 5.3a** displays the TOF-SIMs spectra as a function of ion dosage, **Figure 5.3b** displays the elemental mapping overlays of the different chemical environments of the SEI, and **Figure 5.3c** displays a 3D reconstruction of the TOF-SIMs depth profiles with the elemental mapping overlays.

Concerning the SEI, the use of TOF-SIMs is complementary of XPS analyses as TOF-SIMs can either support or refute the compositional assignments made by XPS, while also providing for better lateral and depth resolution. The work of Otto et al. is a perfect example of the use of XPS and TOF-SIMs as complementary characterization techniques for the analysis of an SEI on a Li-metal anode.[5] This study way able to determine that the inorganic portion of the SEI was primarily composed of lithium hydroxide, with additional the presence of carbonate and

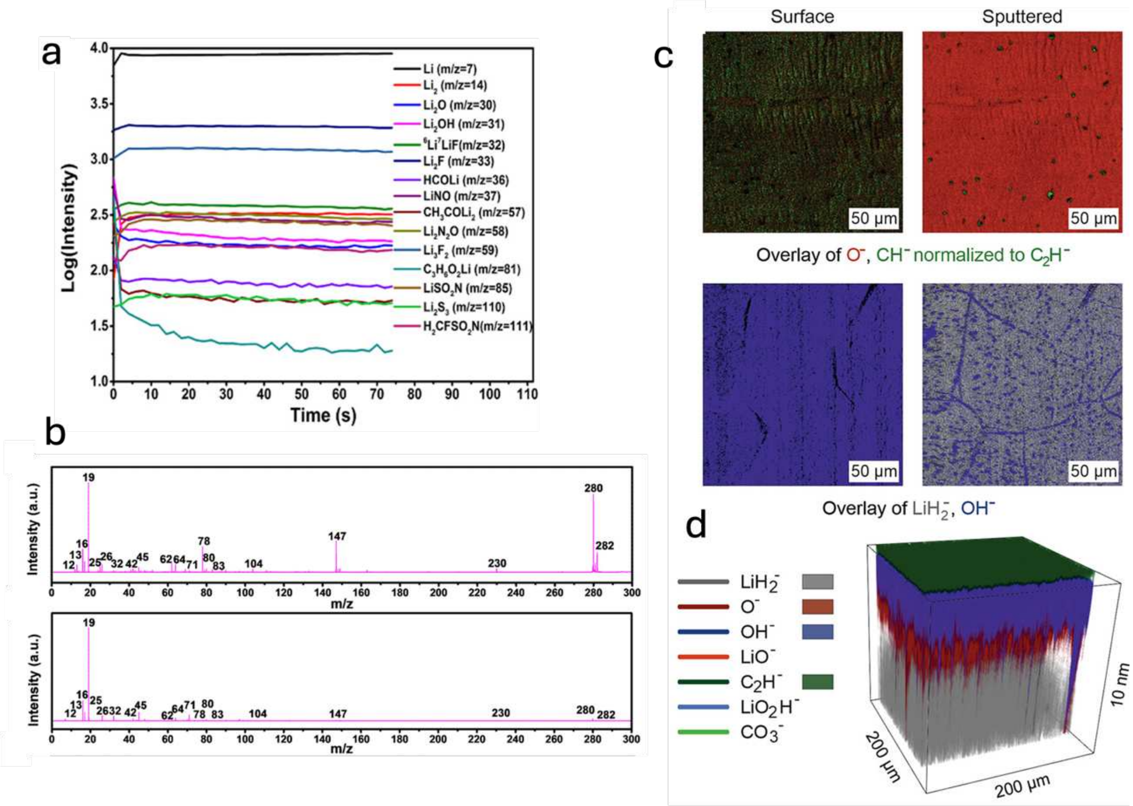

Figure 5.3: Time of Flight Secondary ion Mass Spectrometry (ToF-SIMs) of the SEI on Li-metal anodes. A) Intensity of m/z ratios as a function of time from ToF-SIMs depth profiling, where the highest intensities relate to Li-metal and Li-fluoride species. B) Mass spectra of ToF-SIMs analysis on the surface of the SEI (top) and after depth profiling (bottom). C) Overlay images from ToF-SIMs analysis at the surface and after depth profiling. D) 3D map of ToF-SIMs overlay images showing the heterogeneous nature of the as formed SEI in this system. Panels A and B were adapted from the work of Ma et al. (ref 7). Panels C and D were adapted from the work of Otto et al. (ref 5).

lithium oxide rich regions. The authors were only able to gain this type of insight into the SEI through the implementation of both XPS and TOF-SIMs.

Future work on the early cycle impact of cPAN on the (de)sodiation chemistry of Sb anode in NIBs will require the detailed study of the early cycle SEI in the system using both XPS and TOF-SIMs. The fundamental scientific questions are as follows. How does cPAN impact the composition and concentration of the components in the SEI at early cycles? Does the presence of cPAN increase or decrease the inorganic components of the SEI at early cycles? The leading hypotheses for this proposed work are as follows. The initial higher charge transfer resistance of the cPAN system should reduce the extent of SEI formation at the cPAN@Sb electrode. Also, given the Na 1s and F 1s spectra in **Appendix II**, the inorganic components of the SEI for the cPAN system and the Sb control should not be very different in concentration, which would

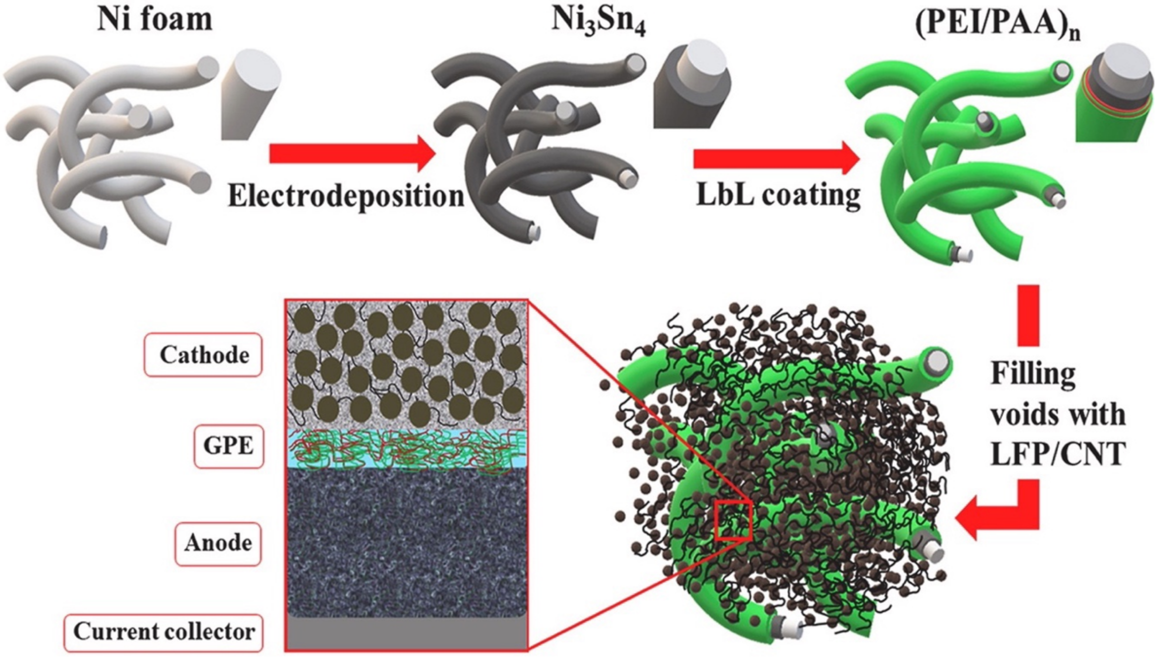

Figure 5.4: Fabrication of an aperiodic 3D lithium-ion battery. This 3D battery system used electrodeposition to for the Ni_3Sn_4@Ni-foam anode. The electrolyte was formulated through a layer by layer co application of polyethylenimine:polyacrylic acid (PEI:PAA) co-polymer that was then annealed to achieve cross-linking. This co-polymer was then gelled with a standard carbonate liquid organic electrolyte. The lithium iron phosphate/carbon nanotube (LFP/CNT) was then spray coated onto the aperiodic structure. This figure was adapted from the work of Tolgankbek et al. (ref 11).

indicate that the resistance related to the inorganic portion of the SEIs are not significantly different. Experimentally, this proposed study will assess the SEI of the cPAN@Sb and Sb systems for pristine electrodes, electrodes after the 1st discharge, electrodes after the 2nd cycle, electrodes after the 5th cycle, and electrodes after the 10th cycle. The quantitative analysis of these electrodes under these cycling conditions will provide insight into how the presence of cPAN affects the early cycle surface chemistry of Sb electrode in NIBs.

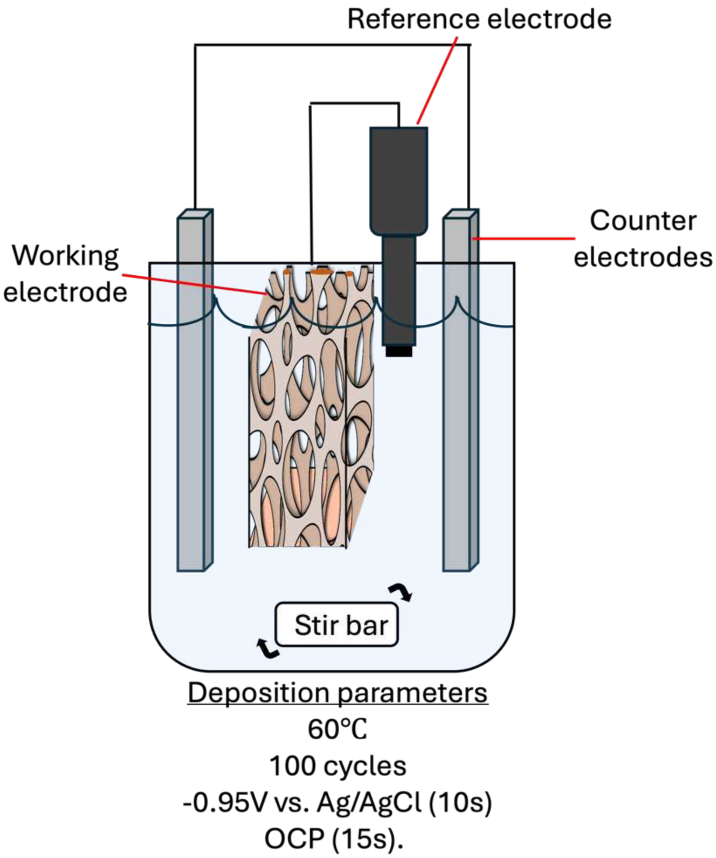

Figure 5.5: Electrodeposition set up used to fabricate Sn_xSb_y@Ni-foam 3D anodes for sodium-ion battery. The Ni-foam substrate was placed between two stainless-steel mesh counter electrodes. The reference electrode (Ag/AgCl) was placed near one of the edges on the Ni-foam substrate.

5.2 Study of the effect of cPAN on conversion electrodes in 3D sodium-ion batteries

Batteries based on 3D architectures have the potential to allow LIBs technologies to be both energy and power dense systems, as detailed in **Chapter 2**. In **Chapter 2**, aperiodic 3D battery architectures are shown to be well suited for large scale battery applications.[10] These aperiodic LIBs 3D batteries have been realized in the literature, as seen in **Figure 5.4**. This aperiodic 3D battery, as described in the work of Tolganbek et al., used a Ni-foam as the substrate for an electrodeposited Sn conversion anode.[11] The authors then used a layer-by-layer (lbl) dip coating method to apply the co-polymer gel-polymer electrolyte (GPE) to the aperiodic structure. Finally, the investigators applied a composite lithium iron phosphate (LFP)/carbon nanotube (CNT) cathode via spray coating. This, to the best of our knowledge, is the first example of an aperiodic 3D LIBs battery in the literature.

There are, however, few examples in the literature of a 3D battery being fabricated such that it functions in the NIBs systems. The development of a 3D NIBs would allow for an expansion of the NIBs applications space, which would provide for cheaper and easier to source battery systems, particularly for larger applications. As with the 3D LIBs system, there is a critical need to improve the energy density, and still applies to 3D NIBs. Previous work in the Prieto group has studied the electrodeposition of tin antimonide (SnSb) conversion anodes to aperiodic Ni-foam structures.[12] The SnSb conversion electrode system is of interest due to its high theoretical specific capacity of 752 mAh g^{-1}.[13] The cycling stability of this anode material, however, is poor due to the inherent mechanical fragility of conversion electrodes resulting from the inherent volume expansion in these materials.[14,15] Thus, if SnSb is to be used as an anode material in a 3D NIB, strides must be made toward the mechanical stabilization of this material on 3D architectures.

As mentioned in **Chapter 3**, cPAN is a popular CPB for the stabilization of conversion electrode materials and has been shown in the work to function in several ways when included in a NIBs.[16,17] Concerning a 3D NIBs system, one could simply take the results highlighted in Chapter 3 to extrapolate the functionality of cPAN toward conversion electrodes in a 3D system. With this line of logic, application of cPAN as a coating for SnSb on a 3D architecture should increase the efficiency, rate capability, and charge transfer resistance of the system. Too often in the battery field, however, the properties of a material are extrapolated to every system can be applied to. This is short sighted, as the manifestation of a material's properties can be greatly affected by the configuration and the fabrication of the system it is applied to.[10,18] So, future work aimed at stabilizing SnSb anodes in a 3D NIBs system, using cPAN, will require a detailed investigation

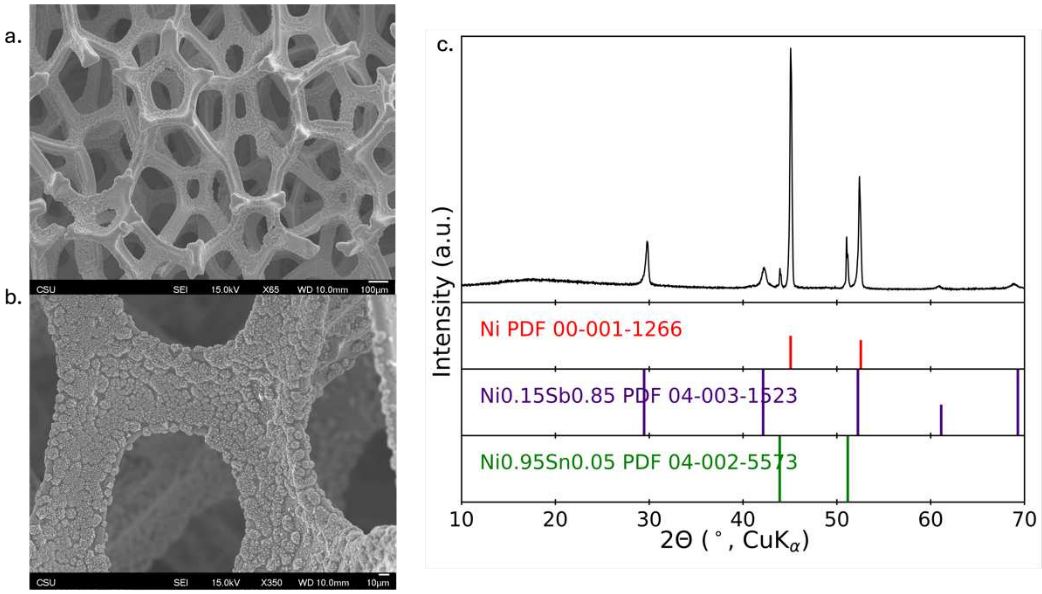

Figure 5.6: Preliminary materials characterization of Sn$_x$Sb$_y$@Ni-foam. A) Scanning electron microscopy (SEM) image at x65 magnification of the as deposited Sn$_x$Sb$_y$@Ni-foam, which shows coverage of the Ni-foam tendrils throughout the depth of the foam. B) An SEM image at x350 magnification, showing bulbous features as a result of the electrodeposition. C) Powder X-ray diffraction (PXRD) pattern of the Sn$_x$Sb$_y$@Ni-foam which was indexed to the following PDFs: Ni (PDF 00-001-1266), Ni$_{0.15}$Sb$_{0.85}$ (PDF 04-003-1523), Ni$_{0.95}$Sn$_{0.05}$ (PDF 04-002-5573). This pattern shows that the crystalline phases present in the foam were either Ni-deficient Ni-Sb phase or a Ni-rich Ni-Sn phase.

into the behavior of the cPAN coating on conversion electrodes deposited onto an aperiodic (3D) Ni-foam.

Previous work has been conducted on this project, by Jeffery Ma Ph.D. and Matthew Valdiviezo M.S., primarily focused on the development of the co-electrodeposition of SnSb anodes on Ni-foams. Dr. Ma initially developed the electrochemical synthesis of this materials, while Matthew Valdiviezo made strides toward the optimization of the electrosynthesis to produce foams which are conformally coated by the SnSb conversion material. The combined work of these students led to electrodeposition parameters that are currently in use for this project, which will be described in Chapter 5.2.3. Details related to the optimization of the electrodeposition process and solution conditions can be found in the dissertation of Dr. Ma.[12]

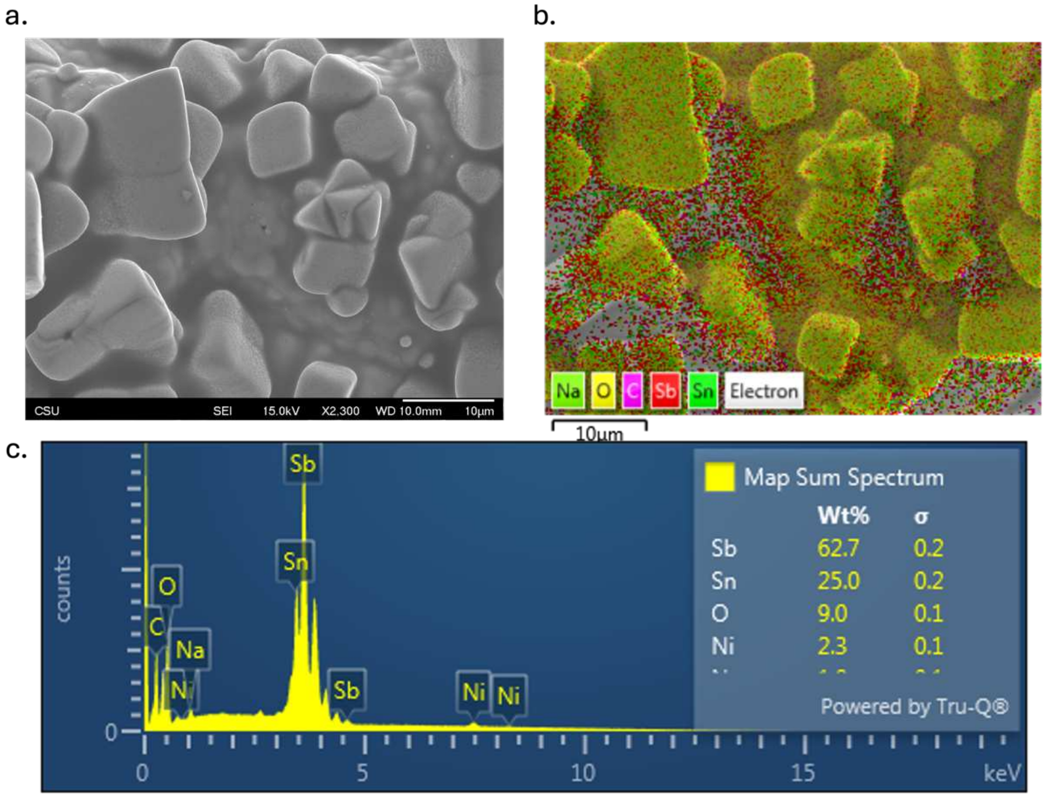

Figure 5.7: Scanning electron microscope:X-ray energy dispersive spectroscopy (SEM:EDS) of Sn$_x$Sb$_y$@Ni-foam. A) An SEM reference image at x2,300 magnification which displays the area in which the EDS spectra were taken. B) The EDS elemental map overlay of the SEM image with Na, O, C, Sb, and Sn environments represented. C) The EDS spectrum with the map sum spectrum in the upper right-hand corner, showing the wt% percentages of the different elements present in the spectrum.

5.2.1 Preliminary results

Prior to assessing the functionality of cPAN as a protective coating for conversion anodes in a 3D aperiodic system, the deposition parameters described by Dr. Ma and Matthew Valdiviezo were reproduced. To do so, a three-electrode beaker cell was arranged such that the working electrode (Ni-foam) was placed between two counter electrodes (stainless-steel mesh), with the Ag/AgCl reference electrode placed near the edge of the working electrode (**Figure 5.5**). The electrodeposition solution (described in detail in Chapter 5.2.3) was composed of 50 mM $SnCl_2$, 50 mM $SbCl_3$, excess citrate in solution, and was titrated to a pH of 7.4. A potential of -0.95 V vs. Ag/AgCl was pulsed for 10 second, followed by at 15 second rest at open circuit potential. This deposition was conducted at 60℃ to reduce the amount of time needed to fully coat the Ni-foam substrate with the SnSb active material. **Figure 5.6** displays SEM images (**Figure 5.6a** and **5.6b**) and PXRD (**Figure 5.6c**) of SnSb@Ni-foam deposited under the above-mentioned conditions. The SEM images show the deposited active material fully coated the tendrils of the of the Ni-foam while containing bulbous, cauliflower like, nodes along the tendrils.

Concerning the composition of the as deposited material, the PXRD pattern in **Figure 5.6c** shows that the active material is composed of a Ni-deficient $Ni_{0.15}Sb_{0.85}$ phase and a Ni-rich $Ni_{0.95}Sn_{0.05}$ phase. These phases were the only crystalline phase detected by PXRD and are certainly not the only phases present in the as deposited material. To gain a broader understanding of the composition of the deposited material, SEM X-ray energy dispersive spectroscopy (EDS) was conducted to generate an elemental map of the SnSb@Ni-foam system (**Figure 5.7**). The SEM image in **Figure 5.7a** represents the area at which EDS was taken, where **Figure 5.7b** shows the overlay of the EDS mapping onto the SEM image. **Figure 5.7c** displays the map sum spectrum of the EDS analysis, where the weight percentages of the elements identified by EDS are reported.

In the map sum spectrum, it is clear to see that the as deposited foams were higher in Sb content compared to Sn. Given that the molar masses of Sn and Sb are so similar, we can use the percentages of Sn:Sb to state that the ratio of Sn:Sb is roughly 1:4. The Sn deficiency of the final product likely arises from the fact that the potential applied (-0.95 V vs. Ag/AgCl) was much closer to the reduction potential of Sb compared to Sn.[19] The work of Dr. Ma supports this notion, as he was able to demonstrate that the reduction potential of Sb was more positive during the cathodic scan compared to Sn, versus the reference electrode used in this study.[13]

Although the composition of the as deposited active material was not 1:1, it was decided that the SnSb@Ni-foam was ready for preliminary testing in a 3D Na-ion half-cell. This decision was made due to the conformal coverage of the SnSb active material, as seen in **Figure 5.6a**, and the high theoretical capacities of both Sn and Sb. Master's student Dylan Medina fabricated the as deposited SnSb@Ni-foam into NIBs half-cells in a pouch cell configuration. In this pouch cell configuration, the SnSb@Ni-foam anode is wrapped with poly-prolyene (PP) separator sheet

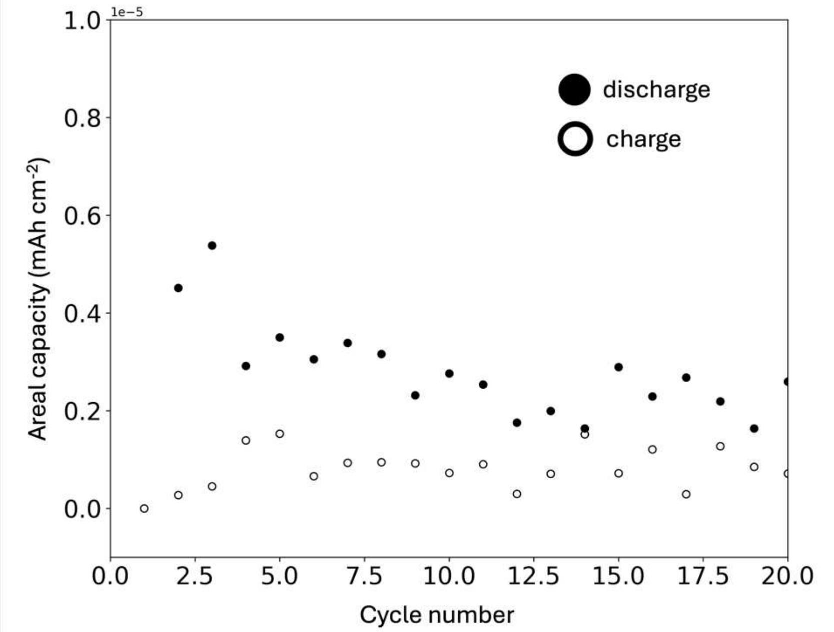

Figure 5.8: Cycle life profile of an Sn_xSb_y@Ni-foam in an Na-ion half-cell cycled at a rate of C/20 over a potential window of 1.5 to 0.1 V vs. Na/Na$^+$.

before being enclosed in a laminate of Na-metal foil which acted as the counter/reference electrode for this system. After the separator and Na-metal were applied to the anode the edges of the pouch cell were sealed, and finally 1.5 mL of 1 M $NaClO_4$ in PC with 5% FEC (by volume) electrolyte was added. The cells were left to rest on the bench top for 24 hours to ensure wetting of every surface in the battery with the electrolyte. **Figure 5.8** displays the cycle life profile of an SnSb@Ni-foam NIBs half-cell cycled at a rate of C/20 and plotted in terms of the areal capacity (mAh cm^{-2}). In the cycle life profile, it is clear to see that the SnSb@Ni-foam NIBs half-cell cycled unstably (large difference between the charge and discharge capacities) with a very small areal capacity (on the order of $0.5x10^{-5}$ mAh cm^{-2}). These data clearly demonstrate that the SnSb@Ni-foam anode is unstable to the conditions present at the electrode during cycling.

5.2.2 Specific research aims

Future worked aimed at understanding the functionality of cPAN as a protective coating for SnSb@Ni-foam anodes is proposed. The fundamental scientific questions leading this investigation are as follows. How do the resistive and mechanical properties of cPAN manifest themselves on 3D SnSb electrodes in NIBs? How does the enhanced interfacial ion transport imparted by cPAN, as seen in the 2D system, affect the charge transfer resistance in an aperiodic foam, due to the likely increase in resistance from the higher surface area of these systems? The main hypotheses for this proposed work are as follows. The mechanical properties of cPAN should improve the cycling stability of the SnSb@Ni-foam system, due to the deep literature understanding of cPAN. The resistive properties of cPAN should initially lead to much higher charge transfer resistance compared to a control, yet as cycling occurs, we would expect cPAN to behave in a similar fashion to what is described in Chapter 3. Experimentally speaking, studies must first be conducted on the efficacy of various coating methods for the cPAN protective layer.

This can be done by a lbl approach, as described by Tolganbek et al., or via spray coating. Once the optimal coating method for PAN is determined, studies into the compositional changes of the SnSb@Ni-foam during the PAN annealing step will be required. After the composition of the SnSb in the ensemble cPAN@SnSb@Ni-foam is determined, the detailed electrochemical investigations can begin.

5.2.2 Experimental Methods

The SnSb deposition solution was comprised of 50mM antimony chloride ($SbCl_3$, Milipore Sigma, ≥99%), 50mM tin chloride dihydrate ($SnCl_2$ $2H_2O$, Milipore Sigma, 98%), 200mM sodium gluconate (Milipore Sigma, ≥99%), and 200mM citric acid (Millipore Sigma, ≥99.5%) were added to 200mL milipore (18 MΩ). This solution was allowed to stir until all constituents of the solution were solubilized (30min-1hr). After the solution was allowed to stir, a titration with 10M KOH was conducted to bring the pH of the solution to 7.4. This titration began with a large aliquot of 17mL KOH, to quickly bring the pH of the solution to roughly 5. The solution was then brought to the desired pH by the dropwise addition of 10M KOH.

After the titration step, the temperature of the solution was brought to 60℃ using a VWR water heater/cooler with a jacketed beaker. Once the solution was at the desired deposition temperature, a nickel foam (Ni-foam) substrate (MTI, 1.6mm T x 300mm W) was prepared as the substrate for the electrodeposition and was massed prior to preparation. The Ni-foam was prepared via sonication in 5M hydrochloric acid (HCl) for 5 minutes, before being rinsed in milipore water (18 MΩ) and absolute ethanol.

After the Ni-foam substrate was prepared, it was introduced to the heated solution as the working electrode and was sandwiched between two stainless-steel mesh counter electrodes (316 stainless steel, Elmhurst, P.O.# AC-75973470). An Ag/AgCl (Pine Research) reference electrode was placed near the edge of the Ni-foam working electrode. A potential of -0.95 V vs. Ag/AgCl was applied to the system for 10s, followed by an OCP rest of 15s. These two steps were repeated 100 times to produce Sn_xSb_y@Ni-foams. It is also important to note that a small stir bar was included in this electrodeposition process and was limited to a range of 30-50 RPM.

The cycling parameters for the initial testing of Sn_xSb_y@Ni-foam anodes were as follows. A C-rate of C/20 (0.0069432 A) was based on the theoretical capacity of Sb, due to the Sb-rich nature of the as formed Sn_xSb_y active material. The potential window used for the cycling experiments was 1.5 to 0.1 V vs. Na/Na^+.

All electrodeposited substrates were characterized via powder X-ray diffraction (Bruker D8 Discover DaVinci, Cu Kα radiation) in the ARC-MMA laboratory. The PXRD patterns were indexed with DRIFFRAC.EVA (Bruker, V5.2) using reference patterns for Ni (PDF 00-001-1266), $Ni_{0.15}Sb_{0.85}$ (PDF 04-003-1523), $Ni_{0.95}Sn_{0.05}$ (PDF 04-002-5573). Scanning electron microscope (JOEL JSM-6500F) images of pre-cycling electrodes were taken in the ARC-ISS.

5.3 References

(1) Schneider, J. D.; Agocs, D. B.; Prieto, A. L. Design of a Sample Transfer Holder to Enable Air-Free X-Ray Photoelectron Spectroscopy. *Chem. Mater.* **2020**, *32* (19), 8091–8096. https://doi.org/10.1021/acs.chemmater.0c01895.

(2) Gimble, N. J.; Prieto, A. L. Spontaneous Solid Electrolyte Interface Formation in Uncycled Sodium Half-Cell Batteries: Using X-Ray Photoelectron Spectroscopy to Explore the Pre-Passivation of Sodium Metal by Fluoroethylene Carbonate before Potentials Are Applied. *Sustain. Energy Fuels* **2022**, *6* (20), 4736–4740. https://doi.org/10.1039/D2SE00888B.

(3) Hobold, G. M.; Khurram, A.; Gallant, B. M. Operando Gas Monitoring of Solid Electrolyte Interphase Reactions on Lithium. *Chem. Mater.* **2020**, *32* (6), 2341–2352. https://doi.org/10.1021/acs.chemmater.9b04550.

(4) Peled, E.; Menkin, S. Review—SEI: Past, Present and Future. *J. Electrochem. Soc.* **2017**, *164* (7), A1703–A1719. https://doi.org/10.1149/2.1441707jes.

(5) Otto, S.-K.; Moryson, Y.; Krauskopf, T.; Peppler, K.; Sann, J.; Janek, J.; Henss, A. In-Depth Characterization of Lithium-Metal Surfaces with XPS and ToF-SIMS: Toward Better Understanding of the Passivation Layer. *Chem. Mater.* **2021**, acs.chemmater.0c03518. https://doi.org/10.1021/acs.chemmater.0c03518.

(6) Gimble, N. J.; Kraynak, L. A.; Schneider, J. D.; Schulze, M. C.; Prieto, A. L. X-Ray Photoelectron Spectroscopy as a Probe for Understanding the Potential-Dependent Impact of Fluoroethylene Carbonate on the Solid Electrolyte Interface Formation in Na/Cu2Sb Batteries. *J. Power Sources* **2021**, *489*. https://doi.org/10.1016/j.jpowsour.2020.229171.

(7) Dopilka, A.; Gu, Y.; Larson, J. M.; Zorba, V.; Kostecki, R. Nano-FTIR Spectroscopy of the Solid Electrolyte Interphase Layer on a Thin-Film Silicon Li-Ion Anode. *ACS Appl. Mater. Interfaces* **2023**, *15* (5), 6755–6767. https://doi.org/10.1021/acsami.2c19484.

(8) Cole, D. A.; Attavar, S.; Zhang, L. Surface Analysis Methods for Contaminant Identification. In *Developments in Surface Contamination and Cleaning*; Elsevier, 2016; pp 333–394. https://doi.org/10.1016/B978-0-323-29960-2.00008-3.

(9) Ma, C.; Xu, F.; Song, T. Dual-Layered Interfacial Evolution of Lithium Metal Anode: SEI Analysis via TOF-SIMS Technology. *ACS Appl. Mater. Interfaces* **2022**, *14* (17), 20197–20207. https://doi.org/10.1021/acsami.2c00842.

(10) Windsor, D.; Nieto, K.; Vishnugopi, B.; Mukherjee, P.; Prieto, A. Performance Metrics and Mechanistic Considerations for the Development of 3D Batteries. *Nat. Rev. Chem.* **2024**, *Accepted*.

(11) Tolganbek, N.; Mentbayeva, A.; Serik, N.; Batyrgali, N.; Naizakarayev, M.; Kanamura, K.; Bakenov, Z. Design and Preparation of Thin Film Gel Polymer Electrolyte for 3D Li-Ion Battery. *J. Power Sources* **2021**, *493*. https://doi.org/10.1016/j.jpowsour.2021.229686.

(12) Ma, J.; Prieto, A. L.; Shores, M.; Finke, R.; Weinberger, C. USING ELECTROCHEMICAL METHODS TO SYNTHESIZE AND UNDERSTAND ENERGY DENSE ANODES FOR LITHIUM-ION AND "BEYOND" BATTERY TECHNOLOGIES, Colorado State University, Fort Collins.

(13) Ma, J.; Prieto, A. L. Electrodeposition of Pure Phase SnSb Exhibiting High Stability as a Sodium-Ion Battery Anode. *Chem. Commun.* **2019**, *55* (48), 6938–6941. https://doi.org/10.1039/c9cc00001a.

(14) He, J.; Wei, Y.; Zhai, T.; Li, H. Antimony-Based Materials as Promising Anodes for Rechargeable Lithium-Ion and Sodium-Ion Batteries. *Mater. Chem. Front.* **2018**, *2* (3), 437–455. https://doi.org/10.1039/c7qm00480j.

(15) Datta, M. K.; Kumta, P. N. Silicon and Carbon Based Composite Anodes for Lithium Ion Batteries. *J. Power Sources* **2006**, *158* (1), 557–563. https://doi.org/10.1016/j.jpowsour.2005.09.016.

(16) Zhang, W.; Sun, M.; Yin, J.; Abou-Hamad, E.; Schwingenschlögl, U.; Costa, P. M. F. J.; Alshareef, H. N. A Cyclized Polyacrylonitrile Anode for Alkali Metal Ion Batteries. *Angew. Chem. - Int. Ed.* **2021**, *60* (3), 1355–1363. https://doi.org/10.1002/anie.202011484.

(17) Shiva, K.; Rajendra, H. B.; Bhattacharyya, A. J. Electrospun SnSb Crystalline Nanoparticles inside Porous Carbon Fibers as a High Stability and Rate Capability Anode for Rechargeable Batteries. *ChemPlusChem* **2015**, *80* (3), 516–521. https://doi.org/10.1002/cplu.201402291.

(18) Nieto, K.; Windsor, D. S.; Kale, A. R.; Gallawa, J. R.; Medina, D. A.; Prieto, A. L. Structural Control of Electrodeposited Sb Anodes through Solution Additives and Their Influence on Electrochemical Performance in Na-Ion Batteries. *J. Phys. Chem. C* **2023**, *127* (26), 12415–12427. https://doi.org/10.1021/acs.jpcc.3c01086.

(19) Bard, J. A.; Faulkner, R. L. *Electrochemical Methods, Fundamentals and Applications*; John Wiley & Sons, Inc: New York City, 2001.

APPENDIX I: Supplementary to Chapter 2

Table A.I.I: Performance metrics from studies investigating full 3D batteries. Literature table summarizing key performance metrics where all components (cathode, anode, and electrolyte) are implemented in the 3D structure. Certain values are not shown in the table as they were either not reported in the study or normalized values were used without providing the necessary information to extrapolate relevant values. The references in the first column relate to the references highlighted in **Chapter 2.7**.

Ref.	Anode	Cathode	Electrolyte	Fabrication	Size/ Application	Capacity (Slower Rates)
[85]	LTO	LFP	$LiAlO_2$-PEO or $Li_{1+x}Al_yGe_{2-y}(PO_4)_3$-PEI	3D printing Electro-phoretic Deposition	Microbattery	450 μAh/cm^2
[3]	Lithiated graphite	MoS_2	Hybrid Polymer Electrolyte Kynar PVDF-2801 With SiO_2	Electroless deposition Electro-deposition Spin Coating	0.2 cm^2 Microbattery	Not reported
[41]	SnN_x	LiV_2O_5	LIPON	ALD	Microbattery	20 μAh cm^{-2} (@ 100 μA cm^{-2})
[26]	NiSn	LMO	1 M LiClO4 EC:DMC 1:1	Electro-deposition of electrodes	Not reported	Not reported
[37]	Si	NCA	SU-8	Silicon dry etching Slurry casting	Microbattery	4.2 mAh cm^{-2} (@ 0.22 mA cm^{-2})
[39]	TiO_2	Li-metal (acting as a reference/ counter electrode)	Li_3PO_4	ALD	Microbattery	300 μAh cm^{-2} (@ C/11)
[84]	LTO	LFP	1M $LiClO_4$ EC/DMC	3D printing	Microbattery	1.5 mAh cm^{-2}
[61]	Li Metal	LFP posts	Ionogel	DIRE etching	Microbattery	1.4 mAh cm^{-2} (@ 50 μA cm^{-2})

[19]	Ni_3Sn_4	LFP/CNT	GPE $(PEI/PAA)_{30}$ 1M $LiPF_6$ EC/EMC/DMC	Anode: electrodeposition Electrolyte: Layer-by-layer Cathode: injection	Not reported	160 mAh g^{-1} (@ C/10)

Table A.I.II: Performance metrics from studies investigating full 3D batteries. Literature table summarizing key performance metrics where all components (cathode, anode, and electrolyte) are implemented in the 3D structure. Certain values are not shown in the table as they were either not reported in the study or normalized values were used without providing the necessary information to extrapolate relevant values. The references in the first column relate to the references highlighted in **Chapter 2.7**.

Ref.	Capacity (Faster Rates)	Voltage Range	Energy Density	Power Density	# of Cycles	Retention
85	115 μAh cm^{-2}	2.2 – 1.0 V	4 mWh cm^{-2} At 4 mW cm^{-2}	Not reported	60	25%
3	Not reported	1.3 V – 2.2 V	10.5 mWh cm^{-1}	Not reported	200	60%
41	11 μAh cm^{-2} (@ 1000 μA cm^{-2})	0.5 – 3.5 V	Not reported	Not reported	100	55%
26	Not reported	2.0 to 4.0 V	15 μWh cm^{-2} μm^{-1}	7.4 mW cm^{-2} μm^{-1}	15	Not Reported
37	2.6 mAh cm^{-2} (@ 1.1 mA/cm^{2})	3.0 to 4.4 V vs. Li/Li^{+}	Not reported	Not reported	40	62%
39	80 μAh cm^{-2} (@ 2C)	1.2 to 2.2 V vs. Li/Li^{+}	Not reported	Not reported	75	25%
84	0.85 mAh cm^{-2} (@ 5C)	1.5 to 2.0 V	Not reported	Not reported	30	56%
61	1.1 mAh cm^{-2} (@ 1000 μA cm^{-2})	2.5 to 4.0 V vs. Li/Li^{+}	3.7 mWh cm^{-2}	@2.8 mW cm^{-2}	80	78.6%
19	120 mAh g^{-1} (@ 1C)	1.3 to 3.6 V	Not reported	Not reported	100	75%

Appendix I.I: Glossary

I.I.I: Lithium concentration gradient

A lithium concentration gradient arises in a battery when the Li-cations, at the electrode-electrolyte interface, are inserted into an electrode. This creates a region of low Li-cation concentration (at the electrode surface) and a region of high Li-cation concertation (in the bulk electrolyte).[96] Concentration gradients can adversely affect the rate performance, SEI formation, and longevity of a lithium-ion battery.

I.I.II: Super capacitor

A super capacitor is an electrochemical storage device that stores charge in the electric-double layer (Edl) and provides for a very quick release of the stored energy (great power density).[97]

I.I.III: Conformal coating

A conformal coating arises when the coating material completely and uniformly covers the material being coated.

I.I.IV: Continuum scale simulations

A continuum scale simulation assumes that the matter which composes a material fills the entire region of space which it occupies. Although materials are composed of discrete atoms and molecules that are separated by empty space, continuum scale simulations describe physical phenomena by considering a substance distributed throughout some region of space.[98]

I.I.V: Monte Carlo Tree Search

Monte Carlo Tree Search is a probabilistic and heuristic based search algorithm that uses tree search techniques and machine learning principles to find optimal decisions in a given domain.[99]

I.I.VI: NASICON

Sodium super ionic conductors (NASICON) are a class of materials with Na-ion conductivities on the order of 10^{-3} S/cm.[100]

I.I.VII: Champion Materials

Champion materials are materials that have been well shown by the literature to have high, and consistent, performance metrics when included in a battery.

I.I.VIII: Self-Standing electrode materials

A self-standing electrode is defined as an electrode that can stand freely without the need for mechanical supports.

I.I.IX: SU-8

SU-8 is an epoxy-based photoresist material that can be modified into a battery electrolyte by gelling the material with a traditional organic liquid electrolyte formulation.[101]

I.I.X: Packaging

For the purposes of this work, the term "packaging" is used to described non-active materials that are required for a battery system to be commercialized.

APPENDIX II: Supplementary to Chapter 3

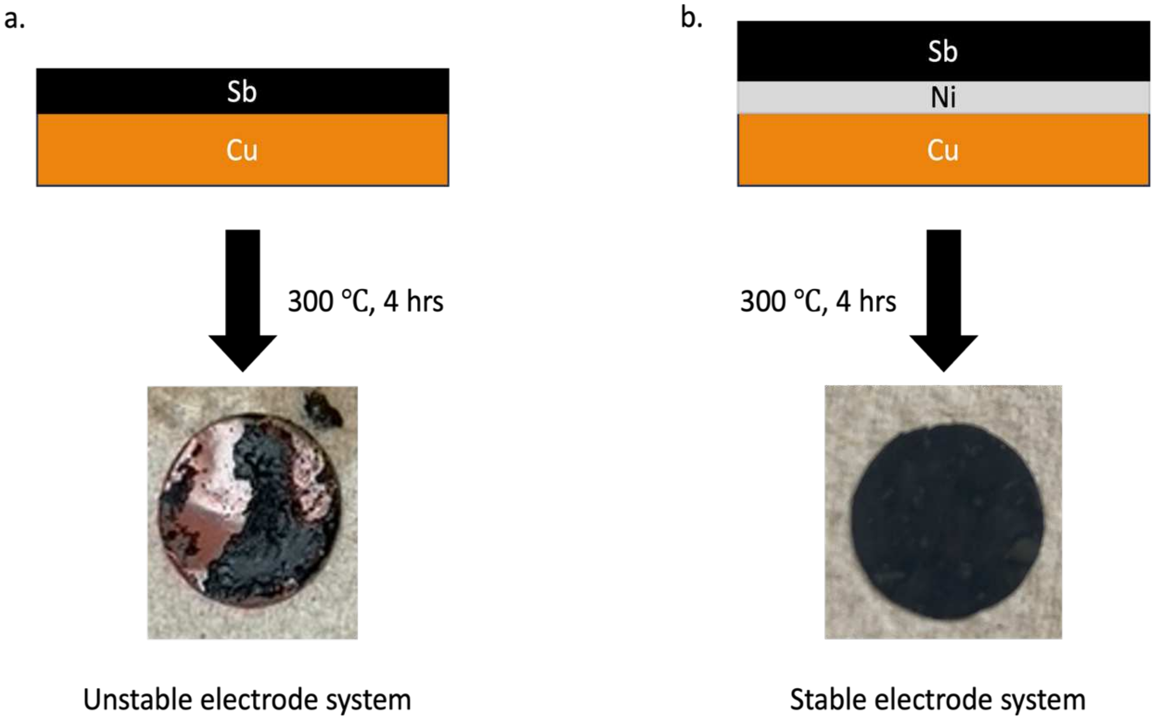

Figure A.II.I: Schematic representation of Sb anode stability after the annealing process. A) An electrodeposited Sb@tCu electrode annealed for 4 hours at 300 °C yielded an unstable electrode system that fractured immediately upon cycling. B) An electrodeposited Sb@Ni@tCu electrode annealed for 4 hours at 300 °C yielded a stable electrode system that did not immediately fracture upon cycling.

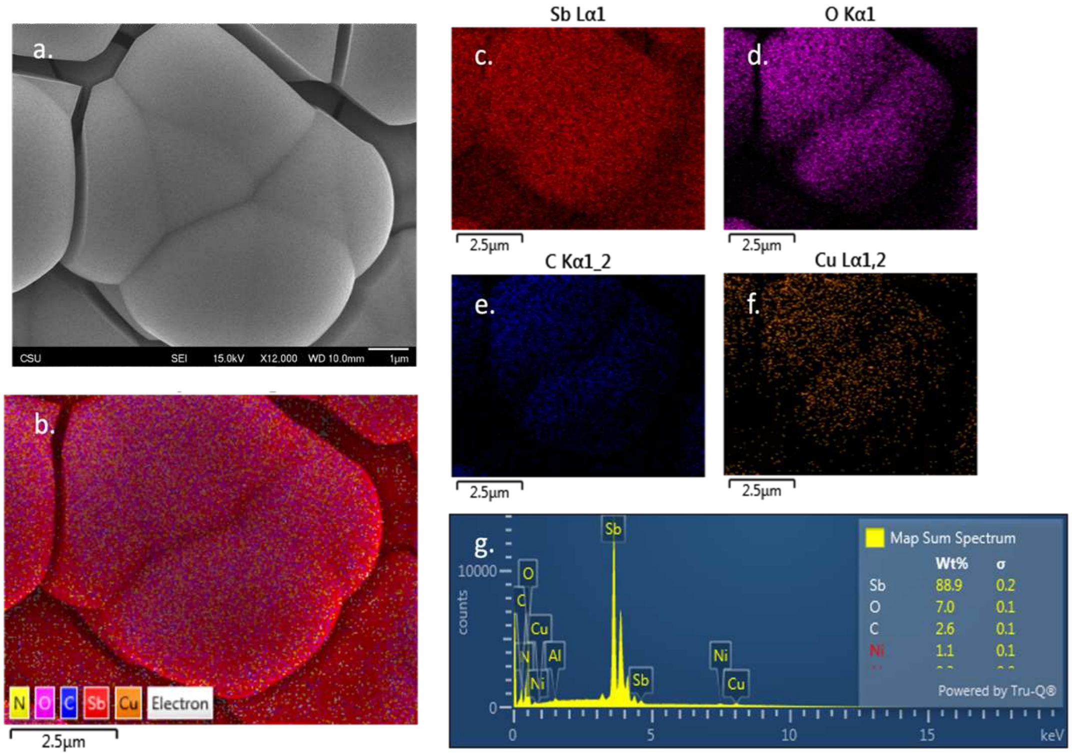

Figure A.II.II: Elemental mapping of pre-annealed an Sb@Ni@tCu electrode. A) SEM image of the pre-annealed Sb active material. B) Overlayed EDS map of the pre-annealed electrode which mostly consists of Sb. C) The Sb component for the elemental map of the anode. D) The O component for the elemental map of the anode, which is on the surface of the Sb structures. E) The C component for the elemental map of the anode. F) The Cu component for the elemental map of the anode. F) EDS spectrum from the elemental analysis which demonstrates that while most of the electrode is made of Sb, there is a small percentage of O that resides on the surface of the particles.

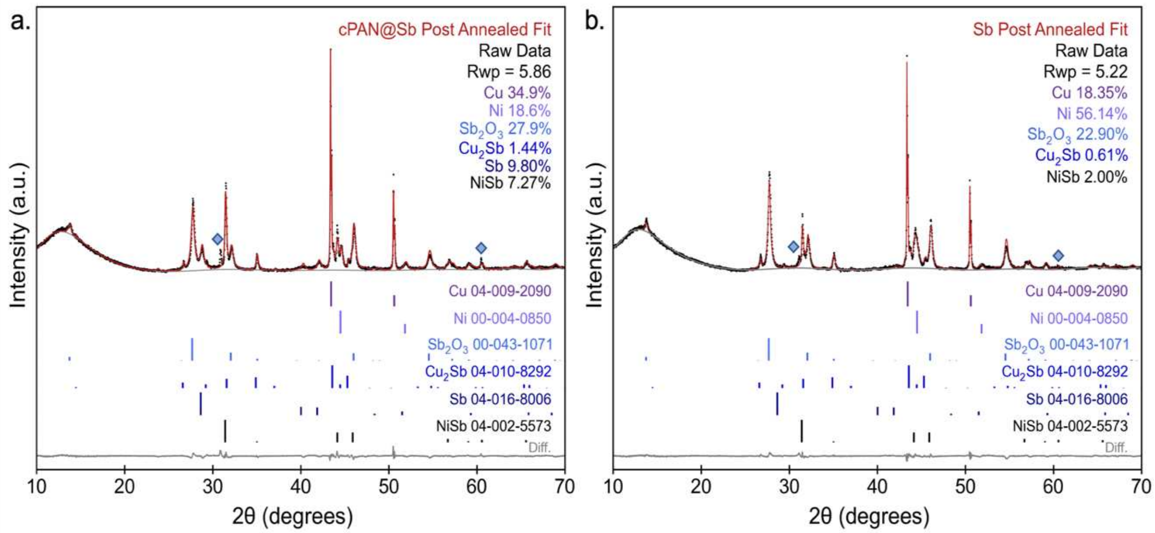

Figure A.II.III: Powder X-ray diffraction (PXRD) quantitative analysis using Rietveld Refinement. A) The Rietveld Refinement of the PXRD pattern from the post-annealed cPAN@Sb system, where the majority of the crystalline phases are comprised of Sb_2O_3. B) The Rietveld Refinement of the PXRD pattern from the post-annealed Sb system, where the majority of the crystalline phases are comprised of Sb_2O_3. The diamonds in both patterns relate to peaks which were unable to be indexed using the reported PDF values. These peaks are hypothesized to relate to Sb-oxide phases of different compositions to the Sb_2O_3 identified phase.

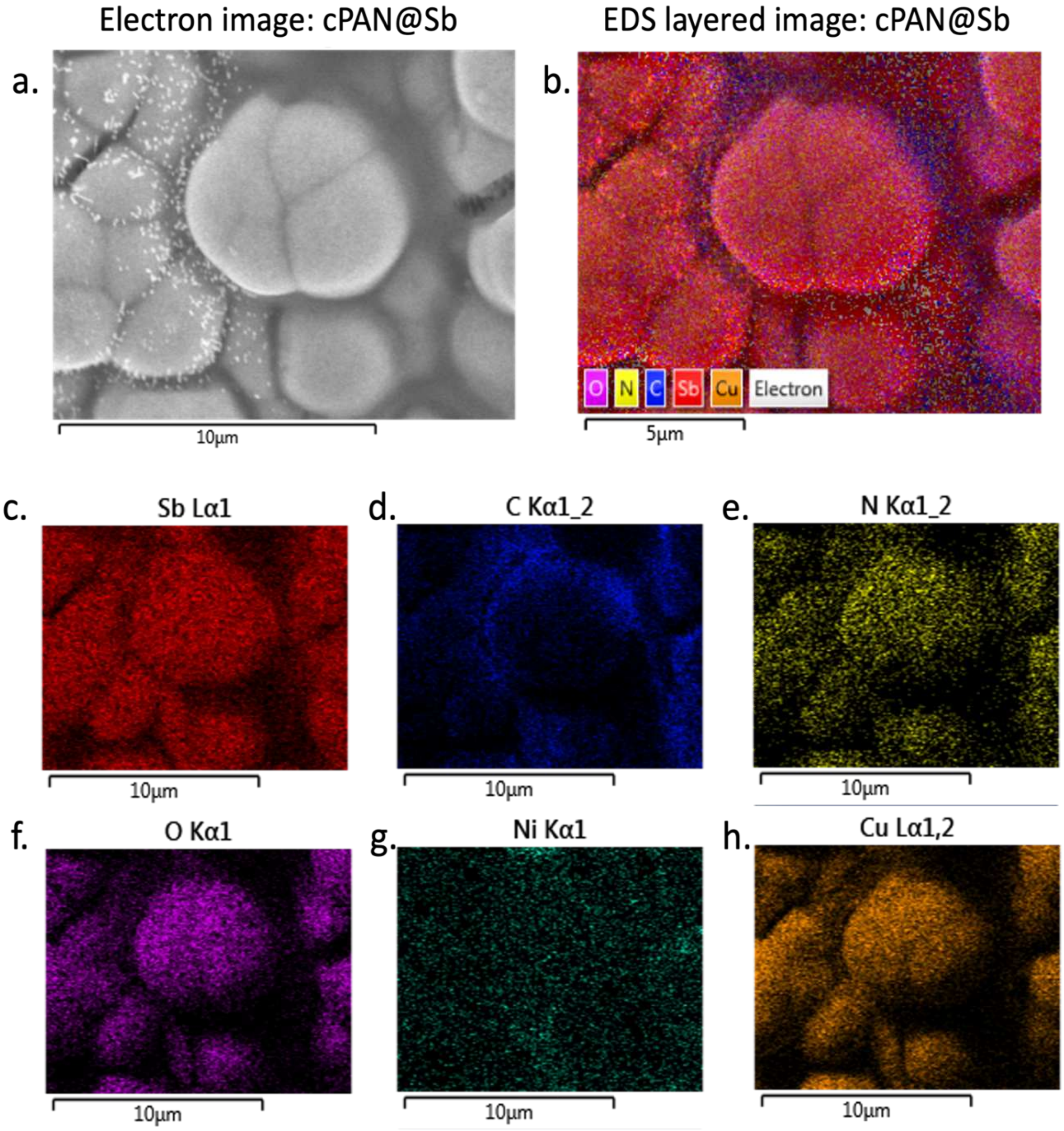

Figure A.II.IV: Energy dispersive X-ray spectroscopy (EDS) elemental mapping of cPAN@Sb anodes prior to battery cycling. A) Electron image of the cPAN@Sb anode system. B) Elemental overlay of electron image with EDS mapping of all identified elements. C) Overlay image of the Sb distribution in the cPAN@Sb anode. D) Overlay image of the C distribution in the cPAN@Sb anode. E) Overlay image of the N distribution in the cPAN@Sb anode. F) Overlay image of the O distribution in the cPAN@Sb anode. G) Overlay image of the Ni distribution in the cPAN@Sb anode. H) Overlay image of the Cu distribution in the cPAN@Sb anode.

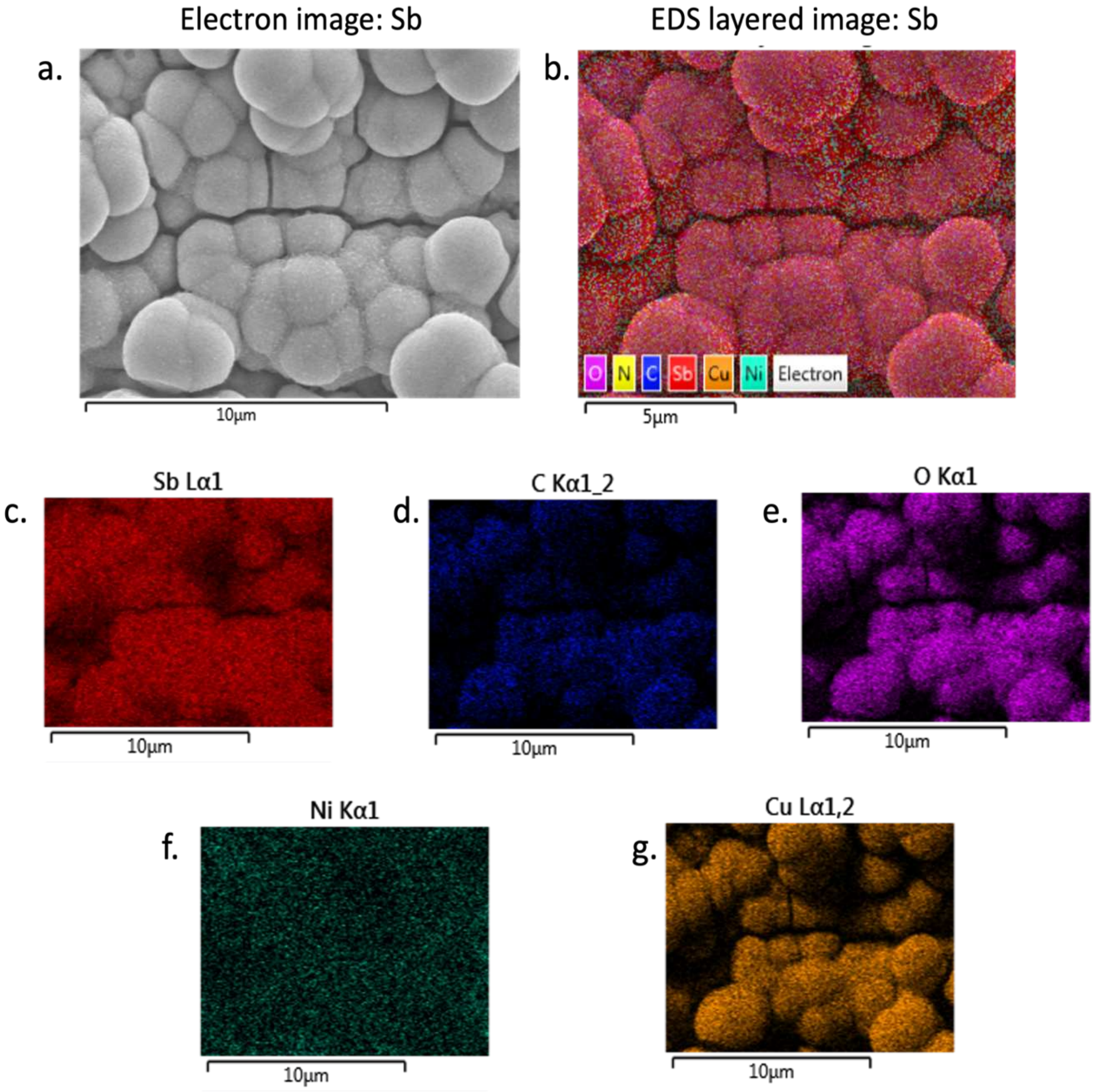

Figure A.II.V: Energy dispersive X-ray spectroscopy (EDS) elemental mapping of Sb anodes prior to battery cycling. A) Electron image of the Sb anode system. B) Elemental overlay of electron image with EDS mapping of all identified elements. C) Overlay image of the Sb distribution in the Sb anode. D) Overlay image of the C distribution in the Sb anode. E) Overlay image of the O distribution in the Sb anode. F) Overlay image of the Ni distribution in the Sb anode. G) Overlay image of the Cu distribution in the Sb anode.

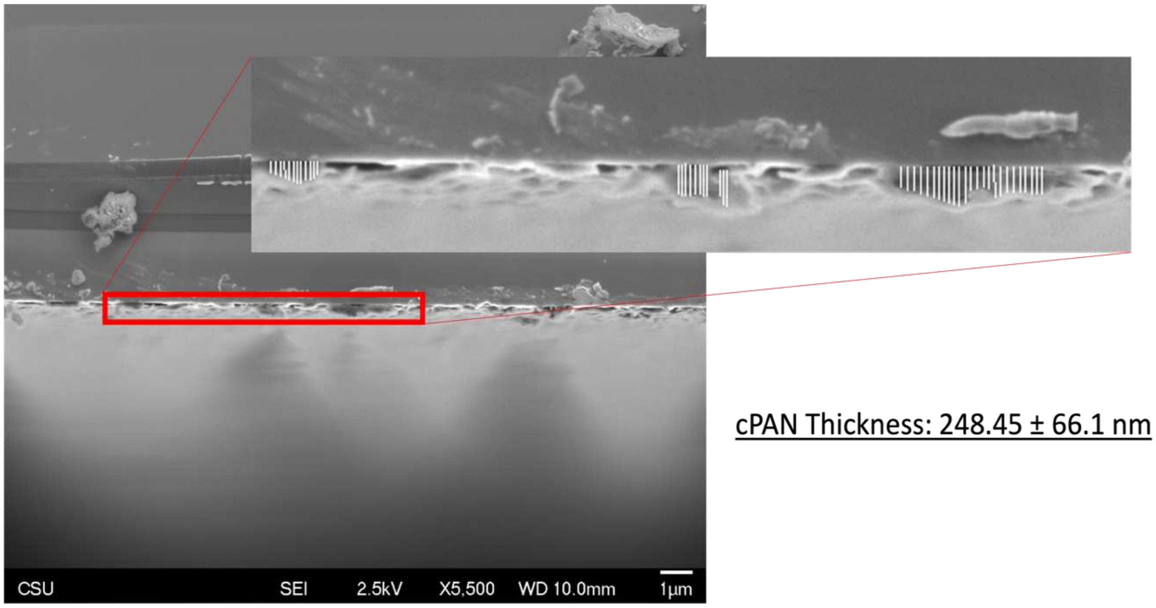

Figure A.II.VI: Cross-sectional SEM of a cPAN@Si-wafer at 2.5kV accelerating voltage. The PAN solution was spin-coated onto the Si-substrate at 0.5mL/min with spinning parameters of 2000 RPM (30s) followed by 8000 RPM (10s). The PAN@Si system was then annealed in a tube furnace at 300°C for 4 hours. The thickness of the cPAN was measured with ImageJ, the red box and the inset image represent where the measurements were taken.

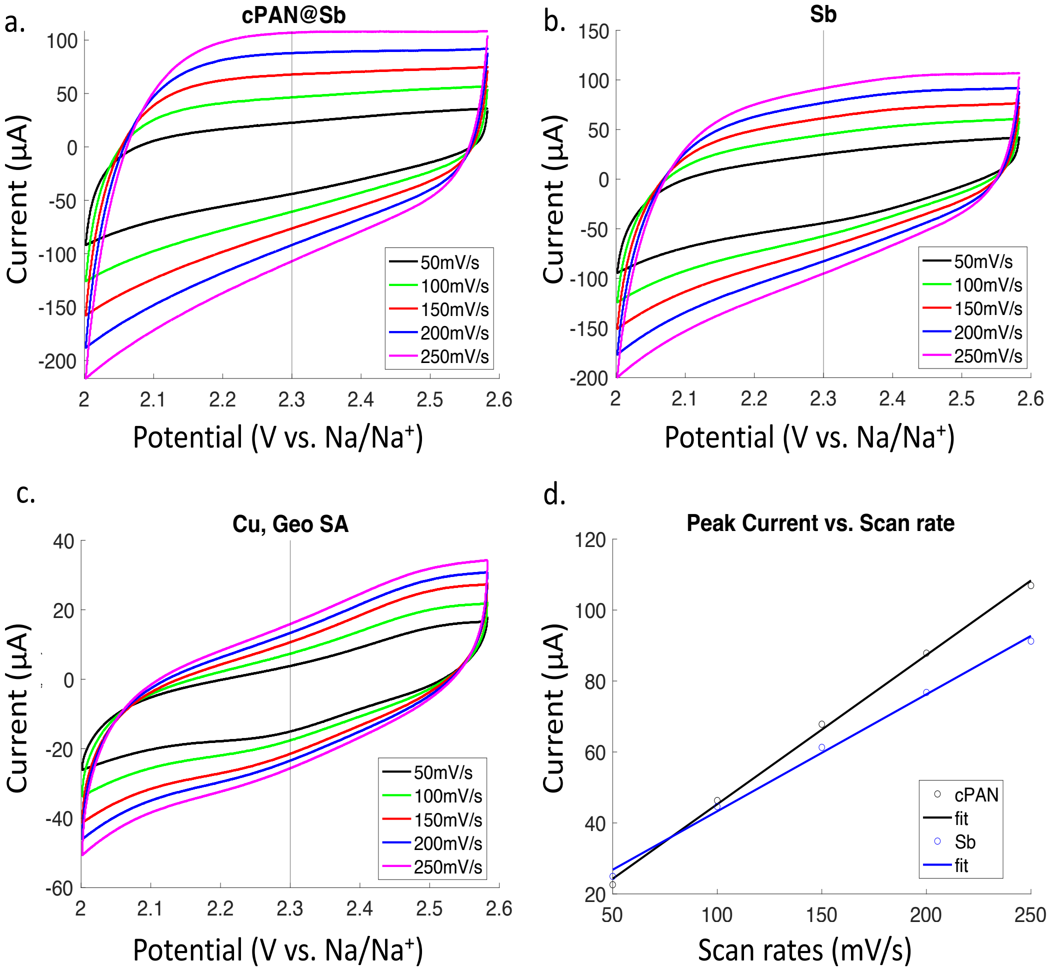

Figure A.II.VII: Electrochemical surface area (ECSA) calculations through variable rate (50 mV/s, 100 mV/s, 150 mV/s, 200 mV/s, and 250 mV/s) cyclic voltammetry over a potential window of 2.6 to 2.0 V vs. Na/Na+. A) Displays the CVs at different scan rates for a cPAN@Sb-based electrode in a three-electrode Swagelok-cell. B) Displays the CVs at different scan rates for an Sb-based electrode in a three-electrode Swagelk-cell. C) Displays the CVs at different scan rates for a copper electrode in a three-electrode Swagelok-cell, acting as a geometric reference for the subsequent analysis. D) Displays the peak currents, selected at 2.3 V vs. Na/Na+ for each CV plotted as a function of scan rate.

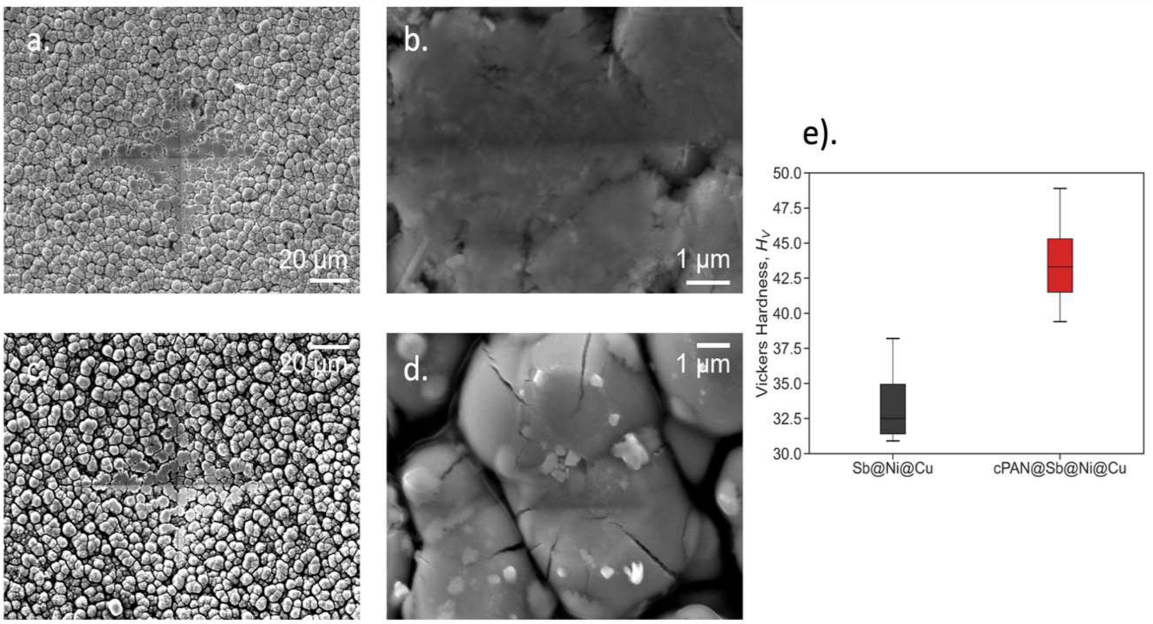

Figure A.II.VIII: Vickers hardness testing with a diamond indenter of cPAN@Sb and Sb systems. A). Representative SEM image of a Vickers diamond indent on the Sb system. B). High-magnification representative SEM image of a Vickers diamond indent on the Sb system demonstrating pulverized grains. C). Representative SEM image of a Vickers diamond indent on the cPAN@Sb system. D). High-magnification representative SEM image of a Vickers diamond indent on the cPAN@Sb system demonstrating cracked, intact, Sb grains. E). Box and whisker plot of Vickers hardness obtained from 25 indents on the cPAN@Sb and Sb samples.

a.

System	Chi-Sqr	Sum-Sqr	Rsol(+)	Rsol(Error%)	Rct(+)	Rct(Error%)	Wc-T(+)	Wc-T(Error%)	Wc-P(+)	Wc-P(Error%)	CPE1-T(+)	CPE1-T(Error%)	CPE1-P(+)	CPE1-P(Error%)
cPAN@Sb	0.00020463	0.023328	12.43	1.1214	375.6	0.66938	0.00019493	0.62792	0.94588	0.2833	2.51E-05	2.6314	0.6665	0.42119
Sb	0.00029166	0.033249	15.26	0.91415	227.4	1.0232	0.00023235	0.9499	0.94529	0.364	4.35E-05	3.7598	0.67898	0.62019

b.

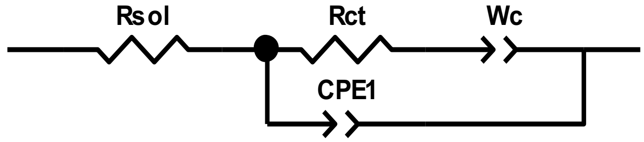

Figure A.II.IX: Equivalent circuit model values from the EIS analysis of pristine cPAN@Sb and Sb system. A) Displays the tabulated values from the equivalent circuit fitting. B). Schematic representation of the Modified Rundles circuit used for the fitting of the EIS spectra.

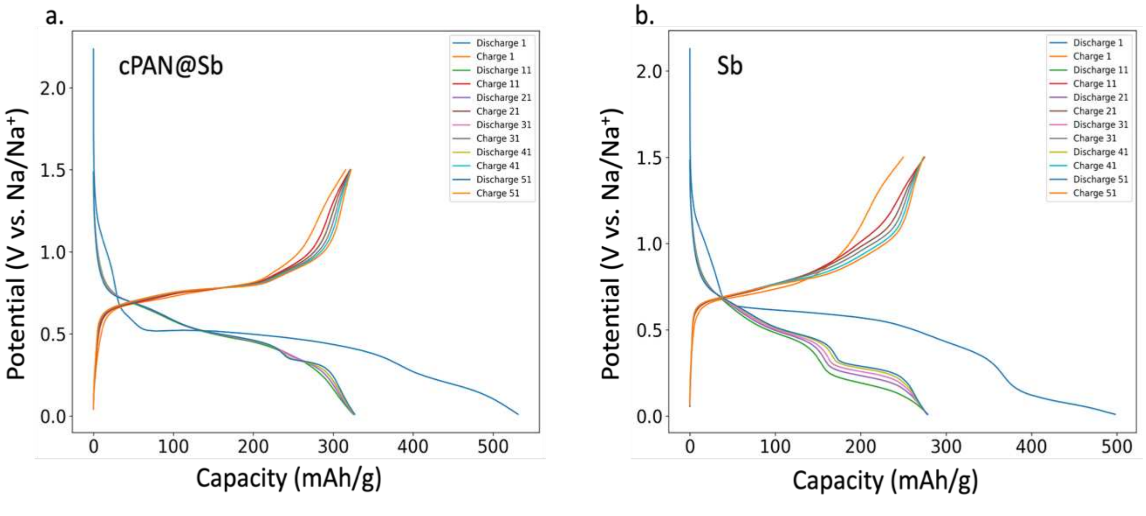

Figure A.II.X: Voltage-capacity profiles of the cPAN@Sb and Sb anode systems. A) Voltage profile of the cPAN@Sb system plotted from cycle 1 to 51 in increments of 10. B) Voltage profile of the Sb system plotted from cycle 1 to 51 in increments of 10.

Methodology for quantitative electrochemical impedance spectroscopy (EIS) analysis using equivalent circuit models (ECMs).

The EIS data were analyzed quantitatively through the fitting of the raw data to an ECM. The ECM utilized in this investigation was a modified Randles Circuit. For the ECM analysis of the pristine cPAN@Sb and Sb electrodes, the modified Randles Circuit displayed in **Figure A.II.IX** was used. The decision to use a CPE instead of a capacitor, to model the electric double-layer (Edl) capacitance, was made to account for inhomogeneous charging of the Edl. This ECM replaced the standard Warburg element with a CPE, as has been seen in previous investigations conducting EIS with ECM fitting for Sb electrodes.[1,2] To aide in the fitting process, the alpha parameter for the CPE_{Wc} was locked to 0.5 for the initial fitting to avoid local minima in the solution of the ECM. After the initial fitting, the alpha parameter was unlocked to aid in the overall fit.

Concerning the EIS analysis seen in **Figure 3.4** of the main text, an SEI component was added to the modified Randles Circuit (**Figure A.II.IX**) to account for the 10 cycles each electrode had undergone prior to the EIS analysis. The SEI component is comprised of a resistor and capacitor in parallel, between the Rsol component and the rest of the Randles Circuit. To aide in the fitting process, the alpha parameter for the $\mathrm{CPE_{Wc}}$ was locked to 0.5 for the initial fitting to avoid local minima in the solution of the ECM. After the initial fitting, the alpha parameter was unlocked to aid in the overall fit. All the ECM fits reported display unlocked values as to maximize the amount of error reported by the software. For the purposes of this investigation, components

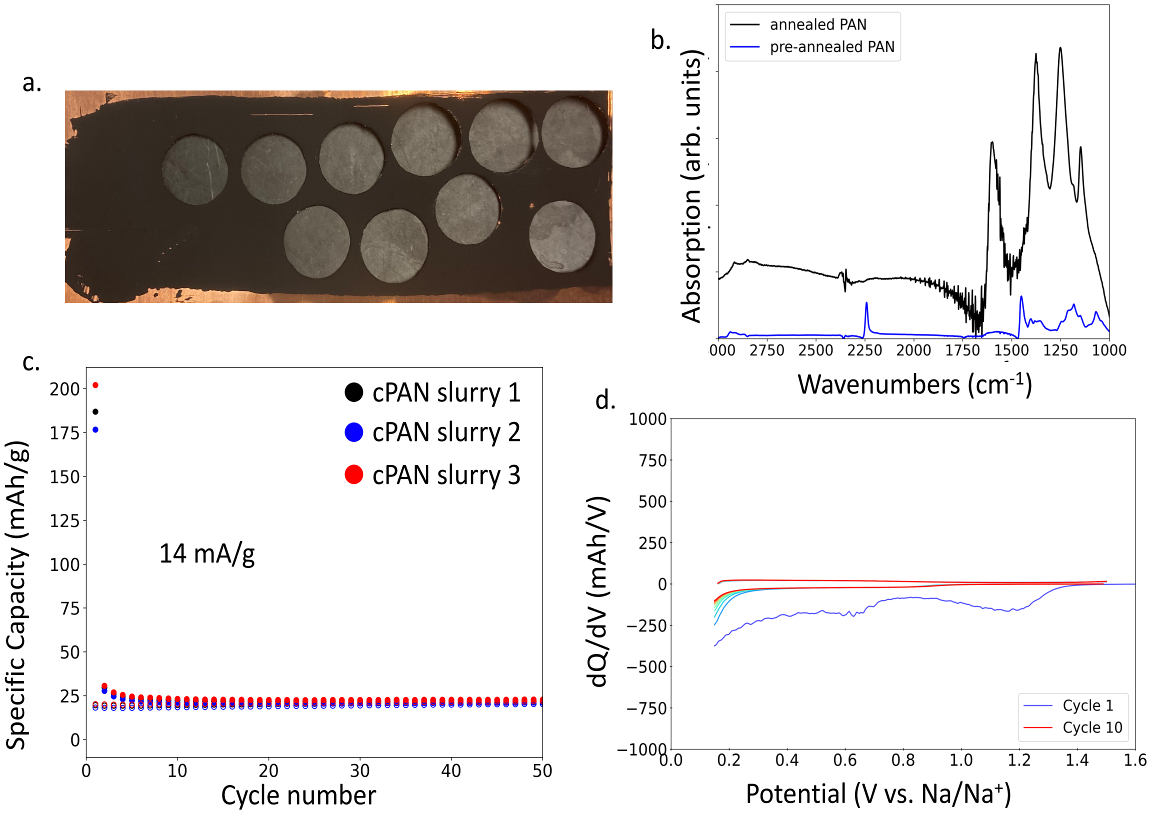

Figure A.II.XI: Physical and electrochemical characterization of a cPAN slurry cast electrode. A) Represents and image of the slurry cast PAN electrode prior to annealing. B) FTIR spectra of a PAN slurry prior to annealing (blue) and a PAN slurry after annealing (black) for 4 hours at 300°C in a tube furnace under flowing argon. C) Cycle life plot of three cPAN slurry electrodes in NIBs half-cells over a potential window of 0.15 to 1.5 V vs. Na/Na$^+$, cycled at a rate of 14 mA/g. D) Differential capacity plot of a single cPAN slurry electrode in a NIB half-cell, with the offset from zero indicating Na-ion storage over the entire potential window.

with greater than 10% error after the conclusion of the fitting were determined to be invalid, and subsequently required the use of another component or a re-fit.

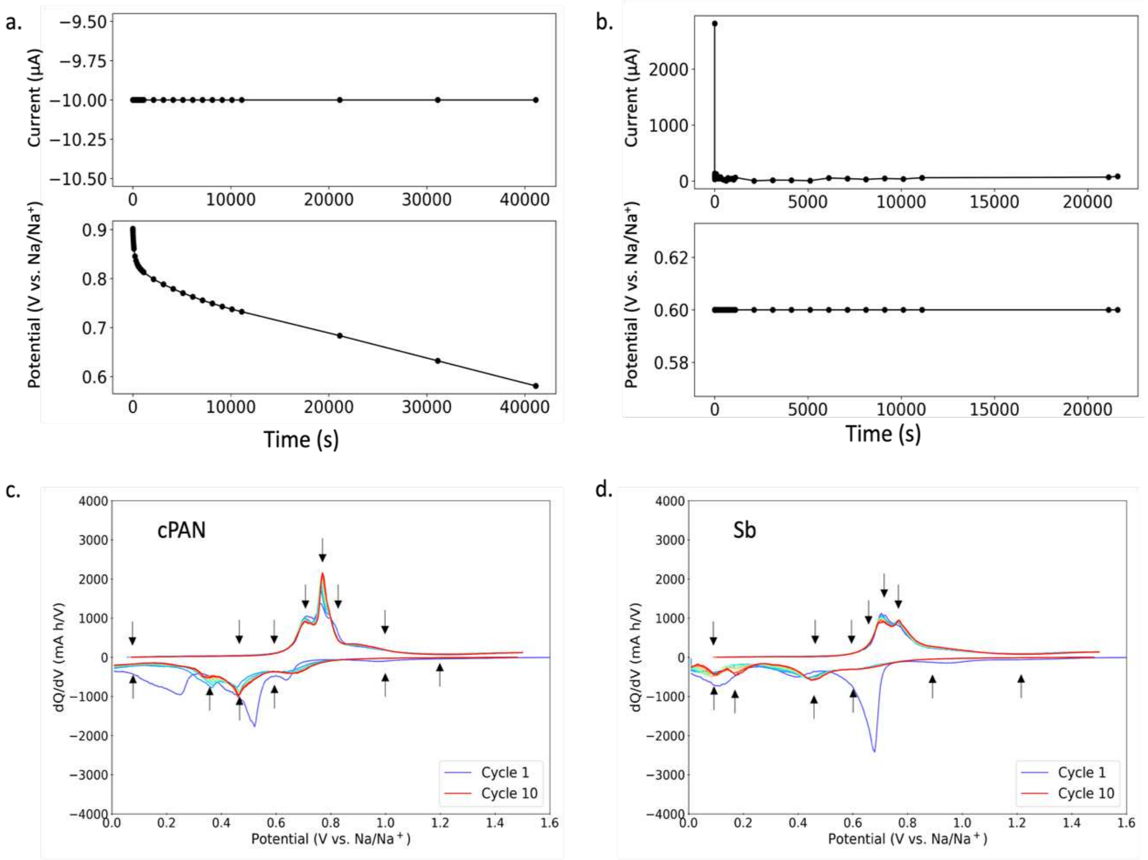

Figure A.II.XII: Constant-Current Constant-Voltage (CCCV) polarization for potential dependent EIS analysis. A) The constant current polarization of the cPAN@Sb electrode from 900 mV vs. Na/Na$^+$ to 600 mV vs. Na/Na$^+$ at a current of -10 μA. B) The constant voltage polarization of the cPAN@Sb electrode at 600 mV vs. Na/Na$^+$. C) The dQ/dV plot for the cPAN system for the 10-cycle formation period with arrows indicating the potentials at which the EIS spectra were taken. D) The dQ/dV plot for the Sb system for the 10-cycle formation period with arrows indicating the potentials at which the EIS spectra were taken.

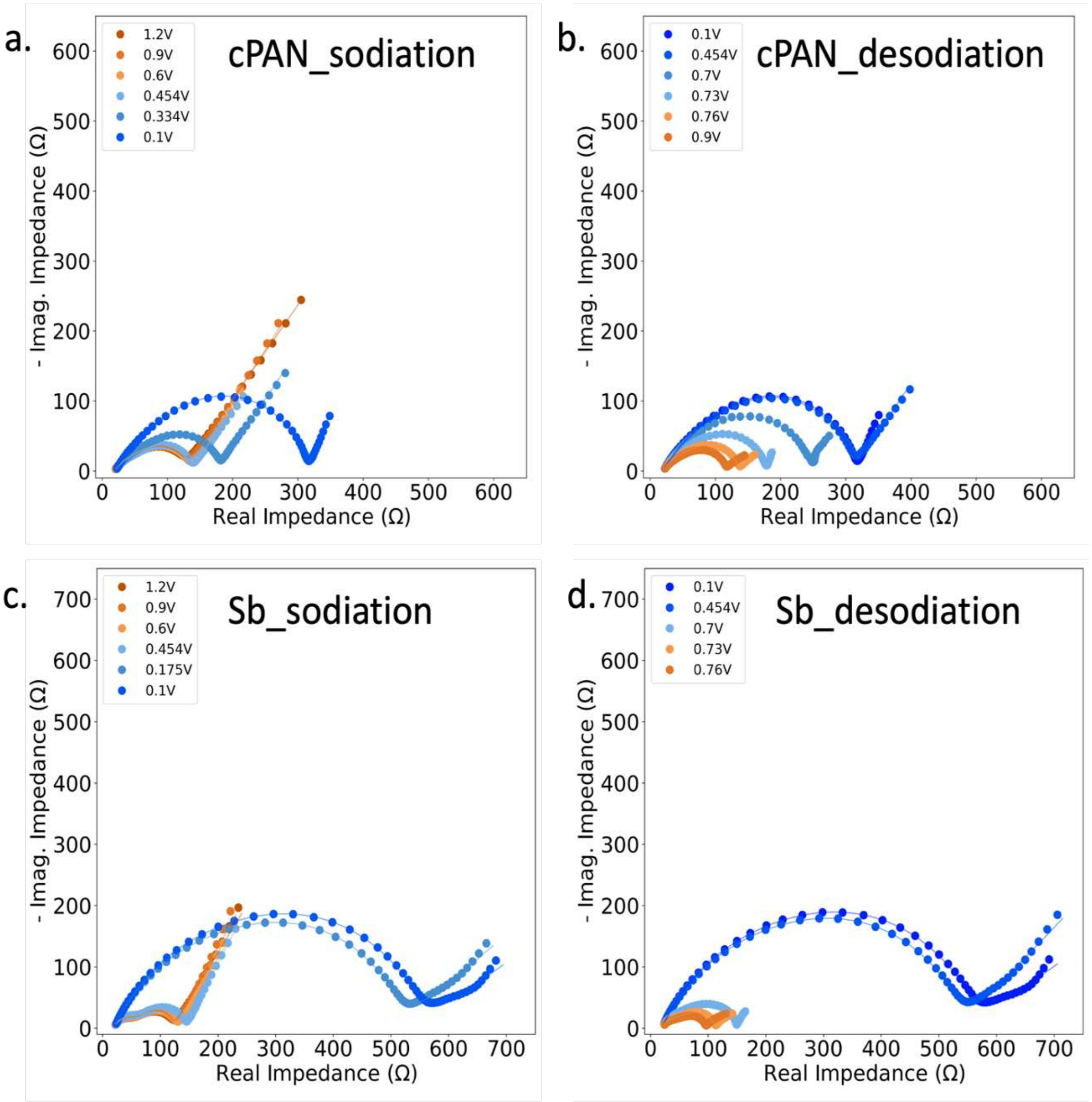

Figure A.II.XIII: Nyquist plots of the fitted EIS spectra from the CCCV+EIS analysis for the cPAN@Sb and Sb systems. A) The fitted EIS spectra for the sodiation sweep for the cPAN@Sb system. B) The fitted EIS spectra for the desodiation sweep for the cPAN@Sb system. C) The fitted EIS spectra for the sodiation sweep for the Sb system. D) The fitted EIS spectra for the desodiation sweep for the Sb system.

Table A.II.I: Equivalent Circuit Model values from CCCV+EIS analysis of a cPAN@Sb electrode after a 10-cycle formation period using a modified Randles Circuit.

Potential (mV vs. Na/Na$^+$)	Chi-Sqr	Sum-Sqr	R1(+)	R1(Error%)	Rsei(+)	Rsei(Error%)	Csei(+)	Csei(Error%)	R2(+)	R2(Error%)	Wc-T(+)	Wc-T(Error%)	Wc-P(+)	Wc-P(Error%)	CPE1-T(+)	CPE1-T(Error%)	CPE1-P(+)	CPE1-P(Error%)
Desodiation																		
900	4.77E-05	0.0053445	20.73	0.79436	19.54	6.1008	2.2986E-05	6.8555	50.01	3.8304	0.046377	3.2102	0.33483	4.7824	5.8697E-05	9.9639	0.62293	1.5212
760	2.45E-05	0.002749	20.8	0.51361	32.87	3.1199	1.5749E-05	3.4257	61.81	2.336	0.031922	1.3718	0.43603	2.044	5.4218E-05	5.6599	0.62785	0.86897
730	3.10E-05	0.0034702	20.8	0.51885	37.72	3.4979	1.5199E-05	3.7211	78.62	2.2101	0.034787	1.663	0.50647	2.3516	5.0765E-05	4.8602	0.63148	0.75456
700	1.01E-04	0.011363	20.9	0.79837	49.33	5.819	1.3594E-05	6.2562	110.1	3.0249	0.042513	3.3566	0.78689	3.4319	3.9573E-05	6.2972	0.65124	0.96238
600	6.06E-05	0.0067833	21.04	0.56816	75.22	4.2227	1.2155E-05	4.3765	154.6	2.4217	0.023334	2.0906	0.74364	2.2905	3.6774E-05	4.2032	0.65802	0.6375
454	1.51E-05	0.0016903	21.09	0.28428	119.9	1.8384	9.8571E-06	1.8515	173.9	1.5937	0.0092477	0.6528	0.61317	0.84883	3.7128E-05	2.0893	0.65713	0.31983
100	9.28E-06	0.0010392	20.66	0.20834	122.3	1.3482	1.0259E-05	1.3573	177.3	1.0987	0.016587	0.73582	0.77178	0.78905	3.7065E-05	1.5185	0.66384	0.23087
Sodiation																		
100	8.76E-06	0.00098112	20.61	0.20161	121.7	1.3194	1.0315E-05	1.3286	176.8	1.0719	0.016868	0.72403	0.77094	0.77703	3.6844E-05	1.4742	0.66494	0.22378
343	2.16E-05	0.0024168	20.56	0.40857	66.55	2.0786	1.4406E-05	2.5358	90.43	1.9382	0.0074495	0.39298	0.60261	0.50314	3.8434E-05	3.9983	0.65696	0.59562
454	7.99E-06	0.00089542	20.39	0.26349	45.36	1.4132	1.9372E-05	1.6729	70.77	1.1943	0.0097535	0.24568	0.5879	0.32664	5.3964E-05	2.8121	0.63526	0.43266
600	3.41E-05	0.0038204	19.29	0.52514	35.31	3.6517	2.6013E-05	3.8454	81.96	2.1836	0.0093566	0.51626	0.59511	0.70879	0.00008002	4.5687	0.60481	0.75563
900	1.60E-05	0.0017888	19.27	0.35539	37.93	2.4161	2.7031E-05	2.6838	74.91	1.7182	0.0051428	0.22567	0.61318	0.30197	7.4587E-05	3.5911	0.61752	0.57592
1200	1.82E-05	0.0020385	18.49	0.3866	37.1	2.5898	2.7364E-05	2.9572	71.3	1.9376	0.0043491	0.21895	0.5936	0.29789	7.2084E-05	4.055	0.62299	0.64043

Table A.II.II: Equivalent Circuit Model values from CCCV+EIS analysis of an Sb electrode after a 10-cycle formation period using a modified Randels Circuit.

Potential (mV vs. Na/Na$^+$)	Chi-Sqr	Sum-Sqr	R1(+)	R1(Error%)	Rsei(+)	Rsei(Error%)	Csei(+)	Csei(Error%)	R2(+)	R2(Error%)	Wc-T(+)	Wc-T(Error%)	Wc-P(+)	Wc-P(Error%)	CPE1-T(+)	CPE1-T(Error%)	CPE1-P(+)	CPE1-P(Error%)
Desodiation																		
900mV_desoda	N/A	N/A	N/A	N/A	N/A	N/A	N/A	N/A	N/A	N/A	N/A	N/A	N/A	N/A	N/A	N/A	N/A	N/A
760mV_desoda	4.73E-05	5.30E-03	19.050	1.577	25.580	3.622	1.28E-05	4.794	48.000	3.049	2.714E-02	1.208	0.404	1.921	2.892E-05	13.063	0.624	1.947
730mV_desoda	4.67E-05	5.23E-03	18.840	1.403	31.290	3.712	1.06E-05	4.604	60.590	2.758	3.024E-02	1.432	0.450	2.148	2.786E-05	10.410	0.624	1.549
700mV_desoda	1.66E-04	1.86E-02	18.650	2.020	38.370	7.843	9.12E-06	8.864	93.320	3.934	3.645E-02	3.298	0.673	3.738	2.258E-05	11.632	0.637	1.715
600mV_desoda	N/A	N/A	N/A	N/A	N/A	N/A	N/A	N/A	N/A	N/A	N/A	N/A	N/A	N/A	N/A	N/A	N/A	N/A
454mV_desoda	1.07E-05	1.20E-03	20.1900	0.293	111.800	4.027	7.21E-06	4.107	408.300	1.317	5.041E-03	0.581	0.503	0.841	7.919E-06	1.284	0.722	0.169
100mV_desoda	1.80E-05	2.01E-03	20.1300	0.381	123.500	5.375	6.55E-06	5.552	414.000	2.041	6.588E-03	1.375	0.386	2.108	7.602E-06	1.699	0.726	0.223
Sodiation																		
100mV_soda	1.59E-05	1.78E-03	20.0100	0.359	122.000	5.058	6.60E-06	5.252	407.600	1.918	6.719E-03	1.282	0.388	1.968	7.569E-06	1.597	0.727	0.209
175mV_soda	1.39E-05	1.56E-03	19.8400	0.347	131.100	3.801	6.33E-06	4.131	363.900	1.688	5.817E-03	0.830	0.435	1.261	8.149E-06	1.513	0.721	0.204
454mV_soda	5.31E-05	5.94E-03	18.1900	1.273	57.710	1.294	1.35E-05	2.352	65.800	1.510	7.375E-03	0.487	0.678	0.501	1.416E-05	7.870	0.674	1.106
600mV_soda	7.67E-05	8.59E-03	17.5000	1.649	49.090	1.707	1.57E-05	3.047	60.390	1.919	8.260E-03	0.597	0.636	0.657	1.688E-05	10.097	0.662	1.450
900mV_soda	1.23E-04	1.38E-02	16.5900	2.274	46.690	2.370	1.82E-05	4.073	61.570	2.547	6.346E-03	0.643	0.668	0.666	2.339E-05	12.827	0.635	1.929
1200mV_soda	1.20E-04	1.34E-02	16.3200	2.314	43.700	2.478	1.93E-05	4.229	60.700	2.586	5.989E-03	0.610	0.634	0.667	2.487E-05	12.929	0.630	1.959

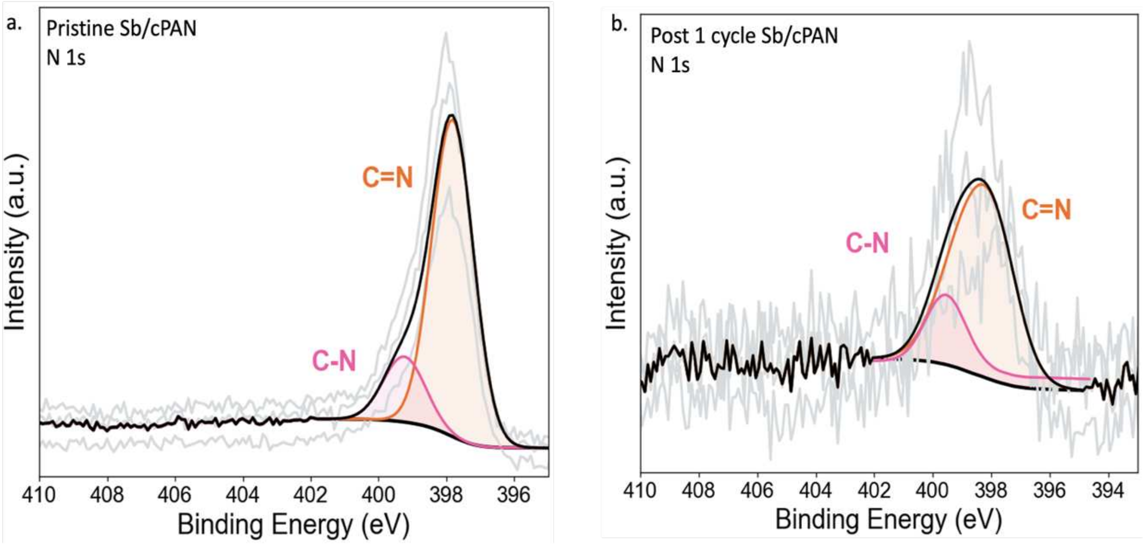

Figure A.II.XIV: X-ray photoelectron analysis of nitrogen 1s environments for the cPAN@Sb system. A) The N1s spectrum for the pristine cPAN@Sb system showing C-N and C=N environments. B) The N1s spectrum for the cPAN@Sb system after the 1st discharge half-cycle showing C-N and C=N environments.

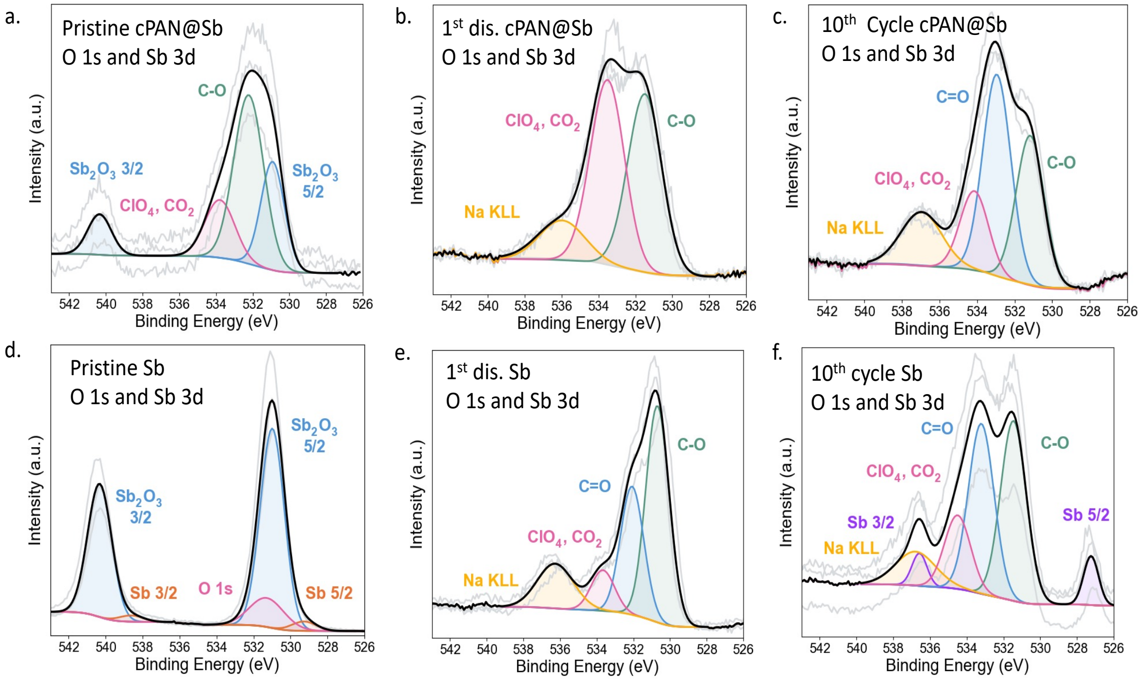

Figure A.II.XV: X-ray photoelectron spectroscopy of the combined O1s and Sb3d environments for the cPAN@Sb and Sb systems. A) The combined O1s and Sb3d environments for the pristine cPAN@Sb electrode. B) The combined O1s and Sb3d environments for the cPAN@Sb after the 1st discharge half cycle. C) The combined O1s and Sb3d environments for the cPAN@Sb after the 10th cycle. D) The combined O1s and Sb3d environments for the pristine Sb electrode. E) The combined O1s and Sb3d environments for the Sb after the 1st discharge half cycle. F) The combined O1s and Sb3d environments for the Sb after the 10th cycle.

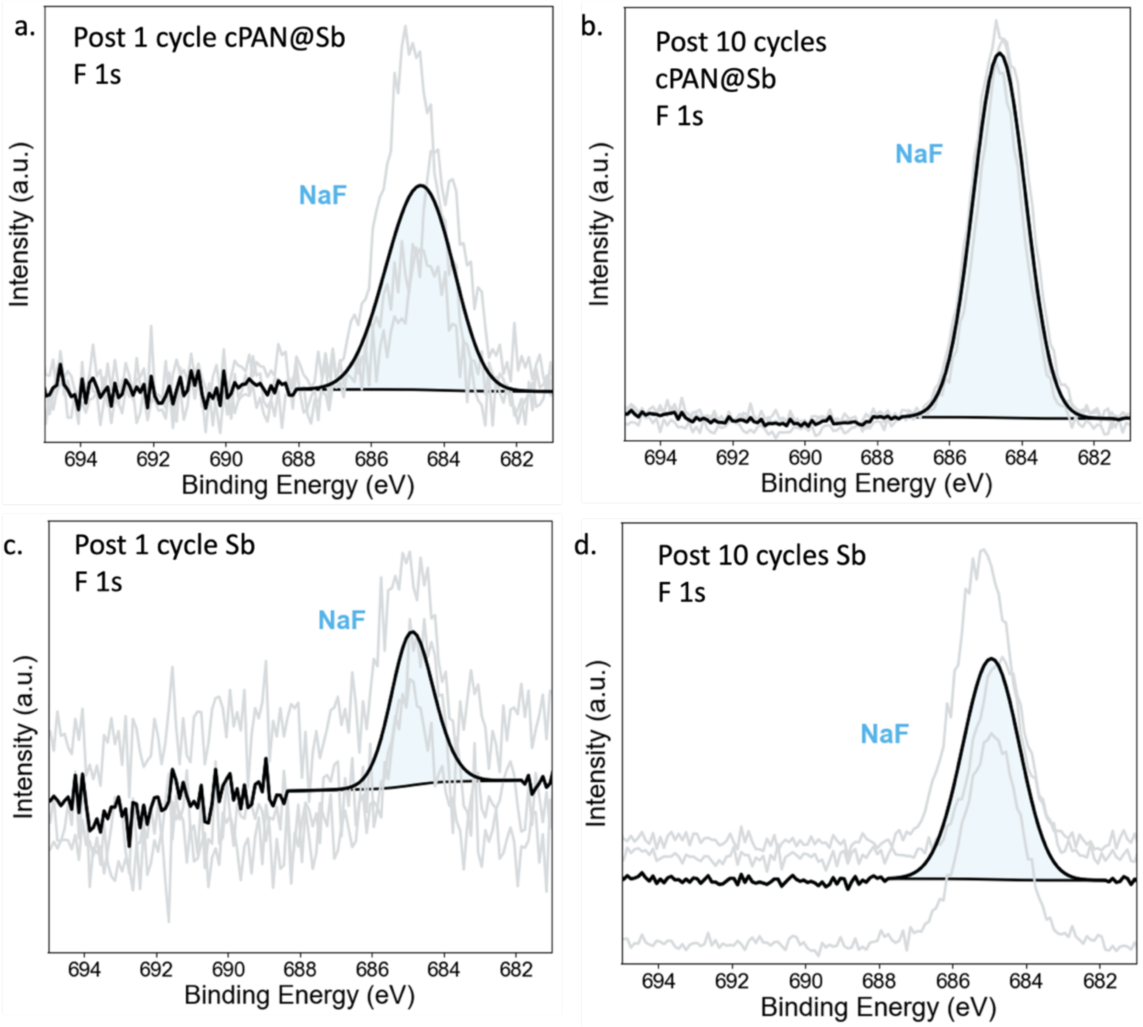

Figure A.II.XVI: X-ray photoelectron spectroscopy for the fluorine 1s environments for the cPAN@Sb and Sb systems. A) The F1s spectrum for the cPAN@Sb system after the 1st discharge half-cycle showing environments which result from the presence of NaF. B) The F1s spectrum for the cPAN@Sb system after the 10th cycle showing environments which result from the presence of NaF. C) The F1s spectrum for the Sb system after the 1st discharge half-cycle showing environments which result from the presence of NaF. D) The F1s spectrum for the Sb system after the 10th cycle showing environments which result from the presence of NaF.

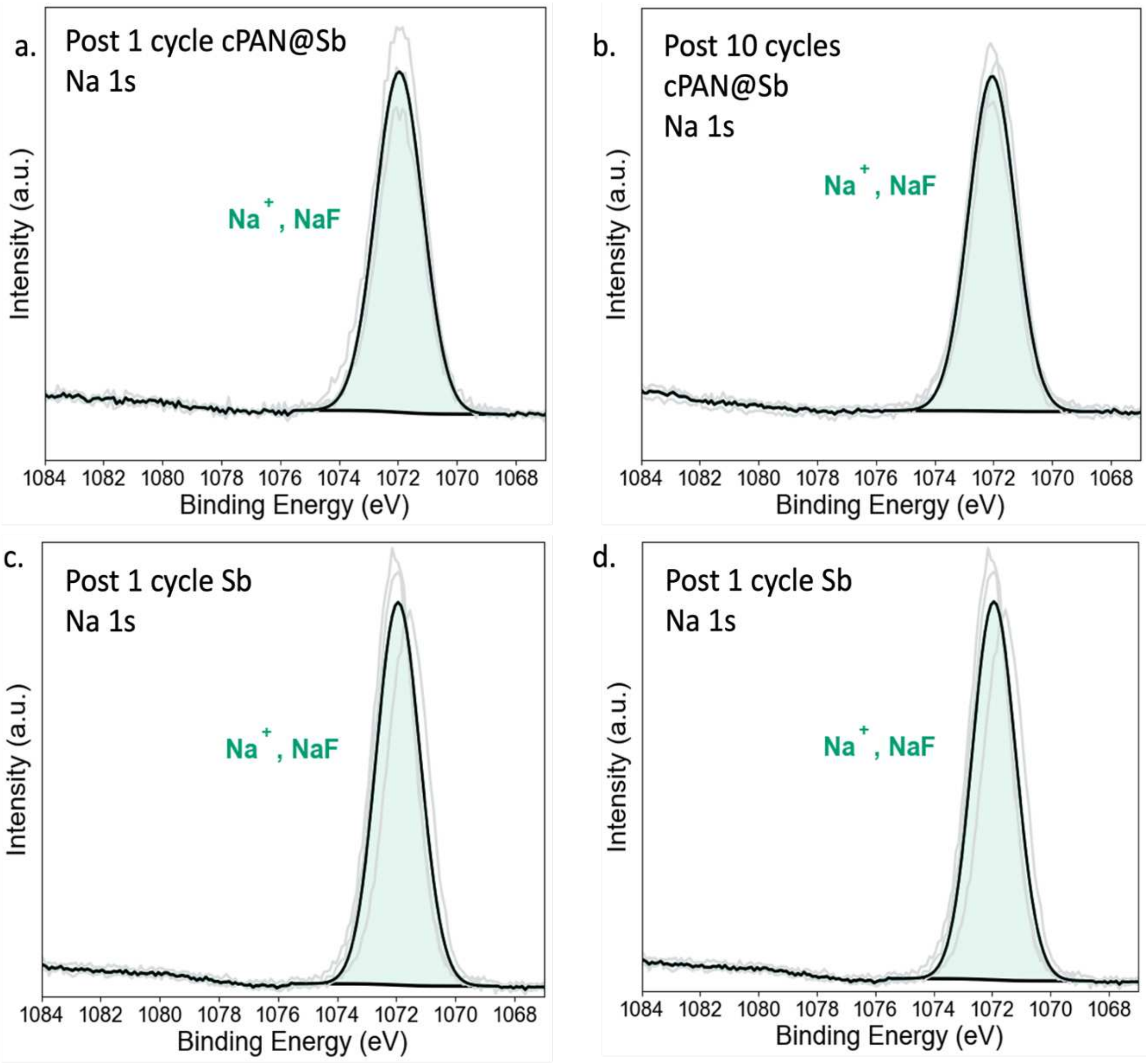

Figure A.II.XVII: X-ray photoelectron spectroscopy for the sodium 1s environments for the cPAN@Sb and Sb systems. A) The Na1s spectrum for the cPAN@Sb system after the 1st discharge half-cycle showing Na^+ environments which result from the presence of NaF. B) The Na1s spectrum for the cPAN@Sb system after the 10th cycle showing Na^+ environments which result from the presence of NaF. C) The Na1s spectrum for the Sb system after the 1st discharge half-cycle showing Na^+ environments which result from the presence of NaF. D) The Na1s spectrum for the Sb system after the 10th cycle showing Na^+ environments which result from the presence of NaF.

References:

(1) Nieto, K.; Windsor, D. S.; Kale, A. R.; Gallawa, J. R.; Medina, D. A.; Prieto, A. L. Structural Control of Electrodeposited Sb Anodes through Solution Additives and Their Influence on Electrochemical Performance in Na-Ion Batteries. *J. Phys. Chem. C* **2023**, *127* (26), 12415–12427. https://doi.org/10.1021/acs.jpcc.3c01086.

(2) Dashairya, L.; Das, D.; Saha, P. Binder-Free Electrophoretic Deposition of Sb/rGO on Cu Foil for Superior Electrochemical Performance in Li-Ion and Na-Ion Batteries. *Electrochimica Acta* **2020**, *358*, 136948. https://doi.org/10.1016/j.electacta.2020.136948.

APPENDIX III: Activities related to Chapter 4

Activity 1

Questions 1.1:

The discussion above derived the impedance, from Ohms Law, with a potential perturbation and a current response. Derive the expression for impedance with a current perturbation and a potential response.

What is the unit breakdown of "ωt", and are these units important for a sine function?

Questions 1.2:

"Calculated the time required for single impedance measurements at the following frequencies: 1kHz, 100 Hz, 1 Hz, 1 mHz, and 1 uHz."

There are three distinct processes that occur in Battery System A. Process 1 occurs at fast time scales, Process 2 occurs at an intermediate time scale, and Process 3 occurs at very slow time scales. What frequency regions would you need to use for your impedance analysis to analyze Processes 1, 2, and 3, respectively?"

Questions 1.3:

Which process would you expect to occur at higher frequencies, movement of ions through an electrolyte or the movement of ions through an electrode material? Why did you make the choice you made?

Figure A.III.I displays a Nyquist plot with two EIS spectra labeled Spectrum_1 and Spectrum_2 in blue and orange, respectively. Both spectra we taken over the exact same frequency range 100kHz to 100μHz. Based only on the shapes of these traces, which plot is dominated by kinetics and which plot is dominated by mass transport?

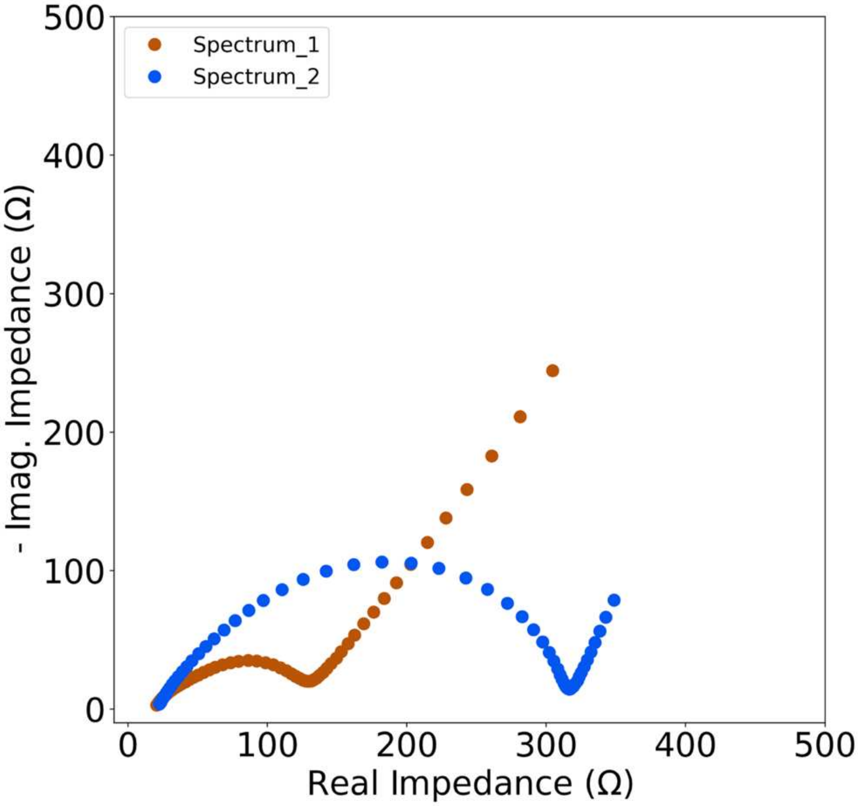

Figure A.III.I: Nyquist plot demonstrating EIS spectra dominated by different processes. Spectrum_1 (orange) and Spectrum_2 (blue) were both collected over a frequency range of 100kHz to 100μHz.

Activity 2

Questions 2.1

Figure A.III.IIa displays a solid-state circuit consisting of a resistor and a capacitor in parallel, proceeded by a resistor in series. Write the expression for the total impedance of this circuit.

Figure A.III.IIb displays a solid-state circuit consisting of a resistor and a CPE in parallel, proceeded by a capacitor in series. Write the expression for the total impedance of this circuit.

For the circuit displayed **in Figure A.III.IIa**, R1 has a resistance value of 100Ω, R2 has a value of 10Ω and the C1 has a capacitance value of 1.99x10^{-5} F. An impedance measurement was conducted on this circuit at a frequency of 100Hz. What is the value of the total impedance for this circuit under these conditions? Keep your answer in terms of the imaginary unit "j".

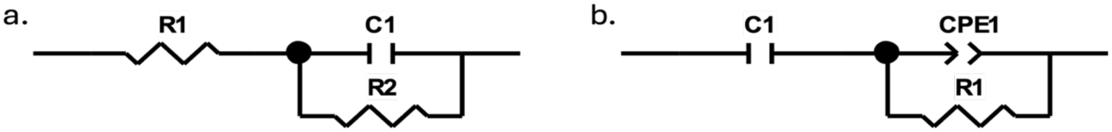

c. $Z_{resistor} = R$

d. $Z_{capacitor} = \frac{1}{j\omega C}$

e. $Z(\omega) = \frac{1}{(j\omega)^{\alpha} Q}$

Figure A.III.II: Equivalent circuit models (ECMs) and total impedance equations. A) An ECM where a resistor (R1) is in series with a Randels element, which consists of a resistor and capacitor in parallel (R2||C1). B) An ECM where a capacitor (C1) is in series with two parallel components, being a constant phase element (CPE1) and a resistor (R1).

Questions 2.2

Figure A.III.III3 shows Nyquist plots with the same EIS spectrum from the same graphite (uncycled) anode in a lithium-ion battery. **Figure A.III.IIIa** was fit with a modified Randels circuit, as seen in the inset of the figure. **Figure A.III.IIIb** was fit with a different modified Randels circuit, as seen in the figure inset. Qualitatively describe the differences in the ECM's and their resulting fits.

Based on the goodness of fit, which model should you select for analysis of the presented EIS spectrum?

Based on the ECMs, which model is the most valid for a pristine graphite anode?

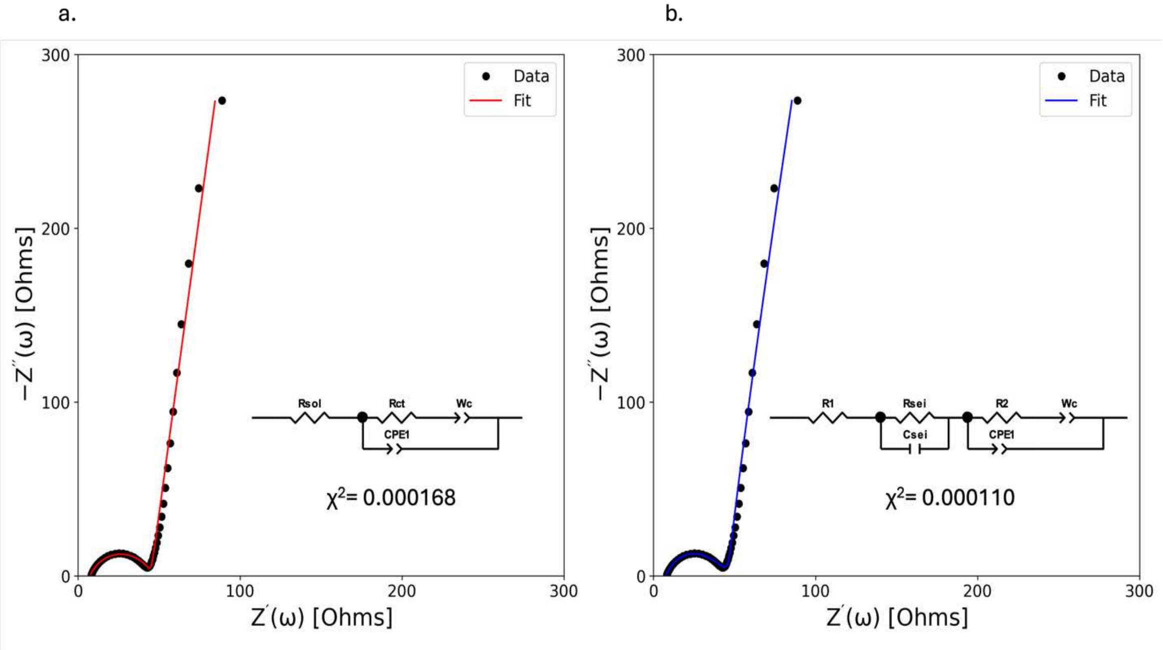

Figure A.III.III: Nyquist plots of the same EIS spectrum of a graphite electrode in a LIBs half-cell at OCP fitted with two different models. A) Nyquist plot fitted with a modified Rundles circuit (inset) with a resulting chi-squared of 0.000168. B) Nyquist plot fitted with a modified Rundles circuit (inset) with a resulting chi-squared of 0.000110.

$$Z_{re} = R_{sol} + R_{ct} + \sigma_W \omega^{-1/2} \tag{A.III.I}$$

Activity 3

Activity 3.1:

Equation A.III.I defines the linear relationship between the Zreal and $\omega^{-1/2}$, where the Warburg coefficient (σ_W) is the slope of the line, which is used to calculate the diffusion coefficient of an active ion in a battery electrode. In this equation, however, Rsol and Rct are also included. Explain why we do not need to consider the Rsol and Rct when we are using this equation to calculate the diffusion coefficient?

For Activities 3.2 and 3.3, you will be using Python scripts to model and fit experimental EIS data to different ECMs. Please follow the *Downloading Anaconda 3* and *GitHub Instructions* to locally download the necessary materials for this activity. These Python codes that accompany these activities was generated in Jupyter Notebook, which is a web-based Python framework.

Activity 3.2:

Open the Jupyter Notebook script titled *jChemEd_EISactivities_Activity3.2_v2*, and follow the imbedded instructions to generate three Nyquist plots of the experimental data with three different ECMs, **Figure A.III.IV**. All the ECM are fitted to the same spectrum. Without knowing anything about the system in question, which ECM would you select for this spectrum? Why did you choose the ECM you chose?

The EIS spectrum is related to a graphite anode in a lithium-ion half-cell at open circuit potential (OCP). With this new information, would you use the same model as you chose in part 1?

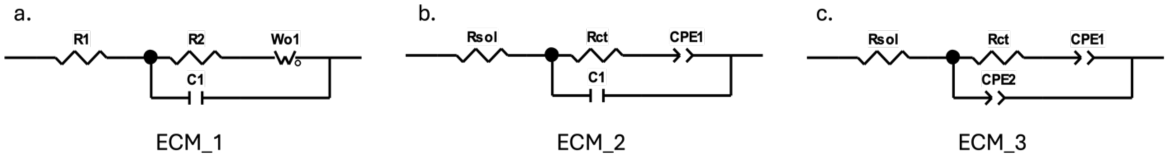

Figure A.III.IV: Equivalent circuit models for quantitative analysis of experimental EIS data. A) Traditional Randels Circuit where a resistor (R1) is in series with components in parallel, being, a resistor (R2) in series with a Warburg-open (Wo1) which are both in parallel with a capacitor (C1). B) Modified Randels Circuit where a resistor (R1) is in series with components in parallel, being, a resistor (R2) in series with a Constant phase element (CPE1) which are both in parallel with a capacitor (C1). C) Modified Randels Circuit where a resistor (R1) is in series with components in parallel, being, a resistor (R2) in series with a Constant phase element (CPE1) which are both in parallel with another CPE (CPE2).

Activity 3.3:

Open the Jupyter Notebook script titled *jChemEd_EISactivities_Activity3.3_v2_SOCdependence* and follow the imbedded instructions to generate a Nyquist plot with two different sets of experimental EIS data. Both sets of experimental data are fitted with the same ECM, **Figure**

A.III.V. The experimental data relate to an Sb anode in a sodium-ion half-cell at 1.2 V and 0.1 V vs. Na/Na$^+$. Tabulate the ECM fitting results. Please describe the changes to the Rsol, Rsei, Csei, and Rct parameters from the two ECM fits. How are these parameters different for the Sb electrode at 1.2 V vs. Na/Na$^+$ and 0.1 V vs. Na/Na$^+$.

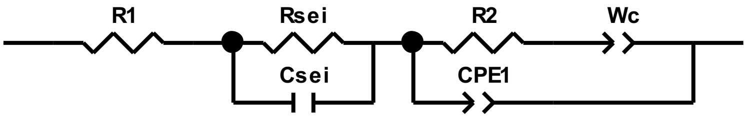

Figure A.III.V: Modified Randels Circuit used for the quantitative analysis of experimental EIS data. This equivalent circuit model (ECM) consists of a resistor (R1) in series with a Randels element (Rsei||Csei), which is then followed by a modified Randels element (R2-Wc||CPE1).

GitHub Instructions

Preamble:

- GitHub is an online repository for all types of code. This document will describe how to access the Python scripts needed for Activity 3.2 and Activity 3.3.

Step 1:

- Click the link below. This will bring you to the GitHub repository for these activities. The image below should match the web page you land on after clicking the link.

- https://github.com/DanShlaepWindsor/JChemEd_EIS_Activities/tree/main

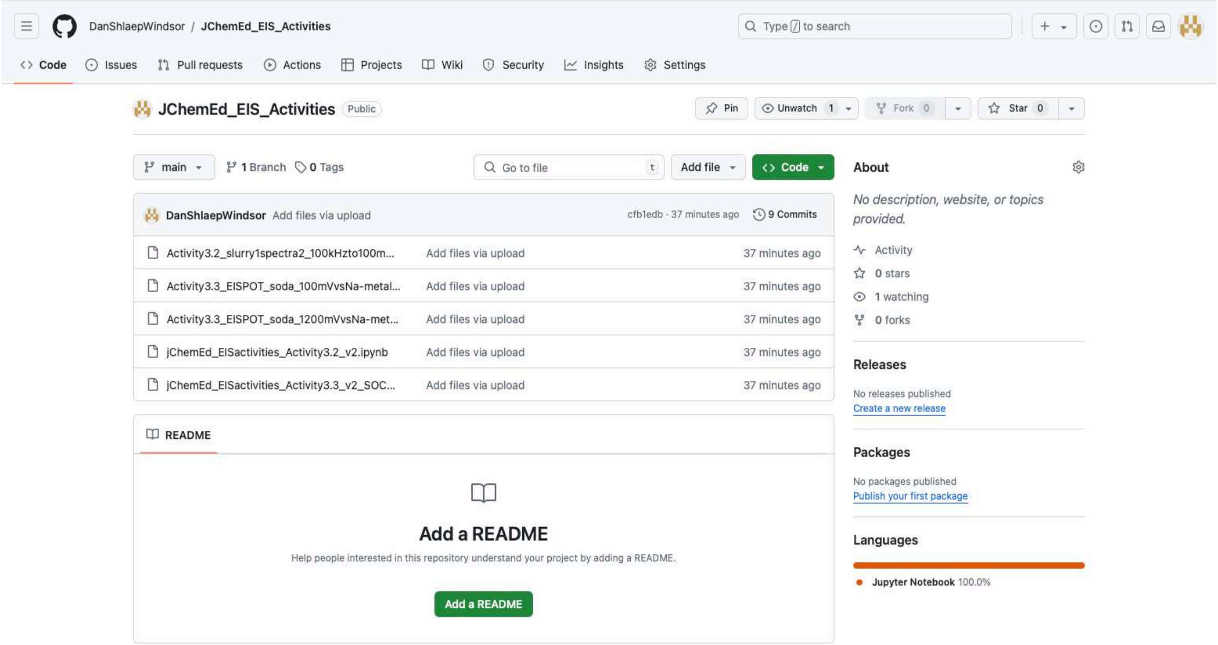

DanShlaepWindsor Add files via upload cfb1edb · 37 minutes ago 9 Commits

Activity3.2_slurry1spectra2_100kHzto100m...	Add files via upload	37 minutes ago
Activity3.3_EISPOT_soda_100mVvsNa-metal...	Add files via upload	37 minutes ago
Activity3.3_EISPOT_soda_1200mVvsNa-met...	Add files via upload	37 minutes ago
jChemEd_EISactivities_Activity3.2_v2.ipynb	Add files via upload	37 minutes ago
jChemEd_EISactivities_Activity3.3_v2_SOC...	Add files via upload	37 minutes ago

Help people interested in this repository understand your project by adding a README.

No description, website, or topics provided.

No releases published

No packages published

Step 2:

- Click the green “Code” button to open a dropdown menu.
- In the drop-down menu, select “Download ZIP” (See image for reference).

Step 3:

- Once you have downloaded the ZIP file, move the ZIP folder to the same location on your computer where you have downloaded Anaconda 3.
- This is a crucial step! If the zipped filed are not in the same file path as Anaconda 3, then the Jupyter Notebook scripts will not be able to run!
- When the ZIP folder is assigned to the same location as Anaconda 3, un-zip the files.
- Now, you are ready to go ahead and complete Activity 3.2 and Activity 3.3.

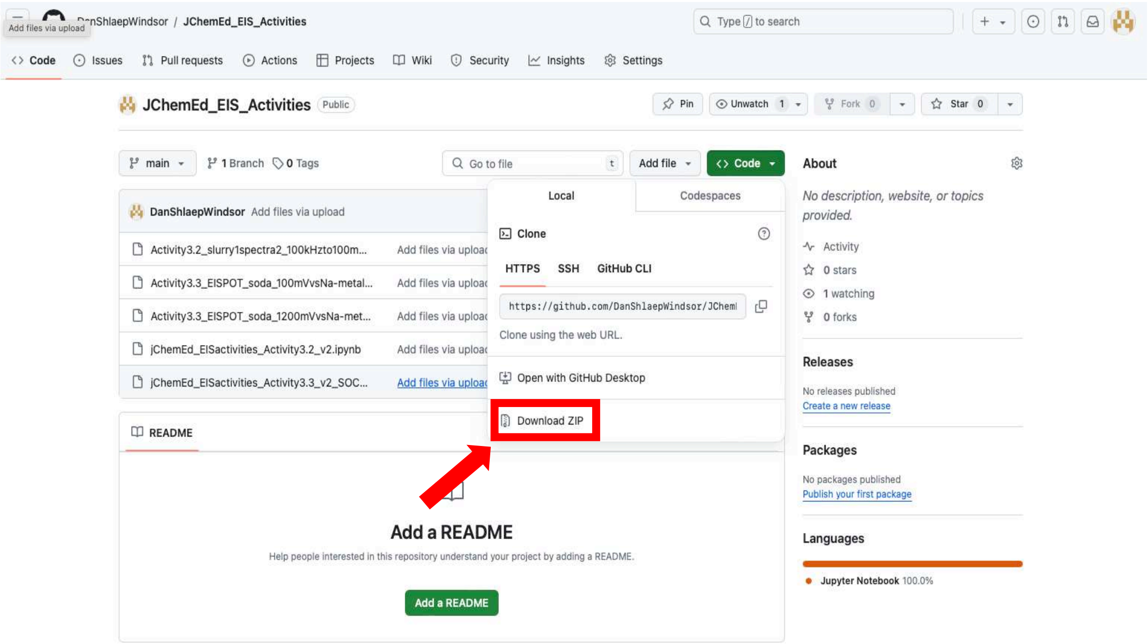

Downloading Anaconda 3

Preamble:

- Anaconda 3 is an application that carries a distribution of Python and R programming languages for data analysis. We will be using Python for the quantitative analysis of experimental EIS data with several equivalent circuit models. Anaconda 3 is free to download and is incredibly useful for any type of data analysis.

Downloading Anaconda 3 for Windows:

- Please follow the instructions in the following link to download this software.
- https://docs.anaconda.com/anaconda/install/windows/

Downloading Anaconda 3 for macOS:

- Please follow the instructions in the following link to download this software.
- https://docs.anaconda.com/anaconda/install/mac-os/

Downloading Anaconda 3 for Linux:

- Please follow the instructions in the following link to download this software.
- https://docs.anaconda.com/anaconda/install/linux/

APPENDIX IV: Soft Skills to Ease the Graduate School Growing Pains

When I began my graduate school journey, I thought most of the learning I would do would be solely related to the chemistry of batteries. The reality was that much of the learning I did in grad school related to the soft, untaught, skills that were required to complete this journey. As such, this section will cover the soft skills I learned along my way to a Ph.D., and advice for 1st year graduate students in the hopes that they will learn these skills faster than I did. These skills include being okay with being wrong, communication, fulfillment, and self-worth.

It's okay to be wrong

One of the most important aspects of conducting good science is feeling comfortable admitting when you are wrong. This can be quite challenging, especially when so much of your life as a graduate student feels wrapped up in getting results in the lab. The key thing to remember though is that the path taken to make a scientific discovery is rarely linear. The path often bends, jumps, and even stops during scientific research. As such, it is important to remind yourself that there are no "bad" results. Results are only results, how you hypothesize and approach the steps forward are what separates good science from bad science.

An easy way to fall into conducting "bad" science is to take parental ownership of the hypotheses that drive the research. This usually arises from confirmation bias on the side of the investigator, where an investigator will refrain from testing an alternative hypothesis because they are too wrapped up in the ideas they have already formed. The results of this parental relationship between a scientist and their hypothesis can be extremely negative. I, in my experience, have engaged in heated arguments with fellow students who simply would not hear a contrary opinion.

Not only does parental attachment to hypotheses lead to heated discussion, but it can also turn a student away from receiving feedback.

All of this is to say that parental attachment to a hypothesis is an easy way to hamstring your science. There is, however, a straightforward way to reduce the possibility of forming such a bond with a hypothesis. Which is…being okay with being wrong. Forming an incorrect hypothesis does not mean you are stupid. It doesn't even mean that you are bad at science. Forming an incorrect hypothesis, in fact, is a good thing…it means you've learned something. Learning, at the end of the day, is the nexus of scientific discoveries. Being wrong is an important part of doing science. My advice to fresh graduate students is to get used to, and be okay with, being wrong. This will help you second guess yourself, which will improve your science as a result.

Communication

At the start of my graduate school journey, I truly thought that I had learned all I had needed concerning communication. I found that I still had much to learn about communication during my time at CSU. Prior to starting my graduate career, I believed that being direct when providing feedback was the only criteria required to provide good feedback. I learned that although this style of feedback works well for me, being direct and clear does not work for everyone. My ignorance toward understanding how other people best receive feedback led to some conflicts with fellow lab mates regardless of the intention behind the feedback I was providing. After some time, I learned that it is imperative to discuss with lab mates how they want to receive feedback. Once I started taking the time to ask people how they want to receive feedback, life in the lab became much easier. Thus, all this section is to say that your life as a graduate student will be much more tranquil if you take the time to understand *how* the person you are working with best receives feedback.

Fulfillment

The journey of a graduate student is that of a solo crusade. The path is long and winding, there are many trials and tribulations, and although lab mates and advisors are present to aid in the crusade the buck ultimately stops with the graduate student in question. Due to the solitary nature of the graduate student experience, it is too easy to feel consumed and overwhelmed by the journey ahead. These feelings can result in the total consumption of a graduate student, where the student will become totally encapsulated and wrapped up in the maelstrom that is graduate school. To avoid this, it is imperative that graduate students find, and maintain, activities and hobbies that provide fulfillment…outside of graduate school. For my part, I found that my passion for cycling was a wonderful way to find this fulfillment outside of the workplace. All the long rides and training allowed me to forget, for a moment, the less than happy feelings I had concerning my work and my studies. This is not to say that every graduate student needs to dress themselves in lycra and sit on a bike for hours out of the week. This is simply to say that continuing to do the things that make you happy are crucial if you want to avoid feeling fully consumed by the graduate school experience.

Self-worth

At the beginning of my graduate school career, I believed that the solution to each hurdle in my way was to use brute force. This entailed leveraging my stubbornness to complete the task in front of me, no matter the cost. The brute force approach, while being effective in the short term, is not sustainable in the long run. What happens when you try to drive a car with no gas? The answer, not surprisingly, is nothing. In terms of graduate school, running on empty can have profoundly negative effects on your experience and productivity. For example, it is extremely difficult to teach yourself something important for a project when it's difficult to get out of bed.

All of this is to say that applying the brute force approach to your investigations is a sure-fire way to burn out. For my part, I found it extremely difficult to get motivated after I passed my preliminary exam. I was just too burned out to feel excited about my science. This burnout persisted for quite some time due to less than advantageous results in the laboratory. For a while, I believed that these feelings would be the defining feature of my graduate school career, until my lovely partner told me a phrase that changed everything.

“Your self-worth is not defined by your results in lab.”

While this phrase may seem obvious, its significance to a graduate student is profound. The reason for this is that the “currency” in academia are publications, which necessitate positive scientific results. The perceived lack of results can torpedo the confidence and motivation of graduate students which directly leads to burnout. I was in this exact position, until the moment I heard the phrase above. Keeping this phrase in mind has helped me navigate the peaks and valleys of graduate school. Before hearing this phrase, a tough day in the lab would lead to hours of consternation at home. After hearing this phrase, I found that tough days in the lab were much easier to manage, and I would find myself ready to tackle whatever was ahead of me the following day.

All of this is to say, the work you do in the lab does not define who you are as a person. It does not define you worth as a human being. It, also, does not define your ability to do science in the future. Your worth as a person is inherent, do **not** let your results in the lab diminish this!

APPENDIX V: Supplementary Information for Chapter 4

Derivation of total impedance from ohms law

Ohm's law (**Eq. A.V.I**) is the fundamental relationship governing all electrical and electrochemical systems.

$$E = IR \tag{A.V.I}$$

Here E is the electric potential, I is current, and R is resistance. Commonly Eq. 1 is written $V = IR$, with V representing voltage; however here will employ electrochemical convention, as the difference in potential between the working electrode (WE) reference electrode (RE) that is measured in an experiment.[1]

This relationship holds when the system in question is operated at DC (direct current) conditions. The application of DC experiments is extremely common, however these experiments struggle to provide information on the electrochemistry of systems when they are from equilibrium, aka a transient measurement.[1] The use of an alternating current (AC) can allow for the analysis of electrochemical systems much closer to equilibrium by applying a small perturbation and measuring the response at steady state, which allows for easier analysis of kinetics and diffusion of the system.[1] To gather this sort of information, an alternating current (AC) is required where a sinusoidal perturbation is used. To gather this sort of information, an alternating current is used, here modeled as a sinusoidal perturbation of the potential and the corresponding current response (**Equations A.V.II and A.V.III**).

$$E = |E|\, sin(\omega t) \tag{A.V.II}$$

$$I = |I| sin(\omega t + \phi) \tag{A.V.III}$$

Here ω is the angular frequency (with units of radians/sec, $\omega = 2\pi f$, where f is the frequency) and in the case of current, ϕ is the phase shift (units of radians), which contains information about the *impedance* of the system. **Figure A.V.I** in the main text represents two waveforms, where the potential perturbation is represented in blue, and the current response is represented in red, offset by ϕ. With this sinusoidal perturbation/response, Ohm's law holds under AC conditions but impedance (Z) takes the place of resistance ($E = IZ$). Impedance is the sum of the resistance (R) and reactance (X) of an AC electrical system.[2] Resistance and reactance both oppose the flow of current, however reactance is dependent on the frequency of the current, while resistance is not.[3] Using **Equations A.V.I-A.V.III**, the impedance is expressed as the ratio of the potential perturbation to the current response (**Equation A.V.IV**).

$$Z = \frac{E}{I} = |Z|\frac{sin(\omega t)}{sin(\omega t + \phi)} \qquad \text{(A.V.IV)}$$

$$Z = |Z|e^{-j\phi} = |Z|\frac{e^{j\omega t}}{e^{j(\omega t+\phi)}} \qquad \text{(A.V.V)}$$

In going from **Equation A.V.IV** to **Equation A.V.V**, Euler's formula was applied—we direct the reader to the SI for details on this derivation and the additional complex analysis details. This allows for the assessment of Ztotal with respect to ϕ, however a more straightforward representation of both the resistance and reactance can be visualized by converting to Cartesian coordinates using **Equations A.V.VI** and **A.V.VII**.[2,4] In the corresponding plot, the real part of the impedance, Zre (the resistance), is plotted on the horizontal axis, and the imaginary part of the impedance (Zim, the reactance) is plotted on the vertical axis.[1,3]

Equation A.V.VI displays how the polar representation of $|Z_{total}|$ are converted to a cartesian representation where |Z| is equal to the square root of Z_{re} squared plus Z_{im} squared, while **Equation A.V.VII** displays the relationship between the phase shift (ϕ) and Z_{re} and Z_{im}. When the impedance of a system is measured over a range of frequencies (i.e. when a *spectrum* is collected), the cartesian and polar representations of the impedance begin describing the impedance phenomena present in the battery system being studied. A Nyquist plot (Figure 2.b) represents such a spectrum in Cartesian coordinates, while a Bode plot does the same in Polar coordinates. Nyquist plots are useful when information related to the resistance (Z_{re}) and reactance (Z_{im}) of the system is desired, whereas Bode plots are useful for assessing the frequency-dependent changes of Z and ϕ.

$$|Z| = \sqrt{(Z_{re})^2 + (jZ_{im})^2} \quad \text{(A.V.VI)}$$

$$\phi = \tan^{-1}\frac{Z_{re}}{jZ_{im}} \quad \text{(A.V.VII)}$$

For batteries, Nyquist plots are the most frequently used representation of impedance data. Bode plots, however, can still be extremely useful in analyzing the impedance of a battery system, owing to the frequency dependent insight provided.

Impedance in series vs. impedance in parallel

For solid-state circuits where electrical components are connected in series, the *impedance* of each individual component are additive. Circuit elements connected in parallel have additive *admittances*, which is the inverse of the impedance (Y=1/Z). The admittance (Y) is the inverse of impedance and can be written as Y=1/Z. This is visualized in **Figure A.V.I**. **Figure 4.4c** shows a capacitor and resistor in series and illustrates an offset from zero on the x-axis, related to the contribution for the resistor, in addition to the line extending up along the y-axis, relating to the contribution from the capacitor in the circuit. The shape of the Nyquist plot changes dramatically, however, when the same circuit elements are placed in parallel. Instead of a vertical line offset from zero on the x-axis, a semi-circular shape centered at centered at zero along the x-axis is present, **Figure 4.4d**. In the Bode representation for **Figure 4.4d**, the τ parameter is the characteristic time constant for the R1||C1 circuit.[4]

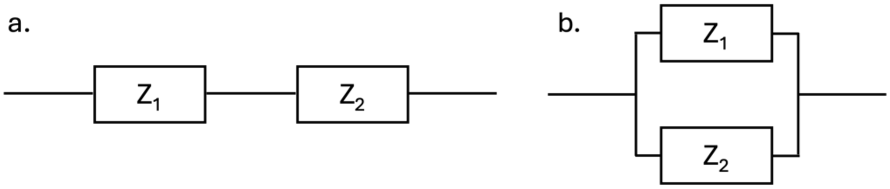

$$Z_{-} = Z_1 + Z_2 \qquad Z_{||} = \left[\frac{1}{Z_1} + \frac{1}{Z_2}\right]^{-1}$$

Figure A.V.I: Schematic representations and total impedance (Z_{total}) expressions for circuit elements. A) Schematic representation for the Z_{total} of a circuit comprised of circuit elements Z1 and Z2 connected in series, where Z_{total} is equal to the Z1 plus Z2. B) Schematic representation for the Z_{total} of a circuit comprised of elements Z1 and Z2 connected in parallel, where Z_{total} is equal to the inverse of 1/Z1 plus 1/Z2.

Machine learning

Recently, there have been efforts to leverage machine learning (ML) to aide in the validation of ECMs for EIS quantitative analysis. A publication by Zhu et al. utilized a support vector machine (SVM) algorithm to avoid human subjectivity in the selection of an appropriate ECM.[10] This study trained the SVM on EIS data sets from 500 publications on energy storage devices in the literature and demonstrated that the SVM algorithm had better performance in selecting an adequate ECM compared to other algorithms. Although this study demonstrated the power of using ML for ECM selection, we implore caution when using these tools. This arises from the fact that the SVM algorithm was only able to reach a probability distribution of 49% for a Randels type circuit belonging to the selected EIS data. With this in mind, we still do not discourage the use of ML for aiding in the selection of an ECM. Instead, we implore the investigator to use ML as a starting point, and not as an absolute.

General considerations when running EIS on a battery

Thus far both qualitative and quantitative analyses with EIS have been discussed. This next section will now transition into what these analyses means for the EIS of rechargeable battery systems. This section will begin with a discussion on important practical considerations for EIS analysis of batteries, finishing with discussion on the impedance behavior of the most common classes of materials used as battery electrodes and electrolytes. Before any discussion on the impedance behavior of rechargeable batteries is undertaken, this work will cover some practical experimental considerations for EIS analyses

Frequency Ranges

Section 4.2 discussed how analysis of the impedance of a system over a spectrum of frequencies allows for the deconvolution of processes which occur at different time scales. Practically speaking, there are three frequency regimes of interest (high, mid, and low) that provide insight into different processes occurring in a battery. The high frequency range (frequencies above 1 kHz) offers insight into the impedance related to the transport of the active ion through the electrolyte.[3,11] If the frequency range extends to very high frequencies, then the external circuitry (i.e. connecting wires) can significantly affect the resulting EIS spectrum and Nyquist plot representation. The impact of the external circuitry at high frequencies in an EIS spectrum manifests as inductive behavior, which is visualized in a Nyquist plot by points that extent to negative values along the Z_{img} axis.[3,12] Concerning how the high frequency region is modeled with solid-state circuit elements in an ECM, a resistor is series with the remainder of the ECM. If inductive affects are present in a Nyquist plot, then an inductor circuit element should be placed, in series, before the resistor modeling the solution resistance of the battery.[12] The middle frequency region provides insight into impedance related to the charge transfer resistance and electric double-layer capacitance at the electrode-electrolyte interface. These processes are molded by a resistor and a capacitor connected in parallel. Often, the capacitor is replaced by a CPE to account for the non-ideal charging behavior of the electric double layer.[13] The middle frequency region can also be affected by the impedance of the SEI. To model this behavior, investigators generally included a section R||C component to the ECM prior to the original R||C component to account for charge transfer at the SEI layer and charging of the SEI layer.[14,15] The low frequency region provides insight into the impedance related to the solid-state diffusion of the active ion through the electrode material. This, traditionally, is modeled by a Warburg element which is included in parallel with the R||C components modeling the charge transfer resistance and electric double layer capacitance.[1,4] As previously mentioned in the discussion on Warburg elements, these components are often replaced with CPEs to account for non-ideal behavior in the low frequency region.

PEIS vs. GEIS

In electrochemistry, the investigator can control the potential to measure the current response, or they can control the current to measure the potential response. This, also, applies to EIS where an investigator can run either potentiostatic-EIS (PEIS) or galvanostatic-EIS (GEIS) to measure the current and potential responses, respectively. Although, based on Ohms law, both PEIS and GEIS should provide the same information, the impedance regime of the system under question is a critical factor when deciding which type of EIS experiment to use. For battery systems which displays high impedances, PEIS is an adequate choice. This results from the fact the if a potential perturbation of 10mV to a high impedance system is conducted, the current response will also be very small. On the other hand, if PEIS is applied to a system with low impedances, then a small potential permutation of 10mV can result is a current response of several amps, which can be dangerous.[16] For low impedances systems, GEIS is the best option as a small current perturbation will result in a potential result that is very small.

Experimental set up

Aside from the type of EIS experiment to select, it is also very important to think about the experimental set up and how it might affect the resulting data. From an external circuitry perspective, the length of the wires connecting the potentiostat to the battery being studied can alter the measured impedance values. The effects of long wires manifest as inductive behavior in the high frequency region.[3] A quick way to qualitatively assess if the wires are affecting the measured impedance is to look for data points that are negative along the Z_{im} axis in the high frequency region of the Nyquist plot.[12]

Control experiments

Control experiments, in all scientific fields, are incredibly important as they help to disprove contrary hypotheses. For EIS, a good control experiment to run is to apply the same impedance perturbation over the same frequency range on a symmetric cell of the counter/reference electrode. This type of experiment will allow the investigator to, either disprove the hypothesis that the impedance behavior of the counter/reference electrode is affecting the impedance signature of the electrode being studied or can demonstrate that the dynamics of the counter/reference electrode are affecting the overall impedance response of the electrode being studied. For half-cell configurations these types of controls are important, as alkali metals (Li, Na, K) are known to perform poorly as counter/reference electrodes for a variety of reasons, including ununiform surface leading to localization of current density, high reactivity with the liquid electrolyte, and voltage drift.[17,18] The work of Marino et al. and Williamson et al. both used symmetric cells to disprove the notion that the counter/reference electrodes were adding to the recorded impedance data for LIBs and NIBs systems, respectively.[14,19] Thus, the key take away is that alkali metal counter/reference electrodes, generally, do not have a significant affected on the measured impedance of the electrode being studied.

CCCV+EIS

Given that EIS spectra for rechargeable batteries are dependent on the SOC of the system, it is important to conduct EIS analysis as a function of SOC (i.e. potential). To do this, the electrode in question must be slowly brought to the SOC's of interest prior to the application of an EIS experiment. This is done through a technique called constant-current constant-voltage (CCCV) polarization. The CCCV polarization starts with a CC step, where the electrode is brought to the potential of interest under a slow (small) constant current. Once this potential is reached, the electrode must be held at this potential until the current reaches 0 A, indicating that all the chemistry related to the selected potential has been completed. This potential hold is the CV step. After the CV step, and before EIS is applied, the electrode must be allowed to rest for several hours to allow the system to reach equilibrium. This rest period prior to the EIS experimentation is crucial, as it allows the system to meet the *Stationarity* criteria required for all valid EIS experiments. In the literature, studies often allow their cells to rest for up to 6 hours to reach equilibrium at a specific potential.[20,21] Once the rest period has been conducted, the system will have been polarized to the potential (i.e. SOC) of interest for the EIS experiment. The steps highlighted above can be repeated as many times as the investigator wants, such that they analyze the impedance phenomena as a function of SOC.

How to help yourself, and the field

As mentioned previously, one of the greatest difficulties regarding EIS is the gap between the ease of data collection and data analysis/reporting. This notion becomes immediately apparent when looking at the literature for rechargeable batteries. Often, studies will conduct EIS and report the resulting data without accounting for the external parameters highlighted in Section 2. Additionally, studies will (even if they have accounted for the external factors) refrain from mentioning the ECM fitting methodology and/or will neglect to mention why a specific ECM was chosen. Studies lacking this information are difficult to follow, as it is challenging to ascertain if the conclusions from the EIS analysis are related to A) what has been seen in the literature and B) if the fitted values are physically relevant or result from over fitting. To avoid this, studies using EIS on rechargeable batteries should attempt to relate their ECMs to a viable model seen in the literature and should also provide insight into where/when the model struggles to accurately fit the data. An excellent example of this arises in the work of Xu et al., where the investigators dedicate an entire subsection of their results and discussion to discuss viability of the applied ECM for the electrode system in question.[22] The inclusion of this type of information is incredibly helpful, as it allows the reader to understand what the authors considered when applying EIS analyses.

Auxiliary insight offered by EIS analysis

Aside from the traditional application of EIS to rechargeable batteries there are, also, different calculations/estimations that can be made from EIS analyses that provide important, and different, information concerning the rechargeable battery. These auxiliary calculations are diffusion coefficient calculations, exchange current density, state of health (SOH) estimation, and calculation of the distribution of relaxation times (DRT). These calculations will be discussed thoroughly below.

Diffusion coefficient calculations

As previously stated, impedance measurements at low frequencies provide insight into the impedance related to the solid-state diffusion of the active ion through the solid electrode material. Impedance measurements in this frequency region can be leveraged to calculate the diffusion coefficient for the active ion in the solid-state electrode. This is done by selecting a series of points over the low frequency region and then plotting the Z_{re} as a function of the inverse of the square root of the angular frequency, as seen in **Equation A.V.VIII**.

$$Z_{re} = R_{sol} + R_{ct} + \sigma_W \omega^{-1/2} \quad \text{(A.V.VIII)}$$

$$D_{ion} = \frac{R^2T^2}{2A^2n^4F^4C^2\sigma_W^2} \quad \text{(A.V.IX)}$$

Where Z_{re} is the real impedance, R_{sol} is the solution resistance, R_{ct} is the charge transfer resistance, σ_W is the Warburg coefficient, and $\omega^{-1/2}$ is the inverse square root of the angular frequency. The relationship between the Z_{re} and $\omega^{-1/2}$ should be linear, resulting in a line of point whose slope is σ_W.[23,24] This value can then be applied to **Equation A.V.IX**, where R is the ideal gas constant, T is temperature, A is the surface area of the electrode, n is the number of electrons transferred in the electrochemical reaction, F is Faraday's constant, C is the concentration of active ion in the electrode, and σ_W Warburg coefficient.[1,3,24] All the listed parameters are critical for the application of this equation; however, the A and C parameters merit further discussion. The active surface area of a battery electrode is rarely the same as the footprint area of the electrode, since the footprint area does not account for the surface roughness or porosity of the electrode. Concerning **Equation A.V.IX**, this implies that the use of the footprint area for the A parameter might not fully account for the active sites present in the electrode. As such, it is imperative to measure the electrochemical active surface area (ECSA). This can be done via a variety of methods, with Brunauer-Emmett-Teller (BET) being the most straight forward. If an investigator does not have access to the proper instrumentation to run BET, we suggest referencing the work of Voiry et al., which describes the calculation of the ECSA through CV experiments over increasing scan rates to measure the non-faradaic current response.[25] The concentration parameter (C) is much easier to estimate than the A parameter, yet it is subject to the influence of SOC. This notion is intuitive, as an electrode at 5% SOC is going to have a lower concentration of active ions in the electrode compared to if the SOC was 95%. All of this is to say that conducting these calculations as a function of SOC, or at a specific SOC, is imperative if viable and sound data is to be extracted. A perfect example of this arrives in the work of Wang et al. which showed that the lithium-ion diffusion coefficients increase as the SOC increased.[24]

It should be noted that estimations of the active ion diffusion coefficients are possible by traditional electrochemical techniques, namely galvanostatic intermittent titration technique (GITT) and potentiostatic intermittent titration technique (PITT). These techniques, while still providing good estimations for the diffusion coefficient, require long experimentation times as these techniques plus the current or the potential incrementally over a wide range of values.[26] Concerning the viability of diffusion coefficient calculations using EIS, a study by Ko et al. demonstrated that the while the diffusion coefficients calculated by EIS are not the exact same as those calculated by PITT, the EIS analysis produces the same general trends seen with PITT.[27] It is important to remember, however, that given the polarization regime required for PITT/GITT, these techniques will provide information more related to the equilibrium. Application of EIS for diffusion coefficients allows for insight into processes with shorter time constants, related to the interfaces and SEI in a battery. This is to say that while EIS does not allow for diffusion coefficient calculations are the electrochemical equilibrium of the redox couple, it does allow for the quick estimation of the diffusion coefficient of an active ion in a solid-state electrode material.[28]

Exchange current density

Another calculation that can be made with EIS data, this time in the middle frequency region, relates to the kinetics of the reaction at the electrode-electrolyte interface. The exchange current density (j_0) is a key electrochemical metric that provides insight into the fundamental kinetics of the electrochemical system being studied.[1] Traditional determination of j_0 (not to be confused with the imaginary unit j) requires steady state measurements which necessitate the use of rotating disk electrode or micro electrodes, which are not applicable for in situ measurements on a rechargeable battery. EIS can help in this regard, as detailed by **Equation A.V.X**, where R is the ideal gas constant, T is the temperature, n is the number of electrons transferred in the electrochemical reaction, R_{ct} is the charge transfer resistance, and A is the surface area.

$$j_0 = \frac{i_0}{A} = \frac{RT}{nFR_{ct}A} \qquad \text{(A.V.X)}$$

When examining **Equation A.V.X**, we can see that only one parameter from ECM fitting is required to calculate the exchange current density, which is significantly more straightforward (practically speaking) compared to traditional approaches for calculation of j_0. The value of j_0, unsurprisingly, is also highly dependent on the state of charge of the electrode. Concerning the equation, we can see that larger values of R_{ct} will result in smaller values due to position of the R_{ct} parameter in the denominator. Simply put, the exchange current density for a system will be higher for a system with a higher conductivity related to the charge transfer process.[24]

SOH. Estimations

The application of EIS for the analysis of rechargeable batteries does not stop at fundamental materials properties. This technique can be applied to larger scale considerations related to the lifetime and health of a rechargeable battery. The state-of-health (SOH) of a battery is a key metric for understanding how aging of the battery affects the performance. With respect to EIS, this is done by tracking how the R_{ct} changes as a function of cycle number/shelf life. The work of Wang et al. determined a relationship between R_{ct} and SOC via computational modeling.[29] Discussions on the details of modeling SOH with EIS are beyond the purview of this work. For the interested reader, we recommend the work of Wang et al.[29], Mingant et al.[30], and Zhang et al.[31]

EIS features of common classes of battery materials

At this point in the work the fundamentals of EIS, how to conduct quantitative analysis, and internal and external factors affecting EIS spectra has been established. This next section will cover, at a surface level, the impedance behavior of classes of materials commonly included in rechargeable batteries. These classes of materials include electrolytes (liquid and solid-state), intercalation electrodes, conversion electrodes, and alkali metal electrodes. This section will not dive into detail about the impedance behavior of specific materials (i.e. Si conversion electrodes). Rather, the objective of this section is to provide an overview of the common features seen within each class of materials.

Electrolytes

The function of an electrolyte in a rechargeable battery is to act as the media in which the active ion is transported between the electrodes. Traditionally, organic liquid electrolytes are included in LIBs due to their high ionic conductivities and high electrical resistance. While these aspects of liquid electrolytes are advantageous, these systems have some safety concerns resulting from the volatility of the organic solvents used in these electrolyte formulations. To address these safety concerns, investigators in the field have been studying solid-state electrolyte systems. Practically speaking, the EIS analysis of electrolyte systems requires the use of a symmetric cell configuration. Symmetric cells (where Li-metal is included at both electrodes) are the best approach, experimentally, for testing the impedance behavior of an electrolyte.[32] The power of using a symmetric cell configuration arises from the fact that the chemistry of the electrodes should not be included in the electrochemical measurements. Thus, EIS measurements can be made on electrolyte systems without accounting for the impedances related to the (dis)charge processes of the electrode materials. This section will begin by discussing the impedance behavior of liquid electrolytes and will conclude with a discussion on the impedance behavior of solid-state electrolytes.

Liquid electrolytes

Liquid electrolytes are generally composed of a mixture of salt and solvents designed to have high ionic conductivity to promote ion transport through the electrolyte between electrodes. In a pristine, uncycled cell, a low resistance value is expected for R_{sol} since high ionic conductivity is a requirement in electrolyte design. Electrolytes have an electrochemical stability window (ESW) within which no degradation of electrolyte components occurs. Ideally, electrolytes will have a very large window to prevent undesired degradation, however practical electrolytes are often used outside of the ESW leading to reduction of components onto the anode forming a solid-electrolyte interphase (SEI). Formation of the SEI occurs during the first cycles consuming active ions and degrading electrolyte components, leading to a decrease in conductivity or an increase in solution resistance (R_{sol}). Therefore, a cycled cell is expected to display a higher solution resistance with the consumption of electrolyte components to form the SEI. In addition to higher R_{sol} values, the SEI also has its own impedance characteristics that must be accounted for in an ECM. To account for the impedance behavior of the SEI, investigators often included an additional R||C component in their ECM to model the resistive and capacitive behavior of the SEI.[14] In this SEI component of an ECM, the resistor models the Faradic impedance of the SEI while the capacitor models the non-Faradaic impedance of the SEI. Specifically, the resistor models the resistance associated with the movement of an ion through the SEI, while the capacitor models the double-layer charging (C_{dl}) of the SEI.[3] The inclusion of an R||C component to model the impedance behavior of the SEI on an electrode material is incredibly common in the battery literature.[14,33,34]

Solid-state electrolytes

A popular approach to address the safety issues posed by liquid electrolytes is to apply a solid-state material that allows the conduction of the active ion while being electrically insulating. This class of materials are called solid-state electrolytes (SSE). There are a plethora of different

SSE materials and discussing the impedance behavior of each sub-class of SSEs is outside of the scope of this work. Instead, the following section will discuss, in general, some impedance phenomena characteristic to ceramic SSEs. For the interested reader, we highly recommend the work of Vadhva et al. which provides a comprehensive review of EIS for SSEs.[32]

Ceramic SSEs are, generally, multinary inorganic systems with interpenetrating cation and anion sublattices which have large voltage stability windows while still providing ion conduction through the material.[35] These materials, however, usually have very low ionic conductivities compared to liquid electrolytes.[32] Concerning EIS, this implies that the R_{sol} (or R_{pol} for SSEs) for SSEs should be significantly more resistive compared to a liquid electrolyte counterpart. In addition to increases to R_{pol}, ceramic SSEs often exhibit increased interfacial impedances due to the contact resistance between the SSE and the electrode in question.[36,37] These high contact resistances are clearly visible in a Nyquist plot, and often require the implementation of an additional component in an ECM to account for these phenomena.[37]

Intercalation electrodes

Intercalation electrode materials are classified as materials that store charge (in the form of active ions) within the layer of the lattice of the material.[38] For a standard LIB the anode and cathode materials are graphite and lithium cobalt oxide (LCO), respectively. Both materials store charge as Li-ions within the layers, yet at different energy ranges. The energy at which each material reacts with Li-ions, and the energy difference of each respective reaction, is what allows LIBs to store so much energy. Concerning EIS, the impedance of intercalation electrodes is generally limited by the diffusion impedance process.[21] This arises from the sluggish ion diffusion kinetics in the material, which can be assessed by the ionic conductivity of the active ion in the intercalation material.[39] For example, the diffusion coefficient of LCO for Li-ions is rough $5x10^{-}$

^{9} cm^{2} s^{-1}, which is incredibly low.[40] For graphite, intercalation, anode electrodes, the Li-ion diffusion coefficient can have a wide range of x10^{-7} to x10^{-11} cm^{2} s^{-1}.[41] The following sections will discuss the impedance behavior of transition metal oxide cathodes and graphite anodes, as these materials are the most common electrode materials used in LIBs.

As transition metal oxide cathode materials are cycled in a battery several times, three main features arise in the Nyquist plots. These features are a low frequency semi-circle, medium frequency semi-circle, and a low frequency tail representing the impedance behavior of the surface layer, charge transfer at the electrode material, and diffusion impedance, respectively.[24,42] Concerning transition metal oxide intercalation materials, in particular, a third semi-circle can also be seen as the SOC of the material is decreases. This third semi-circle arises from changes to the electronic properties of the intercalation material when Li-ions are removed from the lattice.[42] It should be noted, however, that these are generalization and that some intercalation materials may not exhibit these shapes in a Nyquist plot. Thus, it is imperative to reference the literature regarding the specific material under investigation to understand the nuances governing the impedance phenomena of the system in question.

When pristine graphite anode materials in a LIB, three distinct features in a Nyquist plot. These features are a high frequency semi-circle, a medium frequency semi-circle, and a low frequency tail feature relating to graphite particle to current collector resistance, charge transfer at the electrode-electrolyte interface, and diffusion impedance, respectively.[43,44] As graphite anode is cycled the high frequency semi-circle does not exhibit large changes, while the medium and low frequency features demonstrate a large dependence of the SOC of the electrode.[21] As the potential at the graphite anode becomes more negative (more Li-ions inserted) the medium frequency semi-circle decreases in size. The low frequency tail feature, related to the diffusion impedance, becomes more vertical as the SOC of the graphite electrode is increased, which is indicative of the presence of a reflective boundary.

Conversion electrodes

Conversion electrode materials are classified as materials that store charge (in the form of active ions) through the formation of a new phase between the active ion and the host material. The canonical example of these materials is Si, which can store 3.75 Li-ions for each unit of Si in the electrode.[45] These materials allow for much greater charger storage compared to intercalation materials yet are significantly more unstable due to the formation and breakdown of chemical bonds during the (dis)charge processes at a battery electrode. Concerning EIS, the impedance of conversion electrodes is generally dominated by the R_{ct}.[14,46] Another way to think of this is that the kinetics of the conversion reaction (between active ion and electrode material) is the rate limiting step of the ion insertion process, and thus contributes most to the impedance. Although these materials, also, generally have small D_{Li} ($x10^{-11}$-$x10^{-13}$ cm^2 s^{-1} for Si) however the kinetics of the conversion reaction are, usually, the most dominant factor in the impedance spectra for these systems.

A plethora of conversion electrode materials (Si, Sn, Sb, P, etc.) are available for application in rechargeable battery systems and, not surprisingly, each system will have its own characteristic behavior. There are, however, some factors that affect the impedance response of conversion electrodes as a class of materials. These factors include the solid-electrolyte interphase (SEI) and advanced electrode configurations.

An example of the effect of the SEI on EIS spectra for conversion electrodes can be found in the work of Williamson et al. These authors studied how temperature affected the electrochemical characteristics of a Sb nanocrystalline anode for sodium-ion batteries, and by conducting EIS as a function of potential and temperature were able to determine that the charge transfer resistance was the biggest contributor to capacity fade over a wide range of temperatures.[14] This study, also, calculated the exchange current density of the Sb electrodes showing that the j_0 parameter increased as a function of temperature. Concerning the SEI, the EIS spectra exhibited medium frequency regions with oblong charge-transfer semi circles which is characteristic of the presence of SEI on an electrode. To account for this surface film, the authors included an additional R||C component in their ECM to model the resistive and capacitive behavior of the SEI.[14] The inclusion of an R||C component to model the impedance behavior of the SEI on an electrode material is incredibly common in the battery literature.[14,33,34]

Application of advanced electrode configurations (i.e. nanoparticle sized active material or composite electrode systems) have been clearly shown to improve the performance of conversion electrode materials.[47,48] These improvements arise because nano-particle scales active materials are better able to manage the detrimental effects of conversion electrode volume expansion, while application of composite electrode systems can increase both the active surface area and electrical conductivity of these systems. The work of Guo et al. investigated how different composite electrode configurations affected the impedance behavior of Si nanoparticle anodes in LIBs. This study was able to determine that the type of composite formed has a great effect on the resulting impedance measurements.[34]

Alkali metal electrodes

In rechargeable batteries, energy dense electrode materials are of great interest as they can maximize the amount of charge stored per unit mass of material. The most energy dense anode material available for application in LIBs is the Li-metal anode. A Li-metal anode leverages the

Li/Li^+ redox couple which has the lowest redox potential (compared to the normal hydrogen electrode) and a theoretical capacity of 3860 mAh/g.[49] This system, while providing extremely high capacities, is inherently unstable due to the ductility and surface roughness of Li-metal, resulting is extreme dendrite formation which usually leads to shorting of the cell.[50] These anodes, also, have been shown to be unstable when in contact with liquid electrolytes, even when the cell has not been cycled. [51]

Given the potential impact of Li-metal anodes on the amount of charge a LIB can store, massive efforts have been made in the field aimed at stabilizing these systems. Some of the approaches examined for Li-metal anode stabilization include surface engineering[49], investigations into interactions with liquid electrolytes[51], and by changing the stack pressure applied to the Li-metal anode during fabrication.[52]

Concerning EIS, Li-metal anodes still demonstrate spectral dependance on the external factors highlighted in **Section 4.3**.[53] More specifically, symmetric cells are usually used in the EIS analysis of Li-metal cells as this cell configuration provides insight into the stability Li-metal electrodes. The work of Zhang et al. clearly demonstrates how the impedances of Li-metal electrodes increased greatly with cycle number, while the work of He et al. showed that the impedance Li-metal electrodes increased when stored in with liquid electrolyte over several days (Zhang et al. 2005, He et al. 2020).[51,53] Both studies, interestingly, examined the effect of lithium fluoride (LiF) passivation layers on Li-metal anodes to understand how LiF stabilizes this system. Concerning cycle life, LiF layers were shown to reduce the increase in impedance because of battery cycling compared to the Li-metal, not passivated, control.[53] Regarding shelf stability, LiF layers were shown to greatly reduce the increase in impedance seen when Li-metal anodes are stored with liquid electrolytes.

References:

(1) Bard, J. A.; Faulkner, R. L. *Electrochemical Methods, Fundamentals and Applications*; John Wiley & Sons, Inc: New York City, 2001.

(2) Cohen, H. *Complex Analysis with Applications in Science and Engineering*; Springer US: Boston, MA, 2007. https://doi.org/10.1007/978-0-387-73058-5.

(3) Lazanas, A. Ch.; Prodromidis, M. I. Electrochemical Impedance Spectroscopy─A Tutorial. *ACS Meas. Sci. Au* **2023**, *3* (3), 162–193. https://doi.org/10.1021/acsmeasuresciau.2c00070.

(4) Mark E. Orazem; Bernard Tribollet. *Electrochemical Impedance Spectroscopy*; John Wiley & Sons, 2008.

(5) Lasia, A. *Electrochemical Impedance Spectroscopy and Its Applications*; Springer New York: New York, NY, 2014. https://doi.org/10.1007/978-1-4614-8933-7.

(6) Cruz-Manzo, S.; Greenwood, P. An Impedance Model Based on a Transmission Line Circuit and a Frequency Dispersion Warburg Component for the Study of EIS in Li-Ion Batteries. *J. Electroanal. Chem.* **2020**, *871*, 114305. https://doi.org/10.1016/j.jelechem.2020.114305.

(7) Barcellona, S.; Colnago, S.; Codecasa, L.; Piegari, L. Unified Model of Lithium-Ion Battery and Electrochemical Storage System. *J. Energy Storage* **2023**, *73*, 109202. https://doi.org/10.1016/j.est.2023.109202.

(8) Keiser, H.; Beccu, K. D.; Gutjahr, M. A. Abschätzung Der Porenstruktur Poröser Elektroden Aus Impedanzmessungen. *Electrochimica Acta* **1976**, *21* (8), 539–543. https://doi.org/10.1016/0013-4686(76)85147-X.

(9) Cooper, S. J.; Bertei, A.; Finegan, D. P.; Brandon, N. P. Simulated Impedance of Diffusion in Porous Media. *Electrochimica Acta* **2017**, *251*, 681–689. https://doi.org/10.1016/j.electacta.2017.07.152.

(10) Zhu, S.; Sun, X.; Gao, X.; Wang, J.; Zhao, N.; Sha, J. Equivalent Circuit Model Recognition of Electrochemical Impedance Spectroscopy via Machine Learning. *J. Electroanal. Chem.* **2019**, *855*, 113627. https://doi.org/10.1016/j.jelechem.2019.113627.

(11) Iurilli, P.; Brivio, C.; Wood, V. On the Use of Electrochemical Impedance Spectroscopy to Characterize and Model the Aging Phenomena of Lithium-Ion Batteries: A Critical Review. *J. Power Sources* **2021**, *505*, 229860. https://doi.org/10.1016/j.jpowsour.2021.229860.

(12) Deleebeeck, L.; Veltzé, S. Electrochemical Impedance Spectroscopy Study of Commercial Li-ion Phosphate Batteries: A Metrology Perspective. *Int. J. Energy Res.* **2020**, *44* (9), 7158–7182. https://doi.org/10.1002/er.5350.

(13) Lasia, A. The Origin of the Constant Phase Element. *J. Phys. Chem. Lett.* **2022**, *13* (2), 580–589. https://doi.org/10.1021/acs.jpclett.1c03782.

(14) Williamson, G. A.; Hu, V. W.; Yoo, T. B.; Affandy, M.; Opie, C.; Paradis, E. K.; Holmberg, V. C. Temperature-Dependent Electrochemical Characteristics of Antimony Nanocrystal Alloying Electrodes for Na-Ion Batteries. *ACS Appl. Energy Mater.* **2019**, *2* (9), 6741–6750. https://doi.org/10.1021/acsaem.9b01216.

(15) Westerhoff, U.; Kurbach, K.; Lienesch, F.; Kurrat, M. Analysis of Lithium-Ion Battery Models Based on Electrochemical Impedance Spectroscopy. *Energy Technol.* **2016**, *4* (12), 1620–1630. https://doi.org/10.1002/ente.201600154.

(16) Diard, J.-P.; Le Gorrec, B.; Montella, C. EIS Study of Electrochemical Battery Discharge on Constant Load. *J. Power Sources* **1998**, *70* (1), 78–84. https://doi.org/10.1016/S0378-7753(97)02668-2.

(17) Wang, P.; Yan, D.; Wang, C.; Ding, H.; Dong, H.; Wang, J.; Wu, S.; Cui, X.; Li, C.; Zhao, D.; Li, S. Study of the Formation and Evolution of Solid Electrolyte Interface via In-Situ Electrochemical Impedance Spectroscopy. *Appl. Surf. Sci.* **2022**, *596*, 153572. https://doi.org/10.1016/j.apsusc.2022.153572.

(18) Gimble, N. J.; Kraynak, L. A.; Schneider, J. D.; Schulze, M. C.; Prieto, A. L. X-Ray Photoelectron Spectroscopy as a Probe for Understanding the Potential-Dependent Impact of Fluoroethylene Carbonate on the Solid Electrolyte Interface Formation in Na/Cu2Sb Batteries. *J. Power Sources* **2021**, *489*. https://doi.org/10.1016/j.jpowsour.2020.229171.

(19) Marino, C.; Darwiche, A.; Dupré, N.; Wilhelm, H. A.; Lestriez, B.; Martinez, H.; Dedryvère, R.; Zhang, W.; Ghamouss, F.; Lemordant, D.; Monconduit, L. Study of the Electrode/Electrolyte Interface on Cycling of a Conversion Type Electrode Material in Li Batteries. *J. Phys. Chem. C* **2013**, *117* (38), 19302–19313. https://doi.org/10.1021/jp402973h.

(20) Choi, W.; Shin, H.-C.; Kim, J. M.; Choi, J.-Y.; Yoon, W.-S. Modeling and Applications of Electrochemical Impedance Spectroscopy (EIS) for Lithium-Ion Batteries. *J. Electrochem. Sci. Technol.* **2020**, *11* (1), 1–13. https://doi.org/10.33961/jecst.2019.00528.

(21) Meddings, N.; Heinrich, M.; Overney, F.; Lee, J.-S.; Ruiz, V.; Napolitano, E.; Seitz, S.; Hinds, G.; Raccichini, R.; Gaberšček, M.; Park, J. Application of Electrochemical Impedance Spectroscopy to Commercial Li-Ion Cells: A Review. *J. Power Sources* **2020**, *480*, 228742. https://doi.org/10.1016/j.jpowsour.2020.228742.

(22) Xu, C.; Zeng, Y.; Rui, X.; Zhu, J.; Tan, H.; Guerrero, A.; Toribio, J.; Bisquert, J.; Garcia-Belmonte, G.; Yan, Q. Amorphous Iron Oxyhydroxide Nanosheets: Synthesis, Li Storage, and Conversion Reaction Kinetics. *J. Phys. Chem. C* **2013**, *117* (34), 17462–17469. https://doi.org/10.1021/jp405848j.

(23) Dashairya, L.; Das, D.; Saha, P. Binder-Free Electrophoretic Deposition of Sb/rGO on Cu Foil for Superior Electrochemical Performance in Li-Ion and Na-Ion Batteries. *Electrochimica Acta* **2020**, *358*, 136948. https://doi.org/10.1016/j.electacta.2020.136948.

(24) Wang, L.; Zhao, J.; He, X.; Gao, J.; Li, J.; Wan, C.; Jiang, C. Electrochemical Impedance Spectroscopy (EIS) Study of LiNi1/3Co1/3Mn1/3O2 for Li-Ion Batteries. *Int. J. Electrochem. Sci.* **2012**, *7* (1), 345–353. https://doi.org/10.1016/S1452-3981(23)13343-8.

(25) Voiry, D.; Chhowalla, M.; Gogotsi, Y.; Kotov, N. A.; Li, Y.; Penner, R. M.; Schaak, R. E.; Weiss, P. S. Best Practices for Reporting Electrocatalytic Performance of Nanomaterials. *ACS Nano* **2018**, *12* (10), 9635–9638. https://doi.org/10.1021/acsnano.8b07700.

(26) Deng, C.; Lu, W. Consistent Diffusivity Measurement between Galvanostatic Intermittent Titration Technique and Electrochemical Impedance Spectroscopy. *J. Power Sources* **2020**, *473*, 228613. https://doi.org/10.1016/j.jpowsour.2020.228613.

(27) Ko, J. K.; Wiaderek, K. M.; Pereira, N.; Kinnibrugh, T. L.; Kim, J. R.; Chupas, P. J.; Chapman, K. W.; Amatucci, G. G. Transport, Phase Reactions, and Hysteresis of Iron Fluoride and Oxyfluoride Conversion Electrode Materials for Lithium Batteries. *ACS Appl. Mater. Interfaces* **2014**, *6* (14), 10858–10869. https://doi.org/10.1021/am500538b.

(28) Aurbach, D.; Levi, M. D.; Levi, E. A Review on the Solid-State Ionics of Electrochemical Intercalation Processes: How to Interpret Properly Their Electrochemical Response. *Solid State Ion.* **2008**, *179* (21–26), 742–751. https://doi.org/10.1016/j.ssi.2007.12.070.

(29) Wang, X.; Wei, X.; Dai, H. Estimation of State of Health of Lithium-Ion Batteries Based on Charge Transfer Resistance Considering Different Temperature and State of Charge. *J. Energy Storage* **2019**, *21*, 618–631. https://doi.org/10.1016/j.est.2018.11.020.

(30) Mingant, R.; Bernard, J.; Sauvant Moynot, V.; Delaille, A.; Mailley, S.; Hognon, J.-L.; Huet, F. EIS Measurements for Determining the SoC and SoH of Li-Ion Batteries. *ECS Trans.* **2011**, *33* (39), 41–53. https://doi.org/10.1149/1.3589920.

(31) Zhang, M.; Liu, Y.; Li, D.; Cui, X.; Wang, L.; Li, L.; Wang, K. Electrochemical Impedance Spectroscopy: A New Chapter in the Fast and Accurate Estimation of the State of Health for Lithium-Ion Batteries. *Energies* **2023**, *16* (4), 1599. https://doi.org/10.3390/en16041599.

(32) Vadhva, P.; Hu, J.; Johnson, M. J.; Stocker, R.; Braglia, M.; Brett, D. J. L.; Rettie, A. J. E. Electrochemical Impedance Spectroscopy for All-Solid-State Batteries: Theory, Methods and Future Outlook. *ChemElectroChem* **2021**, *8* (11), 1930–1947. https://doi.org/10.1002/celc.202100108.

(33) Nieto, K.; Windsor, D. S.; Kale, A. R.; Gallawa, J. R.; Medina, D. A.; Prieto, A. L. Structural Control of Electrodeposited Sb Anodes through Solution Additives and Their Influence on Electrochemical Performance in Na-Ion Batteries. *J. Phys. Chem. C* **2023**, *127* (26), 12415–12427. https://doi.org/10.1021/acs.jpcc.3c01086.

(34) Guo, J.; Sun, A.; Chen, X.; Wang, C.; Manivannan, A. Cyclability Study of Silicon–Carbon Composite Anodes for Lithium-Ion Batteries Using Electrochemical Impedance Spectroscopy. *Electrochimica Acta* **2011**, *56* (11), 3981–3987. https://doi.org/10.1016/j.electacta.2011.02.014.

(35) Kundu, S.; Kraytsberg, A.; Ein-Eli, Y. Recent Development in the Field of Ceramics Solid-State Electrolytes: I—Oxide Ceramic Solid-State Electrolytes. *J. Solid State Electrochem.* **2022**, *26* (9), 1809–1838. https://doi.org/10.1007/s10008-022-05206-x.

(36) Iriyama, Y.; Kako, T.; Yada, C.; Abe, T.; Ogumi, Z. Charge Transfer Reaction at the Lithium Phosphorus Oxynitride Glass Electrolyte/Lithium Cobalt Oxide Thin Film Interface. *Solid State Ion.* **2005**, *176* (31–34), 2371–2376. https://doi.org/10.1016/j.ssi.2005.02.025.

(37) Xie, J.; Imanishi, N.; Zhang, T.; Hirano, A.; Takeda, Y.; Yamamoto, O. Li-Ion Transport in All-Solid-State Lithium Batteries with LiCoO2 Using NASICON-Type Glass Ceramic Electrolytes. *J. Power Sources* **2009**, *189* (1), 365–370. https://doi.org/10.1016/j.jpowsour.2008.08.015.

(38) Märker, K.; Xu, C.; Grey, C. P. Operando NMR of NMC811/Graphite Lithium-Ion Batteries: Structure, Dynamics, and Lithium Metal Deposition. *J. Am. Chem. Soc.* **2020**, *142* (41), 17447–17456. https://doi.org/10.1021/jacs.0c06727.

(39) Zhu, J.; Ding, Y.; Ma, Z.; Tang, W.; Chen, X.; Lu, Y. Recent Progress on Nanostructured Transition Metal Oxides As Anode Materials for Lithium-Ion Batteries. *J. Electron. Mater.* **2022**, *51* (7), 3391–3417. https://doi.org/10.1007/s11664-022-09662-z.

(40) Mizushima, K.; Jones, P. C.; Wiseman, P. J.; Goodenough, J. B. A NEW CATHODE MATERIAL FOR BATTERIES OF HIGH ENERGY DENSITY. *15* (6).

(41) Nitta, N.; Wu, F.; Lee, J. T.; Yushin, G. Li-Ion Battery Materials: Present and Future. *Mater. Today* **2015**, *18* (5), 252–264. https://doi.org/10.1016/j.mattod.2014.10.040.

(42) Zhuang, Q.-C.; Wei, T.; Du, L.-L.; Cui, Y.-L.; Fang, L.; Sun, S.-G. An Electrochemical Impedance Spectroscopic Study of the Electronic and Ionic Transport Properties of Spinel $LiMn_2O_4$. *J. Phys. Chem. C* **2010**, *114* (18), 8614–8621. https://doi.org/10.1021/jp9109157.

(43) Martinent, A.; Le Gorrec, B.; Montella, C.; Yazami, R. Three-Electrode Button Cell for EIS Investigation of Graphite Electrode. *J. Power Sources* **2001**, *97–98*, 83–86. https://doi.org/10.1016/S0378-7753(01)00592-4.

(44) Wang, C.; Appleby, A. J.; Little, F. E. Electrochemical Impedance Study of Initial Lithium Ion Intercalation into Graphite Powders. *Electrochimica Acta* **2001**, *46* (12), 1793–1813. https://doi.org/10.1016/S0013-4686(00)00782-9.

(45) Bärmann, P.; Krueger, B.; Casino, S.; Winter, M.; Placke, T.; Wittstock, G. Impact of the Crystalline Li 15 Si 4 Phase on the Self-Discharge Mechanism of Silicon Negative Electrodes in Organic Electrolytes. *ACS Appl. Mater. Interfaces* **2020**. https://doi.org/10.1021/acsami.0c16742.

(46) Paloukis, F.; Elmasides, C.; Farmakis, F.; Selinis, P.; Neophytides, S. G.; Georgoulas, N. Electrochemical Impedance Spectroscopy Study in Micro-Grain Structured Amorphous Silicon Anodes for Lithium-Ion Batteries. *J. Power Sources* **2016**, *331*, 285–292. https://doi.org/10.1016/j.jpowsour.2016.09.062.

(47) Li, M.; Liu, Y.; Qin, B.; Lu, C.; Butt, H. A.; Zheng, T.; Zhang, D. Polyaniline-Coated Nanoporous Antimony with Improved Performance for Sodium-Ion Battery Anodes. *J. Alloys Compd.* **2021**, *861*. https://doi.org/10.1016/j.jallcom.2021.158647.

(48) Piper, D. M.; Yersak, T. A.; Son, S. B.; Kim, S. C.; Kang, C. S.; Oh, K. H.; Ban, C.; Dillon, A. C.; Lee, S. H. Conformal Coatings of Cyclized-PAN for Mechanically Resilient Si Nano-Composite Anodes. *Adv. Energy Mater.* **2013**, *3* (6), 697–702. https://doi.org/10.1002/aenm.201200850.

(49) Liu, S.; Ma, Y.; Wang, J.; Zuo, P.; Du, C.; Yin, G.; Gao, Y. Regulating Li Deposition by Constructing Homogeneous LiF Protective Layer for High-Performance Li Metal Anode. *Chem. Eng. J.* **2022**, *427*, 131625. https://doi.org/10.1016/j.cej.2021.131625.

(50) Bieker, G.; Winter, M.; Bieker, P. Electrochemical in Situ Investigations of SEI and Dendrite Formation on the Lithium Metal Anode. *Phys. Chem. Chem. Phys.* **2015**, *17* (14), 8670–8679. https://doi.org/10.1039/C4CP05865H.

(51) He, M.; Guo, R.; Hobold, G. M.; Gao, H.; Gallant, B. M. The Intrinsic Behavior of Lithium Fluoride in Solid Electrolyte Interphases on Lithium. https://doi.org/10.1073/pnas.1911017116/-/DCSupplemental.

(52) Raj, R. Stack Pressure and Critical Current Density in Li-Metal Cells: The Role of Mechanical Deformation. *Acta Mater.* **2021**, *215*, 117076. https://doi.org/10.1016/j.actamat.2021.117076.

(53) Zhang, S. S.; Xu, K.; Jow, T. R. EIS Study on the Formation of Solid Electrolyte Interface in Li-Ion Battery. *Electrochimica Acta* **2006**, *51* (8–9), 1636–1640. https://doi.org/10.1016/j.electacta.2005.02.137.